

**The Effects of Free Stream Turbulence on the Flow Field
through a Compressor Cascade**

Chittiappa Muthanna

**Dissertation submitted to the faculty of the Virginia Polytechnic
Institute and State University in partial fulfillment of the
requirements for the degree of**

**Doctor of Philosophy
in
Aerospace Engineering**

**William J. Devenport, Chair
Saad A. Ragab
Joseph A. Schetz
Roger L. Simpson
Karen A. Thole**

**May 24th, 2002
Blacksburg, Virginia**

Keywords: Compressor, Cascade, Free Stream Turbulence, Hot Wire Anemometry

Copyright 2002, Chittiappa Muthanna

The Effects of Free Stream Turbulence on the Flow Field through a Compressor Cascade

Chittiappa Muthanna

(Abstract)

The flow through a compressor cascade with tip leakage has been studied experimentally. The cascade of GE rotor B section blades had an inlet angle of 65.1° , a stagger angle of 56.9° , and a solidity of 1.08. The final turning angle of the cascade was 11.8° . This compressor configuration was representative of the core compressor of an aircraft engine. The cascade was operated with a tip gap of 1.65%, and operated at a Reynolds number based on the chord length (0.254 m) of 388,000. Measurements were made at 8 axial locations to reveal the structure of the flow as it evolved through the cascade. Measurements were also made to reveal the effects of grid generated turbulence on this flow. The data set is unique in that not only does it give a comparison of elevated free stream turbulence effects, but also documents the developing flow through the blade row of a compressor cascade with tip leakage.

Measurements were made at a total of 8 locations 0.8, 0.23 axial chords upstream and 0, 0.27, 0.48, 0.77, 0.98, and 1.26 axial chords downstream of the leading edge of the blade row for both inflow turbulence cases. The measurements revealed the formation and development of the tip leakage vortex within the passage. The tip leakage vortex becomes apparent at approximately $X/c_a = 0.27$ and dominated much of the endwall flow. The tip leakage vortex is characterized by high streamwise velocity deficits, high vorticity and high turbulence kinetic energy levels. The result showed that between 0.77 and 0.98 axial chords downstream of the leading edge, the vortex structure and behavior changes.

The effects of grid generated turbulence were also documented. The results revealed significant effects on the flow field. The results showed a 4% decrease in the blade loading and a 20% reduction in the vorticity levels within tip leakage vortex. There was also a shift in the vortex path, showing a shift close to the suction side with grid generated turbulence, indicating the strength of the vortex was decreased. Circulation calculations showed this reduction, and also indicated that the tip leakage vortex increased in size by about 30%. The results revealed that overall, the turbulence kinetic energy levels in the tip leakage vortex were increased, with the most drastic change occurring at $X/c_a = 0.77$.

Acknowledgements

I would like to acknowledge some of the people that have been involved both directly and indirectly in making this work possible.

My parents, Takku and Puthuli Muthanna, who gave me the values and lessons in life and the motivation to accomplish goals that I had not thought possible. My grandparents, Muthu thatha, Ponnithai, Sharada avva, and Pitha thatha who have always looked out for me, and given me their blessings. Thank you.

My advisor, and mentor Dr. William J. Devenport, for giving me this opportunity. His guidance, motivation and patience have proved invaluable in helping me complete this work but it was his belief in me that ultimately led to its conclusion.

Dr. S. Ragab, Dr. J. Schetz, Dr. R. Simpson, and Dr. K. Thole for their time and advice while serving on my committee. I would like to mention Dr. J. F. Marchman, and Dr. B. Grossman for enhancing my education while completing this work. Also, I would like to thank Greg Dudding, Bruce Stanger, Kent Morris, Gary Stafford, and Mike Vaught in the Aerospace shop. The support of the Office of Naval Research, under grants N00014-99-1-0230 and N00014-01-1-0406, is gratefully acknowledged.

My friends in the lab, Patrick, Diego, Ruolong, JV, Aurelian, Nicolas, and Derek for helping when needed but more importantly who brought out the lighter side of research work.

And lastly, to Tone and Shaloot, thanks for being there, and helping me to get up whenever I felt down.

Chittiappa.

Table of Contents

Nomenclature	vii
List of Tables	ix
List of Figures.....	x
1. Introduction.....	1
1.1. Motivation and Purpose	1
1.2. Prior Studies on Compressor Cascades.....	2
1.3. Prior Studies on Compressor Rotors	4
1.4. Prior Studies on Free Stream Turbulence Effects on Boundary Layers.....	6
1.5. Prior Studies on Free Stream Turbulence Effects on Turbomachinery configurations.....	8
1.6. Prior Studies in the Virginia Tech Low Speed Cascade Wind Tunnel.....	9
1.6.1. Stationary endwall studies	9
1.6.2. Moving endwall studies	12
1.7. Objectives of the Present Work.....	13
1.8. Approach of the present study	15
1.8.1. Organization of the dissertation	15
2. Apparatus and Instrumentation.....	23
2.1. Virginia Tech Cascade Wind Tunnel.....	23
2.2. Test Section.....	23
2.2.1. Inlet Section	24
2.2.1.1. Boundary Layer Scoops and Upstream Bleeds	24
2.2.1.2. Sidewall Scoops	26
2.2.2. Downstream Section	26
2.2.2.1. Blade Row.....	27
2.2.2.2. Downstream of the blade row.....	30
2.2.2.3. Exit Plane Screens.....	31
2.3. Turbulence Generating Grid	31

2.4.	<i>Hot Wire Anemometry</i>	32
2.4.1.	Hot Wire Probes.....	32
2.4.2.	Anemometry	33
2.4.3.	Probe Mounting and Positioning.....	34
2.4.3.1.	Traverse System.....	34
2.4.3.2.	Four-sensor hot-wire probes.....	34
2.4.3.3.	Single-sensor hot-wire probes.....	35
2.5.	<i>Pressure Measurement System</i>	35
2.5.1.	Pitot-Static Probe and Blade Pressure Ports.....	36
2.5.2.	Pressure Transducers	36
2.5.3.	Probe Positioning.....	37
2.6.	<i>Oil Flow Visualization</i>	37
2.7.	<i>Calibration of the Cascade Tunnel</i>	37
3.	Results and Discussion.....	65
3.1.	<i>Data sampling and presentation</i>	65
3.1.1.	Co-ordinate system	65
3.1.2.	Measurement Conditions	66
3.1.3.	Sampling Schemes.....	67
3.2.	<i>Blade Loading</i>	67
3.3.	<i>Surface Oil Flow Visualizations</i>	69
3.4.	<i>Inflow to the cascade</i>	70
3.4.1.	Axial location $X/c_a = -0.80$	71
3.4.2.	Axial location $X/c_a = -0.23$	74
3.5.	<i>The Potential Core Region</i>	77
3.6.	<i>Lower Endwall Region</i>	79
3.6.1.	Mean Flowfield Structure	79
3.6.1.1.	The Streamwise Vorticity Field, Definition of the Vortex Center	80
3.6.1.2.	Mean Velocity Field.....	85
3.6.1.3.	Circulation in the Tip Leakage Vortex.....	87
3.6.2.	Turbulent Flow Field	89
3.6.2.1.	Turbulence Kinetic Energy	89
3.6.2.2.	Turbulence normal stresses	90
3.6.2.3.	Effects of grid generated turbulence	91

3.6.2.4. Turbulence Kinetic Energy Production	94
3.6.3. Velocity Spectra.....	97
4. Conclusions.....	208
4.1. <i>Conclusions concerning flow structure without grid turbulence.....</i>	<i>208</i>
4.2. <i>Conclusions concerning the effects of grid generated turbulence on the flow structure. ...</i>	<i>210</i>
References.....	212
Appendix: Uncertainty Analysis.....	217
<i>A.1 Pressure Measurements</i>	<i>217</i>
<i>A.2 Hot Wire Measurements.....</i>	<i>218</i>

Nomenclature

c	chord length, $0.254m$
c_a	Axial chord of the blade, $0.138m$
cm	Centimeter
C_p	Co-efficient of pressure defined as $\frac{p - p_\infty}{p_{0\infty} - p_\infty}$
C_{p0}	Coefficient of pressure defined as $\frac{p_0 - p_\infty}{p_{0\infty} - p_\infty}$
δ	Boundary layer thickness
δ^*	Displacement thickness $\int_0^{y_{\max}} (1 - U/U_e) dy$
$E[]$	Expected value
f	Frequency, Hz
ft	Foot
G_{uu}, G_{vv}, G_{ww}	Autospectra defined as $2 \int_0^\infty R_{xx}(\tau) \cos(2\pi f\tau) d\tau$ in the u direction (m^2/s^2)
Γ	Circulation computed as the line integral over an area $\int_{Area} \Omega \cdot \hat{n} dA$
$\Gamma()$	Gamma function
H	Normalized mean Helicity defined as $\frac{\bar{V} \cdot \bar{\Omega}}{ \bar{V} \bar{\Omega} }$
$h.p.$	Horse power
Hz	Hertz, (s^{-1})
in	Inch
k	Turbulence kinetic energy, $\frac{1}{2} \left(\frac{u^2 + v^2 + w^2}{U_\infty^2} \right)$
k	wavenumber, $2\pi f/U_\infty$ (m)
k_e	$0.75/\Lambda_f$ (m^{-1})
$\Lambda_u, \Lambda_v, \Lambda_w$	Lengthscale defined as $\frac{1}{2} \frac{U \int_{-\infty}^\infty R_{uu}(\tau) d\tau}{u^2}$ in the u direction, (m)
m	Meter
mm	Millimeter
ν	Kinematic viscosity
P_t	Total pressure

P_2	Static pressure
P_a	Atmospheric pressure
P_{ref}	Reference pressure
θ	Momentum thickness $\int_0^{y_{max}} (1 - U/U_e) U/U_e dy$
θ_y	rotation about the y-axis
R	autocorrelation function defined as $E[u(t)u(t+\tau)]$
ρ	Density
ρ_∞	Free Stream density
s	Second
τ	time delay
U	Mean Streamwise Velocity, in the x direction
u^2	Fluctuating component of streamwise velocity, also defined as the Reynolds Normal Stress
U_1	Mean Axial Velocity, in the X direction
U_∞	Free stream velocity
$U_{average}$	Average velocity
U_e	Edge velocity
U_i	Instantaneous velocity defined as $U+u$
\vec{V}	Velocity vector
V, V_1	Mean velocity in the y (Y)-direction
v^2	Fluctuating component of velocity in y -direction, also defined as the Reynolds Normal Stress
$Volt$	Volt
W	Mean tangential velocity in the z direction, also defined as the Reynolds Normal Stress
$\vec{\Omega}$	Vorticity vector defined as $\nabla \times \vec{V}$
w^2	Fluctuating component of velocity in z -direction
W_1	Mean tangential velocity, axial tangential co-ordinate system
X	Location in the axial direction
x_c	Distance between the exit of the contraction and the point where the boundary layer thickness is estimated
$X_k()$	Fast Fourier Transform
y, Y	Location in the vertical direction above the lower endwall
Z	Location in the pitchwise direction

List of Tables

<i>Table 2.1: Co-ordinates of the GE rotor B section.....</i>	<i>27</i>
<i>Table 3.1: Rotation angles θ_i to get U, V, W from U_i, V_i, W_i.....</i>	<i>66</i>
<i>Table 3.2: Location of separation line between tip vortex and lower endwall flow (Figure 3.6).....</i>	<i>69</i>
<i>Table 3.3: Uncertainties of measured quantities in the four sensor hot-wire for the two flows (with and without grid generated turbulence)</i>	<i>70</i>
<i>Table 3.4: Characteristics of grid turbulence used to compute the von Kàrmàn interpolation</i>	<i>73</i>
<i>Table 3.5: Boundary layer parameters at $X/c_a = -0.23$.....</i>	<i>77</i>
<i>Table 3.6: Location of vortex centers are determined by peak streamwise vorticity.....</i>	<i>81</i>
<i>Table 3.7: Location of points in vortex where H (normalized mean helicity)=1.....</i>	<i>84</i>
<i>Table 3.8: Location of points in tip leakage vortex in the vicinity of the vortex center of maximum velocity deficit.....</i>	<i>86</i>
<i>Table 3.9: Radius as implied by the peak circumferentially averaged velocity from Figure 3.46b, and the circulation implied by these radii.....</i>	<i>89</i>
<i>Table 3.10: Contributions to the total turbulence kinetic energy production due to streamwise and crossflow velocity gradients.....</i>	<i>96</i>
<i>Table 3.11: Locations of velocity spectra presented in Figures 3.56-3.58,.....</i>	<i>97</i>
<i>Table A1: Uncertainties for the four sensor hot wire probe.....</i>	<i>218</i>
<i>Table A2: Uncertainties for the single hot wire probe, for both flow cases.....</i>	<i>218</i>

List of Figures

Figure 1.1: Sketch showing the various flow features seen in compressor cascade type flows inferred from previous studies.....	17
Figure 1.2: Results from Muthanna (1998) showing (a) Mean streamwise velocity contours and (b) Mean streamwise vorticity contours.....	18
Figure 1.3: Results from Muthanna (1998) showing contours of the normalized turbulence kinetic energy:.....	19
Figure 1.4: Flow features observed in the study by Muthanna (1998). Note the presence of a second vortex in addition to the tip leakage vortex.....	20
Figure 1.5: Results from the computation by Shin (2001) showing (a) Mean streamwise velocity contours and (b) Mean Crossflow velocity contours (Note the presence of a secondary vortex).....	21
Figure 1.6: Results from the computation by Shin (2001) showing the two dimensional calculation of the mean velocity field away at the mid-span location for the flow through the cascade.....	22
Figure 2.1: Virginia Tech Linear Compressor Cascade Tunnel.....	41
Figure 2.2: Plan-view of the Virginia Tech Cascade Wind Tunnel Test Section.....	42
Figure 2.3: Cross section of the inlet section.....	43
Figure 2.4: Cross section of the suction slots.....	44
Figure 2.5: Upstream bleed on the lower endwall.....	44
Figure 2.6: Sidewall scoop covers to control the amount of flow being drawn out of the inlet section.....	45
Figure 2.7: Cross section of the GE rotor B blade used in the Cascade.....	46
Figure 2.8a: Top view of blade support structure.....	47
Figure 2.8b: View of the blade row inserted into the test section.....	47
Figure 2.9: Cascade Geometry Parameters.....	48
Figure 2.10: Upper and Lower Endwall details in the blade row.....	49
Figure 2.11: Downstream sidewall-blade attachment configuration.....	50
Figure 2.12: Upper endwall mounting configuration downstream of Blade Row.....	51
Figure 2.13: Screens at the exit plane of the tunnel.....	52
Figure 2.14: Cascade Tunnel general view.....	52
Figure 2.15: Layout of the grid.....	53
Figure 2.16: Position of grid relative to blade row.....	53
Figure 2.17a: Four Sensor Hot-Wire Probe.....	54
Figure 2.17b: TSI Model 1218 Standard Boundary Layer Probe.....	54
Figure 2.17c: TSI Model 1210 General Purpose Probe.....	54
Figure 2.18: Measurement locations.....	55
Figure 2.19: Traverse System.....	55
Figure 2.20: Mounting arrangement for the Four Sensor Hot-Wire Probes.....	56
Figure 2.21a: Mounting arrangement for the Four Sensor Hot-Wire Probes for the upstream and downstream measurement location.....	57
Figure 2.21b: Mounting arrangement for the Four Sensor Hot-Wire Probes for the inpassage measurement location.....	57

Figure 2.22: Mounting arrangement for the Four Sensor Hot-Wire Probes for the inpassage measurement location.....	58
Figure 2.23: Mounting arrangement for the single-sensor hot-wire probes.....	59
Figure 2.24: Figure of the Pitot-Static Probe.....	60
Figure 2.25: Surface pressure ports on the blades.....	61
Figure 2.26: Velocity distribution at $X/c_a = -0.92$ after calibration of tunnel.....	62
Figure 2.27: Pitot-static measurements taken at $X/c_a = 2.6$ downstream of blade row after calibration of tunnel.....	63
Figure 2.28: Influence of Inflow Turbulence on the periodicity downstream of the blade passage at $X/c_a = 1.26$	64
Figure 3.1: Measurement locations and co-ordinate system.....	99
Figure 3.2: Measurement grids at each axial plane. An average of 180-200 data points were used at each measurement plane.....	100
Figure 3.3a: Measured pressure coefficient distribution over the blade at mid span.....	101
Figure 3.3b: 2-D computed pressure coefficient on blade from Shin(2001).....	101
Figure 3.4 : Surface oil flow visualizations taken under the passage between blades 4 and 5 for the no grid generated turbulence inflow condition.....	102
Figure 3.5 : Surface oil flow visualizations taken under the passage between blades 4 and 5 for the grid generated turbulence inflow condition.....	103
Figure 3.6: Path of the vortex-lower endwall flow separation line for the two inflow cases.....	104
Figure 3.7: Contours of Normalized Mean Streamwise Velocity, U/U_∞ , at $X/c_a = -0.80$	105
Figure 3.8: Vectors of the magnitude of the mean normalized crossflow velocity (V, W) at $X/c_a = -0.80$	106
Figure 3.9: Contours of the square root of the Reynolds Normal Stress $\sqrt{(u^2/U_\infty^2)}$ at $X/c_a = -0.80$	107
Figure 3.10: Contours of the square root of the Reynolds Normal Stress $\sqrt{(v^2/U_\infty^2)}$ at $X/c_a = -0.80$	108
Figure 3.11: Contours of the square root of the Reynolds Normal Stress $\sqrt{(w^2/U_\infty^2)}$ at $X/c_a = -0.80$	109
Figure 3.12: Contours of the normalized turbulence kinetic energy, k/U_∞^2 , at $X/c_a = -0.80$	110
Figure 3.13a : Autospectra (as indicated by the legend on the plot) normalized on U_∞^2 for the case with grid generated turbulence at $X/c_a = 0.80$. Figure 3.13b : Autospectra (as indicated by the legend on the plot) normalized on U_∞^2 for the case without grid generated turbulence at $X/c_a = 0.80$	111
Figure 3.14 : Space Time correlations of the flow at the midheight of the passage at $Z/c_a = -1.7$, and $X/c_a = -0.80$	112
Figure 3.13b : Autospectra (as indicated by the legend on the plot) normalized on U_∞^2 for the case without grid generated turbulence at $X/c_a = 0.80$	112
Figure 3.14 : Space Time correlations of the flow at the midheight of the passage at $Z/c_a = -1.7$, and $X/c_a = -0.80$	113
Figure 3.15: Contours of the lengthscale Λ_u (cm) at $X/c_a = -0.80$	114
Figure 3.16: Contours of the lengthscale Λ_v (cm) at $X/c_a = -0.80$	115
Figure 3.17: Contours of the lengthscale Λ_w (cm) at $X/c_a = -0.80$	116
Figure 3.18: Contours of Normalized Mean Streamwise Velocity, U/U_∞ at $X/c_a = -0.23$	117
Figure 3.19: Vectors of the magnitude of the mean normalized crossflow velocity (V, W) at $X/c_a = -0.23$	118
Figure 3.20: Contours of the square root of the Reynolds Normal Stress $\sqrt{(u^2/U_\infty^2)}$ at $X/c_a = -0.23$	119
Figure 3.21: Contours of the square root of the Reynolds Normal Stress $\sqrt{(v^2/U_\infty^2)}$ at $X/c_a = -0.23$	120
Figure 3.22: Contours of the square root of the Reynolds Normal Stress $\sqrt{(w^2/U_\infty^2)}$ at $X/c_a = -0.23$	121
Figure 3.23: Contours of the normalized turbulence kinetic energy, k/U_∞^2 , at $X/c_a = -0.23$	122
Figure 3.24: Contours of lengthscale Λ_u (cm) at $X/c_a = -0.23$	123
Figure 3.25: Contours of lengthscale Λ_v (cm) at $X/c_a = -0.23$	124

Figure 3.26: Contours of lengthscale A_w (cm) at $X/c_a = -0.23$	125
Figure 3.27: Figure showing locations of the boundary layer profiles indicated by the red points at $X/c_a = -0.23$	126
Figure 3.28: Boundary layer profiles of U/U_e vs y/δ^* at $X/c_a = -0.23$	127
Figure 3.29: Boundary layer profiles of U^2/U_e^2 vs y/δ^* at $X/c_a = -0.23$	128
Figure 3.30: Boundary layer profiles of $(U^2 - U_e^2)/U_e^2$ vs y/δ^* at $X/c_a = -0.23$	129
Figure 3.31: Plan view projection of the potential core flow at $y/c_a = 0.73$. Plotted here are the contours of the mean streamwise velocity, U/U_∞	130
Figure 3.32: Plan view projection of the potential core flow at $y/c_a = 0.73$. Plotted here are the contours of the Reynolds Normal Stress $\sqrt{(u^2/U_\infty^2)}$	131
Figure 3.33: Plan view projection of the potential core flow at $y/c_a = 0.73$. Plotted here are the contours of the Reynolds Normal Stress $\sqrt{(v^2/U_\infty^2)}$	132
Figure 3.34: Plan view projection of the potential core flow at $y/c_a = 0.73$. Plotted here are the contours of the Reynolds Normal Stress $\sqrt{(w^2/U_\infty^2)}$	133
Figure 3.35: Plan view projection of the potential core flow at $y/c_a = 0.73$. Plotted here are the contours of the lengthscale, A_u (cm).....	134
Figure 3.36: Plan view projection of the potential core flow at $y/c_a = 0.73$. Plotted here are the contours of the lengthscale, A_v (cm).....	135
Figure 3.37: Plan view projection of the potential core flow at $y/c_a = 0.73$. Plotted here are the contours of the lengthscale, A_w (cm).....	136
Figure 3.38: Evolution of the normalized autospectra, G_{uu}/U_∞^2 in the potential core of the flow.....	137
Figure 3.39: Evolution of the normalized autospectra, G_{vv}/U_∞^2 in the potential core of the flow.....	138
Figure 3.40: Evolution of the normalized autospectra, G_{ww}/U_∞^2 in the potential core of the flow.....	139
Figure 3.41a: Contours of Normalized Mean Streamwise Velocity, U/U_∞ at $X/c_a = 0.0$	140
Figure 3.41b: Contours of Normalized Mean Streamwise Velocity, U/U_∞ at $X/c_a = 0.27$	141
Figure 3.41c: Contours of Normalized Mean Streamwise Velocity, U/U_∞ at $X/c_a = 0.48$	142
Figure 3.41d: Contours of Normalized Mean Streamwise Velocity, U/U_∞ at $X/c_a = 0.77$	143
Figure 3.41e: Contours of Normalized Mean Streamwise Velocity, U/U_∞ at $X/c_a = 0.98$	144
Figure 3.41f: Contours of Normalized Mean Streamwise Velocity, U/U_∞ at $X/c_a = 1.26$	145
Figure 3.42a: Vectors of the magnitude of the mean normalized crossflow velocity (V, W) at $X/c_a = 0.0$	146
Figure 3.42b: Vectors of the magnitude of the mean normalized crossflow velocity (V, W) at $X/c_a = 0.27$	147
Figure 3.42c: Vectors of the magnitude of the mean normalized crossflow velocity (V, W) at $X/c_a = 0.48$	148
Figure 3.42d: Vectors of the magnitude of the mean normalized crossflow velocity (V, W) at $X/c_a = 0.77$	149
Figure 3.42e: Vectors of the magnitude of the mean normalized crossflow velocity (V, W) at $X/c_a = 0.98$	150
Figure 3.42f: Vectors of the magnitude of the mean normalized crossflow velocity (V, W) at $X/c_a = 1.26$	151
Figure 3.43a: Contours of the normalized streamwise vorticity, $\Omega_{x,d}/U_\infty$, at $X/c_a = 0.27$	152
Figure 3.43b: Contours of the normalized streamwise vorticity, $\Omega_{x,d}/U_\infty$, at $X/c_a = 0.48$	153
Figure 3.43c: Contours of the normalized streamwise vorticity, $\Omega_{x,d}/U_\infty$, at $X/c_a = 0.77$	154
Figure 3.43d: Contours of the normalized streamwise vorticity, $\Omega_{x,d}/U_\infty$, at $X/c_a = 0.98$	155
Figure 3.43e: Contours of the normalized streamwise vorticity, $\Omega_{x,d}/U_\infty$, at $X/c_a = 1.26$	156
Figure 3.44a: Contours of the normalized Helicity, H , at $X/c_a = 0.48$	157
Figure 3.44b: Contours of the normalized Helicity, H , at $X/c_a = 0.77$	158

Figure 3.44c: Contours of the normalized Helicity, H , at $X/c_a=0.98$	159
Figure 3.44d: Contours of the normalized Helicity, H , at $X/c_a=1.26$	160
Figure 3.45: Plot showing various markers of the vortex trajectory as given in Tables 3.2, 3.6 and 3.7.....	161
Figure 3.46: Plots of (a) Circulation and (b) Circumferentially averaged tangential velocity in the tip leakage vortex as a function of normalized radius from the vortex center, measured perpendicular to the x direction.....	162
Figure 3.47a: Contours of the normalized turbulence kinetic energy, k/U_∞^2 , at $X/c_a=0.0$	163
Figure 3.47b: Contours of the normalized turbulence kinetic energy, k/U_∞^2 , at $X/c_a=0.27$	164
Figure 3.47c: Contours of the normalized turbulence kinetic energy, k/U_∞^2 , at $X/c_a=0.48$	165
Figure 3.47d: Contours of the normalized turbulence kinetic energy, k/U_∞^2 , at $X/c_a=0.77$	166
Figure 3.47e: Contours of the normalized turbulence kinetic energy, k/U_∞^2 , at $X/c_a=0.98$	167
Figure 3.47f: Contours of the normalized turbulence kinetic energy, k/U_∞^2 , at $X/c_a=1.26$	168
Figure 3.48a: Contours of the square root of the Reynolds Normal Stress, $\sqrt{(u^2/U_\infty^2)}$, at $X/c_a=0.0$	169
Figure 3.48b: Contours of the square root of the Reynolds Normal Stress, $\sqrt{(u^2/U_\infty^2)}$, at $X/c_a=0.27$	170
Figure 3.48c: Contours of the square root of the Reynolds Normal Stress, $\sqrt{(u^2/U_\infty^2)}$, at $X/c_a=0.48$	171
Figure 3.48d: Contours of the square root of the Reynolds Normal Stress, $\sqrt{(u^2/U_\infty^2)}$, at $X/c_a=0.77$	172
Figure 3.48e: Contours of the square root of the Reynolds Normal Stress, $\sqrt{(u^2/U_\infty^2)}$, at $X/c_a=0.98$	173
Figure 3.48f: Contours of the square root of the Reynolds Normal Stress, $\sqrt{(u^2/U_\infty^2)}$, at $X/c_a=1.26$	174
Figure 3.49a: Contours of the square root of the Reynolds Normal Stress, $\sqrt{(v^2/U_\infty^2)}$, at $X/c_a=0.0$	175
Figure 3.49b: Contours of the square root of the Reynolds Normal Stress, $\sqrt{(v^2/U_\infty^2)}$, at $X/c_a=0.27$	176
Figure 3.49c: Contours of the square root of the Reynolds Normal Stress, $\sqrt{(v^2/U_\infty^2)}$, at $X/c_a=0.48$	177
Figure 3.49d: Contours of the square root of the Reynolds Normal Stress, $\sqrt{(v^2/U_\infty^2)}$, at $X/c_a=0.77$	178
Figure 3.49e: Contours of the square root of the Reynolds Normal Stress, $\sqrt{(v^2/U_\infty^2)}$, at $X/c_a=0.98$	179
Figure 3.49f: Contours of the square root of the Reynolds Normal Stress, $\sqrt{(v^2/U_\infty^2)}$, at $X/c_a=1.26$	180
Figure 3.50a: Contours of the square root of the Reynolds Normal Stress, $\sqrt{(w^2/U_\infty^2)}$, at $X/c_a=0.0$	181
Figure 3.50b: Contours of the square root of the Reynolds Normal Stress, $\sqrt{(w^2/U_\infty^2)}$, at $X/c_a=0.27$	182
Figure 3.50c: Contours of the square root of the Reynolds Normal Stress, $\sqrt{(w^2/U_\infty^2)}$, at $X/c_a=0.48$	183
Figure 3.50d: Contours of the square root of the Reynolds Normal Stress, $\sqrt{(w^2/U_\infty^2)}$, at $X/c_a=0.77$	184
Figure 3.50e: Contours of the square root of the Reynolds Normal Stress, $\sqrt{(w^2/U_\infty^2)}$, at $X/c_a=0.98$	185
Figure 3.50f: Contours of the square root of the Reynolds Normal Stress, $\sqrt{(w^2/U_\infty^2)}$, at $X/c_a=1.26$	186
Figure 3.51a,b: Contours of the turbulence kinetic energy difference.....	187
Figure 3.51c,d: Contours of the turbulence kinetic energy difference.....	188
Figure 3.52a: Contours of the turbulence kinetic energy production, at $X/c_a=0.48$	189
Figure 3.52b: Contours of the turbulence kinetic energy production, at $X/c_a=0.77$	190
Figure 3.52c: Contours of the turbulence kinetic energy production, at $X/c_a=0.98$	191
Figure 3.52d: Contours of the turbulence kinetic energy production, at $X/c_a=1.26$	192
Figure 3.53a: Contours of the turbulence kinetic energy production due to streamwise velocity gradient, at $X/c_a=0.48$	193
Figure 3.53b: Contours of the turbulence kinetic energy production due to streamwise velocity gradient, at $X/c_a=0.77$	194

<i>Figure 3.53c: Contours of the turbulence kinetic energy production due to streamwise velocity gradient, at $X/c_a=0.98$.....</i>	<i>195</i>
<i>Figure 3.53d: Contours of the turbulence kinetic energy production due to streamwise velocity gradient, at $X/c_a=1.26$.....</i>	<i>196</i>
<i>Figure 3.54a: Contours of the turbulence kinetic energy production due to crossflow velocity gradient, at $X/c_a=0.48$.....</i>	<i>197</i>
<i>Figure 3.54b: Contours of the turbulence kinetic energy production due to crossflow velocity gradient, at $X/c_a=0.77$.....</i>	<i>198</i>
<i>Figure 3.54c: Contours of the turbulence kinetic energy production due to crossflow velocity gradient, at $X/c_a=0.98$.....</i>	<i>199</i>
<i>Figure 3.54d: Contours of the turbulence kinetic energy production due to crossflow velocity gradient, at $X/c_a=1.26$.....</i>	<i>200</i>
<i>Figure 3.55a: Contours of the turbulence kinetic energy diffusion, at $X/c_a=0.48$.....</i>	<i>201</i>
<i>Figure 3.55b: Contours of the turbulence kinetic energy diffusion, at $X/c_a=0.77$.....</i>	<i>202</i>
<i>Figure 3.55c: Contours of the turbulence kinetic energy diffusion, at $X/c_a=0.98$.....</i>	<i>203</i>
<i>Figure 3.55d: Contours of the turbulence kinetic energy diffusion, at $X/c_a=1.26$.....</i>	<i>204</i>
<i>Figure 3.56: Normalized Autospectra, $G_{u,u}/U_\infty^2$, for the two inflow conditions in the vicinity of the vortex center.....</i>	<i>205</i>
<i>Figure 3.57: Normalized Autospectra, $G_{w,w}/U_\infty^2$, for the two inflow conditions in the vicinity of the vortex center.....</i>	<i>206</i>
<i>Figure 3.58: Normalized Autospectra, $G_{w,w}/U_\infty^2$, for the two inflow conditions in the vicinity of the vortex center.....</i>	<i>207</i>

1. Introduction

1.1. Motivation and Purpose

The goal of a fluid dynamics study is to realistically model and simulate the corresponding “real world” flow field in order to better understand these flows. To this extent, experimental and computational studies need to and have been done on various types of flows. One area that is of particular interest involves the flow over rotating blades, such as those seen in turbo-machinery and submarine propellers. Consider the flow through the core compressor of an aircraft engine, or through the shrouded propeller of a submarine. The flow entering such configurations is usually fully developed large scale turbulence i.e. the turbulent boundary layer from the hull of the submarine interacting with the propellers, or the turbulent air from the fan interacting with compressor of the aircraft engine. A good understanding of the effects of free stream turbulence on these types of flowfield is needed, as these interactions may affect the performance of the configuration and other characteristics such as noise, heat transfer or cavitation on the blades.

Computational studies on these types of flows are very difficult and expensive in terms of processing capabilities. The complex three dimensional nature of the flow field, and flow features seen in this flow contribute to the difficulty in developing accurate prediction schemes. In order to assist in the development of computational methods, there is a need to have experimental results with which to compare the calculations. Experimental studies also contribute to the understanding of the flows and flow features, and as such are valuable and useful. Trying to measure the rotating flow field of such a configuration is difficult. However, by building a cascade of blades, the flow field can be simulated in the laboratory, and this simplifies the task of making flow field measurements and analysis. However, this technique has a few limitations including the lack of inflow turbulence and the absence of the rotating blade/casing interaction. In the majority of wind tunnel designs, the desire is to have free stream turbulence levels as low as possible, resulting in the lack of an accurate representation of the “real” flow field. However, using grid-generated turbulence, free stream turbulence can be simulated in cascade flows.

The objective of the current study is to experimentally document the effects and influence of grid generated turbulence on the flow through a cascade of compressor blades in order to better understand what these effects are. Understanding how the flow through a compressor is affected by free stream turbulence may help in the design of quieter and more efficient compressor configurations.

1.2. Prior Studies on Compressor Cascades.

Numerous studies have been performed on the flowfield of compressor cascades and rotors. The studies have shown what the flowfield looks like and the mechanisms involved in them. Shown in Figure 1.1, is a sketch of the flow features in such type of flows in a cascade type configuration. The pressure difference between the suction side and the pressure side of the blade drives the flow through the tip gap region of the cascade. At approximately the quarter chord location of the blade, this high shear flow rolls up in the blade passage to form what is commonly called the tip leakage vortex and this vortex may become the dominant flow feature downstream of the blade passage. Secondary vortices may also be present in the flow, but are not as dominant as the tip leakage vortex. As an example, and shown in Figure 1.1, is a tip separation vortex which is formed due to the separation of the tip gap flow over the tip surface. The influences of these vortices are not only seen in the blade passage but also downstream of the blades.

Flow visualizations were done by Bindon (1989) on a 7 blade cascade with exit Reynolds number of 250,000 under the tip gap of the blade. He also made single hole pressure probe measurements, and these results show that there is a separation bubble formed on the blade tip, with the leakage flow going over it. Some of this tip leakage flow may separate to form a tip-separation vortex but studies have shown that the tip leakage flow which stays attached to the blade tip is nearly perpendicular to the blade surface as it exits the tip-gap. This shear flow then rolls up to form the tip leakage vortex at the suction side of the blade.

Storer *et al* (1990) performed an incompressible study of a 5 blade compressor cascade at a chord Reynolds number of 500,000. A flattened pitot-probe and a two-hole probe were used to make pressure measurements within the tip gap along the chord line of the blade. Similar to that seen in Kang *et al.* (1993), the tip gap flow is seen to separate from the blade

tip. Results taken at different tip gaps indicate that for smaller tip gaps (less than 1.0% of the chord), there is no clear indication a tip leakage vortex in the flow, but for tip gaps greater than 2.0% of the chord, there is a tip leakage vortex formed on the suction side of the blade.

Yocum *et al* (1993) made measurements in an 18 blade cascade with a split-film probe. Measurements were made for Reynolds numbers ranging from 57,000 to 200,000 at different stagger angles. The measurements were made primarily to study stall conditions, but the unstalled cases are more insightful as to the nature of the flow. In these experiments, measurements taken at the trailing edge plane of the blade rows showed that of the three vortical structures, the tip-leakage vortex engulfs the other two vortices. Also present in these measurements, is an indication of a passage vortex originating from the pressure side of the blade. However, in most cases, the tip leakage vortex seems to be the most dominant structure of the two. It was also observed that for larger tip gaps, the tip leakage vortex moved further away from the suction side of the blade and closer to the pressure side of the next blade in the cascade.

Kang *et al* (1993, 1994) made measurements in a 7 blade linear compressor cascade at design and off design conditions. The blades had a NACA 65-1810 profile, and had a chord length of 7.87 in, and the Reynolds number based on this chord length for the study was approximately 300,000. Measurements were made with a 5 hole pressure probe at 16 positions which ranged from $0.075c$ upstream of the blades to $0.5c$ downstream of the trailing edges. They also performed flow visualizations on the blade tip using oil films and paint traces. The tip gap flow was shown to be almost perpendicular to the camber line of the blade, and this tip gap flow rolls up to form the tip leakage vortex as it exits the tip-gap region. At about the mid-chord of the blade, the tip gap flow begins to separate and rolls up to form a tip separation vortex. In addition to the tip leakage vortex and tip separation vortex, there is a secondary vortex formed due to separation of flow at the leading edge of the tip of the blade. Pressure measurements downstream of the blade row show that the tip leakage vortex dominates much of the endwall flow region and vorticity plots indicate high vorticity in the vicinity of the core region of the flow. These measurements show that the vortex forms close to the suction side of the blades and begins to move away from the suction side and lower endwall with downstream distance.

1.3. Prior Studies on Compressor Rotors

Experiments performed on compressor rotors differ from those in cascades in that the rotational effects between the tip-gap and endwall are now present. These rotational effects lead to two different pictures of the flow in turbomachinery, one where there is a tip-leakage vortex present, and the other where there is no indication of a tip-leakage vortex, but instead a region of high shear flow on the lower endwall.

Phillips *et al.*(1980) performed smoke flow visualizations in a single fan compressor stage in a rotating rig. The rotor consisted of 22 blades and the visualizations were performed at “low” Reynolds numbers. These pictures did not give any indication of the presence of a tip leakage vortex, instead they show that the large scale motions in the endwall region due to rotational effects swamp and disperse these vortical structures as they emerge from the tip-gap.

Lakshminarayana *et al.* (1981) made measurements in a 21 blade rotor using a triple hot-wire rotating with the compressor blades at design conditions. The blade profiles were a NASA 65 series, and the Reynolds number based on chord was 300,000. These measurements showed that the tip-leakage vortex had moved to the middle of the passage between the blades at the blade trailing edges. In a later experiment by Lakshminarayana *et al.*(1982) in the same setup as that described in his previous study in 1981, but this time concentrating on measurements primarily in the blade passage and goes on to indicate that there is no roll up of the tip-gap flow into vortices within the blade passage, instead claiming that the roll up to the vortex occurs after the blade passage.

Bettner *et al.* (1982) made static pressure measurements and hot wire measurements in a single stage low speed compressor, with NASA 65 series airfoils at design conditions. Similar to that seen in the cascade measurements, results here show evidence of tip vortices extending into the flow.

Popovski *et al.*(1985), using LDV, hot wires, and a 5 hole pressure probe made measurements on the same test apparatus as Lakshminarayana *et al.*(1982), and found the presence of a tip-leakage vortex within the passage contrary to the work by Lakshminarayana (1982). Results from subsequent experiments by Lakshminarayana *et al.* (1987, 1995) on the same test apparatus but at off design conditions i.e. different blade loading, did not reveal the presence of a tip leakage vortex being formed within the blade passage, but regions of high

shear flow on the lower endwall. In another study by Lakshminarayana *et al.* (1990), using an LDV and at design conditions in the same test apparatus described previously, revealed the presence of a tip-leakage vortex and showed that the vortex moved across the passage toward the pressure side with downstream distance while rapidly decreasing in strength.

Inoue *et al.* (1985, 1988), using hot wires and wall mounted pressure transducers, made measurements on a compressor rotor with the same NASA 65 series airfoil shape at design conditions and different tip clearances. These measurements clearly showed the development of a tip leakage vortex within the passage of a compressor rotor. For large tip gaps, the vortex tended to cross the passage, ending up closer to the pressure side by the blade trailing edge.

Chesnakas *et al.* (1990) made LDA measurements on a GE single stage rotor and stator configuration in an axial compressor. The blade profiles were a RAF-6 prop blade with twist and the rotor was run at design conditions. Plots of the cross flow velocity vectors did not indicate the presence of any vortical flows within the blade passage, but instead shows that the tip-gap flow produces a region of high shear flow on the lower endwall of the apparatus.

Poensgen *et al.* (1996), using single and triple hot wire probes measured turbulence levels in a single stage axial compressor. The study was primarily done to investigate stall conditions i.e. different blade loadings, but at unstalled conditions which are near design conditions, the measurements found regions of elevated turbulence kinetic energy in the vicinity of the core. In those cases where the vortex was not formed, the tip gap flow mixes with the mainstream flow and produces regions of high shear and flow separation.

Some of these studies show the development and formation of a tip-leakage vortex. This tip leakage vortex is formed due to flow being driven in the tip gap region driven by the pressure difference between the pressure and suction side of the blades (the blade loading). The studies also highlight the differences that may arise due to different flow conditions affecting the rotor or cascade. Many of the studies that were done at off design conditions for rotors show that there is no formation of a tip leakage vortex. These results imply that, especially for rotating apparatus where the endwall behavior has a greater effect, the flow conditions play a much more significant role as to the nature of such tip gap flows. One such flow condition that is being considered is the presence of inflow turbulence. However, as

mentioned previously, rotational effects will not be covered in this study, but are the subject of other research work that has been carried out on the same apparatus (see section 1.6).

1.4. Prior Studies on Free Stream Turbulence Effects on Boundary Layers

When considering the effects of free stream turbulence on a cascade of blades, we can first consider the effects of free stream turbulence on plane boundaries such as a flat plate of a cascade of flat plates. Detailed experimental and theoretical work has been done to study these effects. For flow over flat plates, the introduction of free stream turbulence hastens transition of the boundary layer from laminar to turbulent flow (Schetz, 1993). These background disturbances would also effect the flow field around the edge of the boundary layer, with there being turbulent mixing and entrainment with the free stream turbulence (Simpson, 1999). Studies by Meir (1980), experimentally observed the development of a boundary layer subject to free stream turbulence, and Volino (1998), who developed a model for free stream turbulence effects on boundary layers show this increased propensity for the boundary layer to transition from laminar to turbulent.

Blair (1983), makes detailed measurements of the flowfield of a turbulent boundary layer over a flat plate (zero pressure gradient) under the influence of grid generated free stream turbulence. Turbulence levels ranged from 0.25 to 6 % (nominal values), but for the cases with 4% and 6% nominal levels, there was substantial decay down the tunnel (decreasing by as much as 2% over the last 1m of test section). Free stream spectral results showed the turbulence to agree with the one-dimensional von Karman spectrum characteristic of fully developed grid generated turbulence. The lower endwall boundary layers were found to be highly two dimensional and fully turbulent. Results showed the suppression of the boundary layer wake region due to high free stream turbulence levels, and show regions of increased interaction between the free stream turbulence and the wake of the boundary layer. Results also indicated that the value of the skin friction coefficient increased with the introduction of free stream turbulence.

Similarly, a study by Hancock and Bradshaw (1989) which looked at the turbulence structure of a boundary layer under the influence of free stream turbulence, showed the same results. However, the study covered a wider range of free stream turbulence lengthscales,

and distinctions between the boundary layer flow and the free stream were made by heating the plate thereby having hot and cold regions of the flow. Results here show that the effect of the free stream turbulence is highly dependent not only on the intensity of the turbulence, but also on the lengthscales.. When free stream turbulence levels are less than the turbulence levels in the boundary layer, the results show a decrease in the u' , v' and w' quantities compared to the no free stream case within the boundary layer. The effect is more pronounced when the lengthscales are reduced in the free stream turbulence. For high free stream intensity levels, the effect of lengthscale is similar, but the most dominant behaviour is the fact that the v' component in the boundary layer is smaller than that in the free stream as well as the case for no free stream turbulence. Results on the triple products, or the transport due to turbulent velocity fluctuations, reveal that more of the energy transport is being done close to the endwall with the introduction of free stream turbulence than without.

Thole and Bogard (1996) also looked at free stream turbulence effects on boundary layers, but increased the free stream turbulence levels to approximately 20%. Here again results revealed that the wake region of the boundary layer is suppressed at higher free stream turbulence levels, but also that the velocity defects in the outer regions of the boundary layers are reduced with increasing turbulence levels. Spectral results here show that at these high levels, the free stream turbulence penetrates deep into the boundary layer. This was revealed due to the fact that the shapes of the spectral curves at different positions within the boundary layer were similar to that seen in the free stream.

Batchelor and Proudman (1954) developed a Rapid Distortion Theory formulation to predict the effects of a distortion on turbulence, and Hunt (1973) extended it to include non-homogenous inflow turbulence and more importantly the non-penetration condition imposed by blades or plates. This non-penetration condition suppresses the wall normal component of the velocity fluctuations. This blade blocking effect, and the turbulence mixing and entrainment effects have been observed in studies by Hunt and Graham (1978), Hancock and Bradshaw (1983), Kullar and Graham (1986), Thole and Bogard (1996), and Graham (1998).

1.5. Prior Studies on Free Stream Turbulence Effects on Turbomachinery configurations.

The above analysis of compressor cascade work and free stream effects gives us a foundation from which to start looking at the effects of free stream turbulence on the flow field of a compressor cascade. A study by Mukhraiya and Ahmed (1998) gives an indication of how free stream turbulence effects can affect the performance of a compressor cascade. Here, a compressor cascade with no tip gap was subject to grid generated turbulence and the performance of the blade in terms of lift and drag was investigated. The influence of free stream turbulence on the lift and drag was highly dependent on the incidence angle of the blade surfaces. In general, a decrease in the static pressure coefficient was observed on the pressure side of the blade. However this decrease in the pressure coefficient was offset by the tendency for the flow to remain attached on the suction side of the blade thereby increasing the lift coefficient. From the studies done on boundary layers, the blade boundary layers tend to resist separation at the trailing edge, and thus increase the blade loading. This change in the blade loading is an interesting phenomenon, since studies on cascades and rotors revealed that the flow is highly dependent on the blade loading and can effect the development of the viscous regions in such configurations.

There has a great deal of research done on the effects of inflow turbulence on turbine configurations. Much of the work done has been primarily on turbulence effects on heat transfer and boundary layer transition in turbines and turbine cascades. This is because downstream of combustors in turbine configurations, the flow is high in temperature, and has high levels of rapidly decaying turbulence, and as the flow passes over the turbine, the effects on the blades and performance of the turbine is heavily influenced by the combusted flow over them. Hoheisel *et al.* (1987), Krishnamurthy and Sukhatme (1989), Zhang and Han (1995), Hoffs *et al.*(1996), and Ames (1997), Gregory-Smith and Cleak (1992), Hobson and Shreeve (1993), Wunderwald and Fottner (1996), Bangert *et al.* (1997), Ames and Plesniak (1997), and Radomsky *et al.* (2000,2001) all study turbine and turbine cascade configurations. The turbulence that the blades see is of very high intensity and at a much higher temperature than the blades, and is rapidly decaying. As a result, the heat transfer between the fluid and blades is very critical to the design and performance of this turbomachinery configuration as large changes in temperature on the blades might cause

undue stress and influence the design. Also, in comparison to compressor blades, turbine blades are highly cambered and thus more susceptible to off design conditions which could cause the flow to stall. However, the scope of the present study is to look at the effects of relatively low (<15%) intensity fully developed turbulence, on blade configurations which are less likely to stall.

1.6. Prior Studies in the Virginia Tech Low Speed Cascade Wind Tunnel

The Virginia Tech Low Speed Cascade Wind Tunnel has been the subject of numerous studies. The facility was originally modified from a turbine cascade configuration in 1996, and has the capability of simulating the rotational effects due to the rotor casing interaction through the use of a moving endwall. The facility has been utilized in both stationary and moving endwall configurations using a variety of measurement techniques.

1.6.1. Stationary endwall studies

A study by Muthanna (1998) in this facility provides detailed experimental measurements of the flowfield at 5 planes downstream of the blade row. A four sensor hotwire probe was used to provide 3 component mean and turbulent velocity data. The hot-wire results revealed the presence of the tip-leakage vortex and its development downstream of the blade row as well as detailed measurements of the blade wakes. The results showed that the tip leakage vortex was a region of high streamwise velocity deficits, and large turbulence kinetic energy levels. Mean flow field measurements revealed the rotating nature of the flow field in the tip leakage vortex, and its center characterized by a localized area of high vorticity. Shown in Figure 1.2a are the contours of the mean streamwise velocity for the measurement location 0.366 axial chord lengths (5.1cm) aft of the trailing edge of the blade row, revealing the streamwise velocity deficit at the center of the vortex. Mean streamwise vorticity contours (shown in Figure 1.2b); reveal the high vorticity in the tip leakage vortex, but also an area of negative vorticity adjacent to the vortex. Contours of the turbulence kinetic energy (shown in Figure 1.3), reveal that the distribution of turbulence kinetic energy levels in the tip leakage vortex is in an arc shape region around the vortex center. This study also showed that the contribution to the turbulence kinetic energy production was primarily due to the

streamwise velocity gradients, and not the crossflow velocity gradients. Reynolds stress measurements revealed the flow in the tip-leakage vortex to be highly anisotropic.

Surface oil-flow visualizations were also made in the lower endwall region and the flow features inferred from the oil flow results are shown in Figure 1.4. From the study, it was hypothesized that there is secondary vortex formed in the passage of the blade row, which is adjacent to the tip leakage vortex, and responsible for the region of negative vorticity shown in Figure 1.2b. A similar study done by Wenger (1998) involving two-point measurements in the same flowfield as Muthanna (1998), established that there was no wandering of the vortex to corrupt the turbulence measurement. Measurements taken in the wake of the blades (which are visible in Figure 1.2a), revealed that the wakes exhibit characteristics typical of two dimensional plane wakes, and suggested that there may have been some vortex shedding from the trailing edge of the blades. The study revealed the complex nature of the flowfield downstream of the blade row, and the suitability of using hot-wire anemometry to make measurements in this complex rotating velocity flow field. While oil-flow visualizations were performed in the blade passage, no hot-wire measurements were taken within the blade row to document the formation of the tip leakage vortex.

A computational study of this flow was done by Shin (2001), who compared his results to the experimental results of Muthanna (1998). In this study, a three dimensional incompressible Reynolds Averaged Navier Stokes code was developed using artificial compressibility and a Spalart-Allmaras eddy viscosity model. The results of the code were validated using several different preliminary test cases, and then applied to the linear cascade model. The mean velocity flow field was computed for the flow regime upstream, through and downstream of the cascade and the results were compared with the experimental investigation of Muthanna (1998). Results downstream of the blade row showed fairly good agreement with the measured results and are shown in Figure 1.5. Presented in the figure are the streamwise velocity contours (Figure 1.5a) and the crossflow velocity vectors (Figure 1.5b). Comparisons with Figure 1.2a showed that the overall qualitative description was similar to the experimental results in the results. However, the magnitude and the position of the vortex showed a slight discrepancy. The crossflow vectors also show the presence of the secondary vortex hypothesized in the experimental study.

Shin's study also presented computational results of the flow through the blade passage. Comparisons with the lower endwall flow oil-flow visualizations showed that the position of the tip leakage vortex in the computation agreed well with the position inferred from the shear lines in the visualization. Shown in Figure 1.6 is the two-dimensional computed velocity field at the mid span of the blade, through the compressor cascade. The figure reveals the acceleration of the flow over the suction side, and the slight deceleration around the pressure side of the blade near the leading edge. Also revealed is the slight expansion of the blade boundary layer near the blade trailing edge. The pressure distribution on the blade was also computed and hence the blade loading was determined. Shin's results however indicated that the blade loading was influenced by the blade span used in the computation. Calculations of the pressure distribution on the blade showed that the pressure difference between the suction side and the pressure side of the blade increases with span (from a span of half to one chord) near the leading edge. The implications of this result are that the lower endwall flow structure plays a significant role on the operation of the cascade, and thus could influence the behavior of the various flow features. Shin's (2001) study also revealed the expense and complexities of applying a RANS computation to the above mentioned flowfield.

In a recent study, De la Riva (2001) developed an RDT (Rapid Distortion Theory) based prediction scheme for the evolution of grid generated free stream turbulence flowing through the cascade. The RDT approach uses the inviscid distortion on the mean flow field by the blade row to predict the effects of this distortion on the evolution of inflow turbulence through the cascade. By using RDT, it is feasible to obtain space time correlation functions of the turbulence as it evolves through the cascade, at a cheaper cost when compared to other methods such as LES. This RDT study utilized the grid generated turbulent inflow data from the current work, to compare with the results of his.

De la Riva made extensive use of the computational results from Shin (2001) to define the mean flow field through the cascade and thus the distortion. The results showed the decay of the inflow turbulence through the cascade, as well as the pressure gradient across the passage width away from the endwall. The calculations were able to predict the general trend of the evolution of the turbulence in the potential core. The experimental results revealed suppression in the normal to the blade surface component of the turbulence

fluctuations due to the non-penetration condition imposed there, which was not adequately modeled in this RDT calculation.

In order to define the potential core region of the flow field, De la Riva performed a preliminary analysis of the flow through the cascade to determine the extent to which the lower endwall flow influences could be seen. This analysis used a subset of the measurements of the present study. The study presented measurements of the flow in the lower endwall region downstream of the half chord location to highlight the dominant flow features (namely the tip leakage vortex), and an initial discussion of the effects of grid generated turbulence. Initial results of the effects of grid generated turbulence indicated that the mean flow fields were qualitatively similar, with the tip leakage vortex growing by approximately 18%, and a subsequent increase in the turbulence kinetic energy levels. Plots of the mean streamwise vorticity showed that the effects of grid generated turbulence were to decrease the levels in the tip leakage vortex, perhaps implying a weakening of the strength of the vortex. However, the focus of the study was on detailed results of the flowfield in the potential core region of the flow not influenced by the lower endwall flow features such as the tip leakage vortex and the lower endwall boundary layers, as it was in these regions where the RDT computation was performed and compared.

Kuhl (2001) made measurements of the flowfield in the tip gap region of the flow using an LDV measurement technique for a tip gap that was twice as large as that for the studies by Muthanna (1998) and De la Riva (2001) using the same turbulence generating grid as used by De la Riva (2001) and the present study. As suggested by Shin, this would change the flow field characteristics due to the implied change in the blade loading, but the results are still relevant as all other conditions are still the same. The most striking effect of the inflow turbulence observed by Kuhl was the suppression of the mean velocities by approximately 7% in the streamwise direction and 30% in the pitchwise direction at the one location he studied in the tip gap. It is this pitchwise velocity that is responsible for the tip leakage vortex, and a reduction in this velocity could imply a reduction in the strength of the vortex. The Reynolds stresses near the blade tip show a slight increase, or approximately 10%.

1.6.2. Moving endwall studies

The limitation of the studies mentioned above and the scope of the present study, is that there are no rotational effects being considered. However the tunnel can also be modified to

accommodate a moving endwall system developed by Wang (1999), and the flow field has also been heavily documented downstream of the blade row. With the introduction of the moving wall, the lower endwall is now a high shear layer and its primary effect is to stretch the tip leakage vortex altering its structure. However, comparing the turbulence kinetic energy production results for the cases with and without the moving endwall, the two flow fields have a very similar distribution in that the region of largest production is where the flow is being lifted off of the lower endwall. Also, the contributions to the turbulence production are primarily due to the gradients in the streamwise velocity, and not the crossflow velocities. This result is significant because it implies that the two flows are very similar in the characteristics of the tip leakage vortex and the various factors that contribute to the turbulence kinetic energy production and thus for the present study, permits the use of using only the stationary wall configuration which enables a far more detailed measurement scheme to be used than with the moving wall configuration.

Ma *et al.* (2000) have made detailed measurements downstream of the cascade with the moving endwall, and with an inflow disturbance created by vortex generators to simulate the rotor stator interaction seen in turbomachinery configurations. This is a more realistic representation of the real world flow field, but the disturbance is mainly confined to the lower endwall region, and the interaction is primarily with the tip gap region and thus the tip leakage flow. Results from this study showed that while the vortices formed by the vortex generator were approximately 80 times as weak as the tip leakage vortex, there were significant changes to the tip leakage vortex, altering its shape, structure and strength. This suggests that the inflow vortices influence the shedding of circulation from the blade tip. Interestingly, the blade loading does not change significantly with the addition of moving wall effects on the cascade.

1.7. Objectives of the Present Work

The studies mentioned above indicate that elevated free stream turbulence may affect the flow field in a compressor type flow field. Numerous studies have been done on the effects of free stream turbulence on boundary layer flows, and turbomachinery type flows. The studies all revealed that the influence of free stream turbulence is not negligible, but primarily concerned the effects the turbulence had on the blades themselves. The nature of

the flows through a compressor cascade is complex and contains viscous flow features, such as the tip leakage vortex and secondary vortices within the blade passages, but the effects of the elevated inflow turbulence on these have not been studied in great detail. Computational studies are difficult and very expensive and due to limitations in present turbulence models, not very accurate. However, the possibility exists for a detailed measurement to document the effects of elevated free stream turbulence to a much greater extent than that presented in previous works.

Previous studies on the flow through turbomachinery have presented detailed measurements and analysis of the flow through both compressor and turbine cascades. The flowfield downstream of the blade row has been well documented; however, the flow through the blade row has not been studied in great detail due to physical challenge of mapping out this flow regime. There seems to be room for additional detailed experimental results of the flow through the blade row. Studies with free stream turbulence effects on compressor cascades are also few, with the majority of the work done on turbine type configurations.

Studies done with a stationary endwall on the Virginia Tech Cascade Tunnel have revealed the complex nature of the flowfield downstream of the blade row in great detail as per Muthanna (1998), but the flow through the blade row was only briefly looked at. Computational studies by Shin (2001) have revealed some hints as to the nature of the flow within the blade row. An second computational study by De la Riva on the grid generated turbulence inflow condition through the blade row has been performed, but concentrating mainly on the flow region away from the influence of the lower endwall characteristics. The effects of grid generated turbulence were briefly looked at by De la Riva, but a detailed analysis was not performed.

Studies done with a moving wall configuration to simulate the rotational effects of the blade-casing have also been done. While the results of the moving wall case show a different flow field than the stationary wall case, the mechanisms and characteristics of the two flows are similar i.e. the turbulence kinetic energy production is through similar mechanisms and the tip leakage vortex shows a behavior similar for the two cases. Thus, using a stationary endwall configuration to study the formation and development of the flow through the blade row, and the effects of grid generated turbulence on it can be performed with the knowledge

that the effects are similar between the two. This reduces the time and complexity of the experiments, and thus enables a far more detailed study to be performed.

The studies presented above highlight work that has been done on these types of flow, but there are certain aspects of the flow which have yet to be looked at. Thus the objectives of the current study are:

1. To experimentally document the flow field through the blade row of a cascade of compressor blades to understand and reveal the formation and development of the lower endwall flow region.
2. To document and analyze the influence of elevated free stream turbulence on the flow field through the compressor cascade.
3. To provide a detailed experimental data set of this flow that could be used in the verification of computational studies done on these complex flow fields

1.8. Approach of the present study

In order to attain the objectives presented above, the flow field through the blade row of the Virginia Tech Compressor Cascade was measured at eight measurement planes upstream, through and downstream of the blade row. Measurements were made using a four sensor hot wire probe capable of measuring all three mean and turbulence velocity components in the flow. In addition to velocity field measurements, the blade loading was also recorded using surface pressure ports fabricated onto the blades. Lower endwall flow features were also mapped out using oil-flow visualizations on the lower endwall of cascade. The effects of grid generated turbulence were studied by placing a bi-planar grid of circular rods upstream of the blade row, and the measurements were taken for both inflow conditions. The results were then analyzed and presented here in this dissertation.

1.8.1. Organization of the dissertation

This report documents the results for the experimental study done on the linear compressor cascade with a fixed endwall subjected to grid generated turbulence and is outlined as follows:

Chapter 2 provides a description of the apparatus and instrumentation used in this study. The chapter begins with an overview of the wind tunnel facility, followed by a description of the test section and the turbulence generating grid used to elevate the free stream turbulence

levels is then described. The measurement system and the various measurement techniques are then presented, and the chapter is concluded with a description of the calibration and set up of the facility for the measurement runs.

Chapter 3 presents the results of the study, plus a discussion of these results. Surface pressure measurements on the blade, oil-flow visualizations are presented first. The results of the hot-wire anemometry are then presented in terms of the inflow to the cascade, the potential core, and the lower endwall region of the flow. Discussions of the effects of grid generated turbulence are also presented in this chapter.

The dissertation is concluded with a summary of the significant findings presented in Chapter 4. The appendix contains descriptions of the uncertainty calculations of the various quantities that are presented in this dissertation.

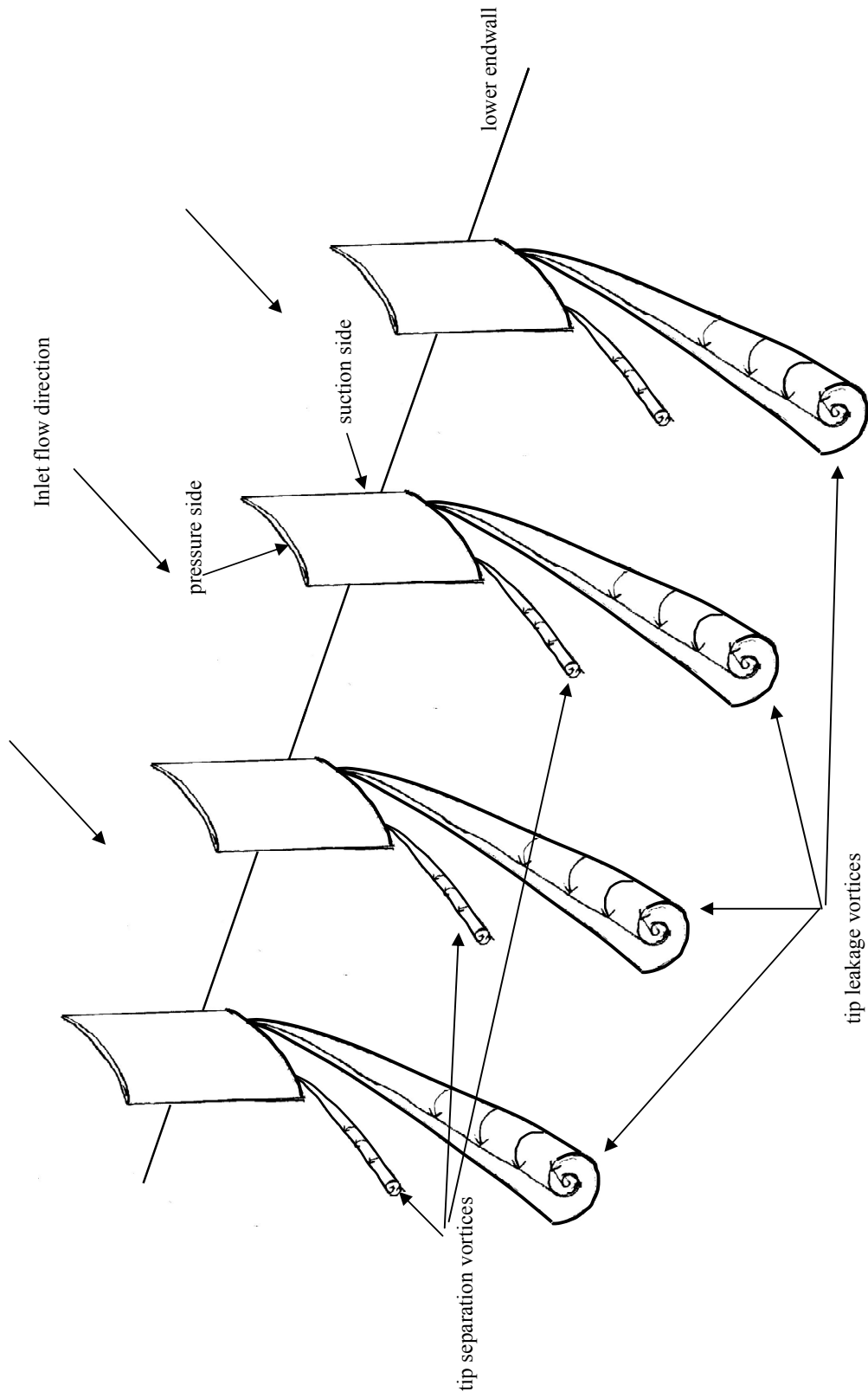


Figure 1.1: Sketch showing the various flow features seen in compressor cascade type flows inferred from previous studies.

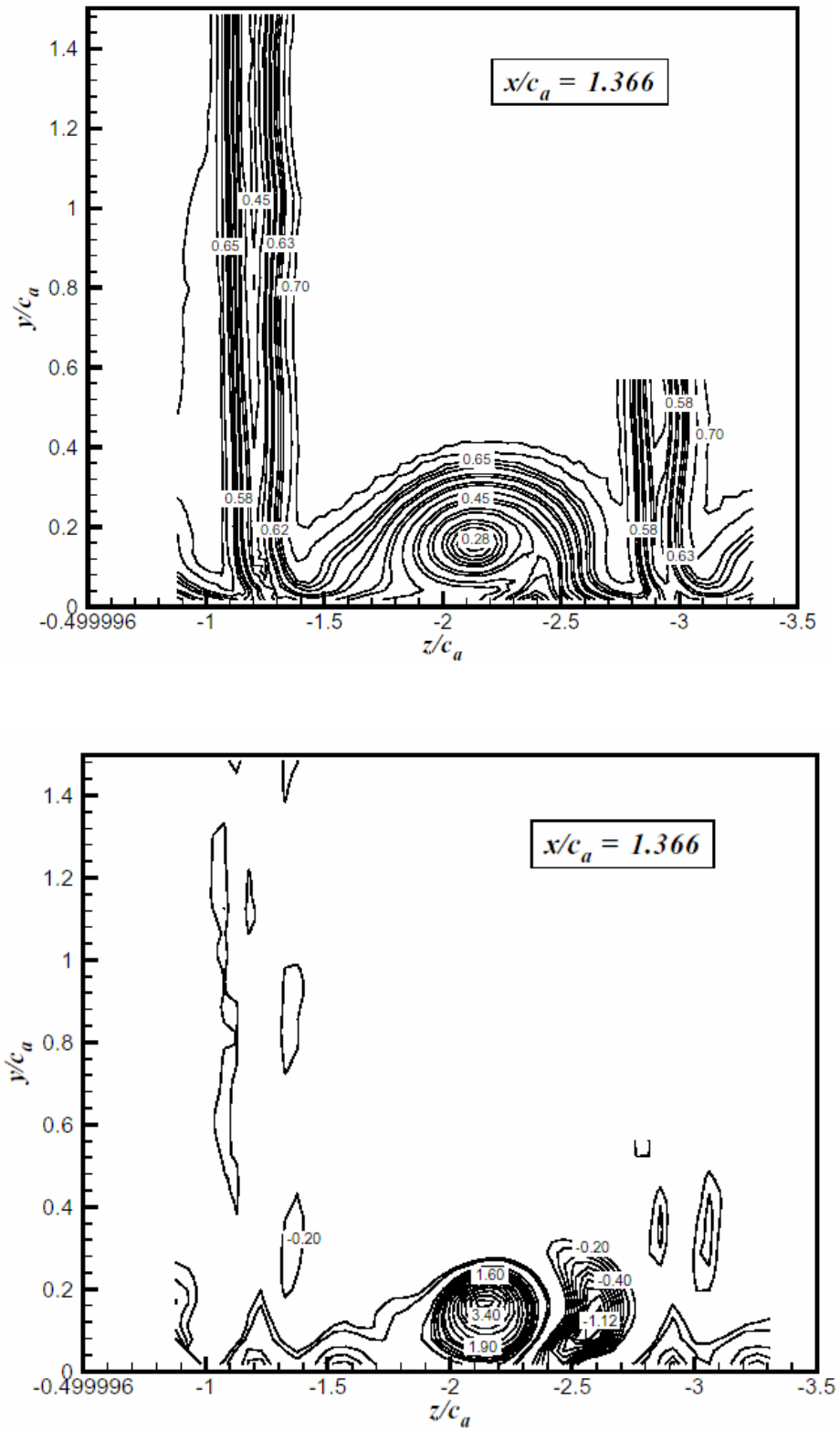


Figure 1.2: Results from Muthanna (1998) showing (a) Mean streamwise velocity contours and (b) Mean streamwise vorticity contours.

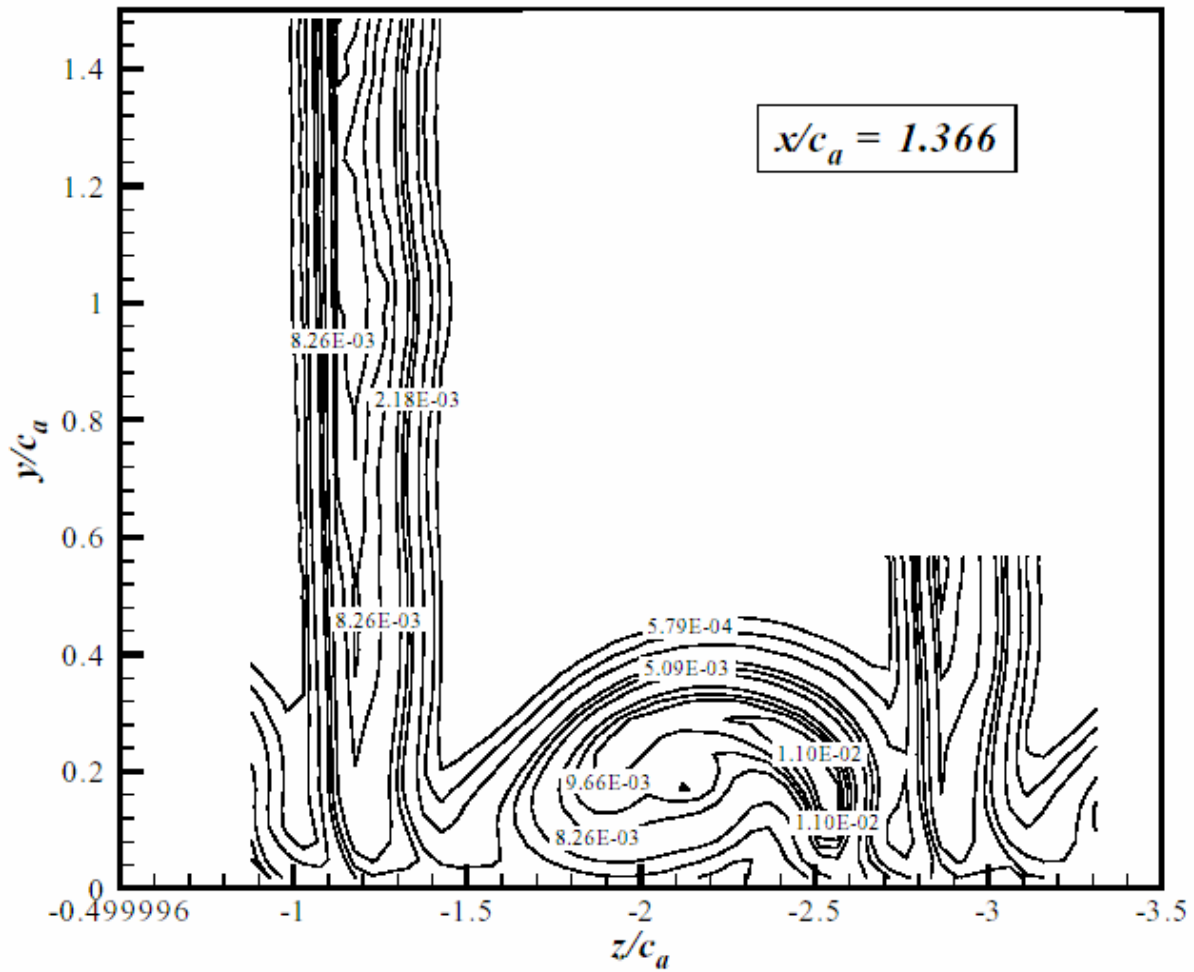


Figure 1.3: Results from Muthanna (1998) showing contours of the normalized turbulence kinetic energy.

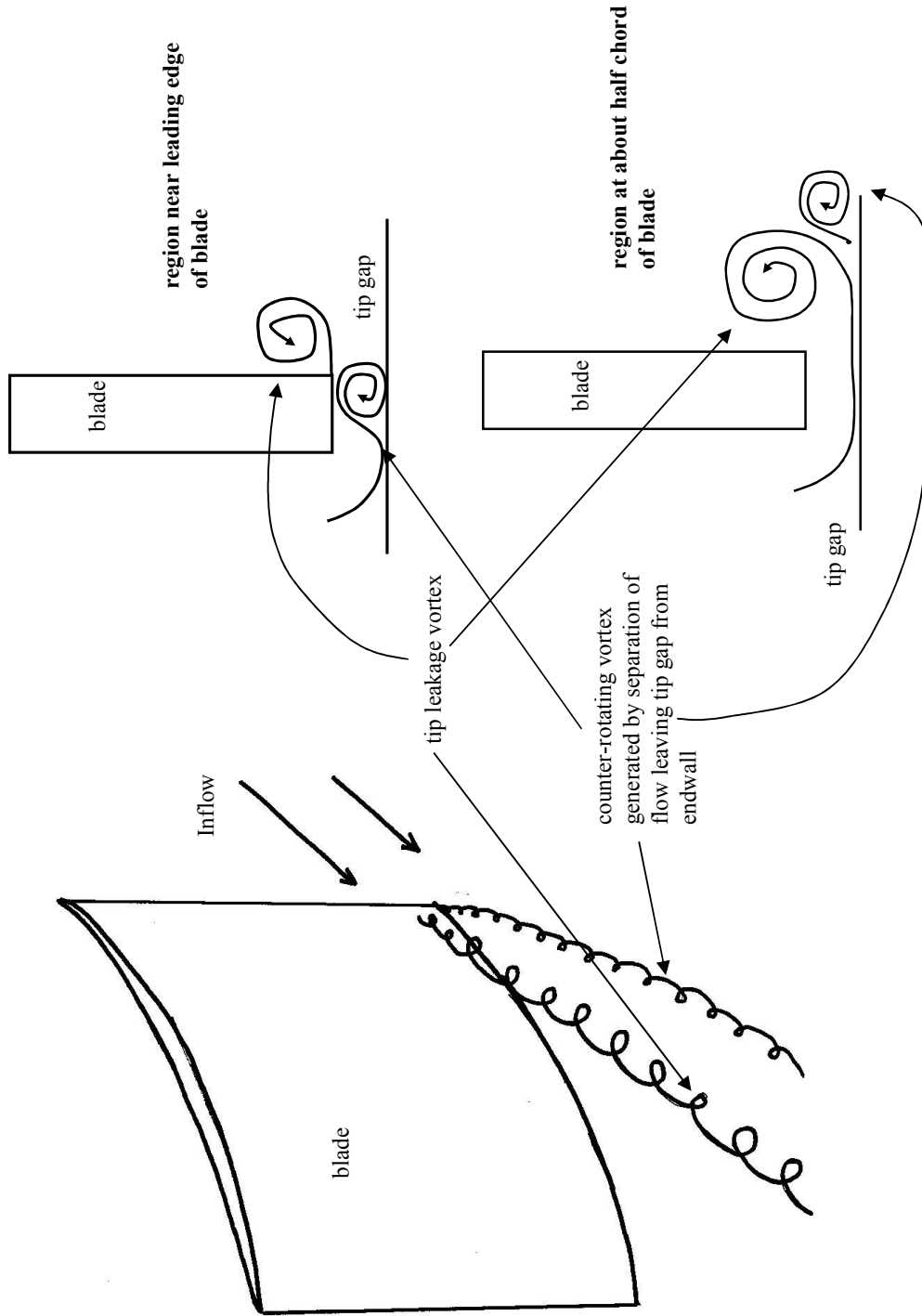


Figure 1.4 : Flow features observed in the study by Muthanna (1998). Note the presence of a second vortex in addition to the tip leakage vortex.

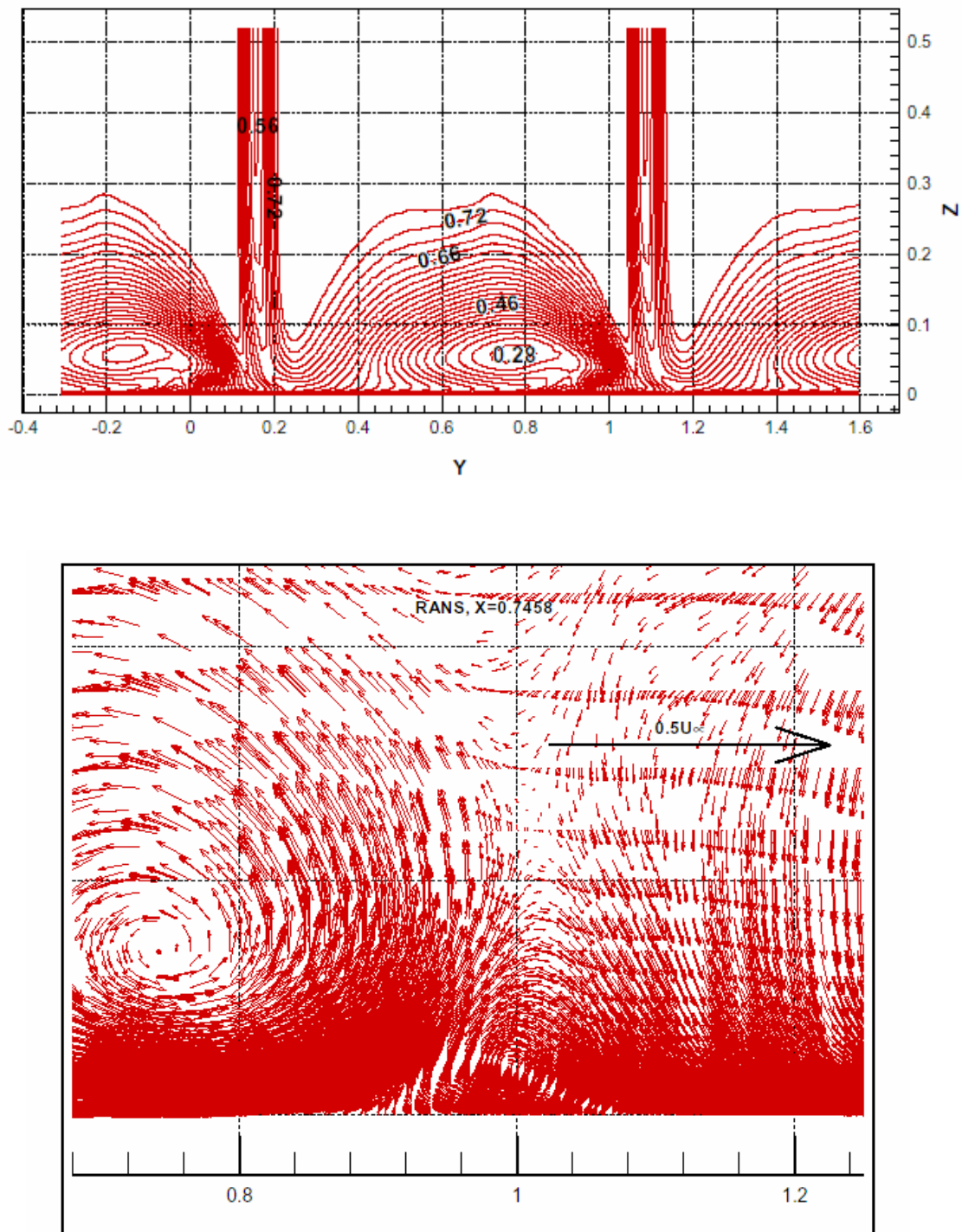


Figure 1.5: Results from the computation by Shin (2001) showing (a) Mean streamwise velocity contours and (b) Mean Crossflow velocity contours (Note the presence of a secondary vortex).

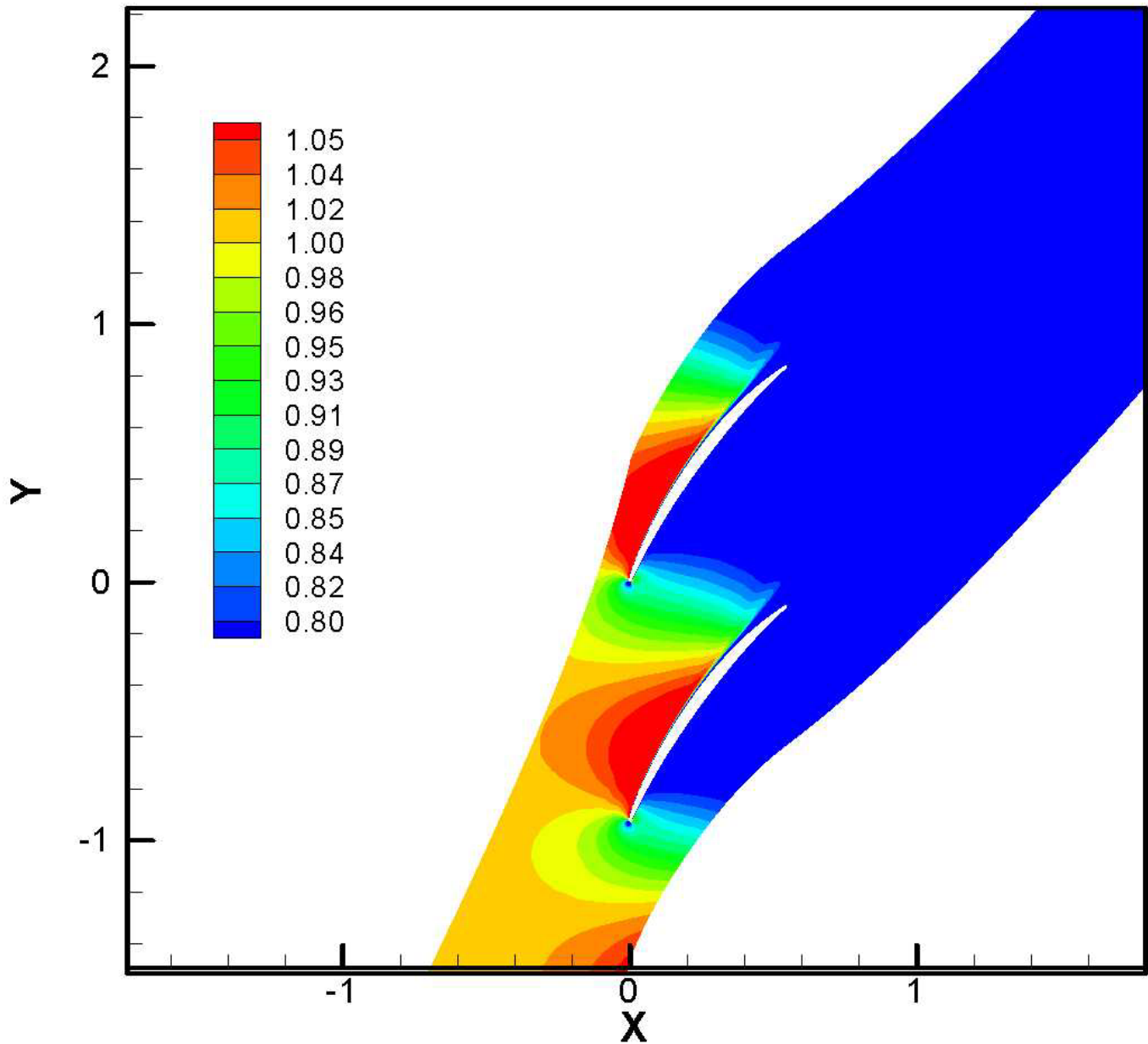


Figure 1.6: Results from the computation by Shin (2001) showing the two dimensional calculation of the mean velocity field away at the mid-span location for the flow through the cascade

2. Apparatus and Instrumentation

To obtain an experimental data set from which the effects of inflow turbulence can be studied, measurements were taken in the Virginia Tech Cascade Wind Tunnel. This facility was designed and constructed in the Department of Aerospace and Ocean Engineering machine shop facility at Virginia Tech. The tunnel and measurement system are described within the sections in this chapter.

2.1. Virginia Tech Cascade Wind Tunnel

Shown in Figure 2.1 is the 8-blade 7 passage linear compressor cascade wind tunnel. This facility was constructed in 1996 and the flow field downstream of the blade row has been documented with great detail in previous studies (Muthanna *et al.*(1998) Wenger *et al.*(1998) Wang *et al.*(1999)). For the purposes of the present study, the tunnel was modified from the original configuration by moving the blade row 0.20m downstream, to provide sufficient development length for the grid generated turbulence as well as room for other capabilities (see Ma *et al.*1998).

The cascade tunnel has an overall length of 11m. Referring to Figure 2.1, the blower section of the tunnel consists of a centrifugal fan powered by a 15h.p. motor with a diameter of 1.12m. This is followed by a diffuser and settling chamber with a combined length of 4.26m. Conditioning screens are placed at the end of the settling chamber, to reduce turbulence levels in the flow. The flow then proceeds through a contraction with a contraction ratio of 6.43:1 at the entrance of the test section.

2.2. Test Section

A plan-view schematic (not to scale) of the test section is shown in Figure 2.2. The test section is divided into two parts, the inlet section and the downstream section, separated by the endwall boundary layer scoops. The test section has a steel frame made from ‘C’-section steel channels which were bolted to the concrete floor of the building housing the tunnel to reduce vibration. The inlet and the downstream sections are joined at the blade row. The

middle of the blade row, between blades 4 and 5, is positioned 1.6m downstream of the contraction exit.

2.2.1. Inlet Section

In the plan-view, Figure 2.2, the inlet section is a quadrilateral, with the flow direction of the potential core being perpendicular to the contraction exit. The plane perpendicular to the potential core has a rectangular cross section with a width of 0.76m and a height of 0.3048m. The inlet section terminates at the boundary layer scoops, and the plane at this location is at an angle of 24.9° to the potential core, with a width of 1.81m. Consequently, the two sides parallel to the potential core are of unequal lengths, the short side being some 0.85m in length, and the long side 2.35m in length.

The lower end-wall was made from 19.1mm thick fin-form plywood with a smooth epoxy surface finish. The sidewall arrangement at both the long and short side is shown in Figure 2.3 (marked as section AA in Figure 2.2). Each of the sidewalls were made of two Plexiglas® sheets each with a thickness of 9.53mm. One sheet of the Plexiglas (the outer sheet) was attached to the steel frame. The second (the inner sheet) was then attached to the outer Plexiglas sheet with double sided tape and reinforced with screws. The height of the inner piece was 304.8mm, and the outer piece was 71.1mm taller. In this manner a step was created, on which the upper endwall made of 6.35mm thick Plexiglas could be placed. The upper endwall was divided into two parts; both of them reinforced with C-section aluminum bars to facilitate removal and insertion of the upper endwall during measurements.

2.2.1.1. Boundary Layer Scoops and Upstream Bleeds

Initial estimates of the boundary layer thickness at the boundary layer scoops were calculated using the 1/7 velocity distribution law leading to the following estimation formula (Young, 1989):

$$\delta = 0.37x_c^{4/5} \left(\frac{\nu}{U_\infty} \right)^{1/5}$$

where δ is the boundary layer thickness, ν is the kinematic viscosity, U_∞ is the free stream velocity and x_c is the distance between the contraction exit and the point where the boundary layer thickness is being estimated in the flow direction. From this relationship, the boundary layer thickness at the leading edge of the suction slot will vary from 0.019m at the

short sidewall, to $0.042m$ at the long sidewall. These boundary layers are removed using boundary layer scoops positioned $0.44m$ upstream of the blade row, the arrangement is shown in Figure 2.4. The figure is presented on a plane (section BB in Figure 2.3) perpendicular to the blade row, thus the distances are not in the free stream direction but at an angle of 65.1° to the free stream direction. The height of each scoop was $0.0254m$ and thus reduces the height of the downstream section to $0.254m$.

The primary mechanism at work here to remove these boundary layers is the pressure difference between the ambient room and the test section. The pressure within the tunnel can be adjusted by means of screens placed at the exit of the downstream section, creating a pressure difference and removing a portion of the endwall flow through the scoops. The back pressure can be adjusted so that a slice of fluid taller than the height of the scoops can be removed, but this will introduce a pressure gradient in the potential core. To avoid pressure gradients in the potential core passing between the upper and lower endwall scoops, they must remove a $25.4mm$ tall slice of flow from the upper and lower endwall. From the initial estimates of the boundary layer thickness, there will be some of the boundary layer spilling over the scoops where the thickness is larger than the scoop height. This would result in an uneven endwall flow entering the blade row due to the residual boundary layer that the scoops are unable to remove. This is particularly important on the flow on the lower endwall as it is the region where the dominant flow features in these type of configurations are formed, and thus an even flow is desired so as to improve the periodicity of the flow. Thus, some additional bleeding is necessary to reduce the size of the boundary layer on the lower endwall.

This was accomplished by means of a porous strip spanning the lower wind tunnel end-wall shown in Figure 2.5. The strip extends $0.0635m$ in the flow direction, and spans the width of the test section ($0.762m$). It is made from perforated stainless steel sheet placed $0.53m$ downstream of the exit of the contraction section. The upstream bleed removes 8% of the flow thereby creating a new boundary layer originating at the upstream bleed. With the bleed, the estimates for the boundary layer thickness are $0.009m$ at the short sidewall of the tunnel, and $0.034m$ at the long sidewall. While there is still a portion of the lower endwall boundary layer taller than the scoop heights, estimates of the height of the new boundary layer at the measurement passage are $0.019m$ (compared to $0.309m$ without the bleed), which

indicates that the lower endwall boundary layer will be completely removed with the scoops for the measurement planes in question. The study by Muthanna (1998) did not have this additional upstream bleed, and thus had a slight pressure gradient in the potential core (a 5% reduction in the potential core velocity was seen at the blade row when compared to the velocity at the contraction exit), but for the present study, the flow quality was improved and did not show any reduction in the potential core velocity in the inlet section.

Further refinement of the amount of flow drawn out by the scoops was accomplished by varying the opening of the adjustable flanges at the exit of the suction slots, shown in Figure 2.4. Due to the removal of the boundary layer, a new boundary layer originating at the leading edge of the boundary layer scoops begins to form. Shown in Figure 2.4 is a square cross section wire 2.54mm on edge spanning the entire length of the scoops, used to trip the new lower end-wall boundary layer. The wire was placed 7mm downstream of the leading edge of the suction slot.

2.2.1.2. Sidewall Scoops

To remove the sidewall boundary layers, there were two openings formed by the gap between the leading edge of the first and the last blades and the inlet sidewalls, and these are shown in Figure 2.3 (labeled as sidewall bleeds). These openings have a span the height of the downstream section from the upper to the lower endwall for a length of 0.254m and make an opening of 0.03m between the sidewall and the blade surface when fully opened. Their size could be varied with the use of adjustable aluminum flanges that can either completely or partially cover the sidewall scoops. This is accomplished by fabricating the aluminum flanges to the shape necessary to give the desired scoop opening and two of these configurations are shown in Figure 2.6.

2.2.2. Downstream Section

The downstream section of the tunnel can also be seen in figure 2.3. The frame was made of steel C-section and was bolted to the floor, similar to that done to the inlet section. The downstream section had a rectangular cross section of $1.626\text{m} \times 0.254\text{m}$, in a plane parallel to the cascade trailing edge plane. The reduction in height of the downstream section is due to the presence of the boundary layer scoops on both the upper and lower endwalls. The upper endwall of the downstream section is fabricated from Plexiglas and the

lower endwall from fin-form plywood, and details of the downstream section will be discussed here. Slots have been cut into the upper endwall Plexiglas to enable the insertion of measurement probes (hot-wire and Pitot-static). Slots not being used during measurement runs are sealed with tape. The slot used for traversing the probes is sealed with a mylar flap such that the amount of flow being bled from the opening is minimized.

2.2.2.1. Blade Row

The blade row leading edge was positioned $0.44m$ downstream of the suction slot leading edge as shown in Figure 2.2. It consists of 8-cantilevered G.E. rotor B section blades, forming 7 passages. Coordinates for the blade cross section are given in Table 2.1 and are plotted in Figure 2.7. The blades have rounded leading and trailing edges, and a maximum thickness of $11mm$ at the 60% chord location.

Table 2.1 : Co-ordinates of the GE rotor B section

Pressure Side		Suction Side	
x/c	y/c	x/c	y/c
0.000000	0.000000	0.000000	0.000000
0.000435	0.000596	0.000060	-0.001491
0.001413	0.001047	0.000923	-0.003169
0.002926	0.001323	0.002598	-0.005009
0.004966	0.001388	0.005091	-0.006975
0.007524	0.001209	0.008414	-0.009021
0.010599	0.000777	0.012579	-0.011102
0.014200	0.000137	0.017595	-0.013180
0.019048	-0.000748	0.023465	-0.015238
0.029117	-0.002550	0.030187	-0.017291
0.039178	-0.004300	0.037745	-0.019400
0.049233	-0.006001	0.045855	-0.021590
0.096961	-0.013419	0.093151	-0.033478
0.144562	-0.019783	0.140592	-0.043940
0.192059	-0.025156	0.188155	-0.053027
0.239468	-0.029599	0.235822	-0.060789

0.286809	-0.033171	0.283572	-0.067278
0.334100	-0.035929	0.331389	-0.072544
0.381356	-0.037929	0.379254	-0.076640
0.428588	-0.039220	0.427156	-0.079613
0.475794	-0.039826	0.475098	-0.081487
0.522983	-0.039750	0.523069	-0.082262
0.570167	-0.038991	0.571058	-0.081938
0.617353	-0.037568	0.619059	-0.080492
0.664516	-0.035603	0.667097	-0.077670
0.711679	-0.032997	0.715151	-0.073277
0.758887	-0.029596	0.763179	-0.067158
0.806192	-0.025241	0.811130	-0.059163
0.853654	-0.019769	0.858947	-0.049143
0.901342	-0.013007	0.906564	-0.036954
0.949328	-0.004778	0.953911	-0.022461
0.959464	-0.002843	0.963827	-0.019107
0.969617	-0.000834	0.973727	-0.015645
0.979787	0.001253	0.983610	-0.012072
0.989977	0.003419	0.993477	-0.008389
0.993047	0.004088	0.996438	-0.007260
0.997043	0.003561	0.999467	-0.004667
1.000000	0.000000	1.000000	0.000000

The blades were chosen based on the work of Wisler (1981), who designed the rotor B section blades as the third stage in the core compressor of an aircraft engine. As stated in Chapter 1, the goal of the current study is to simulate the flow through a core compressor similar to those seen in aircraft engines or the shrouded marine propulsors seen in submarines. Zierke *et al.* (1995, 1996), performed a study on the flow through an axial rotor pump to simulate the flow through a shrouded marine propulsor. The results of Zierke *et al.* with a different blade section, showed a blade loading distribution similar to that seen in the Wisler (1981) study with the rotor B section blades. Thus, the cascade configuration for the

present study is representative of the two types of flows, through the core compressor of an aircraft engine, and that through a shrouded marine propulsor.

Computations by Moore *et al.* (1996) on the Rotor B cascade geometry showed that a 5 passage configuration was found to be sufficient to simulate the flow field of an infinite cascade (periodic flow). By increasing the number of passages, the periodicity is improved. The current configuration of 8 blades/ 7 passages was chosen to maximize the chord size given the limited amount of laboratory space. The blades were fabricated from aluminum using a numerically controlled milling machine to a surface resolution of 0.0254mm . The blades have a chord-length of 0.254m and are inserted into the tunnel flow through the upper endwalls. Shown in Figure 2.8a is the blade support structure, and in Figure 2.8b, the blades immersed in the flow. The support structure was made of $0.0762\text{m} \times 0.0254\text{m}$ aluminum box section and the blades are attached with 6 screws to aluminum angles welded to the support structure. This allowed for adjustment of the sweep and lean of the blades. This mounting arrangement was designed to enable the blade row to be moved as one unit, and allowed for individual adjustment of the blade tip gaps once mounted in the cascade.

The details of the cascade parameters are shown in Figure 2.9. The stagger angle of the cascade was 56.9° , and the inlet angle of the flow was 65.1° . The axial chord, c_a , is also indicated and it signifies the perpendicular distance from the leading edge line to the trailing edge line based on the stagger angle of the cascade. The blade spacing (or pitch) was 0.236m , which implies a solidity of 1.08. As the potential core passes through the blade row, it undergoes a turning of 11.8° from the inlet direction as indicated in Figure 2.9. To set the tip gap between the blades and the lower endwall, the blades were initially adjusted on the support structure such that there was no tip gap between the blade tips and the lower endwall. The tip gaps were then set by placing shims of known thickness under the support structure. The tip gaps were further adjusted using the screws on the support structure (Figure 2.8), and gage blocks placed on the lower endwall so that the tip gap was consistent between the leading edge and trailing edge of all 8 blades by 0.0254mm . In this manner, the tip-gaps under the blades were set to have a nominal tip gap of 1.65% of the chord (4.2mm) for all measurements. Thus, the aspect ratio of the blades when immersed in the tunnel was 0.984.

The boundary layers on both the suction and pressure sides of the blades were tripped 0.0254m from the leading edge of the blade using a 6.35mm strip of 0.51mm diameter glass

beads extending from root to tip. The boundary layers were tripped to ensure that the boundary layers underwent transition to turbulent flow, keeping the flow from detaching from the surface of the blade. The trip strips on the suction side of the blades are shown in Figure 2.8b.

Shown in Figure 2.10 is the upper and lower endwall geometry around the blade row. On both endwalls, the boundary layer scoop is followed by a 5.9mm aluminum spacer. The lower endwall boundary layer scoop also has the boundary layer trip as mentioned previously and is marked in the figure. After the scoop and spacer, the similarity between the two endwalls ends. The upper endwall is primarily 6.35mm thick Plexiglas sheets through which slots were cut to allow the insertion of the blades into the test section. The roots of the blades were sealed at the upper endwall with 0.8mm thick steel sheets that conformed to the blade surface (maximum gap between the blade and sheet was less than 0.8mm). On the lower endwall, the aluminum spacer is followed by 1.6mm Teflon sheet placed over fin form plywood with a thickness of 16mm with a flatness of 0.2mm . There are no steps between the top surfaces of the scoops, aluminum spacers and the Teflon layer. The 0.9mm gap between the aluminum spacer and Teflon bed is covered with a piece of cellophane tape (thickness 0.063mm).

2.2.2.2. Downstream of the blade row.

The sidewalls are hinged at the trailing edges of blades 1 and 8, so that their angle can be adjusted. The tailboards are set to the required angle and then secured by means of clamps attached to the blades and clamps that seal the tailboards to the upper and lower endwall. This arrangement is shown in Figure 2.11.

Downstream of the blade row, the upper endwall consists of 6.35mm thick Plexiglas, externally reinforced with aluminum channels. A series of slots are cut into the roof piece to allow insertion of probes at different axial locations within the test section. As mentioned previously, the slots are sealed with tape when not in use so as to prevent any escape of air from the test section of the tunnel. The upper endwalls are not supported by the sidewalls as in the inlet section, but are supported with aluminum flanges resting on aluminum sections attached to the frame of the section. This is shown in Figure 2.12. The lower endwall downstream of the blade row is made of 19mm thick fin form plywood and extends to the

exit screens at the exit plane of the tunnel $1.78m$ downstream of the blade row and has a flatness of approximately $0.3mm$.

2.2.2.3. Exit Plane Screens

Three screens were located $1.78m$ downstream of the trailing edge of the blade row along the tunnel axis as indicated in Figure 2.2. The screens are used to vary the pressure in the test section of the tunnel which affects the amount of flow being drawn out by the upstream bleed and the boundary layer scoops. These screens were constructed using an aluminum frame and a screen material of an open area ratio of 69.5% and were clamped to the frame of the tunnel. They were used during the calibration process to adjust the back pressure to ensure the proper working of the suction slots. For additional adjustment of the back pressure, $25.4mm$ wide strips of masking tape were attached to the screens. Two strips of tape across the width of the screens, and three strips across the height of the screens were attached at equally spaced intervals as shown in Figure 2.13.

A picture of the assembled cascade tunnel is shown in Figure 2.14, with the upper endwall of the inlet section removed. Visible in the figure is the moving wall mechanism, on the lower right corner of the picture, but as stated previously, this was not used for the present study.

2.3. Turbulence Generating Grid

A turbulence-generating grid was specifically designed for these measurements. The grid was placed at the contraction exit perpendicular to the flow direction. Note that this arrangement leads to a pitchwise turbulence gradient at the blade row, but by placing a grid parallel to the blade row (i.e. at an angle to the potential core in the inlet section), the pressure gradient created by the grid would have turned the flow before reaching the blade row resulting in a change in the inlet angle. Hence, the grid was designed based on the results of Roach (1987) to minimize the turbulence gradient across the blade row given the available development length. The other requirement of the grid was to maximize the lengthscales and the turbulence intensity given the layout of the tunnel.

A bi-planar, square mesh grid of circular cross-section rods was built and is shown in Figure 2.15. The diameters of the rods were $0.0159m$; the grid cell size was $0.0749m$ and the open area ratio 62%. The grid was placed at $1.6m$ upstream of the center of the blade row

leading edge line as shown in Figure 2.16. Flanges on the top of the grid were designed to form a continuous surface with the upper endwall. On the lower endwall, the grid was secured by placing the vertical rods in holes drilled into the fin form plywood. The grid was designed with half cells at the endwalls and sidewalls, with quarter cells in the section corners. With the images in the test section walls, this arrangement provides some simulation of an infinite grid, and thus a more closely homogeneous turbulent flow at the blade row.

When dealing with grid generated turbulence, there is a region of inhomogeneous flow an initial distance downstream of the grid due to the individual wakes of the rods. According to Roach (1997), the flow may be considered homogeneous 10 mesh lengths downstream of the grid. The minimum development length in the test section is 12 mesh lengths at blade 1, and 21 mesh lengths at the measurement passage, implying that the turbulence generated by the grid will be homogeneous. Using the formula of Roach (1997), the turbulence intensity estimated at the entrance to the middle passage in the blade row was 3% and the lengthscale of the turbulence was 0.03m.

2.4. Hot Wire Anemometry

A majority of the measurements presented in this study were taken using hot-wire anemometry. The system being used has been previously used in the studies in the Virginia Tech Cascade Wind Tunnel by Devenport *et al* (1997), Muthanna (1998), Wenger (1998), Wang (200), Ma *et al* (2001).

2.4.1. Hot Wire Probes

Two types of hot-wire probes were used to make velocity measurements in the flow field. Three component velocity measurements were made using a miniature Kovaznay type four-sensor hot-wire probe manufactured by Auspex Corporation (type AVOP-4-100). The probe had eight stainless steel tapered prongs ($75\mu\text{m}$ in diameter at their tips) positioning the sensor wires some 40mm upstream of the main part of the probe. The sensors are etched tungsten wire of $5\mu\text{m}$ diameter with an approximate length of 1.4mm giving a length to diameter ratio of 160. They are arranged as two orthogonal X-wire arrays with each wire inclined at a nominal 45° angle to the probe axis. The total measurement volume is approximately 0.5mm^3 . This probe is shown in Figure 2.17a.

Velocity measurements were also made using a TSI Model 1218 T1.5 standard boundary layer probe, and a TSI Model 1210 T1.5 General Purpose Straight Probe. These probes have a single sensor attached to the stainless steel prongs, and are shown in Figures 2.17b and 2.17c respectively. The Model 1218 was used to make boundary layer measurements upstream of the blade row, and the Model 1210 was used to make pitchwise surveys downstream of the blade row to examine flow periodicity.

2.4.2. Anemometry

Each sensor on the probes (both single and four sensor), were operated separately using a Dantec 56C17/56C01 constant temperature anemometer unit with an overheat ration of 1.7. The hot-wire signals were buffered by four 10 buck-and-gain amplifiers containing calibrated RC filters to limit their frequency response to $50kHz$. The probes are calibrated for velocity using King's Law to correlate the wire voltages to the flow velocities, by placing the probes in the uniform jet of a TSI calibrator. These velocity calibrations were performed approximately every 4 hours of data acquisition. The velocity components are determined by means of a direct angle calibration scheme, where the probe is pitched and yawed over a range of angles from -45° to 45° in both pitch and yaw. Comparing the probe outputs to the known yaw and pitch angles through a look-up table, the true relation between the flow angle and velocities can be determined. The angle calibrations which depend only upon probe geometry (see Wittmer *et al.* 1998) were nevertheless performed both at the beginning and end of the wind tunnel entry which lasted 2 weeks. Details of the anemometer system including accuracy of the system and calibration techniques are given in Wittmer *et al.* (1998) and Wittmer (1998). The anemometer bridges were optimized to give a frequency response greater than $25kHz$, and were calibrated directly by measuring its impulse response. Details of this technique are given in Muthanna (1998) and Bereketab (1999).

Signals from the anemometer system were recorded on a PC based data acquisition system manufactured by Hewlett-Packard (now known as Agilent). The HP E1432A module has a resolution of 16 bits, and is capable of taking 51,200 simultaneous samples per second on each of its 16 data acquisition channels. The module has digital signal processing capabilities, transducer signal conditioning, and anti-aliasing filters. Data is recorded on an Windows® based personal computer through an IEEE 1394 (Firewire®) bus, and archived on CD-ROM discs.

2.4.3. Probe Mounting and Positioning

Shown in Figure 2.18 are the 8 pitchwise planes at which 4 sensor hot-wire measurements were made. Single sensor hot-wire measurements were made at one plane upstream ($X/c_a=-0.23$), and one plane downstream ($X/c_a=1.26$) of the blade row. Axial distances shown in the figure are normalized on the axial chord, $c_a = 0.193m$ (see Figure 2.9). Probes were introduced into the flow through slots cut through the upper endwall roof sections. The probe holders were designed in to keep the angular deviation of the probe axis to the potential core to a minimum to reduce angular uncertainties and flow interference in the measurements. The probes were positioned in the measurement plane by means of a computer controlled traverse system.

2.4.3.1. Traverse System

The probes were mounted in the tunnel and positioned using the traverse system described below. This 2-axis system is shown in Figure 2.19. Each axis is driven by a lead-screw, mounted on a double rail and moved by a Compumotor model S-57-83-MO stepper motor. Stepper motors were controlled by a Parker PDX13 single-axis package mini-step drive. The resolution of the programmable traverse movement was $0.025mm$. Probe holders were affixed to a carriage attached to the lead screws using anti-backlash nuts. TechnoSel manufactured all the anti-backlash, the lead screws, the double rail and the carriage system. The whole traverse system was mounted on an I-section aluminum bar above the windtunnel.

2.4.3.2. Four-sensor hot-wire probes.

Shown in Figure 2.20 are the probe holders for the four-sensor hot-wire probes. There are two different types of mounting arrangements depending on the location of the measurement plane; one for the in-passage measurements ($X/c_a = -0.23, 0, 0.27, 0.48, 0.77$ and 0.98 , and the second for the upstream and downstream passages ($X/c_a=-0.80$, and 1.26). Both designs allowed for the hot wire probe to be yawed and pitched setting its orientation relative to the flow before each set of measurements.

To establish the origin for probe traversing and thus the absolute accuracy of the hot-wire position, probes were aligned with a gage block placed at the surface of the blade on the lower endwall such that a corner of the block corresponded to a point $5.08mm$ away from the blade surface and above the lower endwall at each measurement location. The probe was

lowered so that the measurement volume was aligned with the edges of gage block, and this was verified using a cathetometer to an accuracy of 0.5mm . At measurement locations outside the passage, the origin chosen was marked on the lower endwall and its location measured relative to the blades, and its absolute position thus determined. Overall, the absolute accuracy of the position set by this method was $\pm 0.5\text{mm}$. However, the relative accuracy of the traverse movements was 0.0254mm .

The upper endwall slots through which the probes are inserted, were long enough to allow the probe to traverse the entire pitchwise extent of the measurement plane for $X/c_a = -0.80$ and 1.26 . The type of holder used for these planes is shown in Figure 2.21a. For measurements in the passage, traverses were made in two overlapping planes that were later combined, with the probes aligned as shown in Figure 2.21b. This scheme allowed for the entire pitchwise extent of the passage from the suction side to the pressure side of the blade surfaces to be measured with the four-sensor hot-wire probes. Two-point four sensor hot-wire measurements were also taken at select locations using the same arrangement of probe holders. A photograph of the probe holders downstream of the wind tunnel for this two-point measurement configuration is shown in Figure 2.22.

2.4.3.3. Single-sensor hot-wire probes

Shown in Figure 2.23, is the probe holder arrangement for the TSI 1218 Boundary Layer Type probe and was used to measure the boundary layers at $X/c_a = -0.23$. Also shown in the figure is a sketch of the arrangement for the TSI 1210 Straight probe, which was similar to that of the boundary layer probe, except that the probe was rotated 90° . The probes were oriented with the sensor perpendicular to the apparent flow direction. Establishing the origin for traversing the single-sensor hot-wire probes was done in a manner similar to the four-sensor probes, where the sensor was aligned with a gage block a known distance above the lower endwall. Positioning of the probes was done within the limits of the traverse resolutions (0.025mm).

2.5. Pressure Measurement System

Pressure measurements were made in the cascade tunnel, using Pitot-static probes to measure the total, dynamic and static pressures in the tunnel, and static pressure ports on the blade surface to measure the surface pressure distribution.

2.5.1. Pitot-Static Probe and Blade Pressure Ports

The Pitot-Static probe used is a Dwyer Instruments Standard Model 160 Pitot Probe (Model 167-12), with an insertion length of 305mm , and a tip length of 76mm , and is shown in Figure 2.24. An identical Pitot-static probe was used to monitor the reference pitot-static pressure in the test section and was placed at the mid-height of the inlet section, 0.95m downstream of the contraction exit, and 0.15m away from the longer sidewall in the inlet section (upstream of the passage formed between blades 7 and 8, also shown in Figure 2.24).

The pressure ports on the surface of the blade were made using 1.6mm diameter copper tubing embedded into the blade surface with a port opening of 0.8mm to the flow. Slots were machined into the surface of the blade, and the tubes inserted into the slots. Epoxy was then placed over the tubes and sanded down to the original surface shape before the slots were made. Shown in Figure 2.25 are the pressure ports on the blade surface. Due to the periodic nature of the flow, and the physical constraints of the blades, pressure ports were embedded on the suction side of blade 4, and the pressure side of blade 5, and this is shown in the plot in Figure 2.25. The ports were positioned 123mm from the blade tip. This corresponds to the mid-height of the blade row (127mm above the lower endwall) when the blade is mounted in the tunnel and the tip gap set.

2.5.2. Pressure Transducers

Both the Pitot-static probe and the pressure ports were attached to pressure transducers using Tygon® clear plastic tubing with inner diameters of 3.2mm and 1.6mm respectively. When making pitchwise traverse measurements of the velocity distribution with the Pitot-static probes, the pressures were monitored using 2 Setra model 239 electronic pressure transducers, one with a range of 0-5 in. of water, and the other with a range of 0-15 in. of water. Both transducers had an output voltage range of 0-5V. Transducer output was also recorded by one of the channels of the HP E1432A data acquisition system.

Surface pressure measurements on the blade were made using 2 Dwyer Series 427 Mark III Handheld digital manometers with a range of 0-10 in. of water, with a digital display. Readings were recorded manually from the display on the manometers. One manometer was used to monitor the dynamic pressure in the tunnel as measured with the Pitot-static

probe, and the second manometer was used to simultaneously record the pressure on the surface of the blade.

2.5.3. Probe Positioning

Similar to the procedure outlined with the hot wire probes, the Pitot-static probes were also mounted on the traverse system described in section 2.4.3.1. Again, the origin of the traverse position was set by placing the tip of the Pitot-static probe at a known location, and aligned with the potential core of the flow. This method was accurate to within $\pm 1\text{mm}$.

2.6. Oil Flow Visualization

Oil flow visualizations were taken on the horizontal lower endwall below the blade row. A mixture of Titanium dioxide, kerosene and oleic acid in the ratio of 20:50:1 respectively was applied to a sheet of smooth black self adhesive plastic sheet. The plastic sheet was fixed to the lower endwall beneath the blade tips, and the tip gap adjusted to account for the slight change in the tip gap height. The oil-flow mixture was applied using a sponge brush with the brush strokes roughly perpendicular to the endwall flow direction. The tunnel was run for approximately 8 minutes, by which time, no further changes in the oil flow pattern were observed. It was necessary to repeat the visualizations a number of times to achieve clear views of the flow patterns over the endwall. Visualizations for flows with and without grid generated turbulence were generated. The oil-flow traces sprayed with a clear acrylic coating to preserve them once removed from the tunnel.

2.7. Calibration of the Cascade Tunnel

Before operation of the cascade tunnel, it was calibrated to operate at its optimum flow condition. When the tunnel was first constructed, a systematic approach was developed to calibrate the tunnel (Muthanna, 1998). The current configuration differs slightly from the 1998 study due to the relocation of the blade row, as well as the introduction of the moving wall system. Thus, the tunnel had to be recalibrated for the present study. The same method used previously was applied for the current cascade configuration and the results are presented below. The calibration was first done without the turbulence generating grid.

For the current cascade configuration, this optimum condition implies

- A. The velocity of the flow upstream of the blade row must be maximized.
- B. There must be no velocity gradients upstream of the blade row in the potential core.
- C. There must be no pitchwise pressure gradients in the test section both upstream and downstream of the blade row.

Once these three conditions are satisfied, the cascade tunnel is calibrated and measurements can be made. The primary characteristics that can be adjusted in the tunnel are

- a) Back pressure; through the adjustments of the exit screens.
- b) The turning angle of the flow; through the adjustment of the angle of the tailboards.
- c) The amount of flow removed from the inlet section endwalls and sidewalls through the adjustment of the endwall scoops, upstream bleed, and sidewall scoops.

These controls are interdependent, and so calibration of the tunnel is an iterative process. The technique employed in calibrating the tunnel is as follows; first, the turning angle of the sidewalls is adjusted and set such that there is no pitchwise pressure gradient downstream of the blade row, followed by adjusting the back pressure and scoops to satisfy the conditions A, B, and C mentioned above. This process is repeated between the two conditions until the section is calibrated and conditions A, B, and C are satisfied. Pitot-static measurements determine whether the tunnel is calibrated or not.

Presented in Figures 2.26 and 2.27 are the Pitot-Static probe measurements in the tunnel upstream and downstream of the blade row at the mid-height ($0.92c_a$ above the lower endwall of the section) after calibration. On the horizontal axis of the plot is the normalized pitchwise location of the probe, the origin being the middle of the passage between blades 4 and 5 along the leading edge line of the blade row. The velocity is normalized on the velocity measured by the reference Pitot-static probe. The pressure coefficients C_p and C_{p0} are defined as

$$C_p \equiv \frac{p - p_\infty}{p_{0\infty} - p_\infty}$$

$$C_{p0} \equiv \frac{p_0 - p_\infty}{p_{0\infty} - p_\infty}$$

where p and p_0 are the static and stagnation pressures measured by the measurement Pitot-static probe. Conditions of the inflow, p_∞ and $p_{0\infty}$ are the static and stagnation pressures respectively as measured by the reference pitot-static probe. The normalized local velocity was calculated using the definition of stagnation pressure as $\frac{U}{U_\infty} = \sqrt{C_{p0} - C_p}$.

Figure 2.26 is a plot of the normalized velocity taken upstream of the blade row at $X/c_a = -1.0$. The average velocity at this location is $1.00U_\infty$; verifying that the endwall scoops and bleeds are removing no more flow than necessary by satisfying condition B. This measurement shows cyclic pitchwise variations with a period of $1.7c_a$, equivalent to the blade spacing, revealing the periodic upstream influence of the blade row. Furthermore, the measurements show no net pitchwise pressure gradient across the blade row, implying no turning of the flow before entering the blade row, satisfying criteria B and C.

Figure 2.27 is a plot of the normalized velocity and the two pressure co-efficients defined above taken at $X/c_a = 2.6$ downstream of the blade row. The C_p curve shows that there is no net pitchwise pressure gradient downstream of the blade row satisfying condition C, and that the static pressure in the tunnel remains constant. The variation of the stagnation pressure, C_{p0} , presented in the figure, shows the periodicity of the tunnel across 4 passage widths. Away from the blade wake regions, in the potential core, the ratio is equal to 1, indicating that the stagnation pressure downstream of the blade row remains unchanged from that upstream of the blade row. However, the average velocity ratio in this region has decreased to $0.74U_\infty$, thus by applying Bernoulli's equation in the potential core, the pressure, p , has increased from the value upstream, exactly as should happen in a compressor flow that is being simulated in the facility. In the potential core region, there is no net pitchwise variation in the average velocity indicative of periodicity of the facility, and satisfying condition C.

Single-sensor hot-wire measurements of the pitchwise variation of the flow field downstream of the blade row at $X/c_a = 1.26$ are presented in Figure 2.28. Shown in the two plots are the average normalized velocity, U/U_∞ , and the normalized velocity fluctuation, u^2/U_∞^2 , across three passage widths at a height of $0.95c_a$ above the lower endwall. The measurements reveal that the calibration of the tunnel is not affected with the addition of grid generated turbulence as the average value of the velocity in the potential core is $0.72U_\infty$ for

both inflow turbulence cases. There is a minimal variation in the potential core velocity across the three passages, 0.68% with grid generated turbulence, and 0.47% without grid generated turbulence indicating that the periodicity of the flow and thus the calibration of the tunnel is not adversely affected by the addition of grid generated turbulence.

The variation of the turbulence intensity, u^2/U_∞^2 , not only shows the elevated turbulence levels in the flow due to the presence of the grid, but also the consequence of having the blade row placed at an angle to the grid. Downstream of blade 3, the turbulence intensities are larger than that downstream of blade 6. The development length of the grid generated turbulence is less upstream of blade 3 than blade 6 as indicated in Figure 2.16, and as a consequence the decay is less, which is reflected downstream of the blade row. However, as shown above, the periodicity of the tunnel is not affected by this condition.

The results between the hot-wire measurements and the pitot-static measurements show a slight acceleration of the potential core, from $0.72U_\infty$ to $0.74U_\infty$ with downstream distance. This can be attributed to the slight acceleration the potential core may see due to the developing boundary layers on the endwalls, the growth of the wake of the blades, and possibly being influenced by the viscous regions on the lower endwall which would have a contraction effect.

The above results indicate that the tunnel is calibrated at its optimum condition, and the calibration is not affected by the presence of grid generated turbulence. This implies that the tunnel operating conditions remain the same with and without grid generated turbulence.

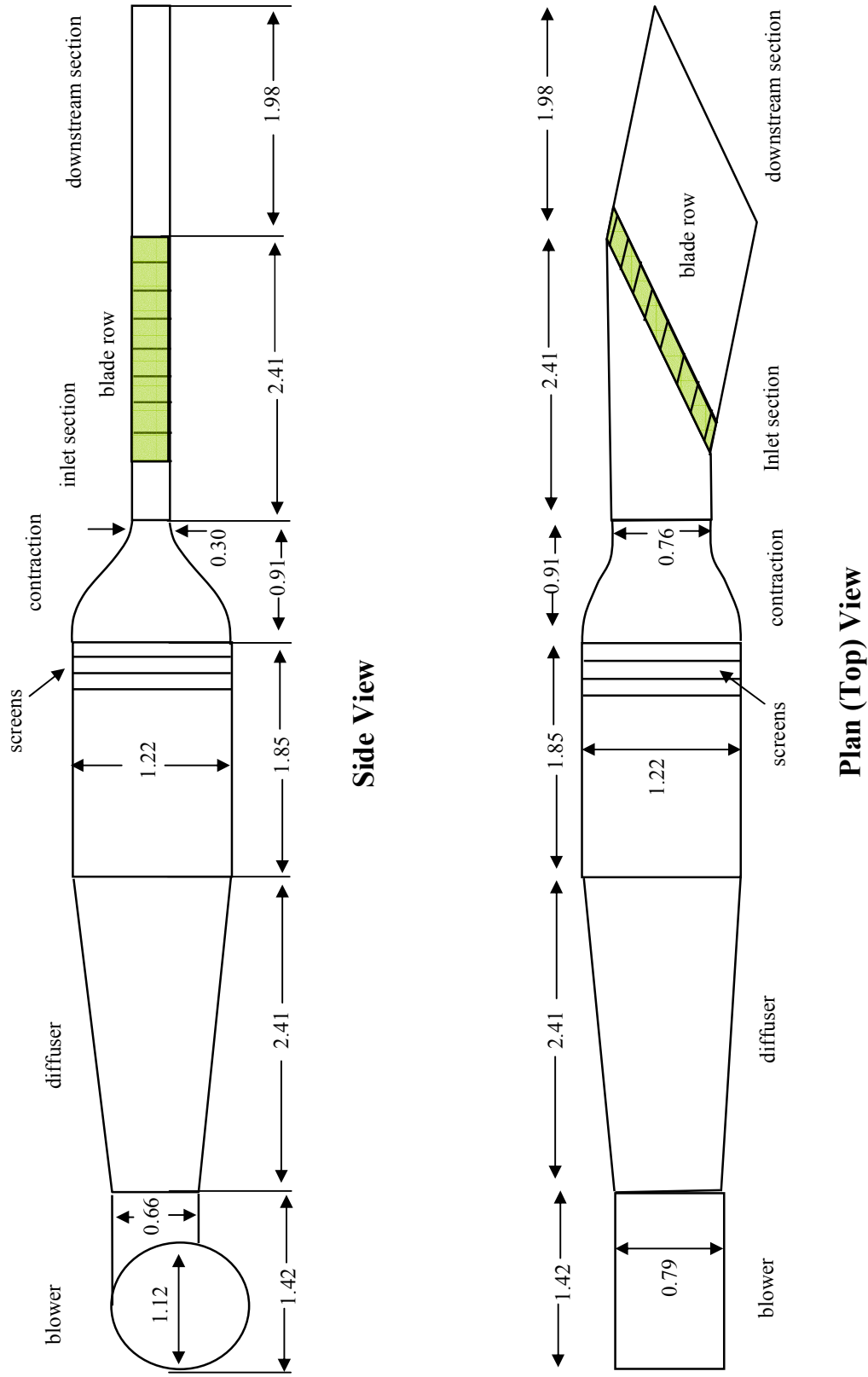


Figure 2.1: Virginia Tech Linear Compressor Cascade Tunnel
 Dimensions in meters

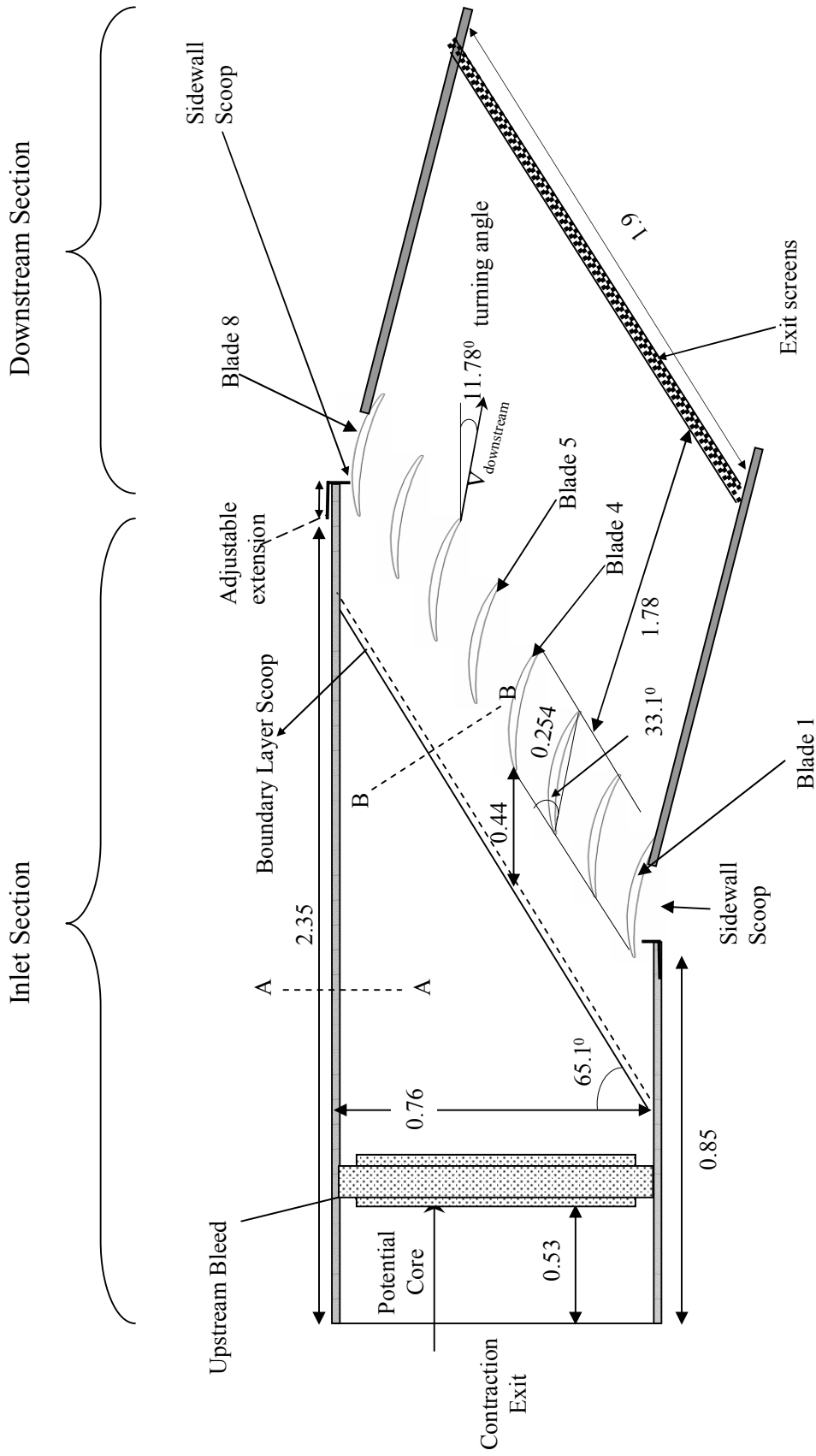


Figure 2.2: Plan-view of the Virginia Tech Cascade Wind Tunnel Test Section. *Dimensions in meters and not to scale*

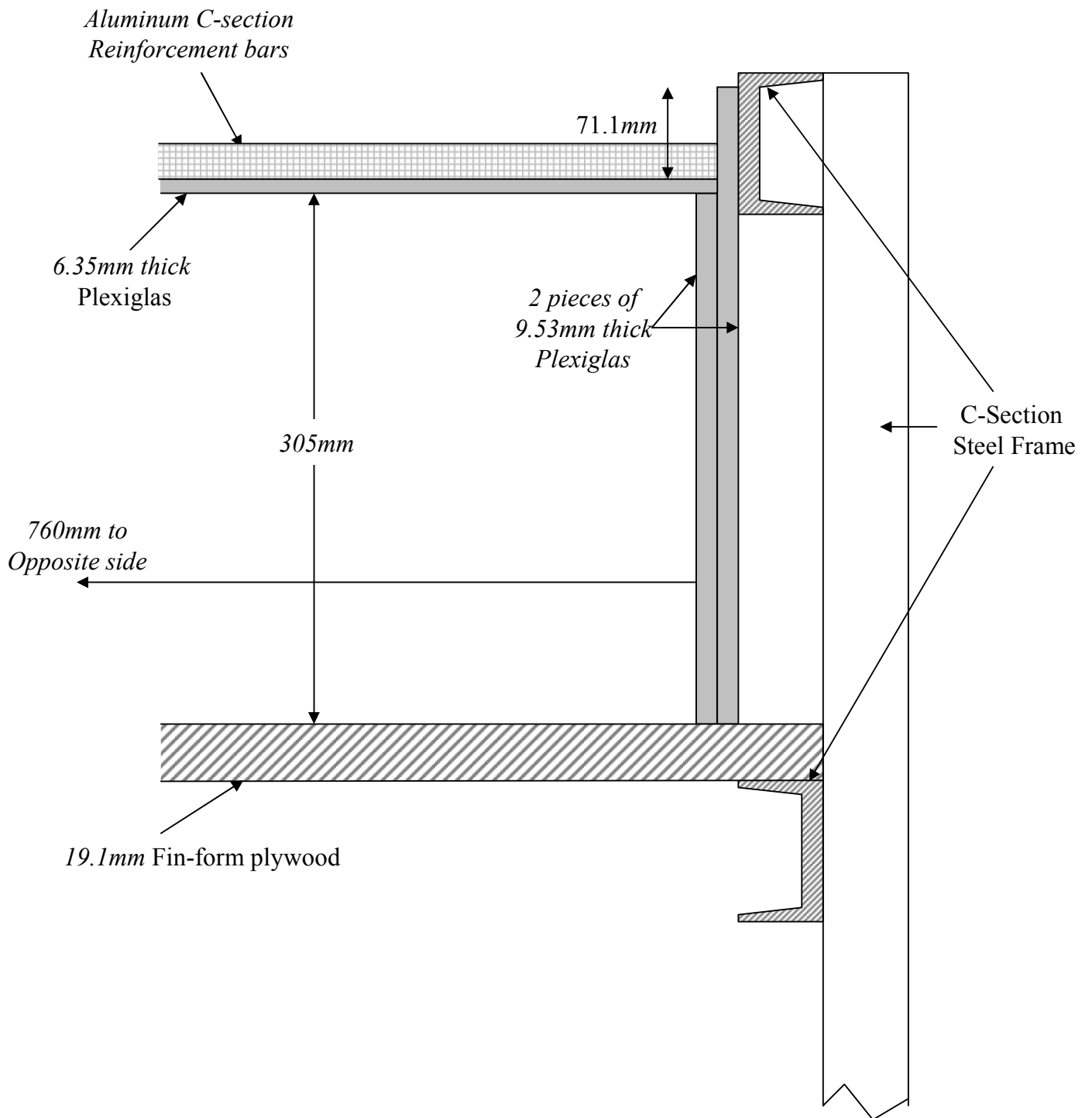


Figure 2.3: Cross section of the inlet section (Section AA in Figure 2.2).
Dimensions in meters and not to scale

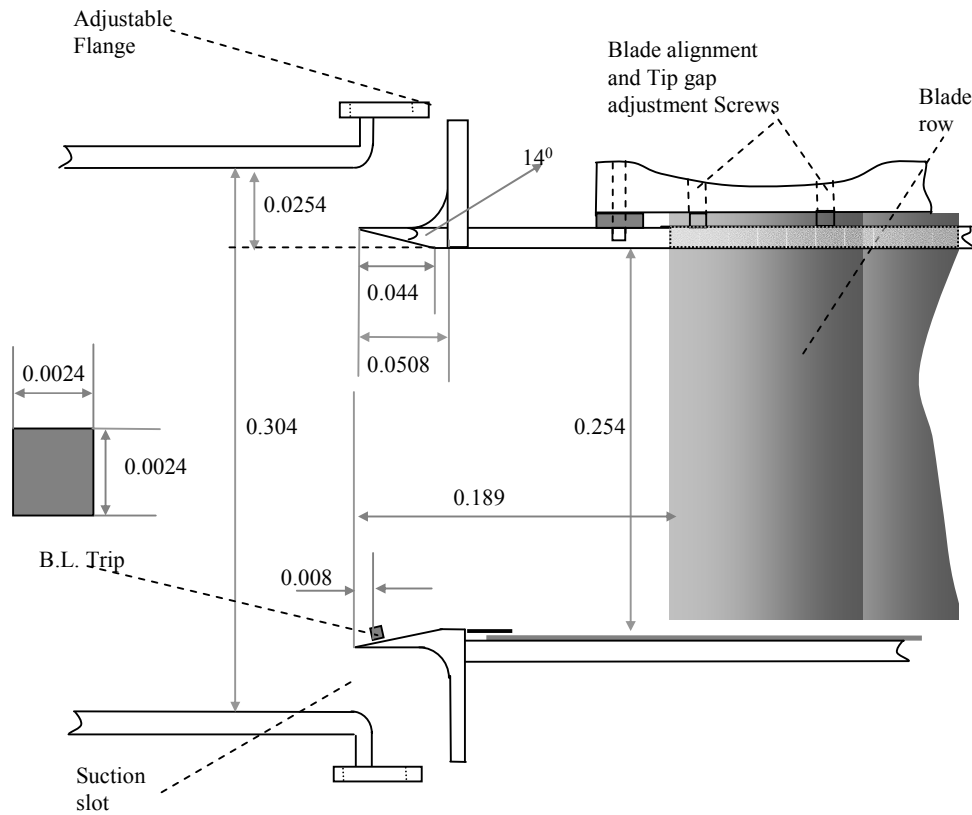


Figure 2.4: Cross section of the suction slots (not to scale)
(Section BB in Figure 2.3) Dimensions in meters

Perforated strip of stainless steel

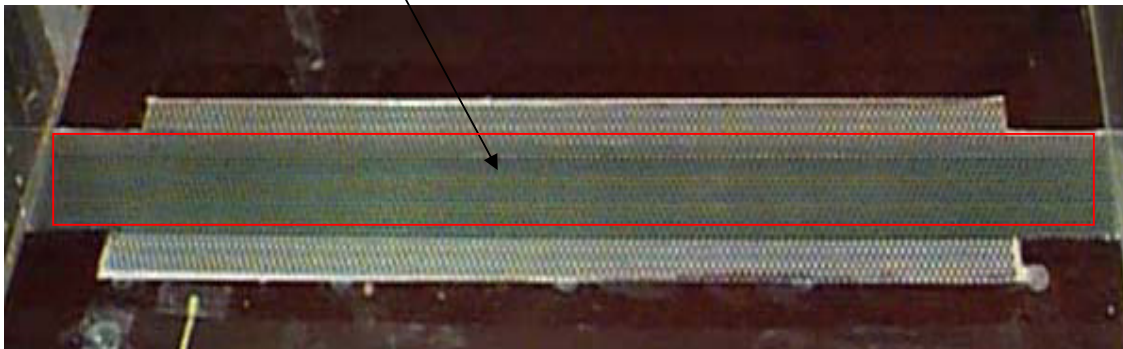


Figure 2.5: Upstream bleed on the lower endwall
Red box indicates open area of the perforated plate.
Remaining area is blocked off with tape

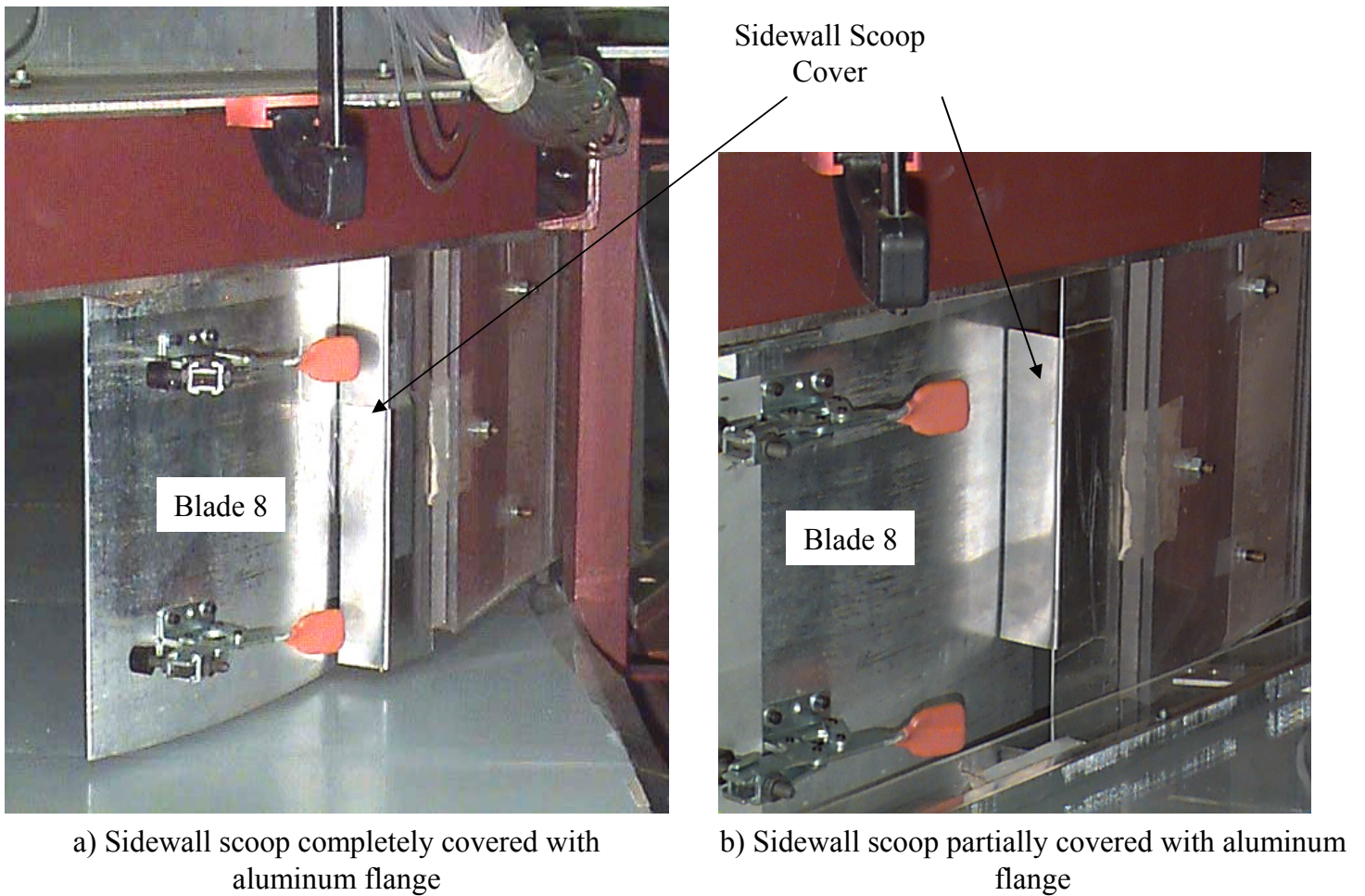


Figure 2.6: Sidewall scoop covers to control the amount of flow being drawn out of the inlet section. As shown on the two pictures, the size of the aluminum flange can be adjusted to partially cover the sidewall scoops.

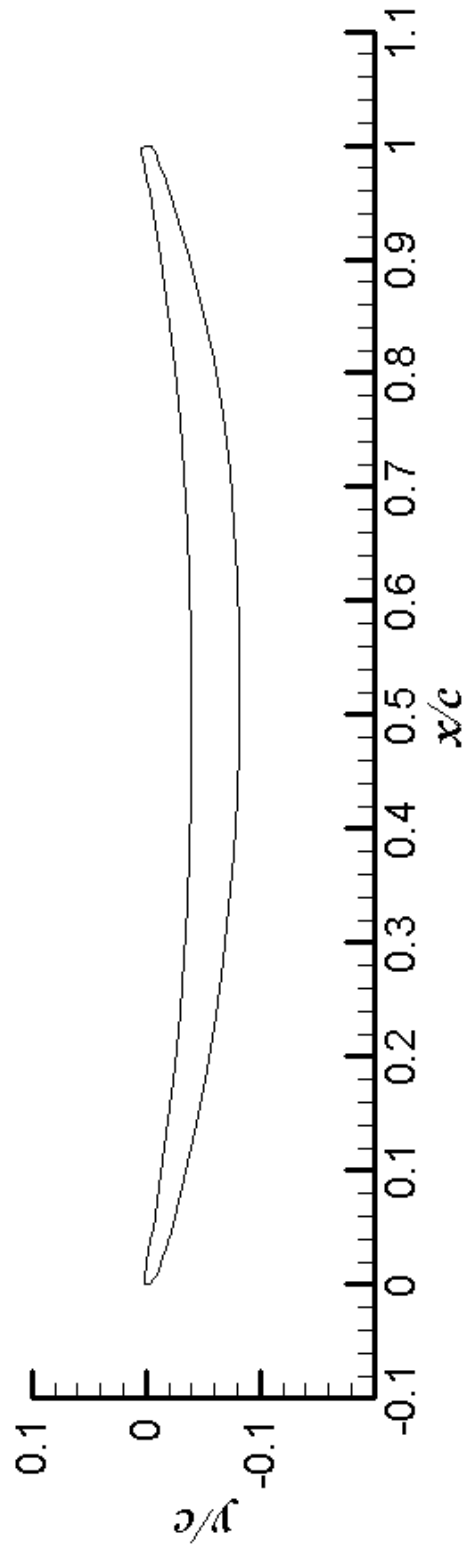


Figure 2.7: Cross section of the GE rotor B blade used in the Cascade

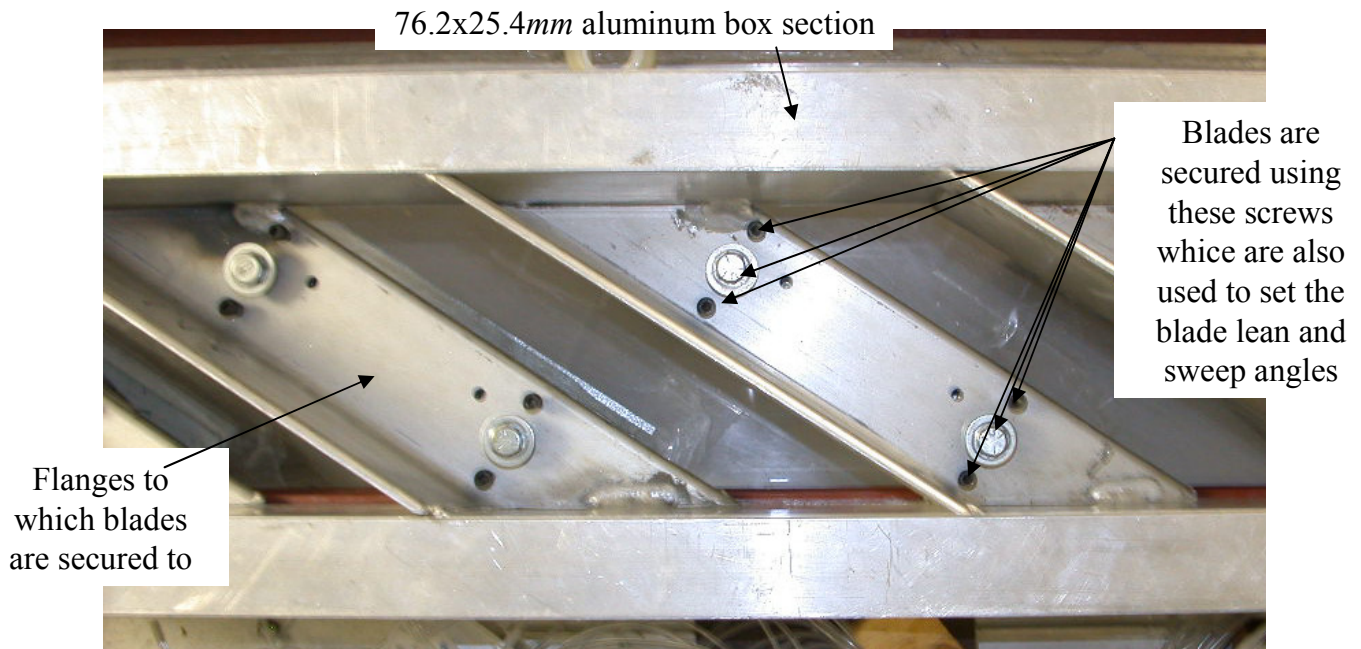


Figure 2.8a : Top view of blade support structure

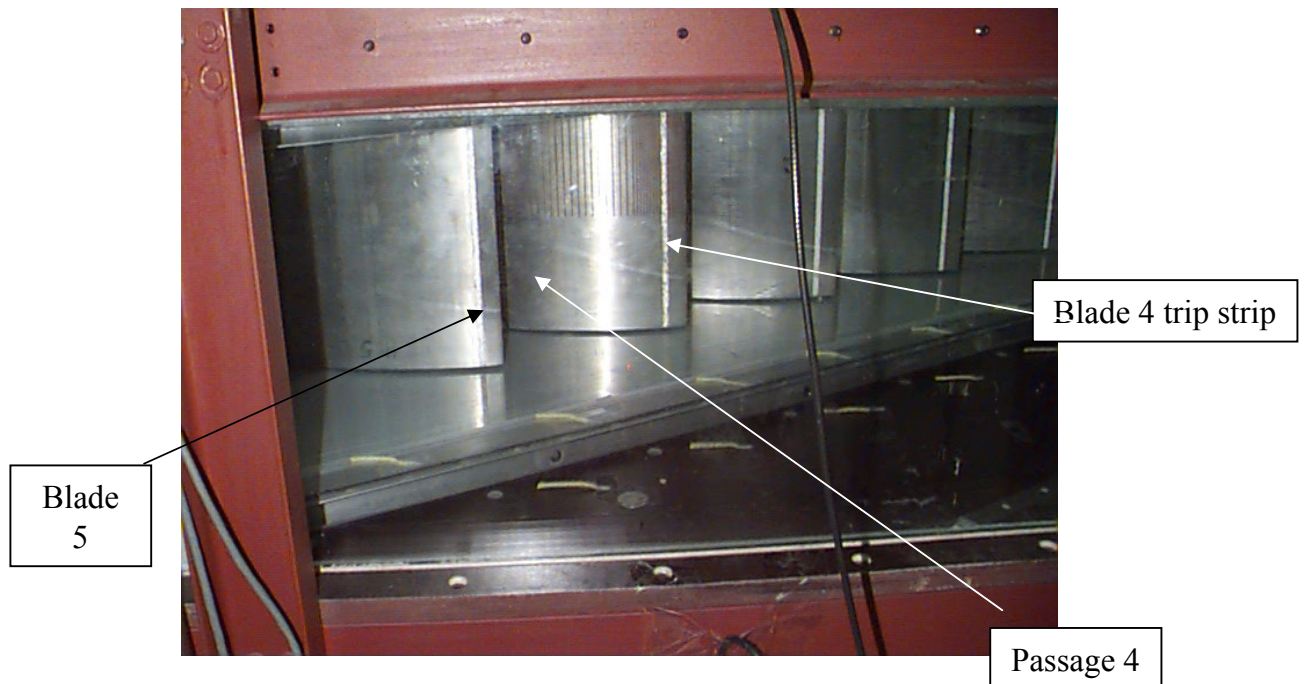


Figure 2.8b: View of the blade row inserted into the test section. Blades are held by the support structure. Passage 4, where measurements have been taken is indicated by the white arrow

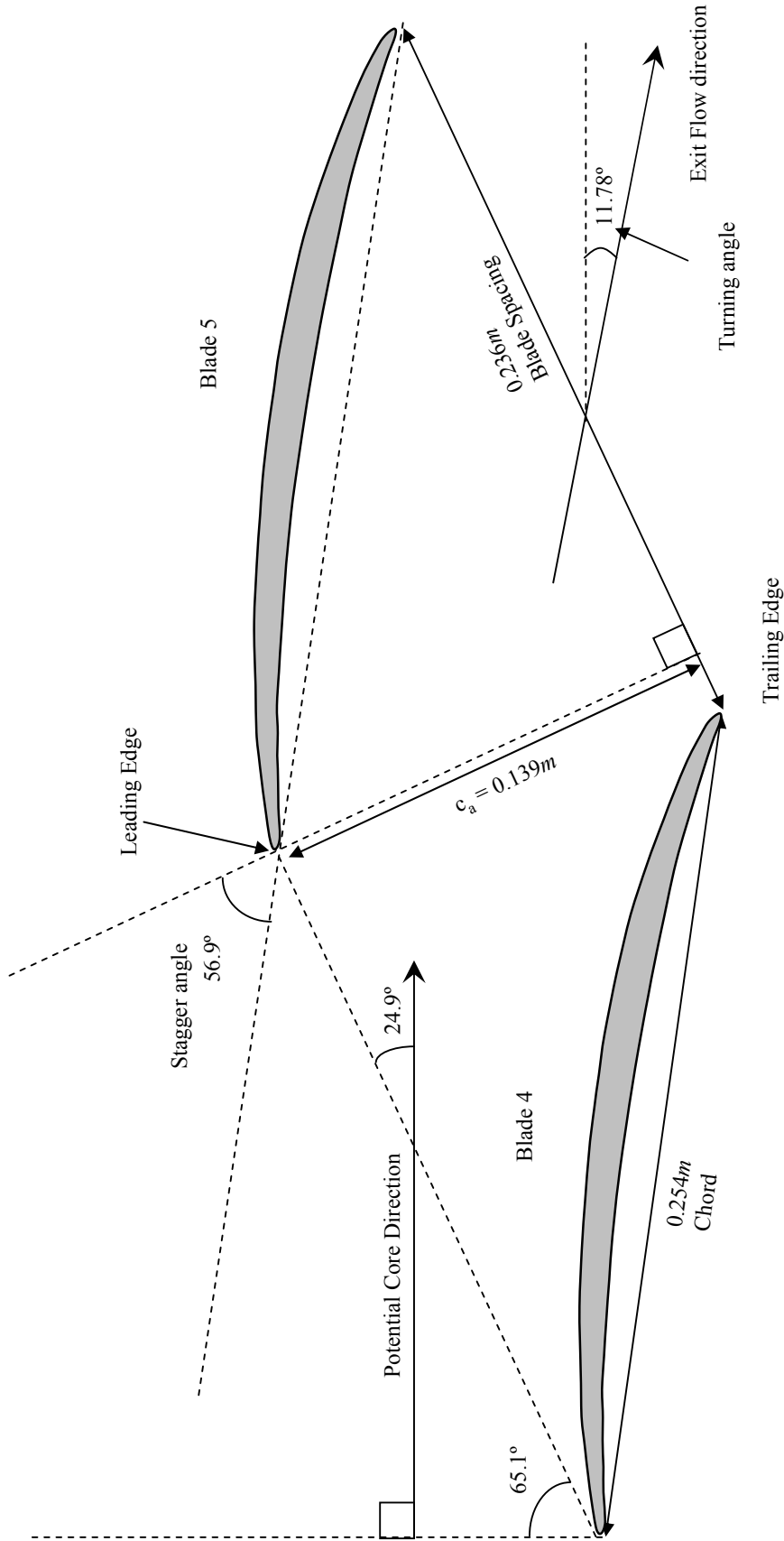


Figure 2.9: Cascade Geometry Parameters

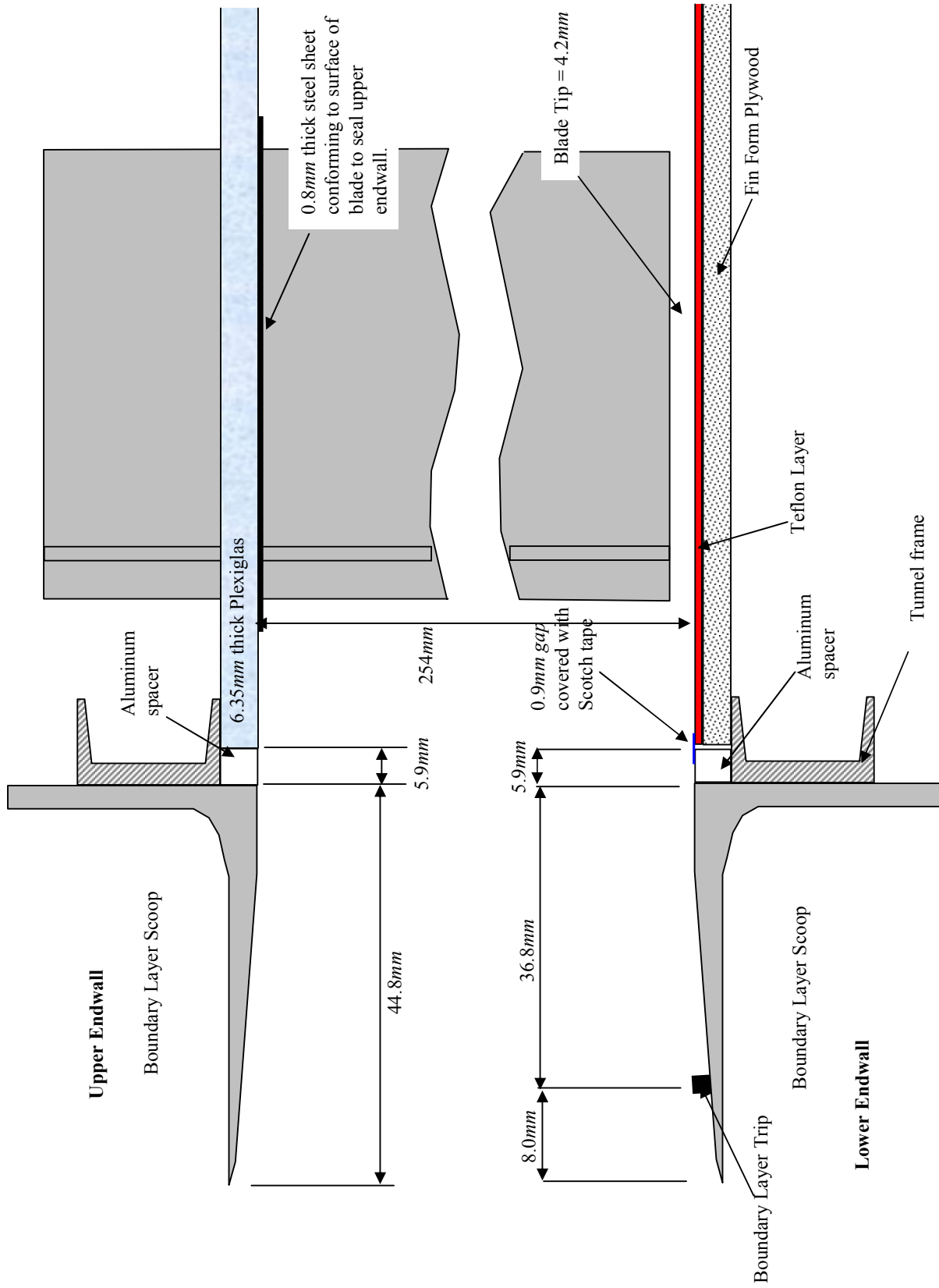


Figure 2.10: Upper and Lower Endwall details in the blade row (section BB in Figure 2.2)

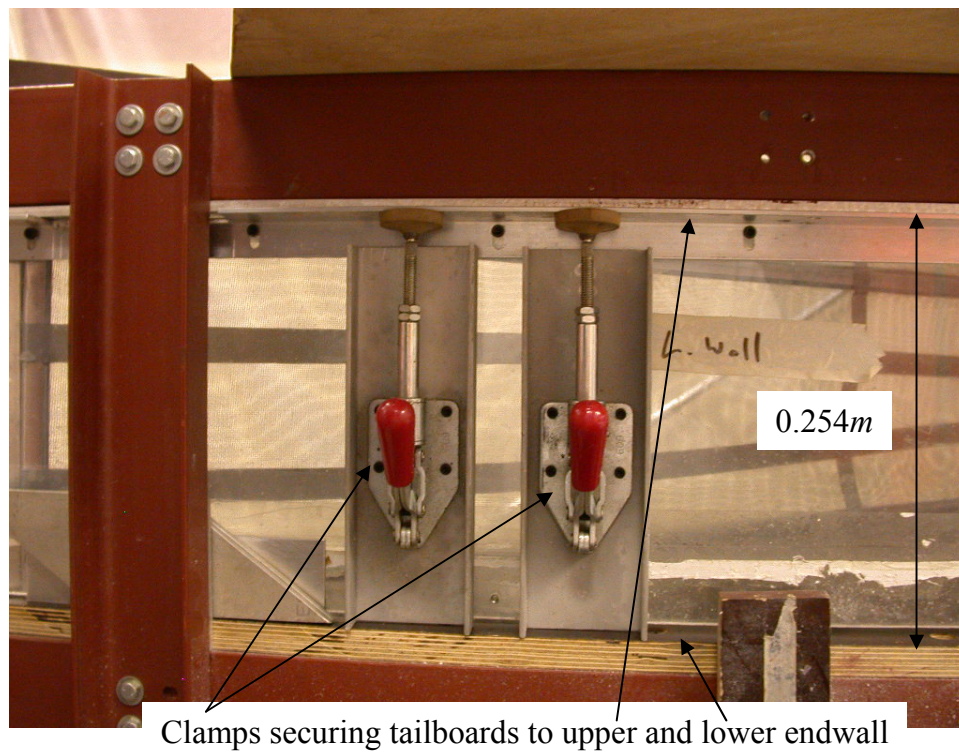
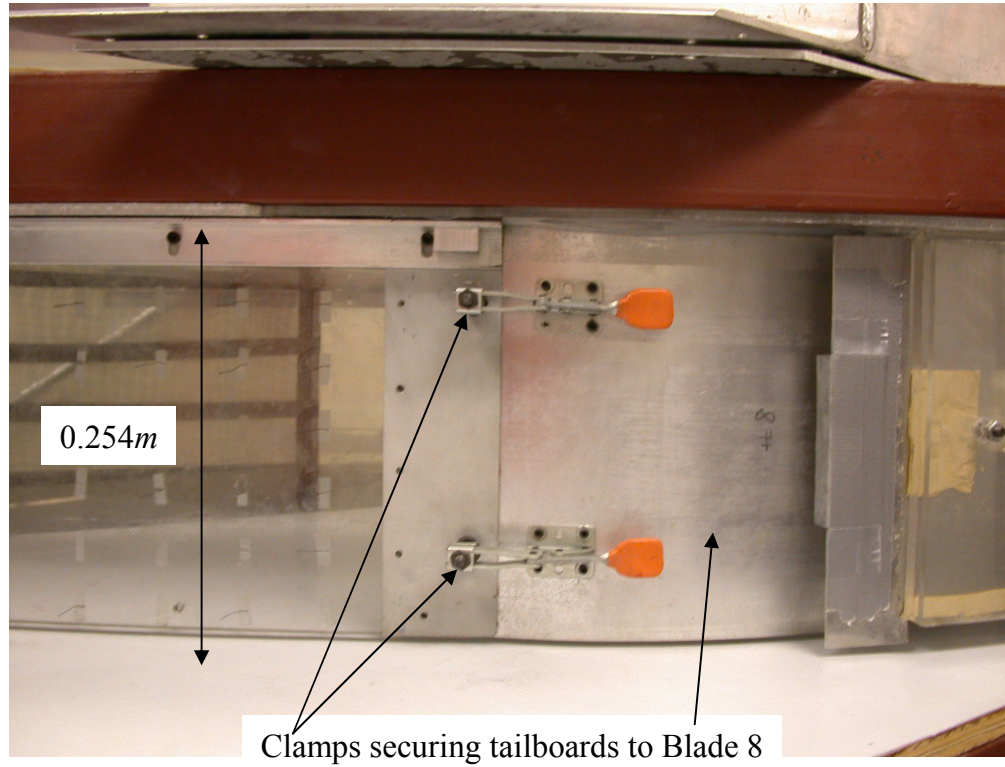


Figure 2.11 : Downstream sidewall-blade attachment configuration

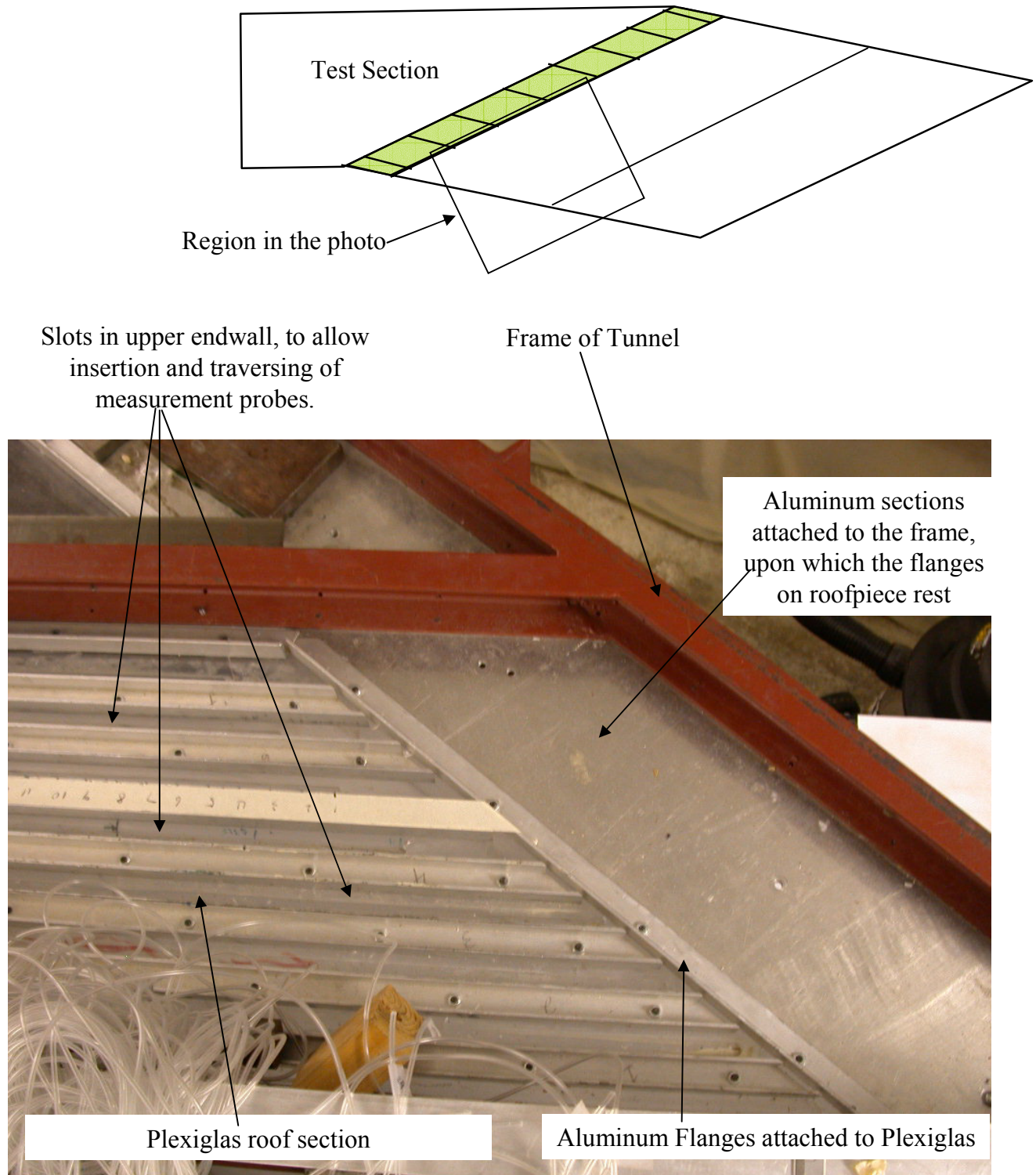


Figure 2.12 : Upper endwall mounting configuration downstream of Blade Row

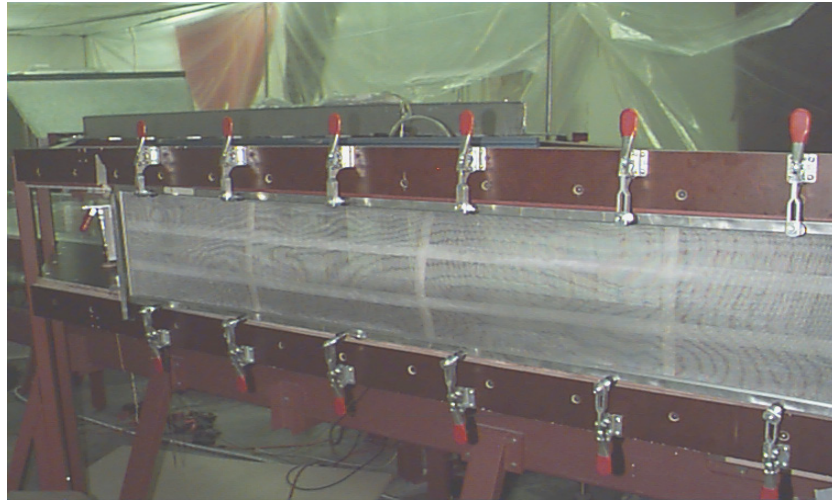


Figure 2.13: Screens at the exit plane of the tunnel.

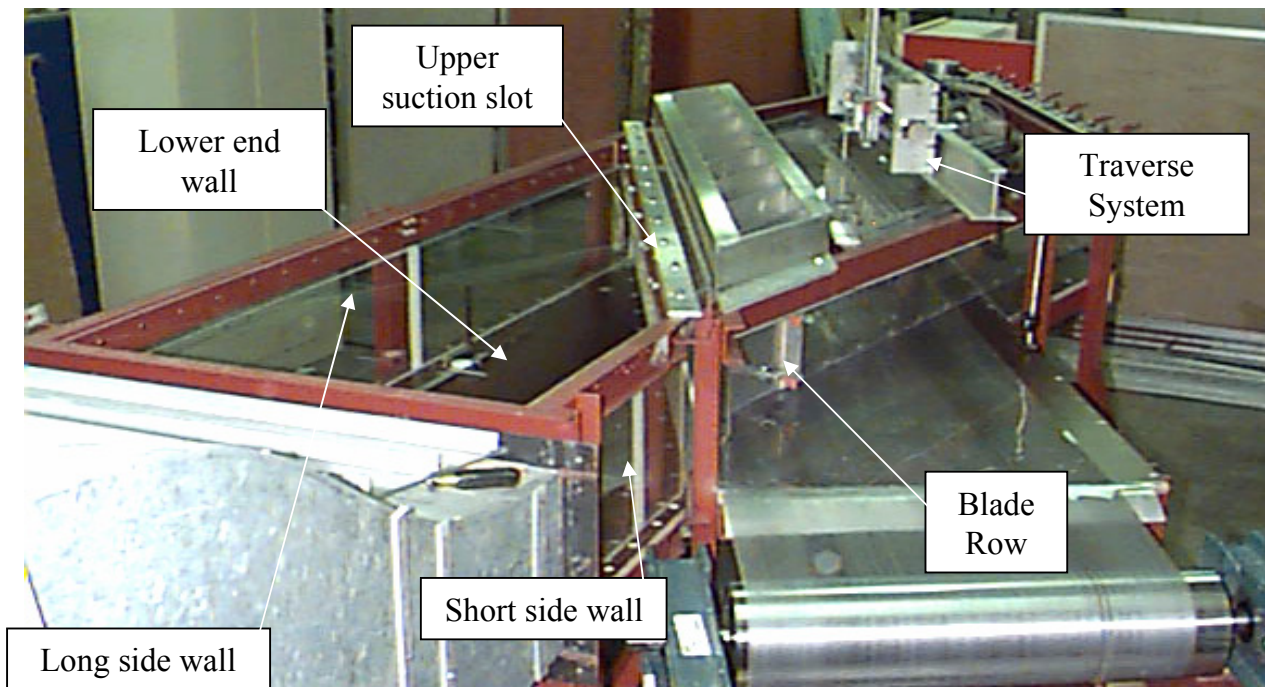


Figure 2.14: Cascade Tunnel general view

15.9mm diameter rod.

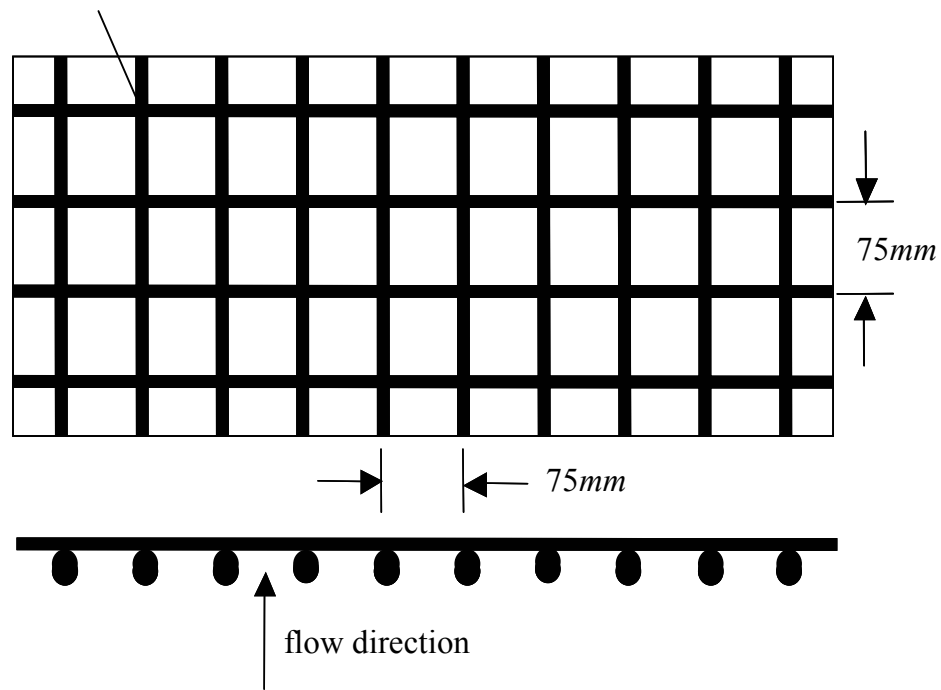


Figure 2.15: Layout of the grid

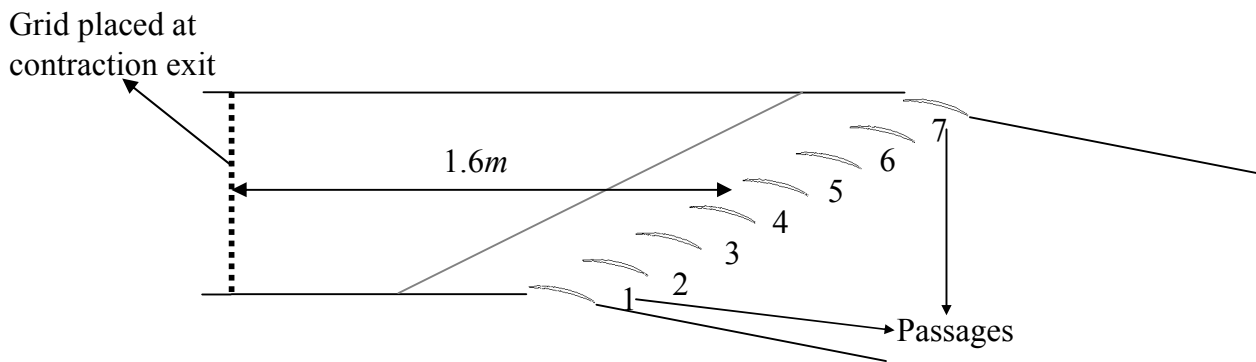


Figure 2.16: Position of grid relative to blade row (1.6m from middle passage)

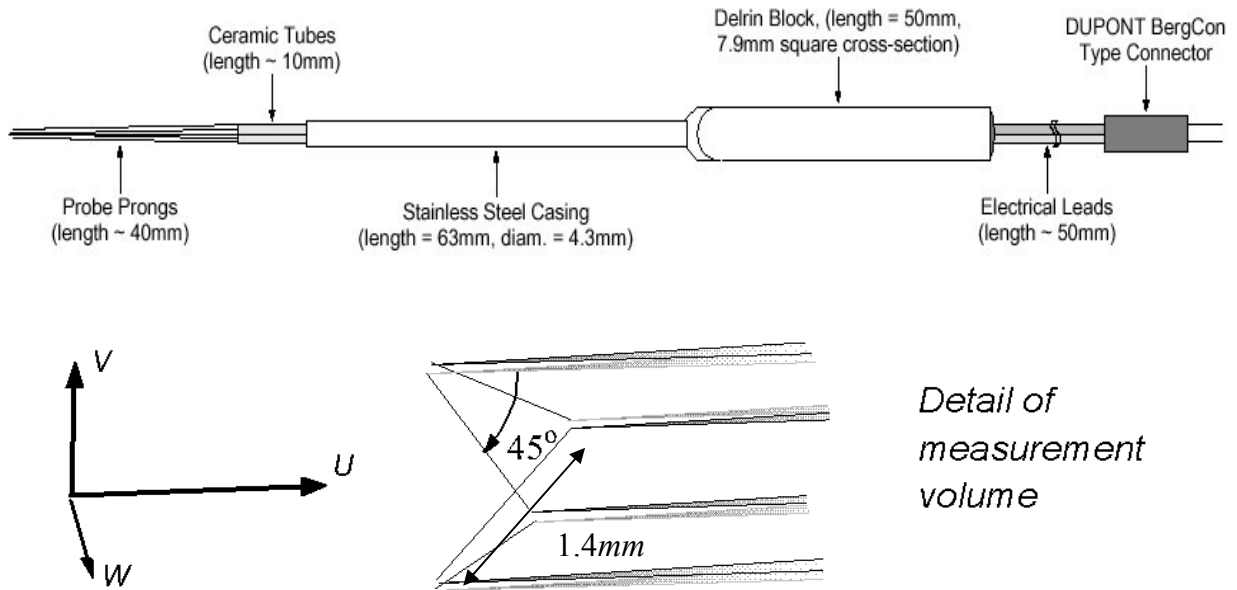


Figure 2.17a: Four Sensor Hot-Wire Probe

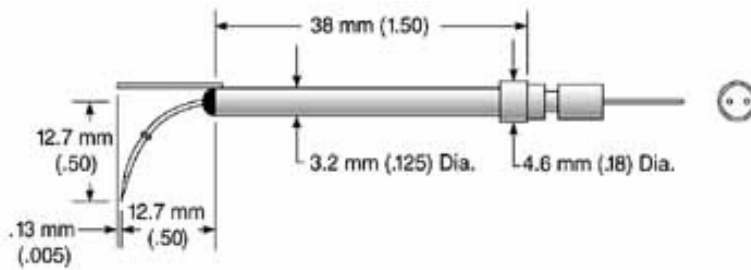


Figure 2.17b: TSI Model 1218 Standard Boundary Layer Probe
(Picture taken from TSI product webpage www.tsi.com)

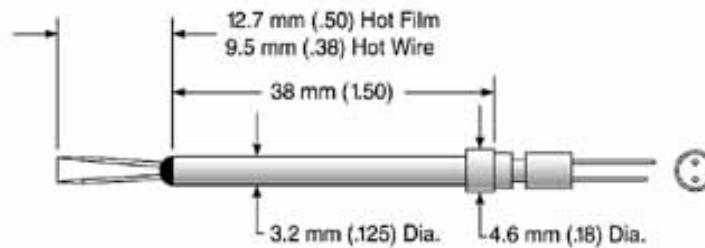


Figure 2.17c: TSI Model 1210 General Purpose Probe
(Picture taken from TSI product webpage www.tsi.com)

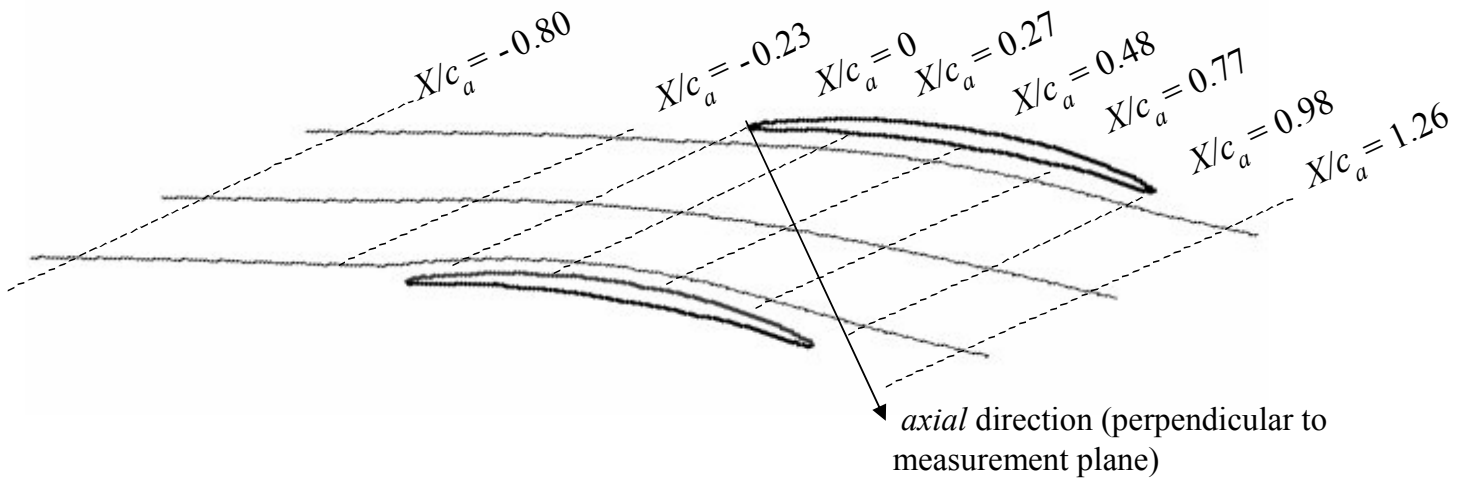


Figure 2.18: Measurement locations

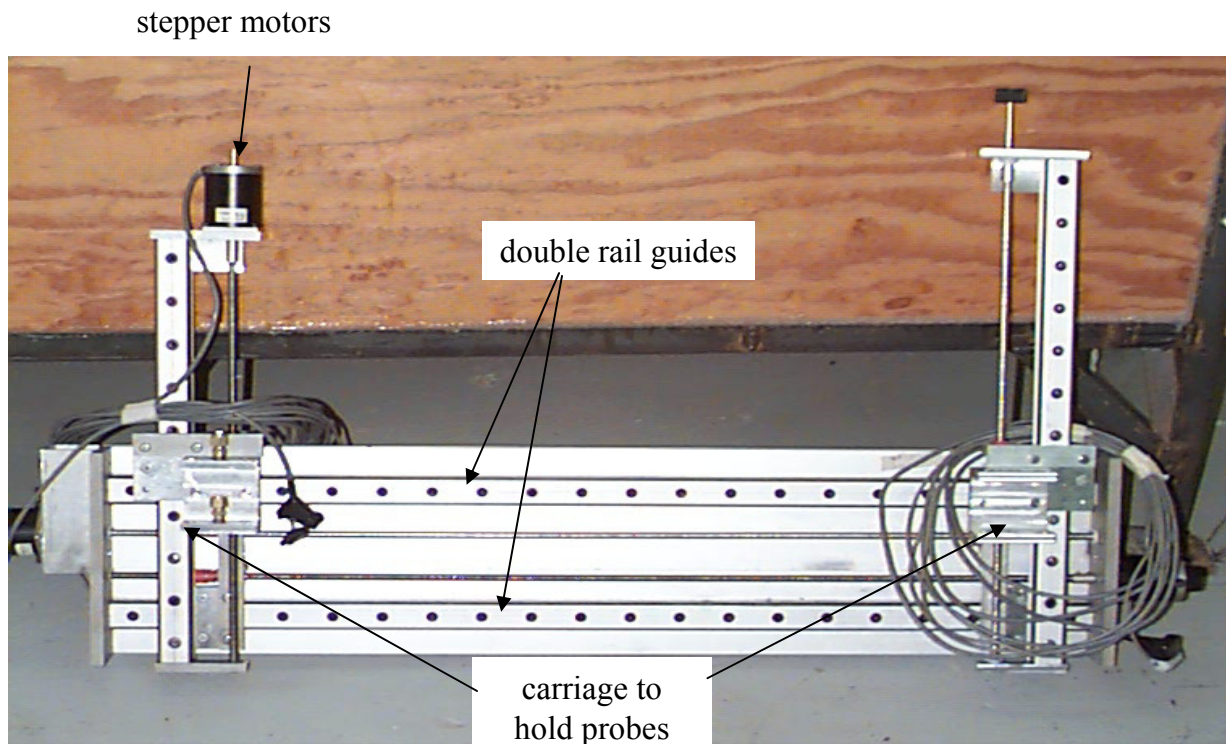


Figure 2.19: Traverse System

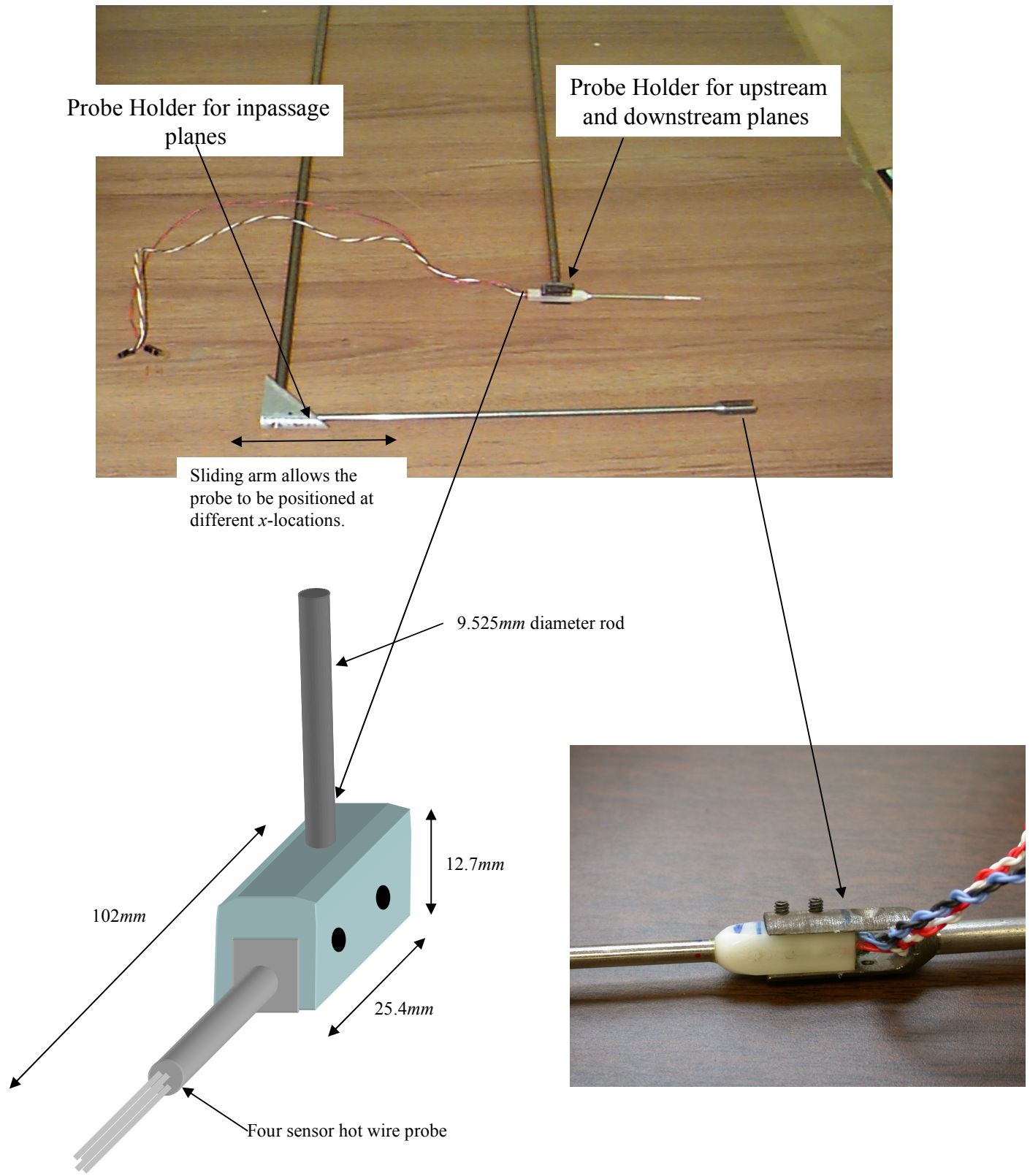


Figure 2.20: Mounting arrangement for the Four Sensor Hot-Wire Probes

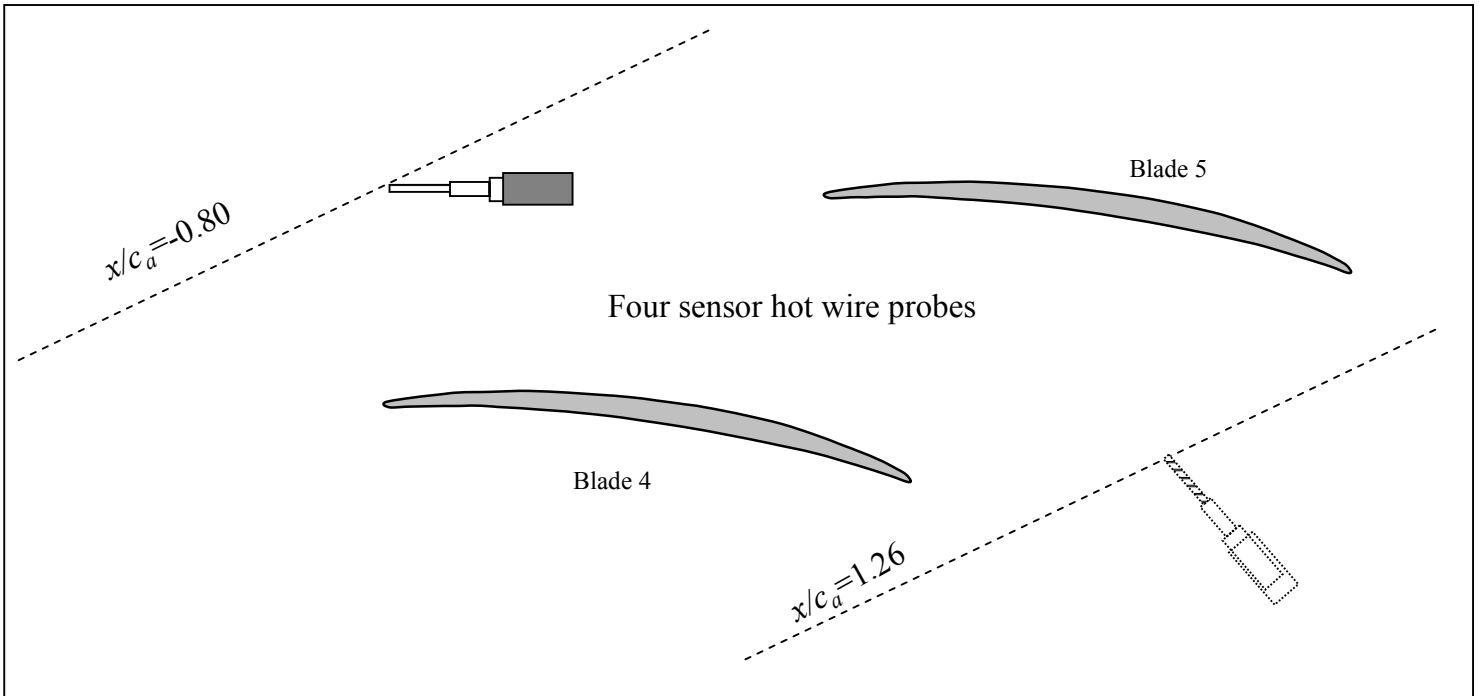


Figure 2.21a: Mounting arrangement for the Four Sensor Hot-Wire Probes for the upstream and downstream measurement location. Note - upstream and downstream measurements done separately, but shown together on this figure.

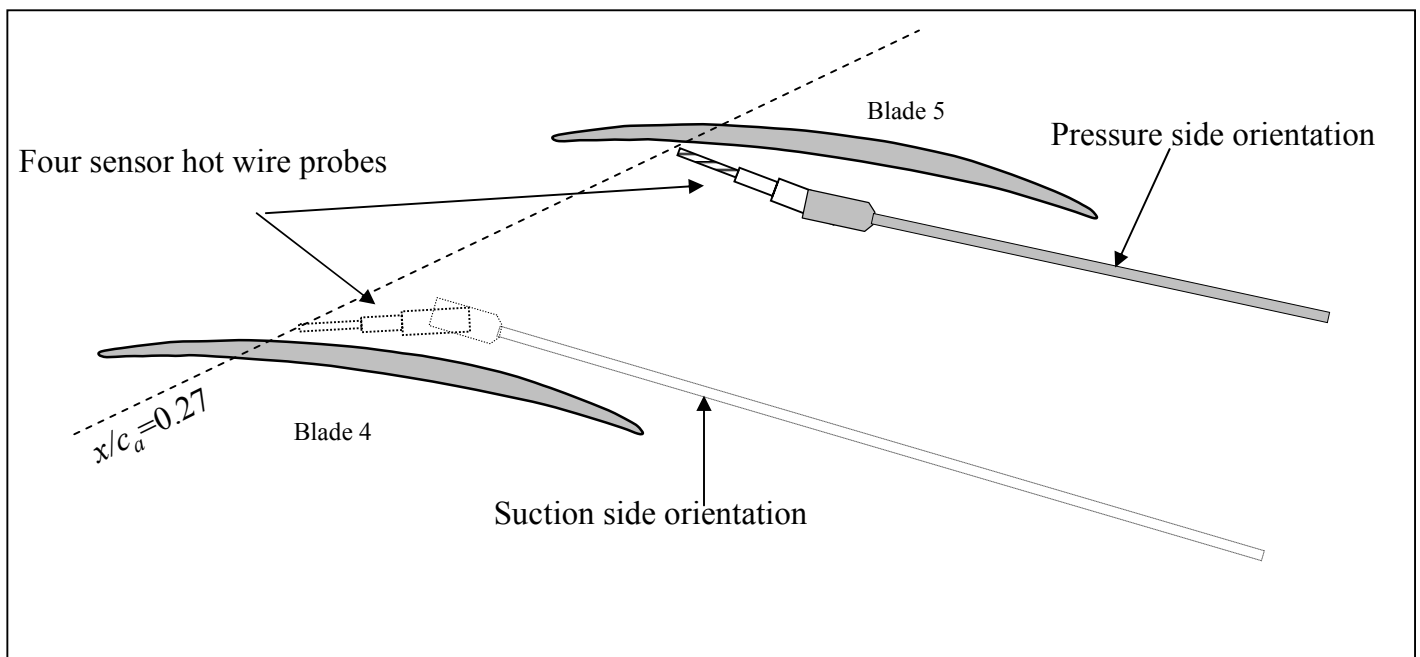
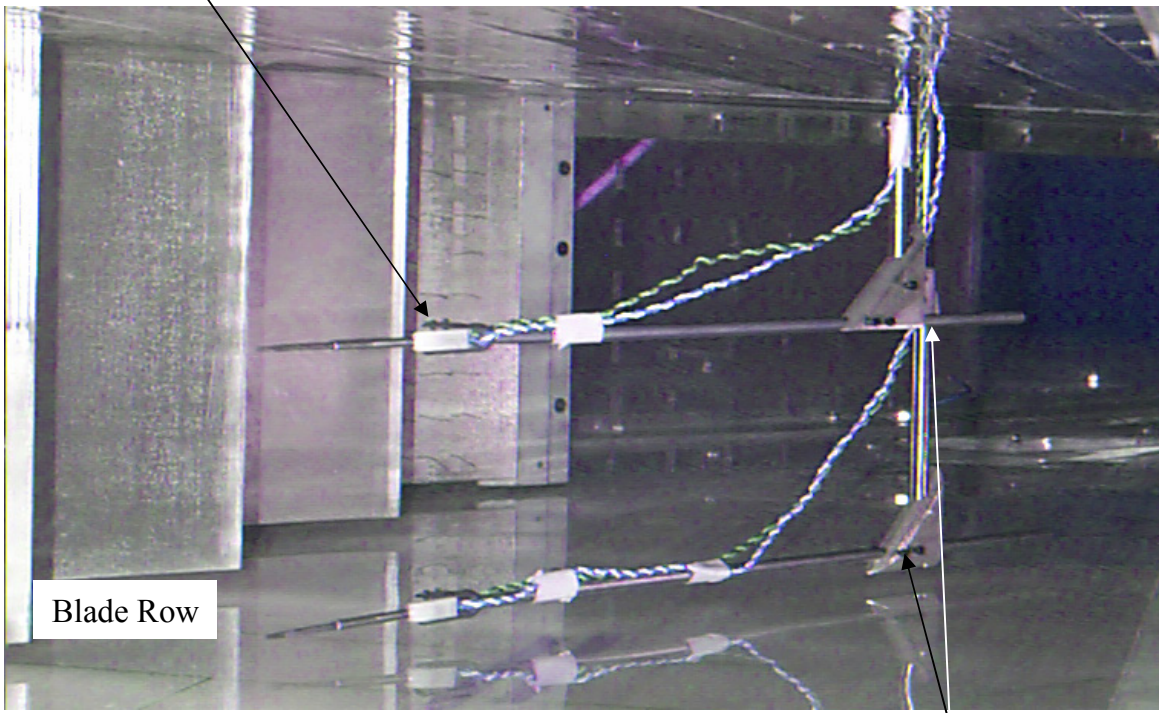


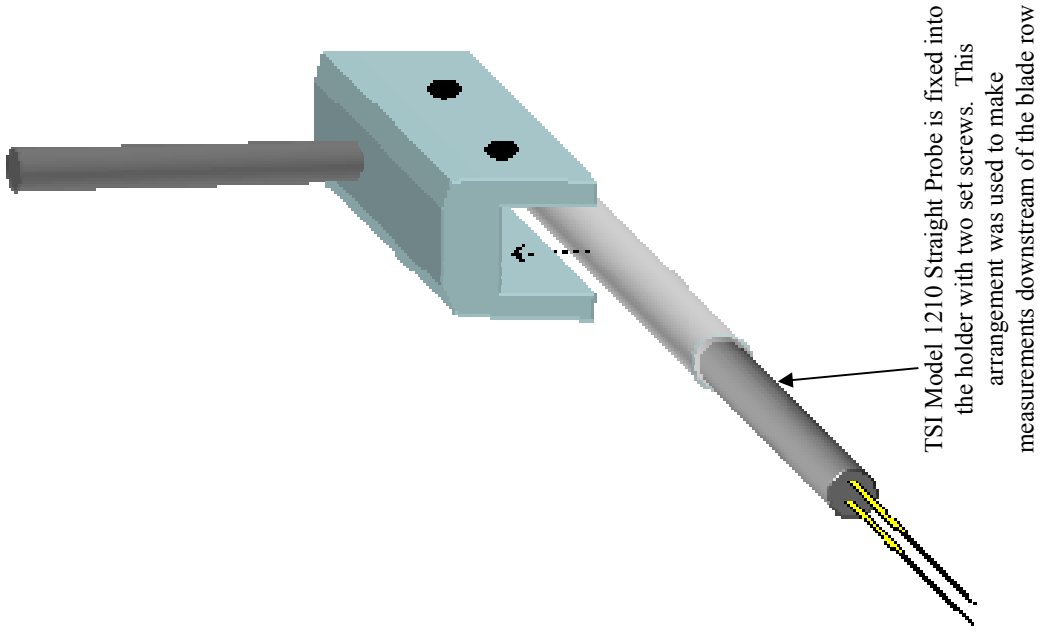
Figure 2.21b: Mounting arrangement for the Four Sensor Hot-Wire Probes for the inpassage measurement location. Note – suction and pressure-side measurements done separately, but shown together on this figure.

Four Sensor Hot Wire Probe

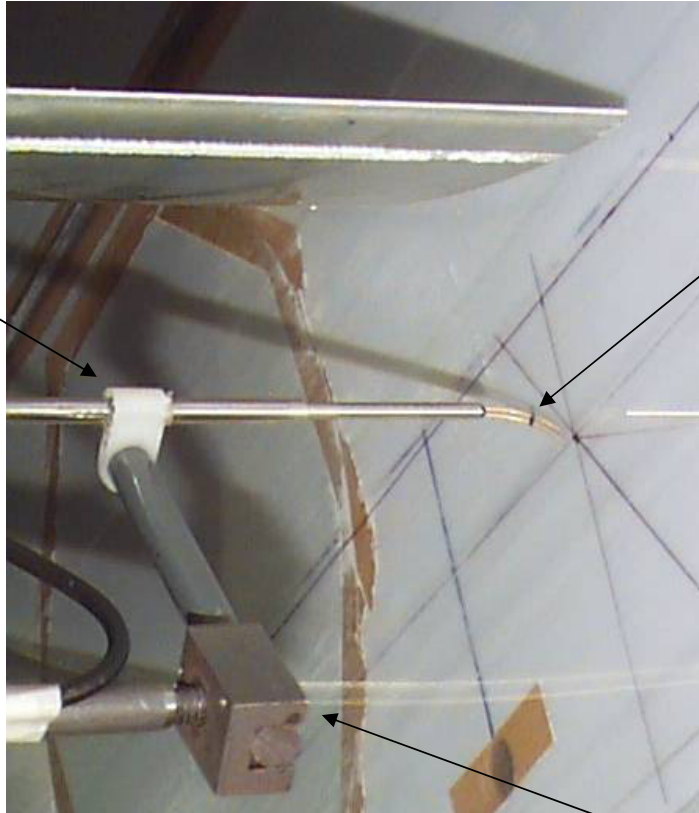


Triangular mount can vary the position of the probe by changing the length of the arm of the holder

Figure 2.22: Mounting arrangement for the Four Sensor Hot-Wire Probes for the inpassage measurement location.



Probe can be yawed so as to align it with flow direction



Holder can change the position of the probe by sliding the arm

TSI Model 1218 Boundary Layer Probe mounted upstream of the blade row

Figure 2.23: Mounting arrangement for the single-sensor hot-wire probes

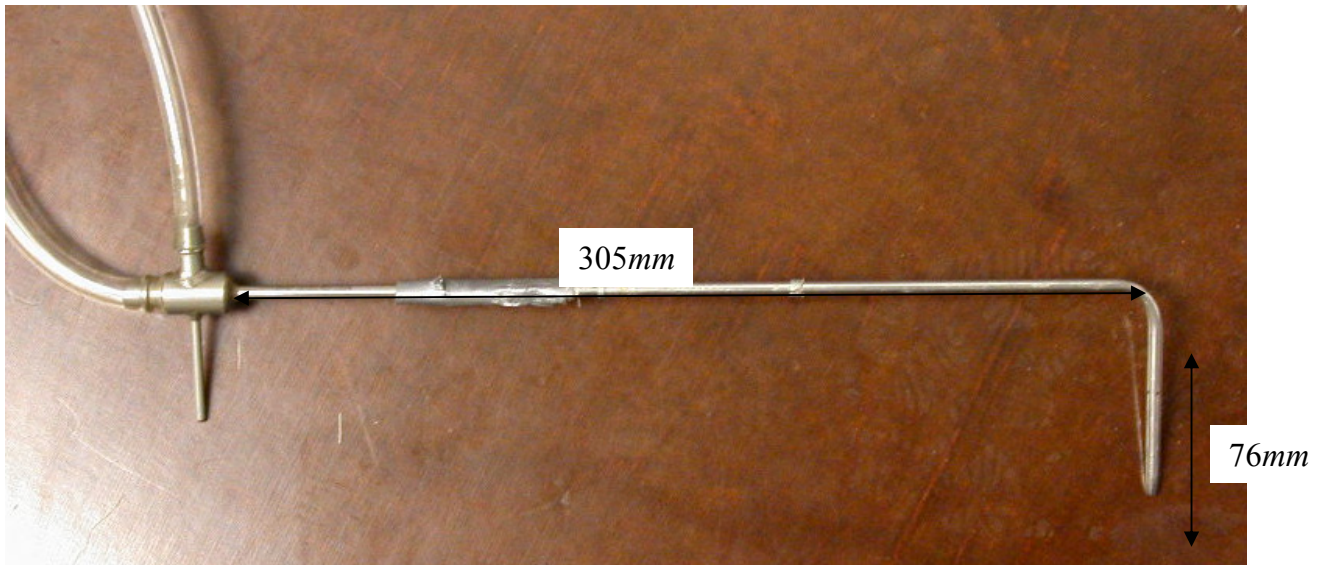
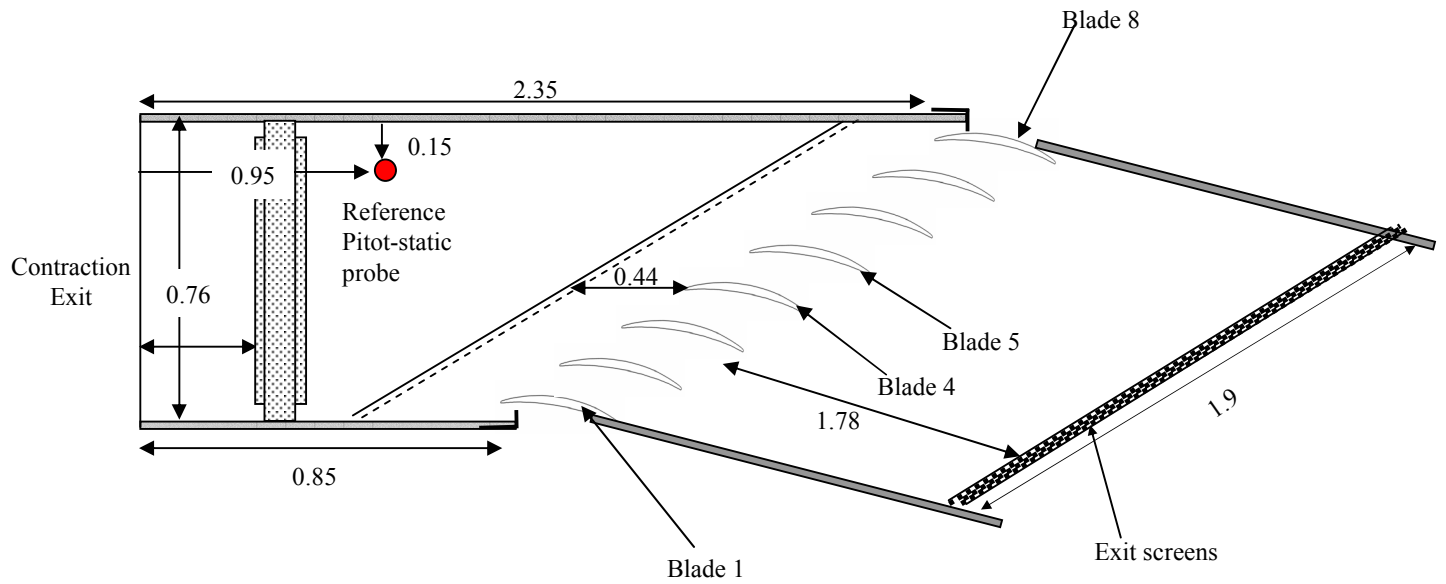


Figure 2.24: Figure of the Pitot-Static Probe.
Figure on top shows the location of the reference probe
in the cascade tunnel

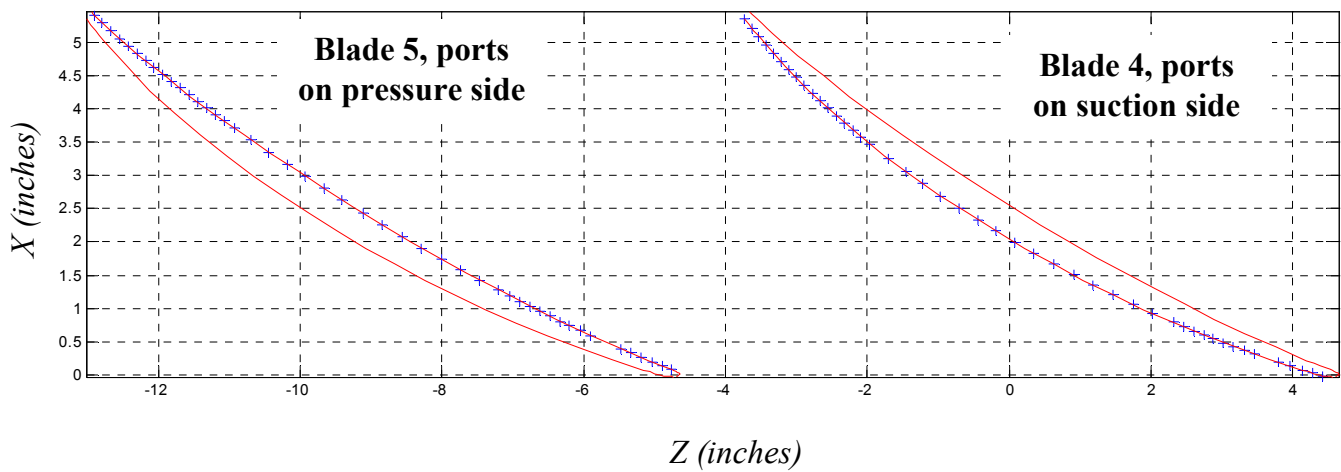
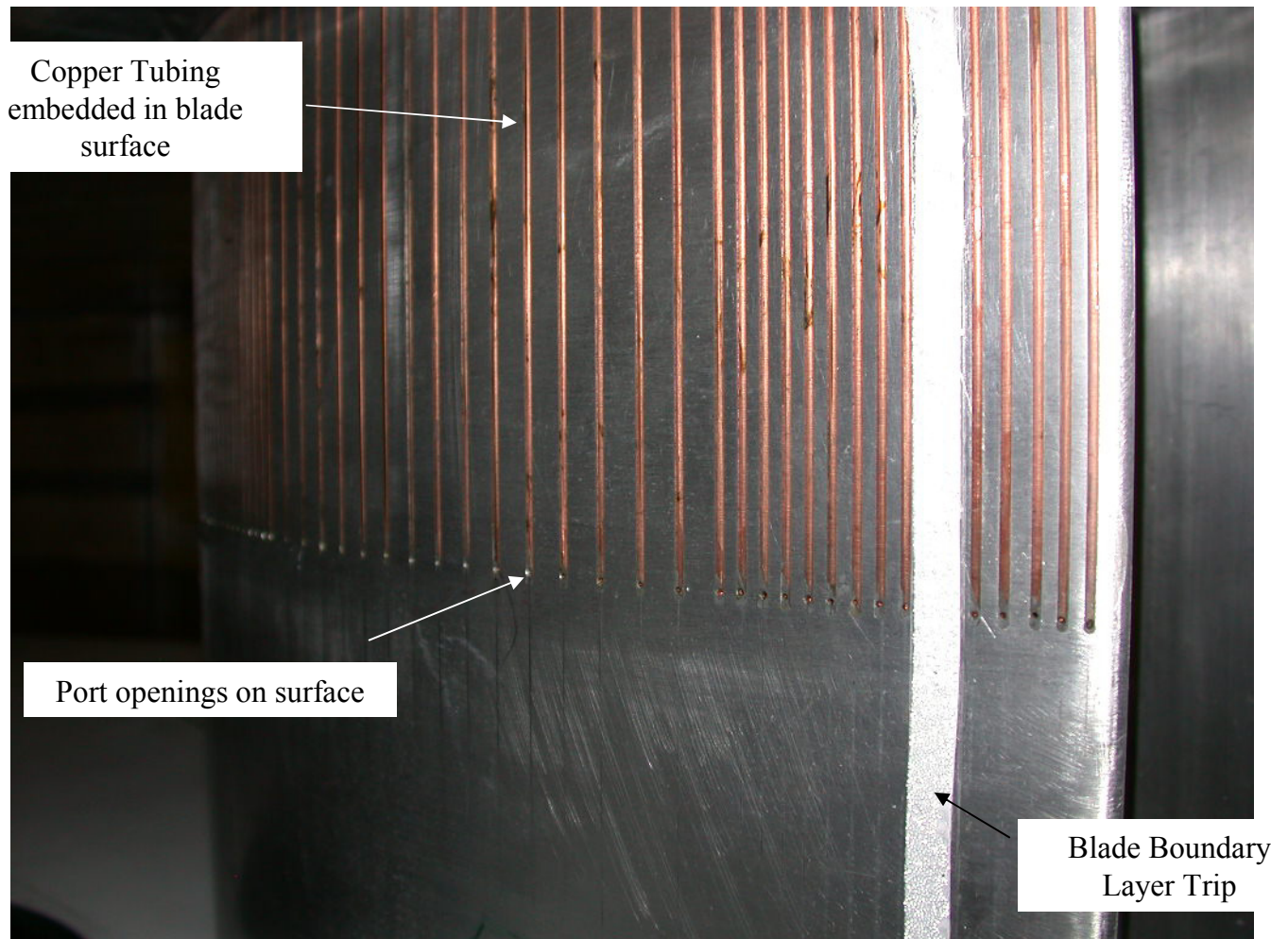


Figure 2.25: Surface pressure ports on the blades. Shown in the photograph are the ports on the suction side of Blade 4. The plot shows the location of the ports on the blades when in the tunnel.

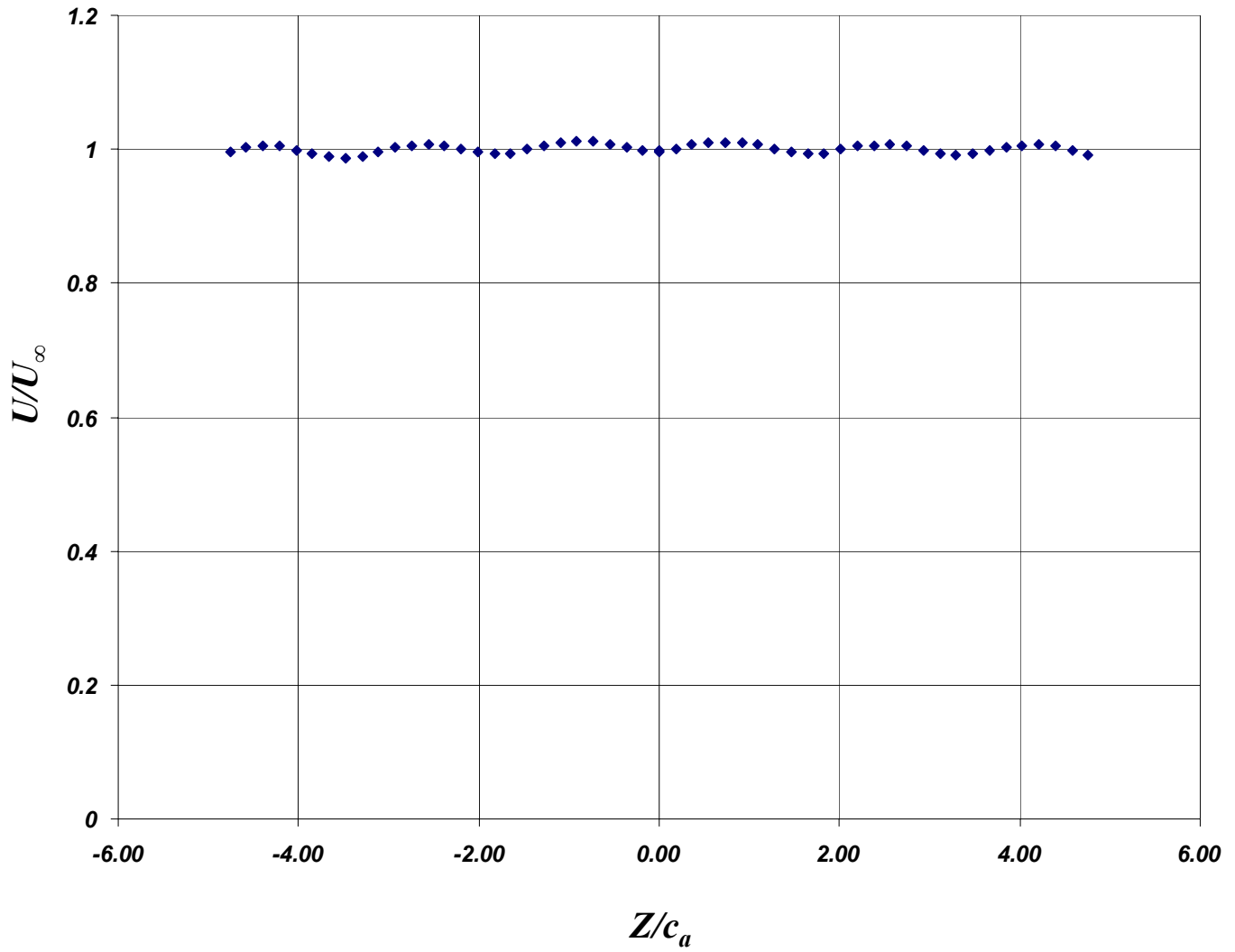


Figure 2.26: Velocity distribution at $X/c_a = -0.92$ after calibration of tunnel.

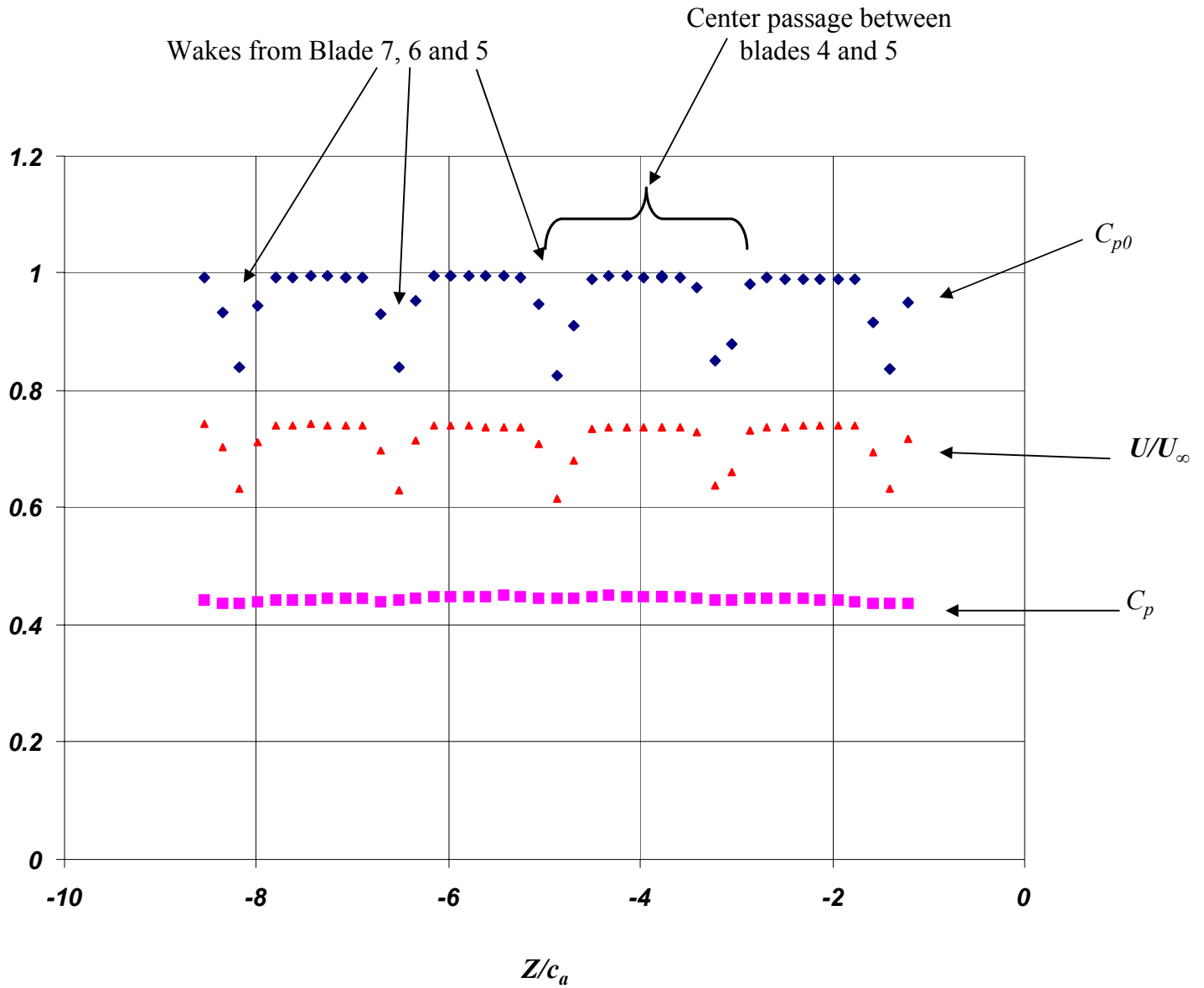


Figure 2.27: Pitot-static measurements taken at $X/c_a=2.6$ downstream of blade row after calibration of tunnel

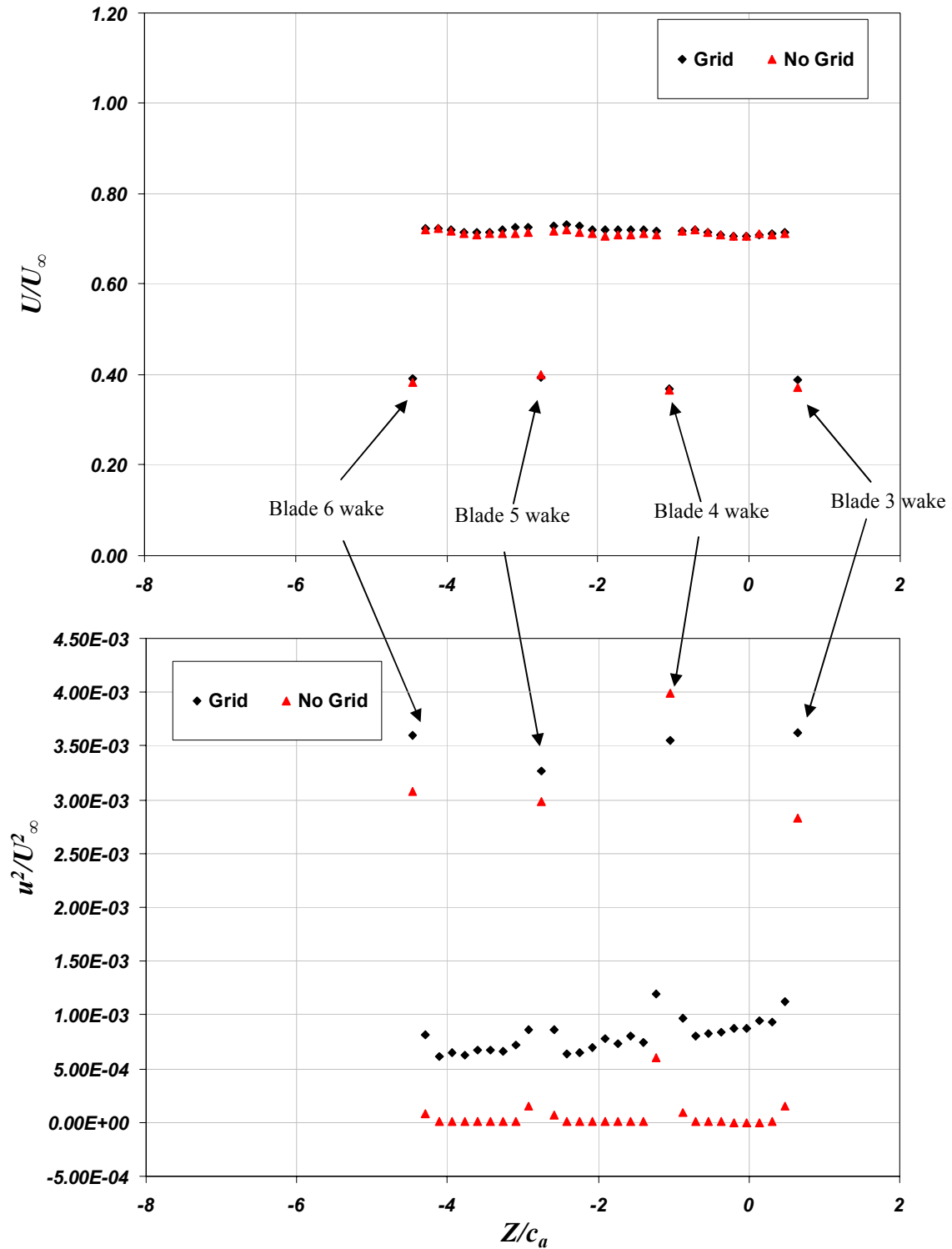


Figure 2.28: Influence of Inflow Turbulence on the periodicity downstream of the blade passage at $X/c_a=1.26$. Measurements were taken with a single-sensor hot-wire probe. The legend gives the inflow turbulence case.

3. Results and Discussion

The Virginia Tech Low Speed Cascade Wind Tunnel has been used to experimentally document and investigate the effects of elevated free stream turbulence on the flow field through the compressor cascade. A bi-planar square mesh grid of circular rods was used to generate elevated free stream turbulence levels in the flow. Oil-flow visualizations, blade loading measurements, and hot-wire anemometry techniques were utilized to study the effects of grid generated turbulence of the cascade. Oil-flow visualizations were generated on the lower endwall beneath the blade row, and blade loading measurements were made using pressure ports embedded in the blade surface. Hot-wire anemometry techniques were used to measure the velocity field at 8 pitchwise planes upstream, downstream and within the blade row of the cascade. The results of these measurements are discussed in the subsequent sections of this chapter.

3.1. Data sampling and presentation

3.1.1. Co-ordinate system

The measurement locations and distances are presented in the axial-pitchwise co-ordinate system shown in Figure 3.1. The axial direction, X , is perpendicular to the line defining the leading edges of the blades, and is defined as positive downstream of the leading edge. The distance, Y , is perpendicular to the lower endwall and defined as positive upward. Completing the right handed co-ordinate system is the pitchwise direction, Z (aligned with the leading edge line). The origin of the axial-pitchwise system, is at the lower endwall midway between the leading edges of the center passage defined by blades 4 and 5 (see Figure 2.2). The axial-pitchwise mean velocity components (U_I , V_I , W_I) are defined in these 3 directions.

The data presented in this chapter is in normalized form. Most distances are normalized on the axial chord of the blades ($c_a = 0.139m$), such that $X/c_a = 0$ corresponds to the leading edge line, and $X/c_a = 1.0$ corresponds to the trailing edge line of the cascade. Consequently, as shown in Figure 3.1, the measurement planes corresponded to locations at $X/c_a = -0.80$, -0.23 , 0 , 0.27 , 0.48 , 0.77 , 0.98 , 1.26 . Also shown Figure 3.1 are three streamlines from the

RANS solution of Shin (2001) corresponding to one streamline through the center of the passage, and two streamlines on the suction side and pressure side of the passage. The streamlines on the suction side and pressure side were chosen to be as close to the blade surface but away from the blade boundary layers.

We also define a center-streamline aligned co-ordinate system rotated about the Y axis, by an angle θ_y , such that the streamwise direction, x , is aligned with the potential core. The relationship between the axial-pitchwise velocity components, and the center-streamline aligned components used here is $(U, V, W) = (U_I \cos \theta_y - W_I \sin \theta_y, V_I, W_I \cos \theta_y + W_I \sin \theta_y)$ where the values of the angle θ_y are listed in Table 3.1.

Table 3.1 : Rotation angles θ_y to get U, V, W from U_b, V_b, W_b

Measurement Plane (X/c_a)	θ_y
-0.8	64.74°
-0.23	66.13°
0	62.18°
0.27	58.07°
0.48	55.85°
0.77	54.18°
0.98	53.40°
1.26	52.51°

Mean velocity and turbulence stress components have been normalized on the inlet free stream velocity (U_∞) which was continuously monitored using by the reference Pitot-static probe described in section 2.5.1.

3.1.2. Measurement Conditions

All measurements were made both with and without the turbulence generating grid. Each axial plane was measured successively with and without the grid, before relocating the probes to subsequent axial planes. This reduced the uncertainty in the location of the probes when making measurements, as well as keeping ambient conditions of the tunnel similar between the two flows. The streamwise turbulence intensities of the inflow without grid generated turbulence were 0.2%, with a streamwise lengthscale of $0.06c_a$ (0.8cm). With the

grid, the intensities were 3.2% with a streamwise lengthscale of $0.16c_a$ (2.2cm). The characteristics of the two inflows will be described in detail in section 3.4. Measurements were taken at a free stream velocity, U_∞ , of 25.5 ± 0.4 m/s, corresponding to a chord Reynolds number of $388,000 \pm 7000$. Details of the uncertainties in the reference Pitot-static measurements can be found in the appendix.

3.1.3. Sampling Schemes

Single-sensor hot-wire measurements were sampled at a frequency of 51.2 kHz. 50 records each of 1024 samples of data were taken at each measurement location at a rate of about 1 record per second. With the four-sensor hot-wire probes, a sampling frequency of 51.2 kHz was used. 50 records of 2048 samples of data were taken at each point at a rate of about 1 record per second. High-pass anti-aliasing filters with a cut-off frequency of 20kHz were used when sampling data for both hot-wire probes. Shown in Figure 3.2, are the measurement grids used at each axial location. An average of 200 data points at each axial station were taken for the four-sensor hot wire probe data. The data files were stored on CD-ROM discs, and reprocessed after the tunnel entry was completed.

3.2. Blade Loading

Using pressure ports embedded in the surface of the blade, the mid-span blade loading was measured for the two inflow cases. Shown in Figure 3.3a is the blade loading for both the grid generated turbulence inflow, and no grid generated inflow cases. Plotted on the vertical axis of the figure is the pressure coefficient, C_p , which is defined as;

$$C_p \equiv \frac{P - P_\infty}{p_{0\infty} - P_\infty}$$

where p is the pressure on the blade, p_∞ is the reference static pressure, and $p_{0\infty}$ is the reference total pressure. Uncertainties in C_p were computed to be 0.5% for the no-grid generated turbulence inflow case, and 0.9% for the grid generated turbulence inflow case, the increase in uncertainty due to the fluctuating nature of the flow downstream of the grid.

Plotted on the horizontal axis of the figure are the pressure port locations in the normalized axial direction, X/c_a .

Shown in Figure 3.3b is the results of a two-dimensional calculation of the pressure coefficient on the blade from the study by Shin (2001). Compared to the experimentally obtained distribution in Figure 3.2a, the two curves are very similar in shape. However, on the pressure side of the blade, the experimentally obtained pressure distribution is lower when compared to the computation. We attribute the difference to the three dimensional flow features that are present on the lower endwall.

Using Bernoulli's equation, the normalized velocity just outside the blade surface boundary layer can be estimated as $\frac{U}{U_\infty} = \sqrt{1 - C_p}$. With this value of velocity, the circulation around the blade can be computed by numerically integrating around the blade surface. Placing a restriction of constant axial velocity and neglecting the loss of total pressure through the cascade, the lift co-efficient can be estimated by applying the Kutta-Joukowski theorem derived for a compressor configuration (Cumpsty, 1989). For the case with no grid generated turbulence, the circulation around the blade was computed to be $0.49 \pm 0.01 c_a U_\infty$, and for the case with grid generated turbulence, the circulation was computed to be $0.47 \pm 0.01 c_a U_\infty$. The lift coefficient implied by this circulation is $C_l = 0.83 \pm 0.02$ without grid generated turbulence, and $C_l = 0.80 \pm 0.02$ with grid generated turbulence. These results indicate that with the introduction of grid generated turbulence, there is a small decrease in the lift on the blade.

Looking at the C_p distribution in Figure 3.3a, this loss of lift is due to a slight decrease in the pressure over most of the pressure side of the blade. Comparing the distribution for the two cases on the suction side, the pressure distribution is similar from the leading edge to approximately $X/c_a=0.7$, after which the pressure is seen to be lower with grid generated turbulence. This implies that the exit pressure is lower with grid generated turbulence, and as a consequence, the flow has a higher exit velocity, which is indicative of a smaller turning angle. The smaller turning angle implies a decrease in the blade loading, and is corroborated by the decrease in the computed lift on the blade.

Changes to the blade loading can play a significant part in the flow through a cascade as it is the mechanism responsible for generating the dominant flow features seen in the lower endwall region, namely the tip-leakage vortex. If there is a change in the loading on the blade, then the behavior and nature of the tip leakage vortex should be affected as well.

3.3. Surface Oil Flow Visualizations

Shown in Figures 3.4, and 3.5 are the surface oil flow visualizations generated on the lower endwall region beneath blades 4 and 5 for both inflow turbulence conditions. The oil flows were generated on self adhesive plastic sheets. Sections of the flows were then digitized using a PC-based scanner, and the subsequent scans merged to create the pictures presented in Figure 3.4 and 3.5. Presented in Figure 3.4 is the case without grid generated turbulence, and in Figure 3.5, the case with grid generated turbulence. The blade profiles and the axial-pitchwise axes have been overlaid onto each of the figures.

The dominant features that can be seen in both flows are the region of high wall shear stress on the lower endwall under the blade tips, and the separation line associated with the tip leakage vortex. The qualitative nature of these two regions is very similar for the two inflows. The periodicity of the cascade is visible, with the spacing between similar regions in the flow being closely equal to the blade spacing. The flow through the tip gap is also similar for the two flows. The flow is at an angle of approximately 80° to the chord line of the blade, through the tip gap region for both inflow cases.

From the oil flow visualization figures, the tip gap flow is seen to leave the tip region at approximately $X/c_a=0.2$ for both inflow cases, but as the flow develops through the passage, the behavior is different. Plotted in Figure 3.6 is the approximate path of the separation line between the tip leakage vortex and the lower end wall flow as indicated from the oil-flow visualizations. The locations of these points are presented in Table 3.2.

Table 3.2 : Location of separation line between tip vortex and lower endwall flow (Figure 3.6)

X/c_a	Z/c_a (No Grid)	Z/c_a (Grid)
0.23	-0.08	-0.09
0.48	0.66	0.65
0.77	1.24	1.28
0.98	1.64	1.70
1.26	2.03	2.11

The separation line may be considered as being indicative of the path of the vortex as it develops through the passage of the blade row. The effect of grid generated turbulence is to reduce the deviation of the vortex path from the axial direction, which implies a reduction in

the turning angle of the flow. This was also seen with the change in the loading of the blade with the introduction of grid generated turbulence.

3.4. Inflow to the cascade

As mentioned in section 3.1, the velocity field measured by the hot wire probes can be defined in terms of a mean velocity field and turbulent velocity field. Applying Reynolds averaging to the velocity field, the instantaneous velocity can be defined as a combination of the mean and the fluctuating component of the velocity field e.g. in the x -direction, $U_i=U+u$, where U_i is the instantaneous velocity, U is the mean velocity which is used to describe the mean flow field, and u is the fluctuating component of velocity. Applying this technique, we can obtain the Reynolds Averaged Navier Stokes equations and the new unknowns that arise from this technique, the Reynolds stresses can be described as a symmetric stress tensor as follows

$$-\rho \begin{bmatrix} \overline{u^2} & \overline{uv} & \overline{uw} \\ \overline{vu} & \overline{v^2} & \overline{vw} \\ \overline{wu} & \overline{wv} & \overline{w^2} \end{bmatrix}$$

The diagonal terms in the matrix are known as the Reynolds normal stresses, and the off diagonal terms are known as the Reynolds shear stresses. Since the flow being investigated here is incompressible ($\rho=\text{constant}$), ensuing discussions of the Reynolds stress in this section will have density implied. The overbar term on the above quantities will also be implied in subsequent discussions of the Reynolds stresses. Uncertainties of measured quantities calculated at 20:1 odds are given in Table 3.3 below:

Table 3.3: Uncertainties of measured quantities in the four sensor hot-wire for the two flows (with and without grid generated turbulence)

Quantity	Uncertainty (20:1 odds)	
	No Grid Case	Grid Case
U, V, W	$\pm 1\% U_\infty$	$\pm 1\% U_\infty$
u^2	$\pm 4\% u^2$	$\pm 4\% u^2$
v^2, w^2	$\pm 8\% v^2, \pm 8\% w^2$	$\pm 8\% v^2, \pm 8\% w^2$
uv, vw, uw	$\pm 4\% \sqrt{(u^2 v^2)}$	$\pm 3\% \sqrt{(u^2 v^2)}$

3.4.1. Axial location $X/c_a = -0.80$

Shown in Figures 3.7 through 3.18 plots of the flowfield at $X/c_a = -0.80$, upstream of the blades for both inflow turbulence cases. Presented in Figure 3.7 are the contours of the normalized streamwise velocity, U/U_∞ . The contours show a uniform inflow with an average value of $0.993U_\infty$ with the no grid inflow condition. In the plot for the grid generated turbulence case, the fluctuations observed in the plot are mostly due to the fluctuations in the measurement of the reference velocity downstream of the grid. With grid turbulence, the velocity field shows no signs of the wakes of the rods, indicating that the grid turbulence is well mixed out.

The cross-flow velocity vectors for both inflow conditions are presented in Figure 3.8. Reference vectors equivalent to $0.5U_\infty$ in the y and z direction are shown in the upper left corner of each plot. The plots reveal that there is no significant turning of the flow verifying in part the proper operation of the boundary layer scoops. The turbulence intensities, $\sqrt{u^2/U_\infty}$, $\sqrt{v^2/U_\infty}$, $\sqrt{w^2/U_\infty}$ are presented in Figure 3.9 through 3.11 respectively for both inflow conditions. The turbulence intensities in the streamwise direction, $\sqrt{u^2/U_\infty}$ plotted in Figure 3.9, are approximately 3% with the grid generated turbulence, and 0.2% without. Also visible in the plots is a slight gradient in the levels with increasing z distance. This is due to the fact that with decreasing z , the development length of the turbulence increases due to the inlet angle of the cascade.

Plotted in Figure 3.10 are the turbulence intensities in the spanwise (y) direction, $\sqrt{v^2/U_\infty}$. Again, similar z -direction gradient is also seen in the plot. However, an interesting aspect of this plot is the gradient in the y -direction, for the case with grid generated turbulence. There is a suppression in the levels of v/U_∞ as you approach the lower endwall, due to the non-penetration condition imposed by the surface. Studies on the influence of elevated free stream turbulence on flat plate boundary layers by Hunt *et al.* (1978), have documented this behavior. The turbulence intensities in the pitchwise direction, $\sqrt{w^2/U_\infty}$, are plotted in Figure 3.11. Intensities are approximately 3% with grid generated turbulence and about 0.2% without, and the levels are decreasing with decreasing z , similar to the trend seen in Figure 3.9.

Shown in fig 3.12 are the contours of the normalized turbulence kinetic energy (k) which is computed as:

$$k = \frac{1}{2} \left(\frac{u^2 + v^2 + w^2}{U_\infty^2} \right)$$

As seen in the figures, the turbulence kinetic energy associated with the grid is significantly higher than the case without grid generated turbulence, by a factor of more than 10. For the case with the grid generated turbulence, there is a reduction in k with decreasing z -distance, which is again due to the fact that the development length downstream of the grid is greater at smaller z values. The z -variation in the turbulence levels away from the wall can be used to estimate the streamwise rate of decay of the turbulence kinetic energy and thus the dissipation. The decay in the streamwise direction, x , was computed to be $0.00033U_\infty^2/m$, and is equivalent to a 18% loss over 1 chord length ($1.83c_a$) of the blade.

The flowfield can further be described by looking at the integral length scales of the turbulence, or the distance over which the influence of turbulence extends. The longitudinal integral lengthscales may be determined using Taylor's hypothesis as (Hinze, 1975)

$$\Lambda_u = \frac{1}{2} \frac{U \int_{-\infty}^{\infty} R_{uu}(\tau) d\tau}{u^2}. \text{ Similarly, the lateral integral lengthscales can be determined as}$$

$$\Lambda_v = \frac{1}{2} \frac{U \int_{-\infty}^{\infty} R_{vv}(\tau) d\tau}{v^2}, \text{ and } \Lambda_w = \frac{1}{2} \frac{U \int_{-\infty}^{\infty} R_{ww}(\tau) d\tau}{w^2}. \text{ The autocorrelation (or time-delay}$$

correlation) functions, R , are defined as (e.g. in the longitudinal direction) $R_{uu}(\tau) = E[u(t)u(t+\tau)]$. The one-sided auto spectrum in the limit of zero frequency can be related to the autocorrelation functions as, $G_{uu}(f)|_{f \rightarrow 0} = 2 \int_{-\infty}^{\infty} R_{xx}(\tau) d\tau$. With the above definitions and relations, the lengthscales can thus be estimated from the measured spectra as

$$\Lambda_u = \frac{U}{4u^2} G_{uu}(50), \text{ where } G_{uu}(50) \text{ is the spectral value at the lowest frequency bin in the data, which based on the sampling scheme used is 50Hz.}$$

Velocity spectra taken at the mid height of the passage at $z/c_a=1.7$ for the case with and without grid generated turbulence are presented in Figures 3.13a and 3.13b. The spectra were influenced by electrical noise beyond $20kHz$, and when processing the results, the

contribution beyond this value was removed. Also plotted, from an analysis by Devenport (2001), is the von Kàrmàn interpolation formula for isotropic turbulence from Hinze (1975) given as

$$G_{uu}(f) = \frac{2\Gamma(5/6)}{\sqrt{\pi}\Gamma(1/3)} \frac{u^2}{k_e} \left[1 + \left(\frac{k}{k_e} \right)^2 \right]^{-5/6} \frac{2\pi}{U_\infty}$$

$$G_{vv}(f) = G_{ww}(f) = \frac{\Lambda_u u^2}{6\pi} \frac{\left(3 + 8 \left(\frac{k}{k_e} \right)^2 \right)}{\left(1 + \left(\frac{k}{k_e} \right)^2 \right)^{1/6}} \frac{2\pi}{U_\infty}$$

where k is the wavenumber defined as $2\pi f/U_\infty$, k_e is defined as $0.75/\Lambda_f$, and $\Gamma()$ is the gamma function.

Comparison of the two curves in Figure 3.13a shows that the spectra for the case with grid generated turbulence can be well represented by the von Kàrmàn curve, implying that it is reasonably isotropic. For the case without grid generated turbulence (Figure 3.13b) the results show that the turbulence is non-isotropic, with the measured spectra not conforming to either the von Kàrmàn or Gaussian representations for isotropic turbulence. Presented in Figure 3.14, are the space time correlations of the flow with grid generated turbulence. The results of the two point measurement taken at the mid height of the passage at $Z/c_a=1.7$ are compared with the von Kàrmàn formula, and similar to the velocity spectra, the comparisons show good agreement, once again implying the grid generated turbulence is isotropic.

Given in Table 3.4 below, are the characteristics of the grid generated turbulence that were used to compute the von Kàrmàn interpolation formula presented in Figures 3.13 and 3.14. The characteristics were obtained by averaging the values over the boundary layer region of the flow.

Table 3.4 : Characteristics of grid turbulence used to compute the von Kàrmàn interpolation

X/c_a	Z/c_a	$U_\infty(m/s)$	U/U_∞	u^2/U_∞^2	$\Lambda_f(m)$	$k_e(m^{-1})$
-0.8	1.7	24.1	1.0	0.00101	0.0218	34.3

Plotted in Figures 3.15 – 3.17 are the integral lengthscales in the three directions, A_u , A_v , and A_w respectively. The longitudinal lengthscales (Figure 3.15) are approximately $0.16c_a$ (2.2cm) with grid generated turbulence, and about $0.03c_a$ (0.4 cm) without grid generated turbulence. The lateral lengthscales are plotted in Figures 3.16 and 3.17. The average lateral lengthscale A_v was $0.082 c_a$ (1.1 cm) for the case with grid generated turbulence and $0.10 c_a$ (1.4 cm) without. Average values for A_w was $0.076 c_a$ (1.0cm) for the case with grid generated turbulence and $0.10 c_a$ (1.4cm) without. Comparisons of the longitudinal and lateral lengthscales for the two cases highlight the isotropy of the grid generated turbulence where the lateral lengthscales are approximately half of the longitudinal lengthscales. The same cannot be said of the inflow without grid generated turbulence where the lateral lengthscales are larger than the longitudinal lengthscales, indicative of anisotropic turbulence. The surface blocking that was observed in the $\sqrt{v^2/U_\infty}$ contours with grid generated turbulence (Figure 3.10), is also seen in Figure 3.16 by the reduction in A_v closer to the lower endwall.

3.4.2. Axial location $X/c_a=-0.23$

Presented in Figure 3.18-3.26 are plots of the flowfield at $X/c_a=-0.23$, closer to the blade row. Presented in Figures 3.27-3.29 are boundary layer measurements taken at this measurement plane. Contours of the normalized mean streamwise velocity, U/U_∞ are plotted in Figure 3.18 and the cross flow velocity vectors are plotted in Figure 3.19. The cross-flow vectors show the actual measurement locations of the data set presented in these figures, which is a combination of two measurement data sets, as outlined in section 2.4. The data set on the pressure side of the passage extended to $Z/c_a=0.79$, and the data set on the suction side extended to $Z/c_a=0.66$. To create the merged data set, measurement points at $Z/c_a = 0.79$ and 0.61 from the pressure side data were deleted, and all of the suction side data ($Z/c_a>0.66$) were kept. The merged data set covers a pitchwise distance of $1.33c_a$, or 78% of the passage width ($1.7c_a$ which is equivalent to the blade spacing). Also shown on the plots, is the upstream projection of the origin of the axial-pitchwise co-ordinate system (see section 3.1.1), corresponding to the middle of the passage, indicated by the broken line positioned at $Z/c_a=0.495$ when $X/c_a=-0.23$. The upstream projections of the leading edge of blades 5 and 4

which bound the measurement passage correspond to $Z/c_a = -0.355$ and 1.345 , at $X/c_a = -0.23$, and are beyond the limits of the measurement grid presented here.

The upstream influence of the blades on the flow field is revealed in Figure 3.18. Locations at $Z/c_a < 0.495$ correspond to the upstream shadow of the pressure side of the blade, and the velocity is larger than for values $Z/c_a > 0.495$, which are upstream of the suction side of the blade. Comparisons with calculations performed by Shin (2001), show a similar variation where the velocity upstream of the pressure side is higher than that upstream of the suction side of the passage. The change in the streamwise velocity would suggest that there is a pressure gradient and thus some turning of the flow upstream of the blade row. The crossflow vectors plotted in Figure 3.19 near the lower endwall region show a slight deviation of the flow towards the pressure side of the passage, in anticipation of the blade row. One of the interesting influences of grid generated turbulence is that at $Z/c_a = 0.65$, the lower endwall boundary layer is larger compared to other Z locations, and this effect is amplified with grid generated turbulence.

Presented in Figures 3.20-3.22 are the turbulence intensities, $\sqrt{u^2/U_\infty}$, $\sqrt{v^2/U_\infty}$, $\sqrt{w^2/U_\infty}$. The streamwise fluctuations, $\sqrt{u^2/U_\infty}$, in Figure 3.20 show that the intensities are approximately 2.75% away from the lower endwall region with grid generated turbulence and 0.2% without grid generated turbulence. The lower endwall boundary layer extends to a height of approximately $0.1c_a$, and similar to what was seen in Figure 3.18, the boundary layer is larger at $Z/c_a = 0.65$ with the introduction of grid generated turbulence. At this point, the flow has been decelerating, implying an adverse pressure gradient, which would result in the boundary layer being larger. Overall, apart from $Z/c_a = 0.65$, the boundary layer thickness is similar for the two cases, and will also be shown in a subsequent discussion.

Plotted in Figure 3.21 are the spanwise fluctuations, $\sqrt{v^2/U_\infty}$, for both inflow cases. Similar to what was seen in Section 3.4.1, the surface blocking effect seen near the lower endwall is also visible here, where the intensities are reduced closer to the lower endwall. The pitchwise fluctuations, $\sqrt{w^2/U_\infty}$, plotted in Figure 3.22, show smaller levels with decreasing Z , similar to what occurred at $X/c_a = -0.80$. The turbulence kinetic energy distribution, presented in Figure 3.23, indicates that compared to the axial location at $X/c_a = -0.80$, the turbulence kinetic energy of the grid generated turbulence has been reduced by 14%

between the two measurement planes. The decay in the turbulence kinetic energy occurs over a streamwise distance of $1.4c_a$ which is equivalent to a decay of 18% over the length of one chord of the blade, which was consistent with the decay rate observed at $X/c_a = -0.80$.

The longitudinal and lateral integral lengthscales are presented in Figures 3.24-3.26. Noticeable in the figures, particularly in the case without grid generated turbulence for the lateral lengthscales are distinct vertical features between $Z/c_a = 0.6$ and 0.8 . This behavior is due to the merging of the two sets of data files as outlined in section 2.4 where the overlapping points in the data set cause the differences due to the uncertainties in the measurement quantities. However, the surface blocking effect on the lower endwall is highlighted in the behavior of the lateral lengthscale, Λ_v , decreasing as the lower endwall is approached. The results indicate that by this axial location the influence of the blade row begins to assert itself, primarily in the streamwise velocity.

Measurements of the boundary layer upstream of the blade passage at $X/c_a = -0.23$ were made using a single (1 component, U) hot wire probe at three Z/c_a locations. The locations were $z/c_a = -0.355$, 0.495 , and 1.345 , and corresponded to points in the measurement plane that are upstream of the leading edge of the two blades and the center of the blade passage and are shown in Figure 3.27.

Figure 3.28 shows the mean flow boundary layer profiles plotted normalized with the boundary layer parameters, U/U_e vs y/δ^* . The boundary layer profiles all tend to collapse to one shape, with a slightly fuller shape at the center of the passage, indicating slightly larger boundary layer thickness. Comparisons between the two flow with and without grid generated turbulence can be made by estimating the boundary layer parameters, δ^* , the displacement thickness, and θ , the momentum thickness for the two inflow conditions. The displacement and momentum thickness are defined as

$$\delta^* = \int_0^{y_{\max}} (1 - U/U_e) dy$$

$$\theta = \int_0^{y_{\max}} (1 - U/U_e) U/U_e dy$$

and were numerically estimated. The results are given below in Table 3.5.

Table 3.5: Boundary layer parameters at $X/c_a = -0.23$

Z/c_a	$\delta^*(in)$		$\Theta(in)$	
	<i>Grid</i>	<i>No Grid</i>	<i>Grid</i>	<i>No Grid</i>
-0.355	0.059	0.060	0.053	0.054
0.495	0.083	0.084	0.071	0.071
1.345	0.052	0.051	0.046	0.045

From the above results, the boundary layer parameters are similar for both inflow cases. This implies that with the introduction of grid generated turbulence, the cascade sees the same inflow condition in terms of mass and momentum as with the no grid case. The results also show that the boundary layer upstream of the center of the passage is slightly larger than upstream of the blade row. This could be due to the upstream influence of the blades on the boundary layer.

Similarly, presented in Figure 3.29 and 3.30, are the normalized boundary layer profiles of the turbulence intensities plotted against y/δ^* . Plotted in Figure 3.29, is the variation of the streamwise turbulence intensities, u^2/U_∞^2 , and in Figure 3.30 is the variation of the differences between the edge of the boundary layer $(u^2 - u_e^2)/U_\infty^2$. Upstream of the blade leading edges ($Z/c_a = -0.355$ and 1.345), the boundary layer profiles are similar in shape and form in Figure 3.29 for the two cases for $y/\delta^* < 5$, but then begin to differ approaching the free stream. The boundary layer upstream of the center of the passage ($Z/c_a = 0.495$), differs from the other profiles showing lower turbulence intensities within the boundary layer. Observing the differences in intensities as plotted in Figure 3.30, the boundary layer upstream of the center of the passage shows a different behavior compared to the other locations. Also noticeable in Figures 3.29 and 3.30 is the periodicity of the cascade tunnel, as the two boundary layer profiles upstream of the blade leading edges are similar for both inflow turbulence conditions.

3.5. The Potential Core Region

The flow through the compressor cascade can be divided into two distinct regions; the potential core region and the region under the influence of viscous effects. In the compressor cascade, viscous effects may be thought of as flow features such as the lower endwall region

which encompasses the tip leakage vortex, and the blade wakes. The region not dominated by these features is the potential core region. Presented in Figures 3.31-3.37 are plan view plots of the flow field at $Y/c_a=0.73$. The plots were generated by linearly interpolating values between axial measurement locations.

The variation of the normalized streamwise velocity, U/U_∞ , through the cascade is shown in Figure 3.31. For both inflow cases, with and without grid generated turbulence, the qualitative flow features are similar. The double peak trend seen in the contour levels at the middle of the passage is a consequence of combining the two measurement sets at each plane. Observing the velocity distribution, we see that on the pressure side of the passage, the velocity reaches its exit value at approximately $X/c_a=0.4$, and on the suction side, at approximately $X/c_a=0.8$. Looking back at the blade loading distribution, we see that the grid generated turbulence effect only starts to play an effect at approximately these locations on the plot (Figure 3.3a).

The final turning angle of the facility is 11.78° and the measured velocity ratio downstream of the blade row away from the lower endwall was 0.72, or a 28% deceleration for both inflow turbulence cases. For the given turning angle of the facility, the continuity equation predicts an average velocity ratio of 0.705 calculated as

$$U_{average} = U_\infty \frac{\cos(65.1^\circ)}{\cos(65.1^\circ - 11.78^\circ)}$$

This difference is the result of the velocity deficit associated with the endwall flow and blade wakes. This result shows that in the measurement, there is an additional 1.5% acceleration of the flow as it passes through the blade passage.

Presented in Figures 3.32-3.34 are the turbulence intensities, $\sqrt{u^2/U_\infty}$, $\sqrt{v^2/U_\infty}$, $\sqrt{w^2/U_\infty}$, and their variation through the cascade. In general, the the variation of $\sqrt{u^2/U_\infty}$, and $\sqrt{v^2/U_\infty}$, is similar, showing increased values with the presence of grid generated turbulence. As the flow develops through the passage, the variation of $\sqrt{u^2/U_\infty}$, and $\sqrt{v^2/U_\infty}$ shows a slight decrease in the levels. In contrast, the $\sqrt{w^2/U_\infty}$ distribution shows a significant decrease in the levels through the cascade. This decrease can be attributed to the surface blocking effect of the blade row and the distortion it applies to the flow field in the

pitchwise direction similar to that seen in the lower endwall region in sections 3.4. The surface blocking effect is primarily on the fluctuation normal to a surface, and in the case of the flow through the passage of the cascade, this component would $\sqrt{w^2/U_\infty}$. Approaching both surfaces of the blade, this effect is seen by the reduction in the $\sqrt{w^2/U_\infty}$ levels.

Presented in Figure 3.35-37 are the longitudinal and lateral integral lengthscales in the potential core of the flow for both flow cases. It is interesting to note that the longitudinal lengthscale is larger for the case with grid generated turbulence, but the lateral lengthscales are larger for the case without grid generated turbulence. The surface blocking effect of the blades can once again be seen in the lateral lengthscale, Λ_w , near the blade surfaces in Figure 3.37. The surface blocking effect is more clearly visible in the case without grid generated turbulence as the lengthscales are larger (by about 1cm in the inflow region).

The evolution of the turbulence in the potential core region can also be seen in the velocity spectra plotted in Figures 3.38-3.40. The spectra of the streamwise component is defined as $G_{uu}(f) = 2 \int_0^\infty R_{xx}(\tau) \cos(2\pi f\tau) d\tau$, and likewise in the other directions. Both inflow turbulence conditions are shown in the plots, and the legend indicates the axial location. The spectral points correspond to the intersection of the center streamline at the axial locations indicated in the legend. Figures 3.38 and 3.39, which are plots of G_{uu}/U_∞^2 and G_{vv}/U_∞^2 , show that with the introduction of grid generated turbulence, at frequencies less than 1 KHz, the spectral values have approximately the same magnitude. However, in Figure 3.40, the plot of G_{ww}/U_∞^2 , we see that through the passage, the spectral levels are reduced at frequencies less than 1kHz. The spectral evolution for the case without grid generated turbulence shows a different behavior where the levels increase with downstream distance in G_{uu}/U_∞^2 and G_{vv}/U_∞^2 . However, G_{ww}/U_∞^2 , shows a decreasing behavior to the trailing edge, and then an increase in the level at $X/c_a=1.26$.

3.6. Lower Endwall Region

3.6.1. Mean Flowfield Structure

Presented in Figures 3.41-3.44 are the two mean velocity flowfields through the blade row. Presented in Figures 3.41 and 3.42 are the contours of normalized mean streamwise

velocity and the crossflow vectors respectively at axial locations corresponding to $X/c_a = 0.0, 0.27, 0.48, 0.77, 0.96$ and 1.26 (see Figure 3.1). A detailed discussion of these two plots is presented in section 3.6.1.2 but briefly, the plots reveal the presence of the tip leakage vortex as the region of high velocity deficits (Figure 3.41), and an apparent rotating velocity field (Figure 3.42) beginning at $X/c_a = 0.27$. Note that at $X/c_a = 1.26$, the wakes of the blades are visible in the plots, but due to the resolution of the data set, the wakes are not accurately represented and thus are not the subject of discussion in this study.

Also shown in the figures are the vortex centers to facilitate the discussion of the lower endwall flow region. The vortex centers are determined using the locus of points of peak vorticity in the flow field and is presented in section 3.6.1.1 below.

3.6.1.1. The Streamwise Vorticity Field, Definition of the Vortex Center

The vortex center can be defined as the location of peak streamwise vorticity after computing the vorticity in the flow field. With the dense measurement grid (see Figure 3.2), and 3 component velocity measurements, the gradients implicit in the vorticity can be determined using finite difference approximations. Similarly, the normalized helicity can also be computed, and with these two factors, one has an alternate means of determining the vortex center than using the location of peak velocity deficit.

The vorticity is computed as the curl of the velocity vector, with each of the components defined as shown below:

$$\begin{aligned}\Omega_x &= \frac{\partial W}{\partial y} - \frac{\partial V}{\partial z} \\ \Omega_y &= \frac{\partial U}{\partial z} - \frac{\partial W}{\partial x} \\ \Omega_z &= \frac{\partial V}{\partial x} - \frac{\partial U}{\partial y}\end{aligned}$$

where Ω_x is defined as the streamwise vorticity. The derivatives in the streamwise, x , direction, are assumed to be zero i.e. $\frac{\partial}{\partial x} = 0$. The derivatives $\frac{\partial}{\partial y}$, and $\frac{\partial}{\partial z}$ were computed using a finite difference calculation based on an interpolated grid of points. The interpolated grid was generated using a cubic spline fit of the data between the measured grid points. The

normalized helicity was also computed as $H = \frac{\vec{V} \cdot \vec{\Omega}}{|\vec{V}| |\vec{\Omega}|}$. Based on this definition, one would

expect the vortex center to lie close to the point where H has a value of 1 (or -1 depending on the direction of the vortex).

Plotted in Figures 3.43a-e are the contours of the normalized mean streamwise vorticity, $\Omega_x c_a / U_\infty$, both with and without grid generated turbulence for the measurement planes at $X/c_a = 0.27, 0.48, 0.77, 0.98$ and 1.26 . Vorticity calculations are not presented upstream of $X/c_a = 0.27$ since these plots reveal no significant streamwise vorticity within the measurement grids at these stations. Also shown on the plots indicated by the circular cross, are the locations of the vortex centers defined as the locations of maximum streamwise vorticity. These locations and corresponding values for the maximum vorticity are given in Table 3.6. The vortex center location is not presented for $X/c_a = 0.27$ as the vortex center appears to be below the range of the data set and cannot be accurately determined at this location.

Table 3.6 : Location of vortex centers are determined by peak streamwise vorticity.

X/c_a	No Grid Generated Turbulence			With Grid Generated Turbulence		
	Z/c_a	Y/c_a	$\Omega_x c_a / U_\infty$	Z/c_a	Y/c_a	$\Omega_x c_a / U_\infty$
0.48	-0.44	0.08	18.17	-0.40	0.07	18.61
0.77	-0.87	0.11	9.56	-0.86	0.12	8.96
0.98	-1.39	0.15	4.12	-1.33	0.16	3.03
1.26	-1.90	0.13	3.34	-1.85	0.13	2.68

The plots in Figure 3.43 again show qualitatively similar flow fields for the two inflow turbulence cases and both flows will initially be discussed together, with the differences due to grid generated turbulence to follow. At $X/c_a = 0.27$, the vorticity field is characterized by a region of high streamwise vorticity near the suction side of the passage close to the lower endwall. Interestingly, there is a region of negative vorticity above this centered near $Y/c_a = 0.13$ approximately. Also, barely visible at $Z/c_a = -0.2$ close to the lower endwall, there is a second region of negative vorticity.

At $X/c_a = 0.48$, the vorticity region containing the tip leakage vortex is better defined because of its greater size relative to the measurement grid (Figure 3.2). The flow in the lower endwall region is characterized by a region of high streamwise vorticity in the vicinity

of the vortex center. This region of large positive vorticity is surrounded by a region of negative vorticity toward the left of the vortex center as seen in Figure 3.43a. This region of negative vorticity lies to the left of the separation line inferred from the oil flow visualizations, as indicated by the dashed lines in the plots. The presence of these regions of negative vorticity might indicate a secondary vortex present in the passage, as was initially suggested in the study by Muthanna (1998) and shown in Shin (2001). However, comparisons with the crossflow vectors presented in Figures 3.42 do not give an indication of a secondary vortex. The negative vorticity is therefore attributed to the strong crossflow that presumably passes underneath the tip leakage vortex from the tip gap. This crossflow coupled with the no slip condition on the lower endwall (analogous to a boundary layer type flow) generates flow with vorticity of opposite sign to the tip leakage vortex. As this flow crosses the passage it is being lifted off the lower endwall at the separation line, and pulled around the vortex, forming the regions shown here in the plots. Also visible in the plots is the pressure side blade boundary layer, as the region of elevated vorticity.

At $X/c_a=0.77$, the structure of the vorticity field is similar to that at $X/c_a=0.48$, with a region of high vorticity around the vortex center, surrounded by the arc like region of negative vorticity. The vorticity levels have been reduced in the flow region, and the vortex center has now moved away from the lower endwall to approximately $Y/c_a=0.11$ (See Table 3.6). Again, there is a region of negative vorticity is to the left of the separation line. The region of positive vorticity around the vortex center has expanded, and occupies a larger area of the lower endwall flow. A description of the vortex size through vorticity contours is difficult and speculative, but an objective criteria for determining the vortex size will be presented in section 3.6.1.3.

Proceeding to $X/c_a=0.98$, the region of both positive and negative vorticity has grown to dominate much of the lower endwall region in the passage. The influence of the vortex extends to $Y/c_a=0.4$. The contour levels are given in the legend and have been altered from previous locations to distinguish the contour levels as the vorticity levels have decreased. The arc like region of negative vorticity surround the region of positive vorticity around the core is clearly visible, and has also grown in size. Visible in the figures are the vorticity levels associated with the blade boundary layers on the suction side of the passage. Comparisons of the two flow fields and the influences of grid generated turbulence are

revealed in this plot, showing that the vorticity levels are reduced with the introduction of grid generated turbulence.

Downstream of the blade row at $X/c_a=1.26$, the tip leakage vortex dominates the lower endwall region in the flowfield bounded by the two blade wakes. Once again, the region of positive vorticity is bounded by the region of negative vorticity. Comparisons of the two flowfields again show a reduction in vorticity levels with the presence of grid generated turbulence. Visible in the plots are the blade wakes, and as mentioned, the resolution of the measurement grid is not sufficient to accurately define the flowfield in the blade wakes.

Effects of the grid generated turbulence on the flow field can be seen in the plots and were briefly mentioned and presented in the preceding paragraphs. Overall, the effects of elevated turbulence levels are to decrease the levels of streamwise vorticity within the tip leakage vortex by approximately 20%. This would suggest that with the introduction of grid generated turbulence, the strength of the vortex is reduced if we assume that vorticity is indicative of the strength. Since the vortex is formed due to the roll up of the tip gap flow, and the tip gap flow is driven by the pressure differences on the blade, a reduction in strength of the vortex would imply that the lift on the blade is reduced as the tip gap flow is reduced. This is in agreement with the results presented in Section 3.2 where there was a reduction in lift on the blade due to the presence of grid generated turbulence.

Also shown in the results presented in Table 3.6, are the effects of grid generated turbulence on the locations of the apparent center of the vortex. With the introduction of grid generated turbulence, the vortex center appears to move slightly closer to the suction side of the passage than without grid generated turbulence. Curiously, this is the opposite of the trend seen in the oil-flow visualizations, where the separation line was seen to lie further from the suction side with the grid turbulence. If we were to use the theory of inviscid fluid mechanics and say that the vortex is convected by its image due to the wall, this would agree with the implication that the strength of the vortex is reduced with the introduction of grid generated turbulence.

The mean normalized helicity in the vicinity of the tip leakage vortices is plotted in Figures 3.44, and one would expect the vortex center to lie close to the location of H has a value of 1. Given in Table 3.7, are the locations where the contours indicate $H=1$.

Table 3.7 : Location of points in vortex where H (normalized mean helicity)=1

	No Grid Generated Turbulence			With Grid Generated Turbulence		
X/c_a	Z/c_a	Y/c_a	H	Z/c_a	Y/c_a	H
0.48	-0.41	0.09	1.00	-0.40	0.08	0.99
0.77	-0.89	0.11	1.00	-0.90	0.12	1.00
0.98	-1.45	0.15	0.99	-1.43	0.14	0.99
1.26	-1.88	0.14	0.99	-1.85	0.14	0.99

As can be seen from the plots and comparison of Tables 3.6 And 3.7, the locations of $H=1$ lie close to the vortex center locations (the largest difference seen at $X/c_a=0.98$). The location of peak helicity is only slightly influenced by the grid generated turbulence similar to what was seen with the locations of the vortex centers. Comparisons of the vortex center and the locii of peak helicity are shown in Figure 3.45. Also shown on the plot is the location of the separation line as determined from the oil flow visualizations (similar to Figure 3.6). The results do show a slight shift in the indicators of vortex path towards the suction side with the presence of grid generated turbulence, but similar to what was seen with the effects of grid generated turbulence on the blade loading, the effects are minimal. At the most downstream location, this shift appears to be about $2.5\%c_a$ in the pitchwise direction.

An interesting aspect of the plot is that it shows as the tip leakage vortex develops through the passage, the location of both the peak streamwise vorticity and peak normalized helicity rapidly shifts towards the pressure side of the passage between locations $X/c_a=0.77$ and 0.98 . The behavior of the separation line does not show this trend. Also, results from Muthanna (1998) where the path of the vortex center was plotted downstream of the blade row does not show any rapid changes in position, but a fairly straight path with no deviations. One possible explanation of this behavior comes from the observation of the flow field in the potential core of the flow (section 3.5), at approximately $X/c_a=0.77$, a thickening of the blade boundary layer is noticeable resulting in a reduction of the effective width of the passage. This reduction means that the streamlines in the potential core ceases to follow the contours of the blade surface, and thus are deflected further towards the middle of the passage, convecting the tip leakage vortex with it.

3.6.1.2. Mean Velocity Field

Returning to Figure 3.41, the contours of the normalized streamwise velocity, U/U_∞ are presented for both inflow turbulence conditions in each of the plots. The contour levels are given in the legend, using the same scale for all 6 measurement planes. Note that the plots in Figure 3.41 reveal the velocity gradient across the passage in the potential core region discussed in Section 3.5, and shown in Figure 3.31. The figures show that qualitatively the flow fields for the two inflow conditions are very similar and as such the discussion of the mean streamwise velocity will apply to both. Also shown on the plots in Figure 3.41b-f, are the locations of the separation line as dashed lines inferred from the oilflow visualizations given in section 3.3 and shown in Figure 3.45 and the vortex centers as circular crosses.

The influence of the tip leakage vortex begins to be visible at an axial location of $X/c_a = 0.27$ at approximately $Z/c_a = -0.2$ as a $30\%U_\infty$ deficit in the streamwise velocity near the lower endwall. However, comparisons of the mean streamwise vorticity Figure 3.43a, shows that this region of velocity deficit is not coincident with the peak positive vorticity which is around $Z/c_a = 0$, but the region of negative vorticity. The presence of the tip leakage vortex is more clearly visible at $X/c_a = 0.48$, and extends from a region of $Z/c_a = -0.3$ to -1 , to a height of $Y/c_a = 0.18$. The vortex centers are marked on the plots, and similar to the flow structure at $X/c_a = 0.27$, the peak velocity deficit is not at the vortex center but at the region to the left of the vortex center. This deficit, which is about $50\%U_\infty$ is slightly to the left of the separation line as indicated by the black dashed line.

Further downstream, at $X/c_a = 0.77$, the flow structure is similar to that seen at the two previous axial locations. Again, the region of high deficit, approximately $60\%U_\infty$, is on the lower endwall region and to the left of the separation lines. Interestingly, the contours show that this region of high deficit is being pulled and wrapped up into the vortex center region as indicated by the blue contour levels. This region of high deficit at $X/c_a = 0.77$ is located at approximately $Z/c_a = 1.3$ and extends into the vortex to about $Z/c_a = -1$ and $y/c_a = 0.15$.

However, at $X/c_a = 0.98$ and 1.26 , the flow structure of the streamwise velocity field changes significantly. At $X/c_a = 0.98$, there is still a region of high velocity deficit at the lower endwall at $Z/c_a = -1.8$, which appears to wrap up into the tip leakage vortex. But unlike the previous locations, there now is a very well defined region of velocity deficit in the vicinity of the vortex center. The tip leakage vortex now dominates the lower endwall flow

region and extends from $Z/c_a = -1$ to -2 , and to a height of $Y/c_a = 0.3$. This flow structure is similar to that at $X/c_a = 1.26$, with a region of high deficit near the lower endwall at approximately $Z/c_a = -2.25$, and a well defined velocity deficit near the vortex core. At $X/c_a = 1.26$, the influence of the tip leakage vortex now extends across the entire width of the passage bounded by the wakes of the two blades. The location and velocity at this high deficit region near the vortex center is given in Table 3.8 for both $X/c_a = 0.98$ and 1.26 . Results in the table indicate that there is a $2\%U_\infty$ increase in the deficit in the vortex center with the introduction of grid generated turbulence.

Table 3.8 : Location of points in tip leakage vortex in the vicinity of the vortex center of maximum velocity deficit.

X/c_a	No Grid Generated Turbulence			With Grid Generated Turbulence		
	Z/c_a	Y/c_a	U/U_{inf}	Z/c_a	Y/c_a	U/U_{inf}
0.98	-1.46	0.15	0.27	-1.44	0.14	0.24
1.26	-1.88	0.13	0.25	-1.84	0.13	0.23

From Figure 3.45, the path of the vortex center showed a drastic change in direction between axial locations $X/c_a = 0.77$ and 0.98 . Observing the development of the streamwise velocity field, between these two axial locations, a significant change in the flow structure was also observed. This suggests that the tip leakage vortex might still be forming and becomes well defined somewhere between $X/c_a = 0.77$ and 0.98 . This agrees with results from Muthanna (1998) which showed that downstream of the cascade, the tip leakage vortex had a well defined center characterized by this region of high velocity deficit.

The rotating nature of the velocity field is revealed in Figures 3.42a-f of the normalized crossflow velocity vectors. The length of the arrows represents the magnitude defined as $\sqrt{(V^2 + W^2)}/U_\infty$. The reference vector placed at the top left corner in each plot corresponds to a magnitude of $0.5 U_\infty$. The crossflow velocity field through the passage complements what was seen in the plots of the mean streamwise velocity. At $X/c_a = 0$ we see no indication of the tip leakage vortex as expected. However, close to the blade suction side, the vectors show that the flow is beginning to turn into the passage. At $X/c_a = 0.27$, the first signs of the tip leakage vortex can be seen with the large crossflow vectors near the suction side of the passage. The rotating nature of the vortex is not visible due to it being below the range of the

measurement grid. At the pressure side of the passage near the lower endwall, the vectors reveal the flow entering the tip gap region of the blade row. At $X/c_a=0.48$, the rotating nature of the flowfield becomes more apparent, as the vectors reveal a flow rotating around the vortex center. Again, the flow entering the tip gap region is also revealed in the plot. A similar crossflow velocity field is also visible at $X/c_a=0.77$, with the rotating flow field around the tip leakage vortex more clearly defined as now the vortex has moved away from the lower endwall. Again, flow entering the tip gap region is apparent on the pressure side near the lower endwall. As in the case with the mean streamwise velocity the crossflow field for these three locations are similar in structure.

At $X/c_a=0.98$ the flow structure again changes. While the tip leakage vortex is still visible as a region where the vectors are rotating around a central point near the vortex center, there is no further flow entering the tip gap region near the lower endwall at the pressure side of the passage. In fact, there does not seem to be any large pitchwise component to the velocity field. The vectors all seem to be influenced by the tip leakage vortex, and there does not seem to be any influence of the tip gap lower endwall flow at this downstream location. This same trend is seen at $X/c_a=1.26$ as well, where the cross-flow velocity field is now under the influence of the tip leakage vortex in the passage region between the wakes of the blades.

It was mentioned that the flowfield presented in the plots are qualitatively similar for both inflow turbulence conditions, and this statement has been shown to be true from the results presented in Figures 3.41 and 3.42. However, as per the discussion in section 3.3, where the oil-flow visualizations showed that there may be an effect on the position of the tip leakage vortex through the passage due to inflow turbulence, the results from Figure 3.41 and 3.42 show that the position of similar flow regimes for the two cases are similar and that the effects of grid generated turbulence are minimal. Table 3.5 supports this conclusion, but does show that the deficits observed in the flow fields are slightly higher for the case with grid generated turbulence than without. This is further shown in Figure 3.41.

3.6.1.3. Circulation in the Tip Leakage Vortex

Vortex strength is more commonly defined by computing the circulation. The circulation can be computed numerically using Stokes theorem, where the circulation is the net outflow of vorticity through an area and computed as shown below;

$$\Gamma_{\text{line integral}} = \int_{\text{Area}} \Omega \cdot \hat{n} dA$$

In the equation, “Area” represents that through which the vorticity outflow is considered. However, the size of the tip leakage vortex is not well defined in the figures and thus determining the area of the tip leakage vortex is difficult. One method of determining the area under the influence of the tip leakage vortex, and thus computing the circulation is to compute the variation of circulation with radius away from the vortex center. Not only does this give us a consistent means of comparing the two flow fields (with and without grid generated turbulence), but also an indication of the size and extent of the vortex. This approach provides a more objective comparison between the two flows compared to De la Riva (2001), who used a criteria that the area under the influence of the tip leakage vortex is bounded by a line where the velocity is 99% of the value in the potential core region.

Presented in Figure 3.46a is the variation of circulation, $\Gamma/(U_{\infty}c_a)$, on circular paths as seen projected along the x -direction as a function of radius from the center of the tip leakage vortex. Results are presented with and without grid generated turbulence at the four axial locations as shown in legend on the plots. Similarly, plotted in 3.46b is the variation of the circumferentially averaged tangential velocity, $\Gamma/(U_{\infty}c_a 2\pi r)$ with radius away from the vortex center. When performing the above calculation, for radii that extended below $Y/c_a < 0.037$ (the limits of the data set), the streamwise vorticity was assumed to be zero.

Supporting the implication that the vortex strength is reduced with the introduction of grid generated turbulence, Figure 3.46a shows a reduction in circulation under the presence of grid generated turbulence. However, the shape of the circulation distribution changes between $X/c_a = 0.77$ and 0.98 . The circulation does not rise as rapidly in the case of $X/c_a = 0.98$ when compared to 0.77 . This is expected given that the structure of the tip leakage vortex is changing between these two locations as previously discussed. It is also interesting to note that at $X/c_a = 1.26$, the circulation actually increases when compared to $X/c_a = 0.77$.

Figure 3.46b shows the variation of circumferentially averaged tangential velocity with radius. With the introduction of grid generated turbulence, the velocity decreases. Again, there is a distinct change in the shape of the curves between $X/c_a = 0.77$ and 0.98 similar to what was seen in Figure 3.46a. The extent of the tip leakage vortex can be determined by the location of the peak circumferentially averaged tangential velocity as presented in Figure

3.46b. These values are presented in Table 3.9, as well as the circulation implied by these radii.

Table 3.9 : Radius as implied by the peak circumferentially averaged velocity from Figure 3.46b, and the circulation implied by these radii.

X/c_a	Radius (No Grid)	Radius (Grid)	$\Gamma/(U_\infty c_a)$	$\Gamma/(U_\infty c_a)$
0.48	0.058ca	0.068ca	0.075	0.074
0.77	0.059ca	0.070ca	0.066	0.070
0.98	0.126ca	0.131ca	0.101	0.094
1.26	0.116ca	0.132ca	0.084	0.082

From the results in the table, the extent of the tip leakage vortex increases with the introduction of grid generated turbulence but the circulation implied show that the circulation decreases, except at $X/c_a = 0.77$.

From the above discussion of the mean flow field, there is an apparent change in the structure of the tip leakage vortex between axial locations $X/c_a = 0.77$ and 0.98. Grid generated turbulence effects on the mean flow field are present, showing an increase in size of the tip leakage vortex but a reduction in strength.

3.6.2. Turbulent Flow Field

3.6.2.1. Turbulence Kinetic Energy

Presented in Figures 3.47a-f, are the contours of the turbulence kinetic energy at $X/c_a = 0.0, 0.27, 0.48, 0.77, 0.96$ and 1.26. Both inflow turbulence conditions are presented, and all 6 figures here are plotted on the same contour scale, shown on the legend. Also plotted on the figures are the vortex center locations as defined in Table 3.6 to facilitate the discussion. Again, the flow field is qualitatively similar for the two inflow turbulence cases and so initially both cases are discussed together.

The formation and development of the tip leakage vortex is characterized by regions of elevated turbulence kinetic energy and is clearly visible in the figures. The high turbulence kinetic energy associated with the tip leakage vortex starts to become apparent near the lower endwall at $X/c_a = 0.27$, at approximately $Z/c_a = -0.2$. As mentioned previously, at this measurement location, the vortex is below the measurement grid, and hence the turbulence

kinetic energy distribution barely visible but as the flow develops downstream, the tip leakage vortex grows in size revealing the full turbulence kinetic energy distribution. At $X/c_a = 0.48$, the elevated turbulence kinetic energy associated with the tip leakage vortex is more clearly revealed. Effects of grid generated turbulence are also visible, showing slightly elevated turbulence kinetic energy levels in the tip leakage vortex. At $X/c_a = 0.77$, the tip leakage vortex has now extended to $Y/c_a = 0.3$, and dominates the lower endwall region of the flow. Further downstream, at $X/c_a = 0.98$ and 1.26 , we see that the influence of the tip leakage vortex extends across the entire lower endwall region between the blades. . Effects of grid generated turbulence are also visible, showing slightly elevated turbulence kinetic energy levels in the tip leakage vortex for all measurement planes. A more detailed description of the effects of grid generated turbulence is presented in 3.6.2.3.

One interesting feature of the turbulence kinetic energy distribution is that the regions of elevated turbulence kinetic energy actually form a band that extends around the center of the tip leakage vortex at $X/c_a = 0.48, 0.77$ and 0.98 at approximately $0.15-0.3c_a$ above the lower endwall. At $X/c_a = 1.26$, this region of elevated turbulence kinetic energy is now beginning to move towards the pressure side of the passage, $Z/c_a = -2.25$, but is still above the lower endwall at a height of $0.2c_a$. Muthanna (1998), showed that downstream of the cascade, this region of elevated turbulence kinetic energy tended to be where the flow was lifting off the lower endwall, and the results of the current measurement do show this trend beginning to form. However, at axial locations, $X/c_a = 0.48$, and 0.77 , the figures show that there are regions of high levels of turbulence kinetic energy at the center of the vortex as indicated by the circular cross. Conversely, at $X/c_a = 0.98$, the vortex center does have a slightly elevated region of turbulence kinetic energy, but the predominantly high turbulence kinetic energy levels are seen in a band above the core, and at $X/c_a = 1.26$, there does not seem to be a region of elevated turbulence kinetic energy at the center of the vortex.

3.6.2.2. Turbulence normal stresses

Further insight as to the turbulence flow field can be gleaned from the Reynolds normal stresses. The distribution of the square root of the Reynolds normal stresses, $\sqrt{u^2/U_\infty}$, $\sqrt{v^2/U_\infty}$, and $\sqrt{w^2/U_\infty}$ are shown in Figures 3.48, 3.49 and 3.50 respectively for the flow through the blade row. Once again, the contour levels are the same for all three figures and

are shown on the legend in each. The locations of the vortex center are also shown in the plots with the circular cross symbol.

The high turbulence kinetic energy levels associated with the band surrounding the apparent core of the vortex are primarily due to the $\sqrt{u^2/U_\infty}$ stress, or the fluctuations in the streamwise direction. At the center of the vortex, the high turbulence kinetic energy levels are primarily due to the $\sqrt{v^2/U_\infty}$ stress, while the vortex seems to be developing through the passage at $X/c_a=0.48$, and 0.77 . At the trailing edge of the blade row, $X/c_a=0.98$, high $\sqrt{v^2/U_\infty}$ levels are now seen in a band around the upper bound of the vortex. Similarly, the $\sqrt{w^2/U_\infty}$ levels show increased levels at $X/c_a=0.48$ and 0.77 around this vortex center, but as the vortex develops downstream the $\sqrt{w^2/U_\infty}$ levels tend to be elevated over much of the vortex region and are not concentrated along a band as in the other two stresses. From these figures, it can be concluded that as the vortex is forming, the high turbulence kinetic energy levels at the vortex center are due to fluctuations of all three velocity components, but further downstream, the dominant terms are due to the axial and the spanwise fluctuations.

3.6.2.3. Effects of grid generated turbulence

The effects of grid generated turbulence on the flow field in the lower endwall region has been discussed in terms of the mean flow field. Initial comparisons of the contours of the turbulence kinetic energy levels in Figure 3.47 And the Reynolds normal stresses in Figures 3.48-50 shows that on average, the introduction of grid generated turbulence increases the turbulence kinetic energy levels in the tip leakage vortex.

One advantage of the measurement scheme used in this study is that for both flows, the measurement grids are coincident, hence direct comparisons of the effects of grid generated turbulence in the flow can be made. With this grid, the differences in the turbulence kinetic energy levels between the two cases can be computed at each measurement point. Shown in Figure 3.51 are the contours of the turbulence kinetic energy differences between the two flows normalized on the difference in the turbulence kinetic energy levels in the potential

core, computed as $\frac{(k_{grid} - k_{nograd})}{(k_{grid} - k_{nograd})_{potentialcore}}$. In the plots, a value of 1 implies that the

difference is equivalent to the difference in the turbulence kinetic energy levels in the

potential core of the flow. Red and yellow contours signify increases in the turbulence kinetic energy levels, and blue contours a decrease in the levels.

At $X/c_a=0.48$ (Figure 3.51a) the differences are slight, with a region of increased turbulence at approximately $Z/c_a=-0.4$, and a region of decreased turbulence at $Z/c_a=-0.55$ and $y/c_a=0.16$. This region of increased turbulence coincides with the vortex center as indicated in, and also is a region of high turbulence kinetic energy levels as shown in Figure 3.47c. Further comparisons with Figure 3.47c, indicates that the decreased turbulence kinetic energy levels are in the arch shaped region of high turbulence kinetic energy.

The effects of grid generated turbulence are clearly revealed at $X/c_a=0.77$ (Figure 3.51b), showing a large increase (between 3 and 4 in $\frac{(k_{grid} - k_{nogrid})}{(k_{grid} - k_{nogrid})_{potentialcore}}$) in the difference

between turbulence kinetic energy levels with the grid than without the grid. The largest differences are found in an arch shaped region above the vortex center similar to that seen in the turbulence kinetic energy distribution in Figure 3.47d, and in a region near the vortex center. This suggests that there is an enhancement of turbulence kinetic energy due to mixing effects, which is consistent with the increased size of the vortex with grid generated turbulence. Also, between these regions there is a region of negative differences. This suggests that the mixing interaction between the free stream turbulence, and the turbulence in the vortex reduces the levels in this region, i.e. the energy is being transferred into the high turbulence kinetic energy regions.

The differences in the turbulence kinetic energy levels between the two flows at $X/c_a=0.98$ (Figure 3.51c), are very different to that seen at $X/c_a=0.77$. The magnitude of the differences $\frac{(k_{grid} - k_{nogrid})}{(k_{grid} - k_{nogrid})_{potentialcore}}$ in the vortex center is not as large as at $X/c_a=0.77$,

possibly due to the fact that the turbulence kinetic energy levels in the center have been reduced (See Figure 3.47e). The magnitude of the differences in turbulence kinetic energy levels between the two flows in the arch shaped region is not as large, between 1 and 3 in $\frac{(k_{grid} - k_{nogrid})}{(k_{grid} - k_{nogrid})_{potentialcore}}$ as opposed to 5 at $X/c_a=0.77$. The highest differences are seen

towards the suction side of the passage, and the regions of negative differences have grown. Again, this could be due to the mixing effects that occur between the free stream turbulence

and the tip leakage vortex. As stated before, between $X/c_a = 0.77$ and 0.98 , the tip leakage vortex changes in its characteristics, and this is clearly reflected in the interaction of the vortex and the free stream turbulence, showing enhanced mixing while the vortex is still developing in the passage.

Near the pressure side of the passage, there is a region of negative differences in $\frac{(k_{grid} - k_{nograd})}{(k_{grid} - k_{nograd})_{potentialcore}}$ underneath the region of positive differences at $X/c_a = 0.98$. This region of negative differences extends down to the lower bound of the measurement grid at $Z/c_a = -1.2$. and was not noticeable at $X/c_a = 0.77$ at the pressure side of the passage. This region is where the flow is lifted off the lower endwall. At $X/c_a = 0.77$, the vortex has higher crossflow velocities, which would enhance the mixing effects, whereas at $X/c_a = 0.98$, the magnitude of the crossflow vectors reduces, and thus reducing the mixing effect in this region. At $X/c_a = 1.26$ (Figure 3.51d), the plot looks similar to that at $X/c_a = 0.98$, however, the region of negative differences seen at $X/c_a = 0.98$ has grown in size at the pressure side of the passage, at $Z/c_a = -2.5$. These regions of negative differences in $\frac{(k_{grid} - k_{nograd})}{(k_{grid} - k_{nograd})_{potentialcore}}$ at $X/c_a = 0.98$ and 1.26 in this arch shaped region near the pressure side indicate that as the vortex decays, the interaction between the free stream turbulence and the tip leakage vortex changes, in that the free stream turbulence removes some of the turbulence kinetic energy from the tip leakage vortex.

Also revealed in Figure 3.51d, at $X/c_a = 1.26$, there is negative difference in $\frac{(k_{grid} - k_{nograd})}{(k_{grid} - k_{nograd})_{potentialcore}}$ in the wakes of the blades at $Z/c_a = -1$, and -2.8 . While it has been mentioned that the wakes were not measured with sufficient resolution to accurately depict them, the results here do give an indication of the influence of grid generated turbulence on this aspect of the flow. The reduced turbulence kinetic energy levels in the wakes of the blades can be attributed to the fact that the presence of grid generated turbulence reduces the velocity fluctuations normal to the blade surface on the blade boundary layers, and it is these blade boundary layers that become the wakes, and thus the reduced turbulence kinetic energy levels.

3.6.2.4. Turbulence Kinetic Energy Production

Applying the Reynolds averaging technique to the conservation of mass and momentum, the equation for turbulence kinetic energy can be derived. From this, the production term is defined as the Reynolds stresses multiplied by the rate of strain and can be expressed

$$\text{as } -v^2 \frac{\partial V}{\partial y} - w^2 \frac{\partial W}{\partial z} - uv \left(\frac{\partial U}{\partial y} \right) - uw \left(\frac{\partial U}{\partial z} \right) - vw \left(\frac{\partial V}{\partial z} + \frac{\partial W}{\partial y} \right).$$

This can be calculated from the measured data set in a manner similar to the computation done for the vorticity (ignoring streamwise, x derivatives). Contours for this production term are plotted in Figure 3.52a-d for the measurement planes at $X/c_a = 0.48, 0.77, 0.98,$ and 1.26 for both inflow turbulence cases. In the contour plots, the red and yellow contours indicate positive production, and the blue and green contours indicate negative production.

At $X/c_a = 0.48$, there is a region of high production at $Z/c_a = -0.6$ extending to -0.7 where the flow is being lifted off the lower endwall and to the left of the vortex center. At $X/c_a = 0.77$, the region of production has moved to an area above the vortex center at $Y/c_a = 0.25$. This region of positive turbulence kinetic energy production is in an arc shape region around the vortex center. In both axial locations there is a region of negative production concentrated about the center of the vortex. At $X/c_a = 0.98$ the distribution of the turbulence kinetic energy production level has slightly changed with the dominant levels being the positive production in an arc around the vortex core, similar to what was seen at $X/c_a = 0.48,$ and 0.77 . However, moving downstream to $X/c_a = 1.26$, the location of high production levels has shifted from being to the right of the vortex center, to now being at the left of the vortex center, with a slight increase in the levels when compared to $X/c_a = 0.98$. The effects of inflow turbulence on the production levels are to decrease the levels, but the distribution and trends are the same for the two cases.

The production term is a function of the Reynolds stresses, and the rate of strain. This term can be looked at as a combination of contributions due to streamwise velocity gradients, and those due to contributions due to crossflow velocity gradients. Streamwise contributions can be thought of as the generation of turbulence due to streamwise velocity deficits, and the crossflow contributions due to the rotating motion of the tip leakage vortex. Ignoring streamwise, x , derivatives, we define the turbulence kinetic energy production due to

streamwise components as $-uv\left(\frac{\partial U}{\partial y}\right) - uw\left(\frac{\partial U}{\partial z}\right)$, and the turbulence kinetic energy

production due to crossflow components as $-v^2 \frac{\partial V}{\partial y} - w^2 \frac{\partial W}{\partial z} - vw\left(\frac{\partial V}{\partial z} + \frac{\partial W}{\partial y}\right)$.

The streamwise and crossflow contributions to the production are shown in Figure 3.53 and 3.54 respectively for both with and without grid generated turbulence conditions at four measurement planes. The plots show that at $X/c_a = 0.98$, and 1.26, the dominant contribution to the turbulence kinetic energy production is due to the streamwise components of the flow field within the tip leakage vortex. This implies that once the tip leakage vortex has fully established its rotating flow field, the dominant sources of turbulence kinetic energy production are due to the interaction of the tip leakage vortex and the mean streamwise velocity, and not due to the rotating motion of the vortex. This same result was also shown in Muthanna (1998) in a similar flow field but at locations further downstream of the blade row i.e. once the tip leakage vortex was fully developed.

However at $X/c_a = 0.48$, and 0.77, there is also a significant contribution to the turbulence kinetic energy production due to the crossflow components around the vortex center. Above the vortex center at these two axial locations, there are also significant turbulence kinetic energy production contributions due to streamwise gradients. It is also interesting to note that the regions of negative production seen in Figures 3.50 are primarily due to these crossflow contributions, implying that as the vortex is forming the rotating velocity field is the primary source of turbulent kinetic energy in the flow.

The contributions to the total turbulence kinetic energy production integrated with respect to area over these measurement planes due to these two terms are presented in Table 3.10 for both flows (with and without grid generated turbulence) at the four measurement planes presented here.

Table 3.10: Contributions to the total turbulence kinetic energy production due to streamwise and crossflow velocity gradients

X/c_a	Streamwise Contributions		Crossflow contributions	
	No Grid	Grid	No Grid	Grid
0.48	80%	109%	20%	-9%
0.77	138%	138%	-38%	-38%
0.98	97%	102%	3%	-2%
1.26	79%	83%	21%	17%

The results in the table show that the primary contribution to the turbulence kinetic energy is due to the streamwise velocity gradients as was the case in Muthanna (1998). An interesting aspect of this result is that at $X/c_a = 0.77$, there is a large negative contribution to the production term due to the gradients in the crossflow. The effects of grid generated turbulence on these flows can also be seen in that at $X/c_a = 0.48$, there is a tendency to increase the contribution to the turbulence kinetic energy production by streamwise velocity gradients, and reduce the crossflow contributions to the turbulence kinetic energy production.

Presented in Figure 3.55 are the contours for the turbulence kinetic energy diffusion computed using the triple velocity correlations. At $X/c_a = 0.48$, there is large area of negative diffusion coincident to the arc like region of high turbulence kinetic energy shown in Figure 3.49. This region of negative diffusion is bounded by regions of positive diffusion, which implies that the turbulence kinetic energy is being transferred from the high turbulence kinetic energy region to the outlying regions. At $X/c_a = 0.77$, this region of high turbulence kinetic energy corresponds to a negative diffusion region, and this is bounded by two regions of positive diffusion where the turbulence kinetic energy is being transferred. This same trend is seen in the other downstream locations, where the regions coincident with high turbulence kinetic energy levels all have a negative contribution to the diffusion, and are bounded by regions of positive diffusion. Thus, in the tip leakage vortex, there is a diffusion of turbulence kinetic energy from regions of high turbulence kinetic energy to low turbulence kinetic energy.

3.6.3. Velocity Spectra

Presented in Figures 3.56-58 are the velocity spectra taken at measurement points near the vicinity of the vortex core. The points do not coincide with the vortex centers due to the fact that the vortex centers are determined from an interpolated grid from the measured data set. Shown in Table 3.11 are the locations of the velocity spectra, and can be compared with Table 3.6 of the vortex centers.

Table 3.11: Locations of velocity spectra presented in Figures 3.56-3.58,

X/c_a	Z/c_a	Y/c_a
0.48	-0.43	0.07
0.77	-0.87	0.11
0.98	-1.43	0.15
1.26	-1.92	0.15

Normalized autospectra of the streamwise velocity component, G_{uu}/U_∞^2 , which is defined as $G_{uu}(f) = 2 \int_0^\infty R_{xx}(\tau) \cos(2\pi f\tau) d\tau$, is plotted in Figure 3.56 for the 4 axial locations at $X/c_a=0.48, 0.77, 0.98$ and 1.26 and both flows (with and without grid generated turbulence). Plotted in Figure 3.57 are the autospectra of the spanwise component, G_{vv}/U_∞^2 , and in Figure 3.58 of the pitchwise component, G_{ww}/U_∞^2 , defined and plotted in a similar manner as G_{uu} (Figure 3.56). At frequencies greater than 1000Hz, the spectral shapes are similar for the three components, but at lower frequencies, the differences between the three components are more apparent. Overall, between the 4 axial locations, the levels at $X/c_a=0.48$ are in general about 1 decade higher than at the other three locations at these higher frequencies.

Looking at the autospectra, G_{uu}/U_∞^2 (Figure 3.56), we see that for the 4 axial locations, there is a different behavior exhibited in the spectral distribution. At $X/c_a=0.48$ and 0.77 , at frequencies less than 500Hz, the difference between the two flows is much higher than that at $X/c_a=0.98$. And at $X/c_a=1.26$, the no grid turbulence case shows a higher spectral value. It is also interesting to note that the spectral values at $X/c_a=0.48$ and 0.77 at these frequencies are lower than that at $X/c_a=0.98$ and 1.26 , implying an increase in the streamwise fluctuations in the vortex center. This difference in spectra could be a result of the fact as hypothesized earlier, the structure of the tip leakage vortex changes between $X/c_a=0.77$ and

0.98, thus changing the spectral distribution as well. At the frequencies greater than 500Hz, we also see differing trends between the 4 axial locations. At $X/c_a=0.48$ and 1.26, the two flows are the same, but at $X/c_a=0.77$, the grid case is higher and at $X/c_a=0.98$, the no grid case is higher.

Plots of the autospectra, G_{vv}/U_∞^2 , in Figure 3.57, show a slightly different behavior as the flow develops through the cascade. Unlike the G_{uu}/U_∞^2 spectra, the spectral levels are higher at $X/c_a=0.48$ and 0.77, when compared to 0.98 and 1.26 at frequencies lower than 500Hz. This could be attributed to the fact that the vortex is closer to the lower endwall, and hence the larger spanwise fluctuations. Again, it is interesting to note that at $X/c_a=1.26$, the spectral levels are higher for the no grid case, than the grid case. One more interesting aspect is that comparing the spectral levels between $X/c_a=0.98$ and 1.26, for the case with no grid turbulence, the levels increase with downstream distance, whereas the levels decrease with grid turbulence. At frequencies greater than 500Hz, the spectral levels are similar for the two cases at the 4 locations.

Spectral results of the pitchwise component, G_{ww}/U_∞^2 , shown in Figure 3.58, show that for frequencies less than 500Hz, the spectral levels are all higher for the case with grid generated turbulence than without, at $X/c_a=0.48$ and 0.77. Downstream, at $X/c_a=0.98$ and 1.26, this trend is only seen for frequencies less than 200Hz. Above these frequencies, the trend is for the spectral levels with grid turbulence to be lower than without grid turbulence. It is also interesting to note that there seems to be a peak in the spectral levels at approximately 200Hz for the case without grid generated turbulence, and at approximately 100Hz for the case with grid generated, at $X/c_a=0.98$ and 1.26, where the levels drop off both above and below these frequencies. The results of the velocity spectra strengthen the hypothesis that the structure of the tip leakage vortex changes significantly as it develops through the blade row of the cascade between the axial locations $X/c_a=0.77$ and 0.98.

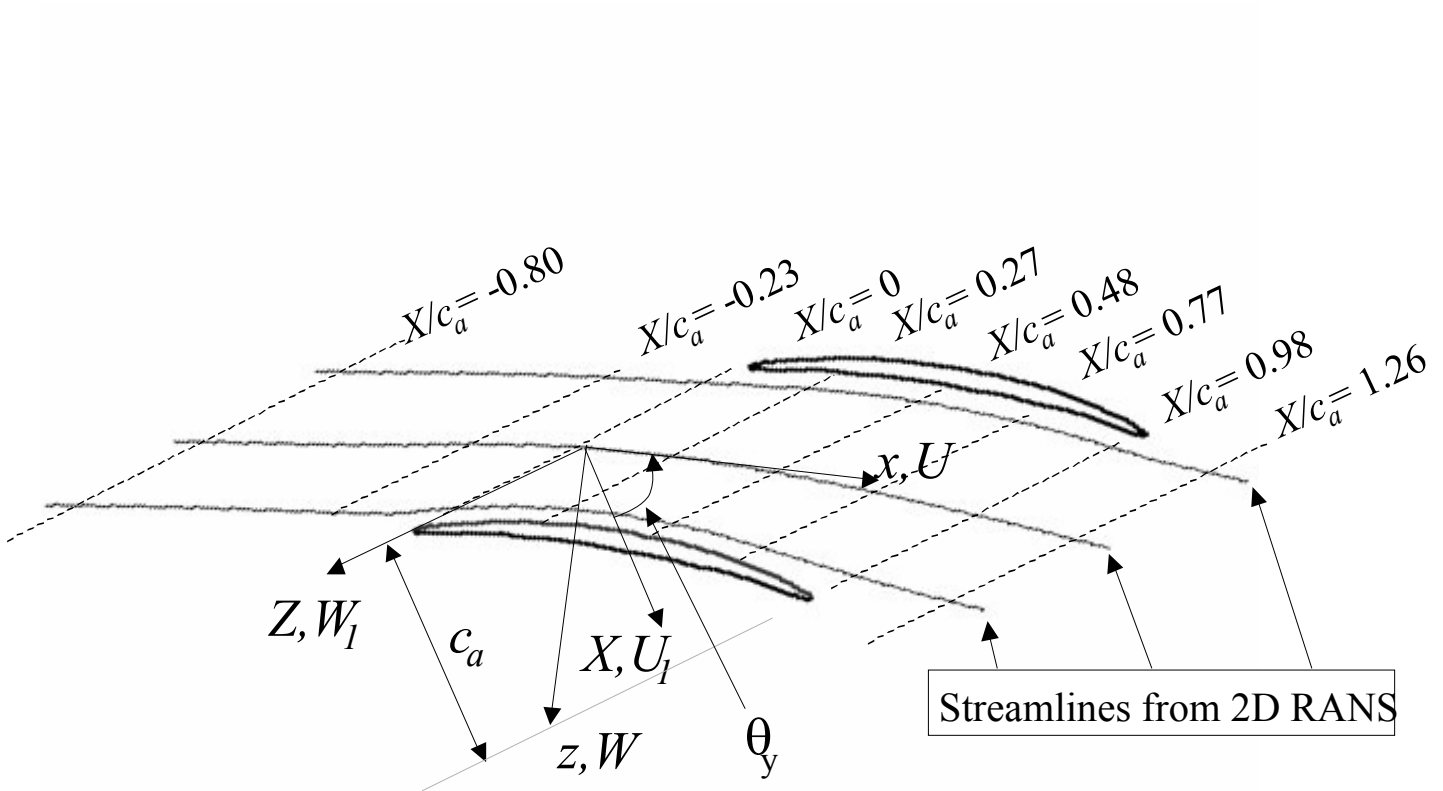


Figure 3.1: Measurement locations and co-ordinate system.
Y direction is out of paper.

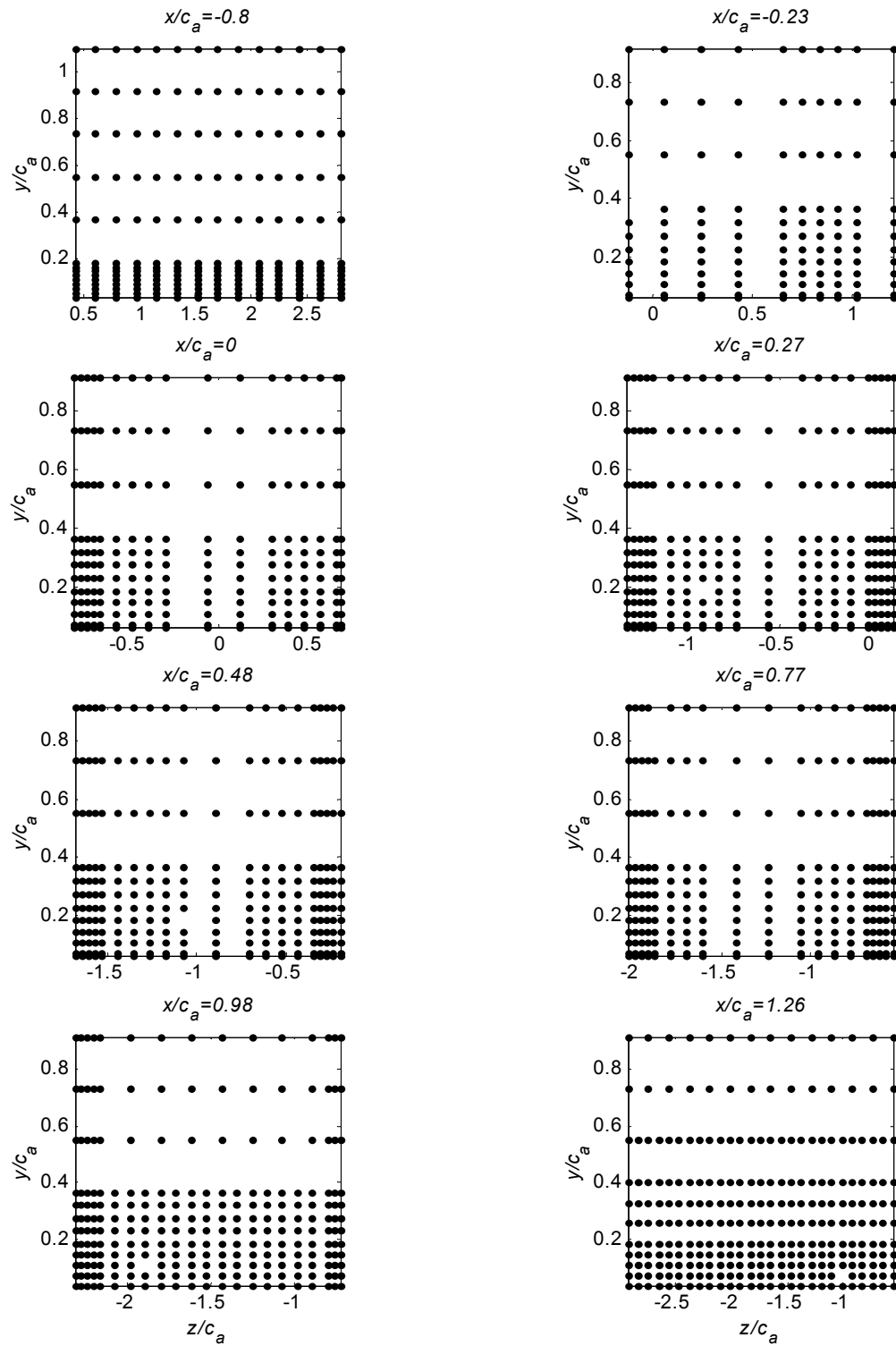


Figure 3.2: Measurement grids at each axial plane. An average of 180-200 data points were used at each measurement plane

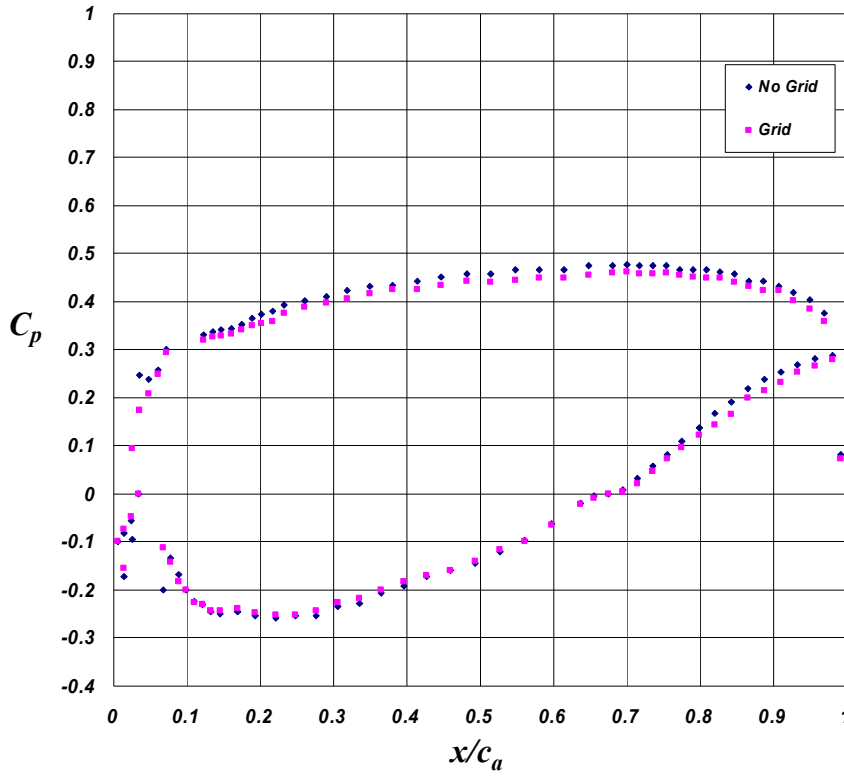


Figure 3.3a: Measured pressure coefficient distribution over the blade at mid span. Legend indicates inflow condition.

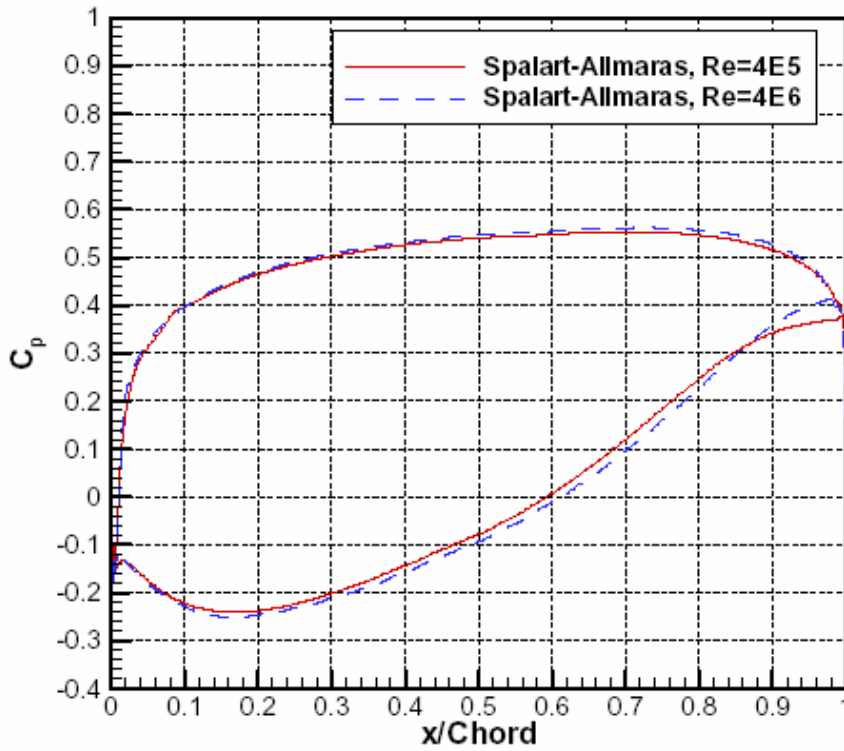


Figure 3.3b: 2-D computed pressure coefficient on blade from Shin(2001). Legend indicates modeling conditions.

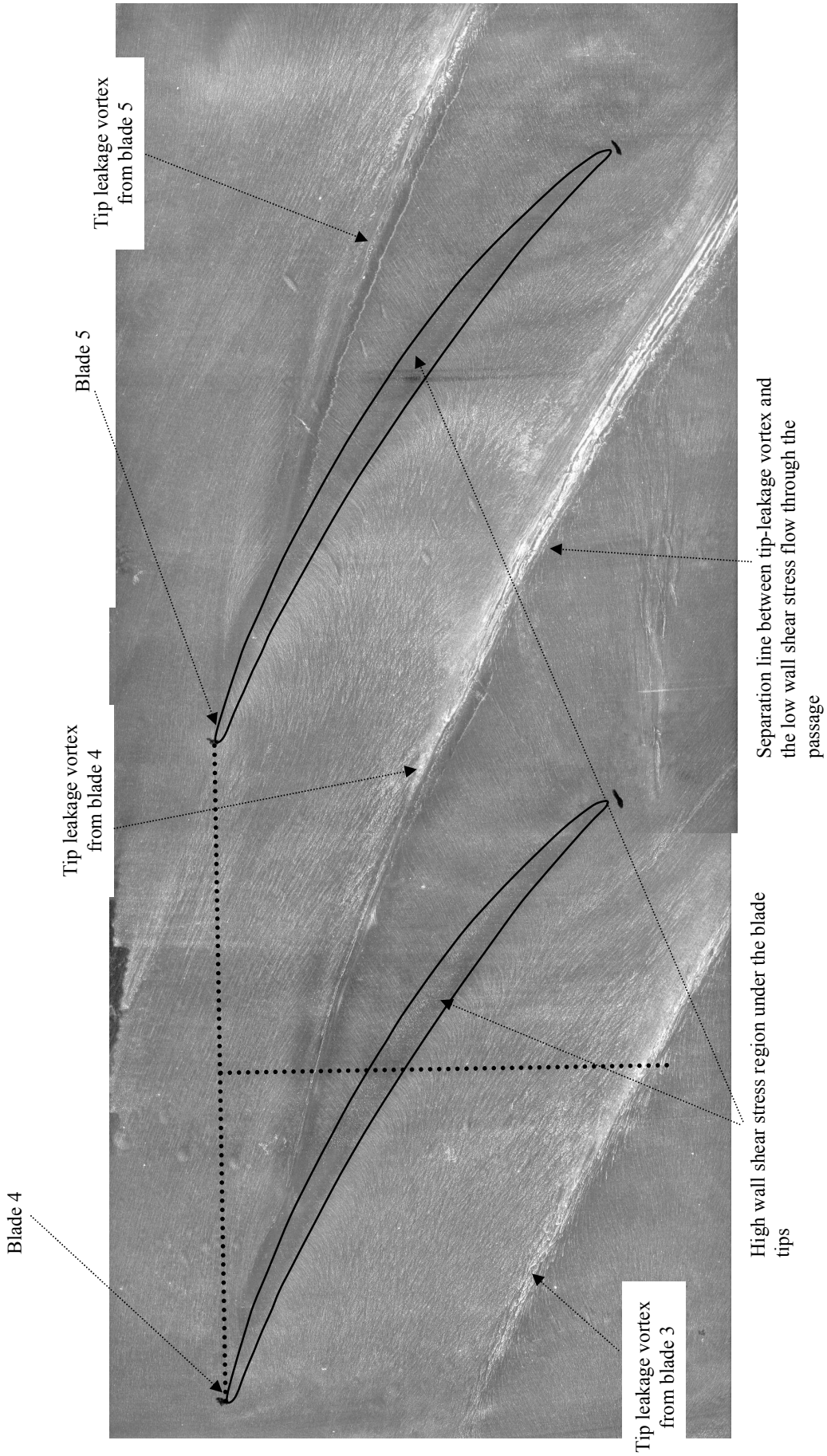


Figure 3.4: Surface oil flow visualizations taken under the passage between blades 4 and 5 for the no grid generated turbulence inflow condition.

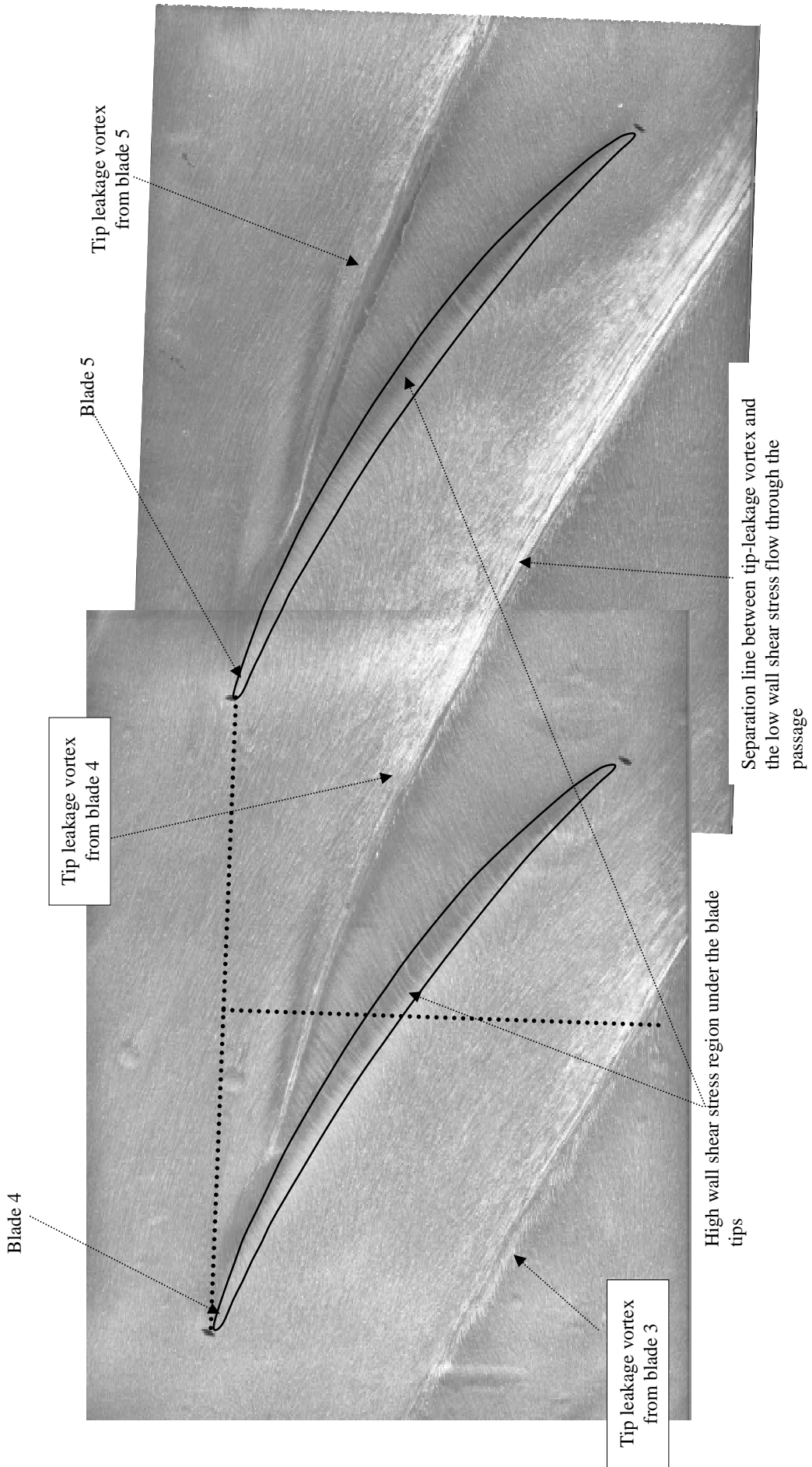


Figure 3.5: Surface oil flow visualizations taken under the passage between blades 4 and 5 for the grid generated turbulence inflow condition.

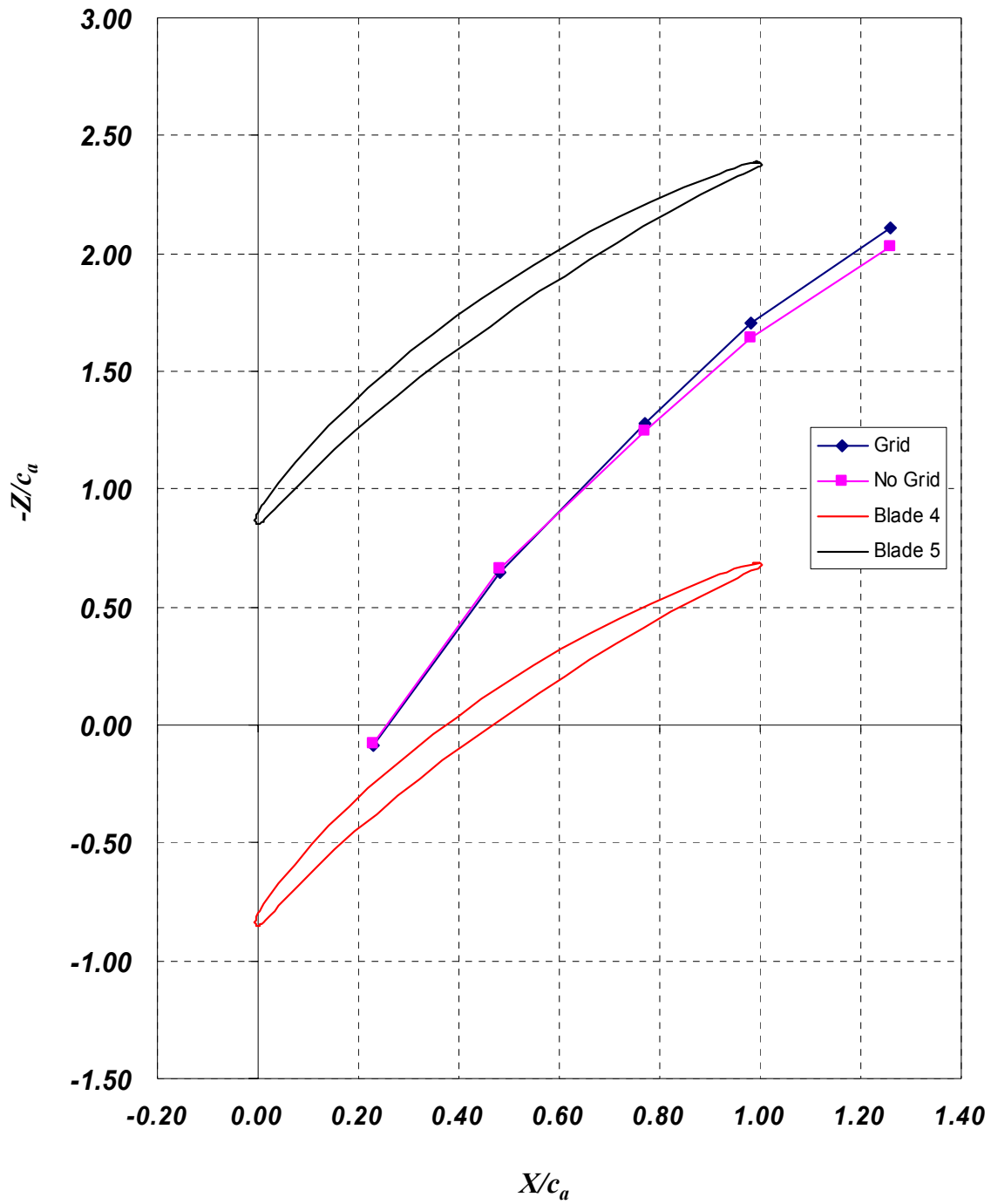


Figure 3.6: Path of the vortex-lower endwall flow separation line for the two inflow cases. Note the reduction in the angle the vortex path with the axial direction under the influence of grid generated turbulence.

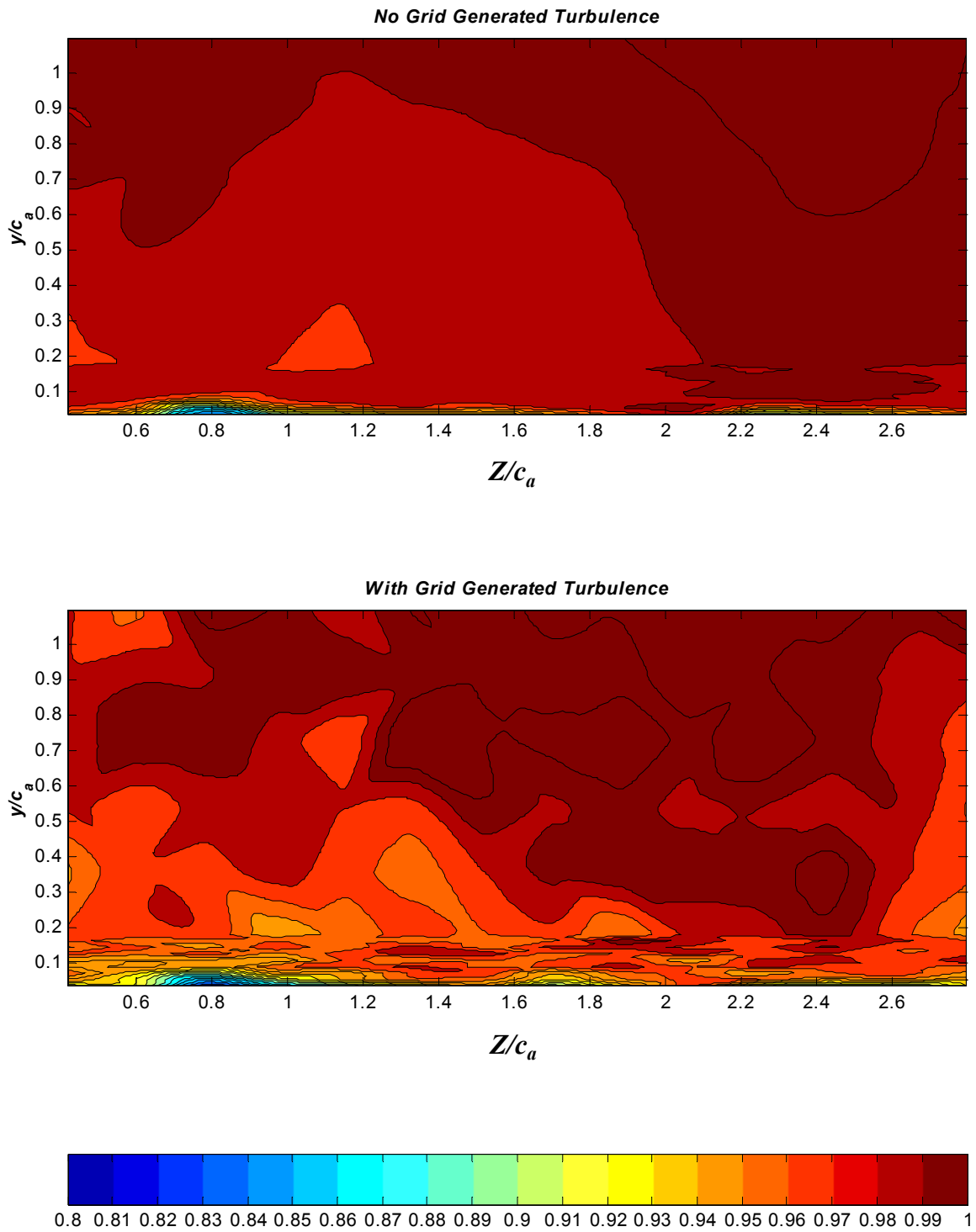


Figure 3.7 : Contours of Normalized Mean Streamwise Velocity, U/U_{∞} , at $X/c_a = -0.80$, Titles on plots indicate inflow turbulence condition

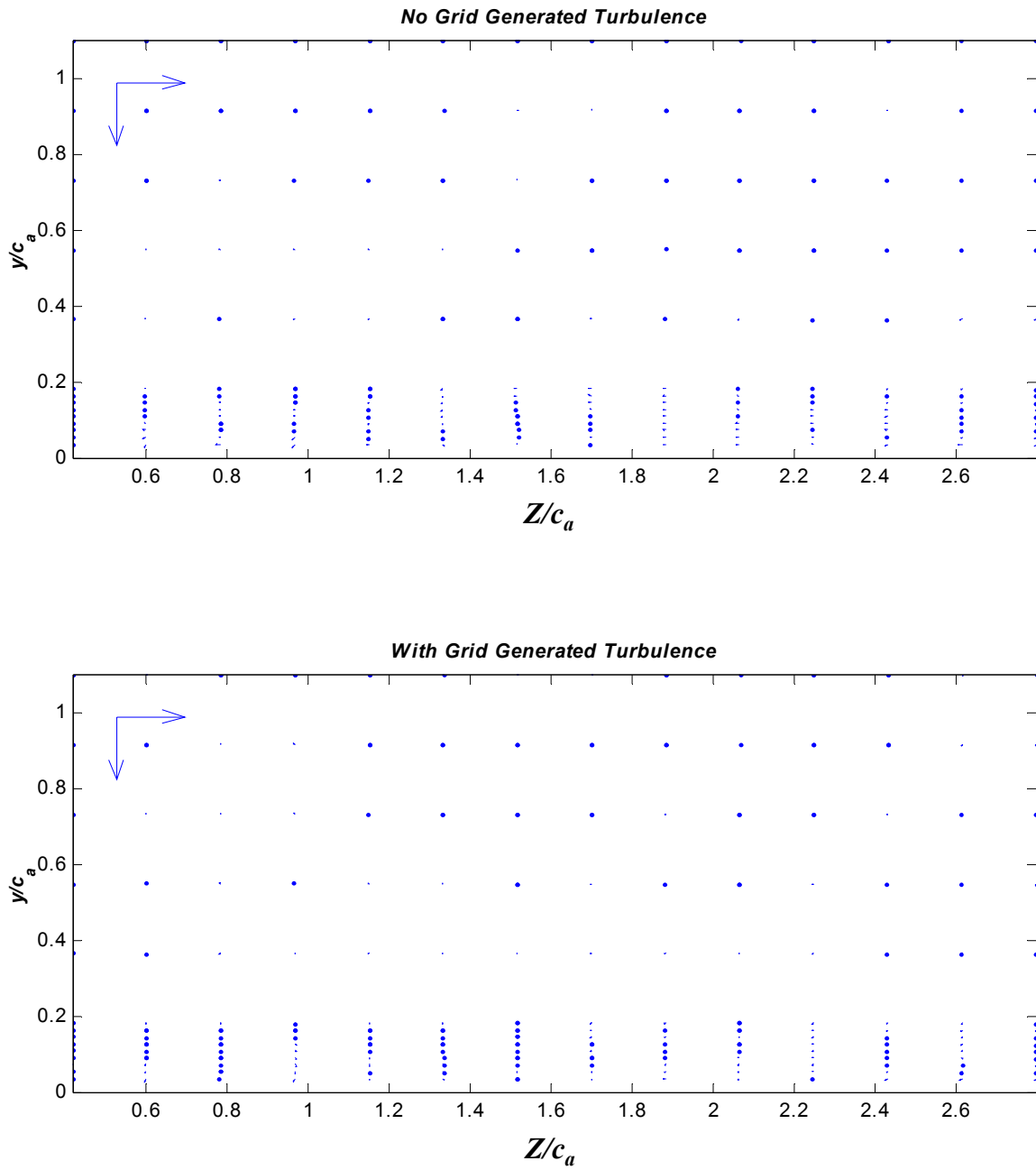


Figure 3.8 : Vectors of the magnitude of the mean normalized crossflow velocity (V , W) at $X/c_a = -0.80$. Reference vectors of magnitude $0.5U_\infty$ in the y and z direction are given in the top left corner of each plot. Titles on plots indicate inflow turbulence condition

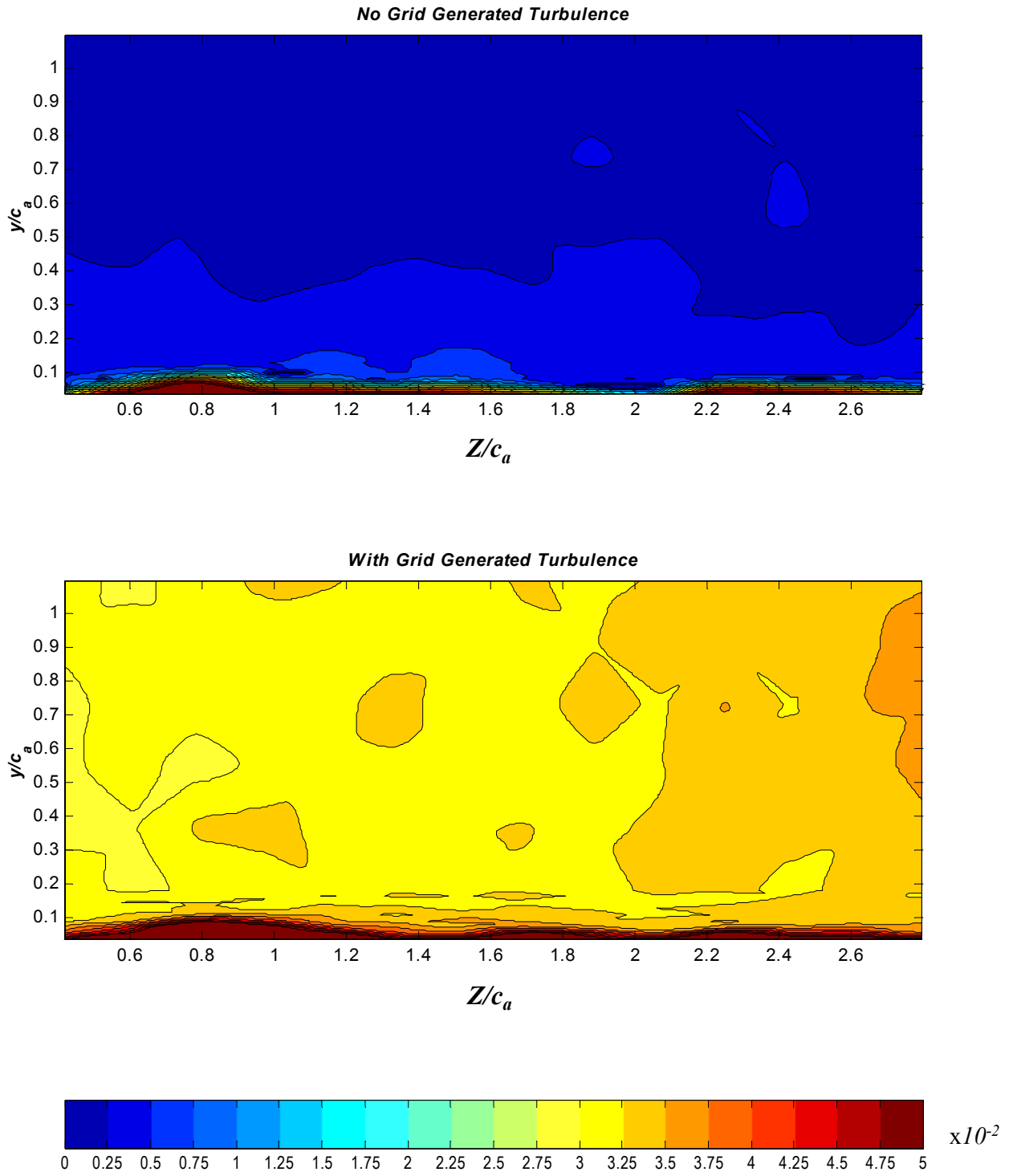


Figure 3.9 : Contours of the square root of the Reynolds Normal Stress $\sqrt{(u^2/U_\infty^2)}$ at $X/c_a = -0.80$. Titles on plots indicate inflow turbulence condition

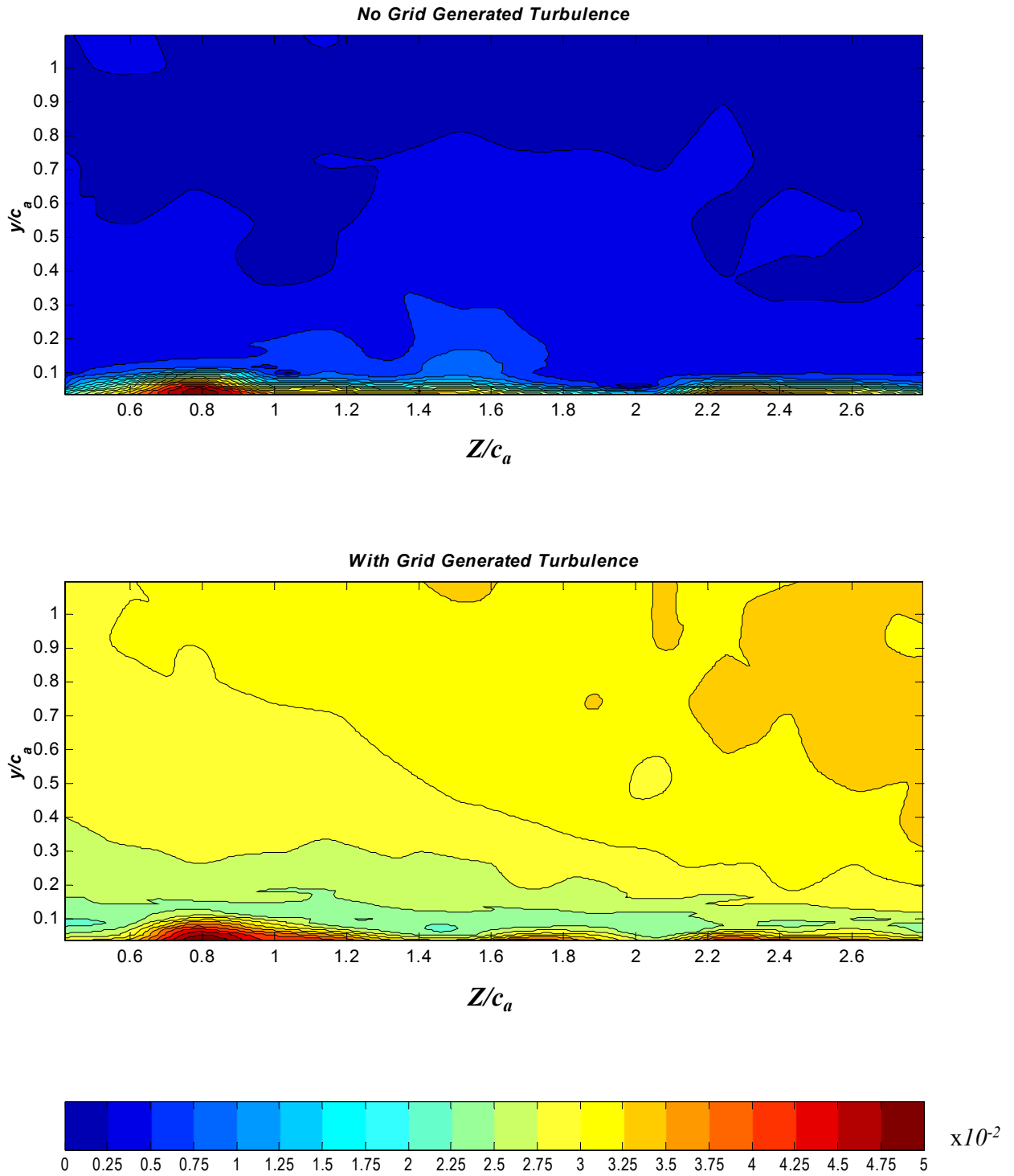


Figure 3.10 : Contours of, the square root of the Reynolds Normal Stress $\sqrt{(v^2/U_\infty^2)}$ at $X/c_a=-0.80$. Titles on plots indicate inflow turbulence condition

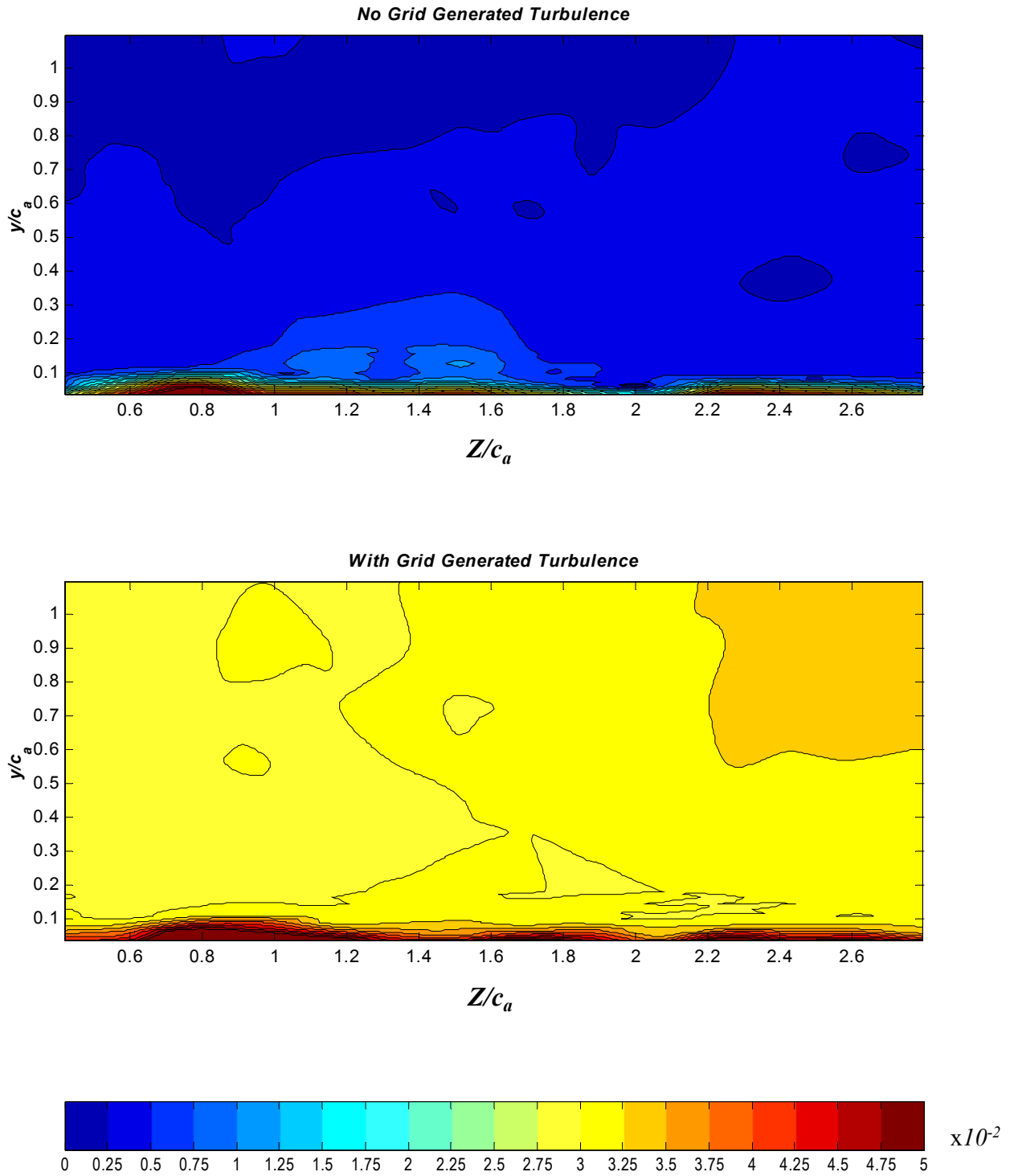


Figure 3.11 : Contours of the square root of the Reynolds Normal Stress $\sqrt{(w^2/U_\infty^2)}$ at $X/c_a = -0.80$. Titles on plots indicate inflow turbulence condition

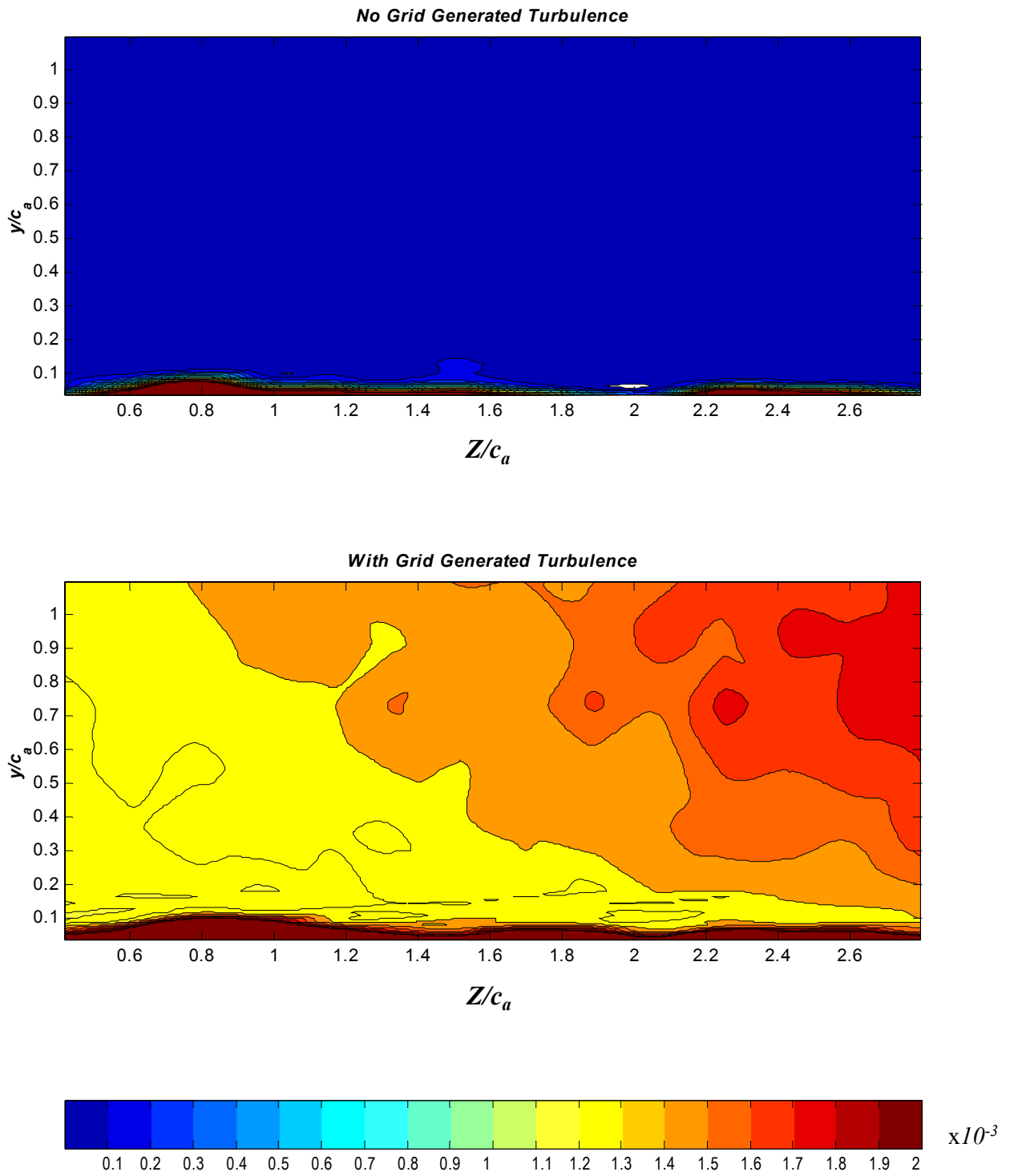


Figure 3.12 : Contours of the normalized turbulence kinetic energy, k/U_∞^2 , at $X/c_a = -0.80$. Titles on plots indicate inflow turbulence condition

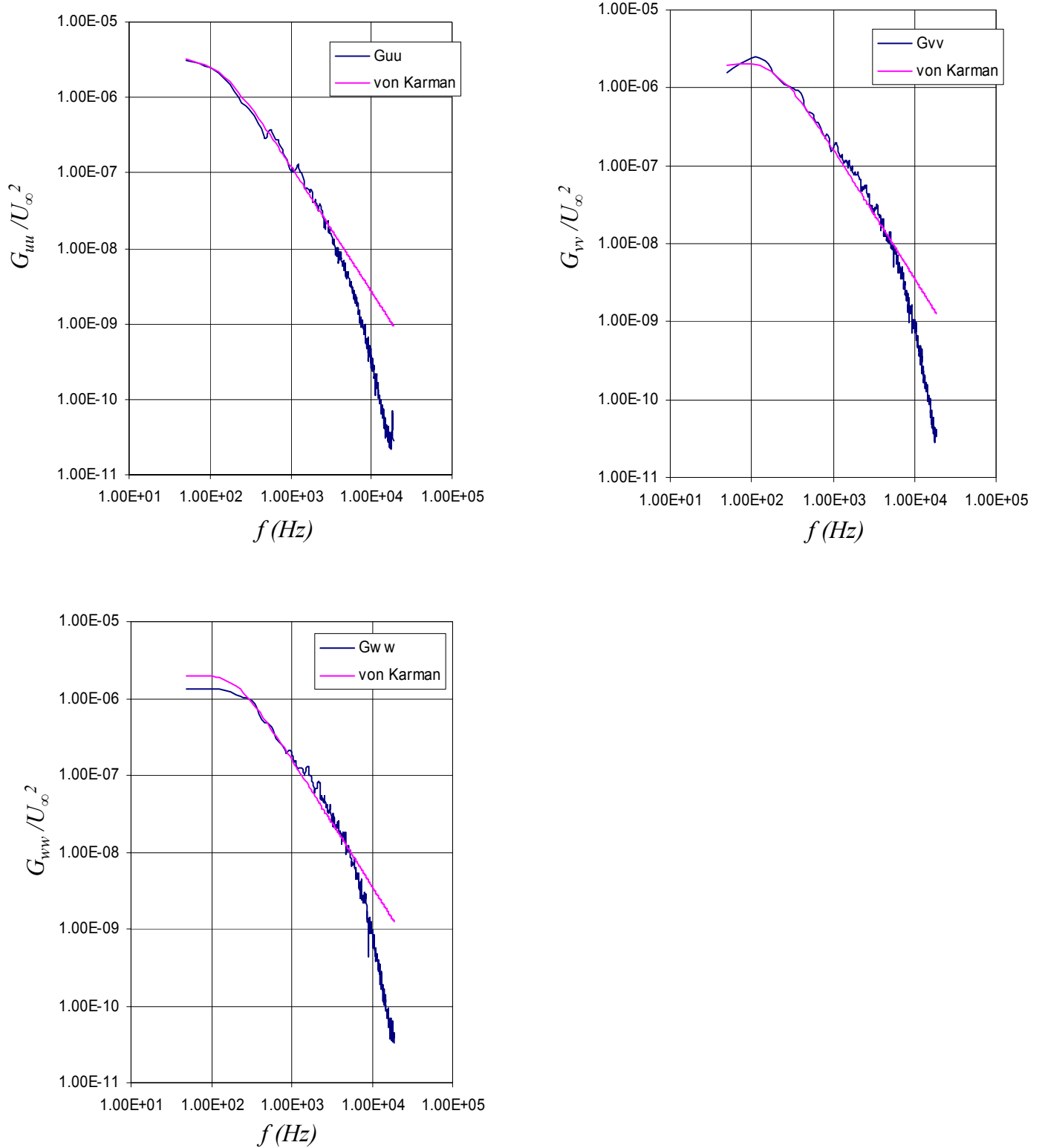


Figure 3.13a : Autospectra (as indicated by the legend on the plot) normalized on U_∞^2 for the case with grid generated turbulence at $X/c_a=0.80$. Also plotted are the von Karman interpolation formula for isotropic turbulence.

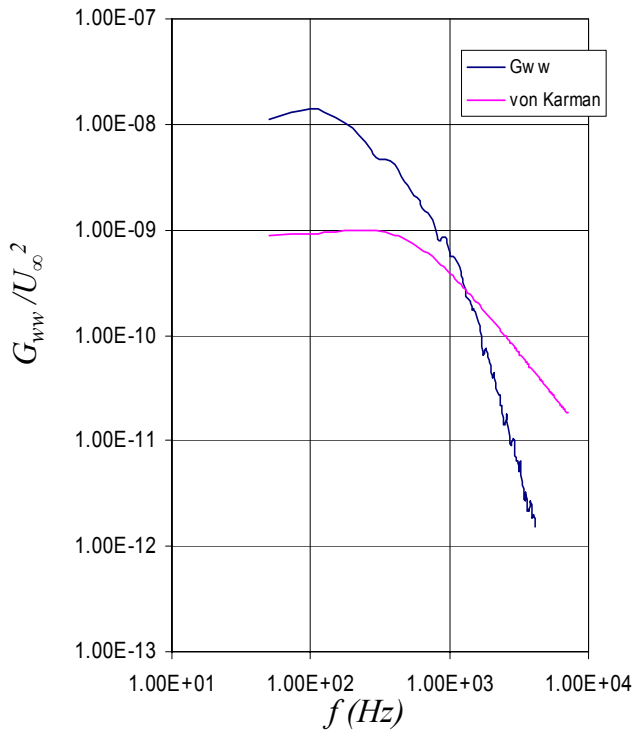
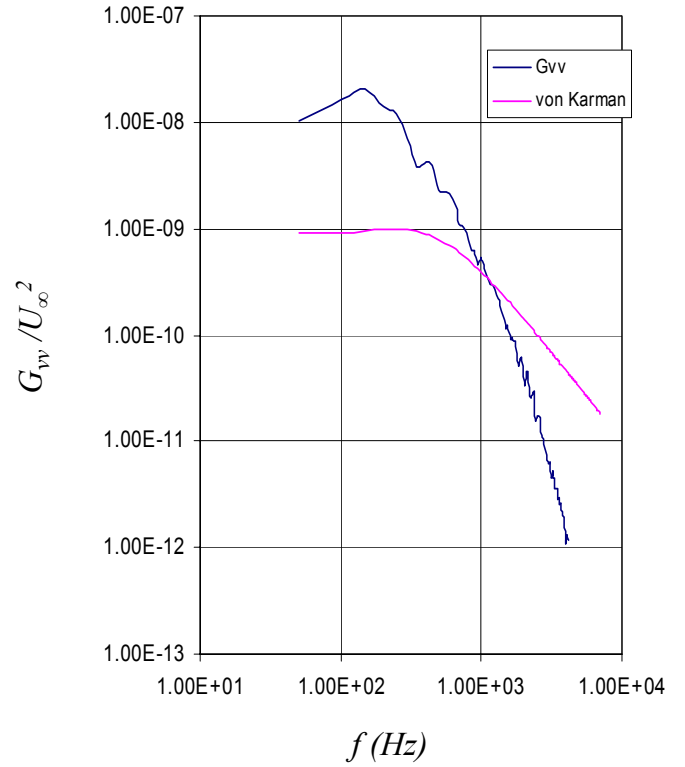
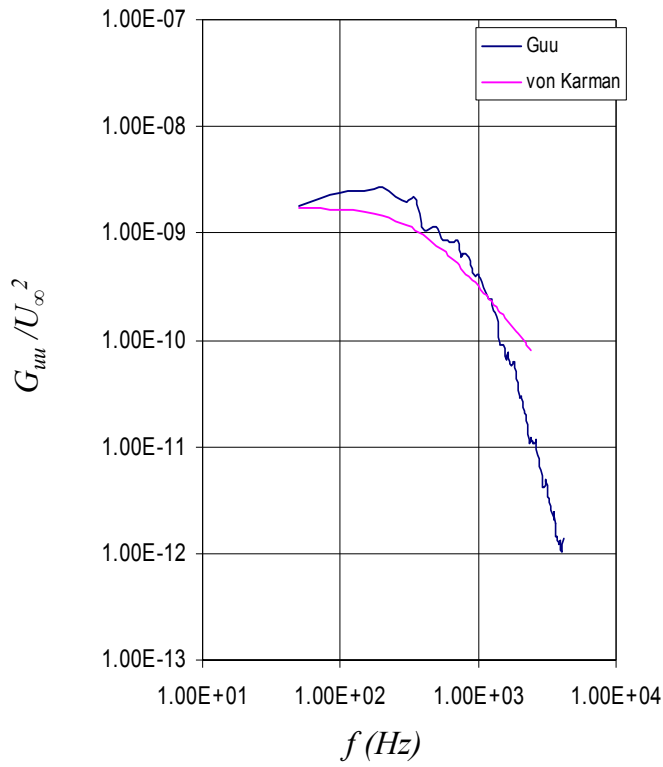


Figure 3.13b : Autospectra (as indicated by the legend on the plot) normalized on U_∞^2 for the case without grid generated turbulence at $X/c_a=0.80$. Also plotted are the von Karman interpolation formula for isotropic turbulence.

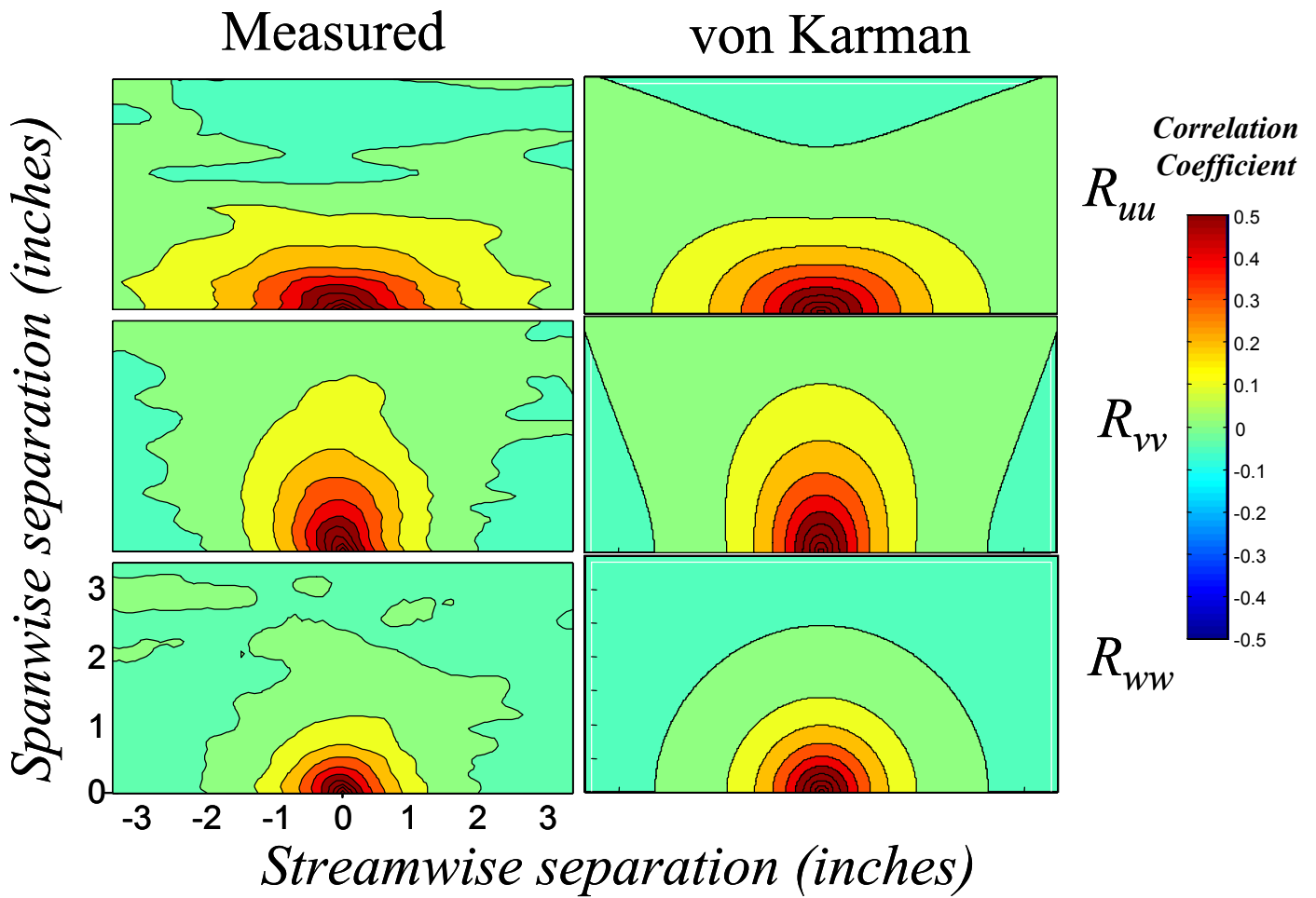


Figure 3.14 : Space Time correlations of the flow at the midheight of the passage at $Z/c_a = -1.7$, and $X/c_a = -0.80$. Shown on the plots are the comparisons with the experimental and von Karman interpolation formulae, showing the turbulence is isotropic. Streamwise separation inferred from Taylor's Hypothesis

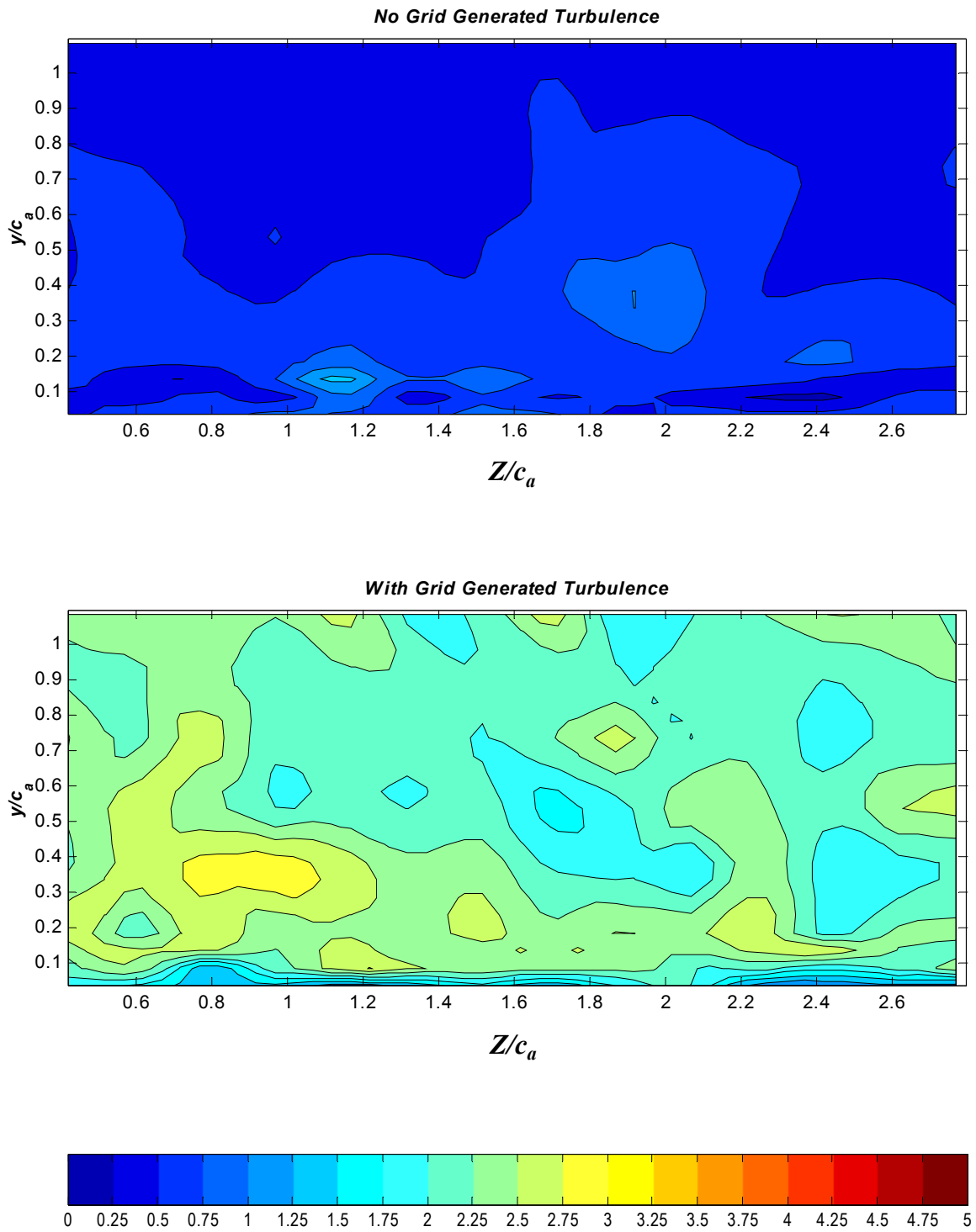


Figure 3.15 : Contours of the lengthscale λ_u (cm) at $X/c_a = -0.80$. Titles on plots indicate inflow turbulence condition

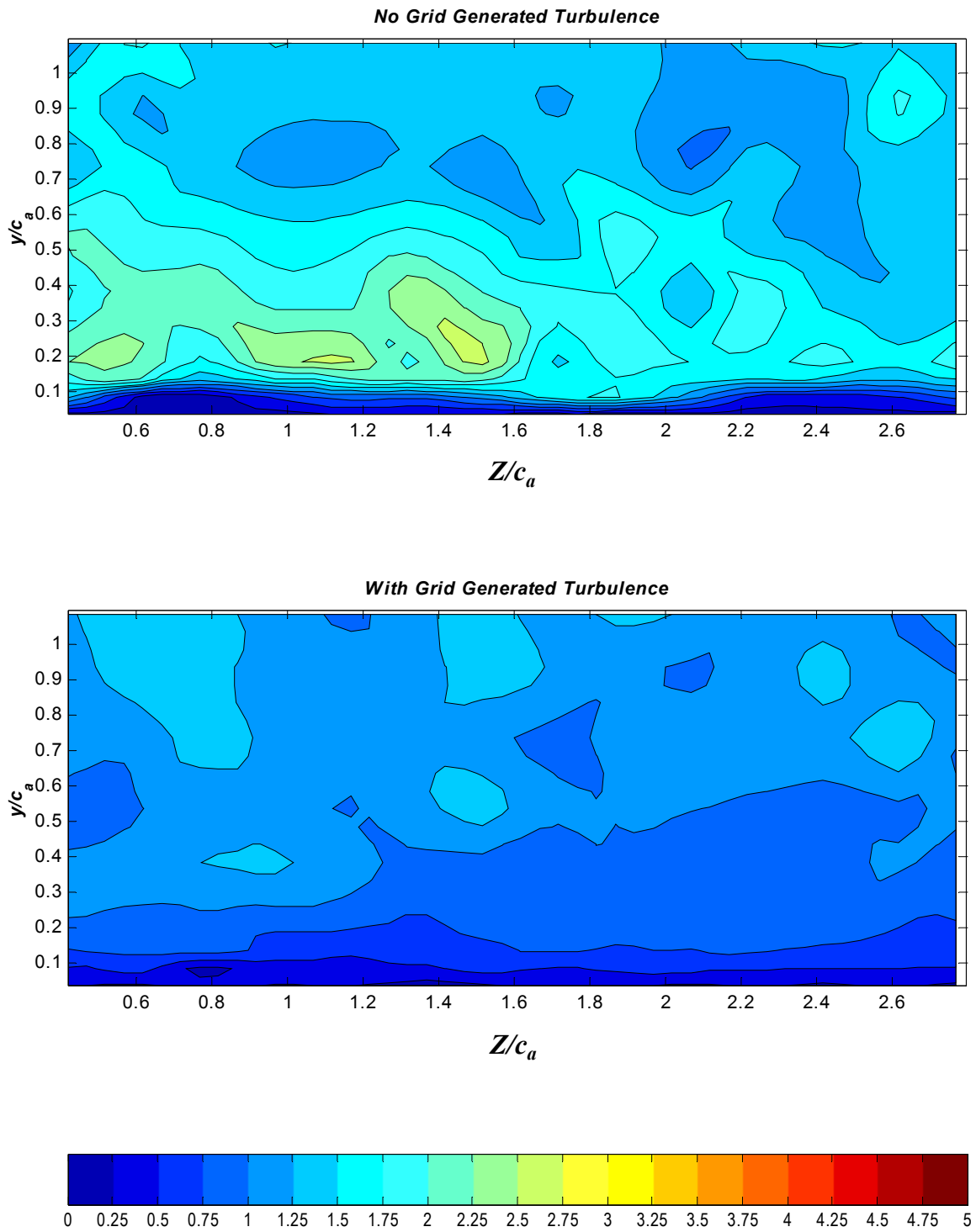


Figure 3.16 : Contours of the lengthscale λ_v (cm) at $X/c_a = -0.80$. Titles on plots indicate inflow turbulence condition

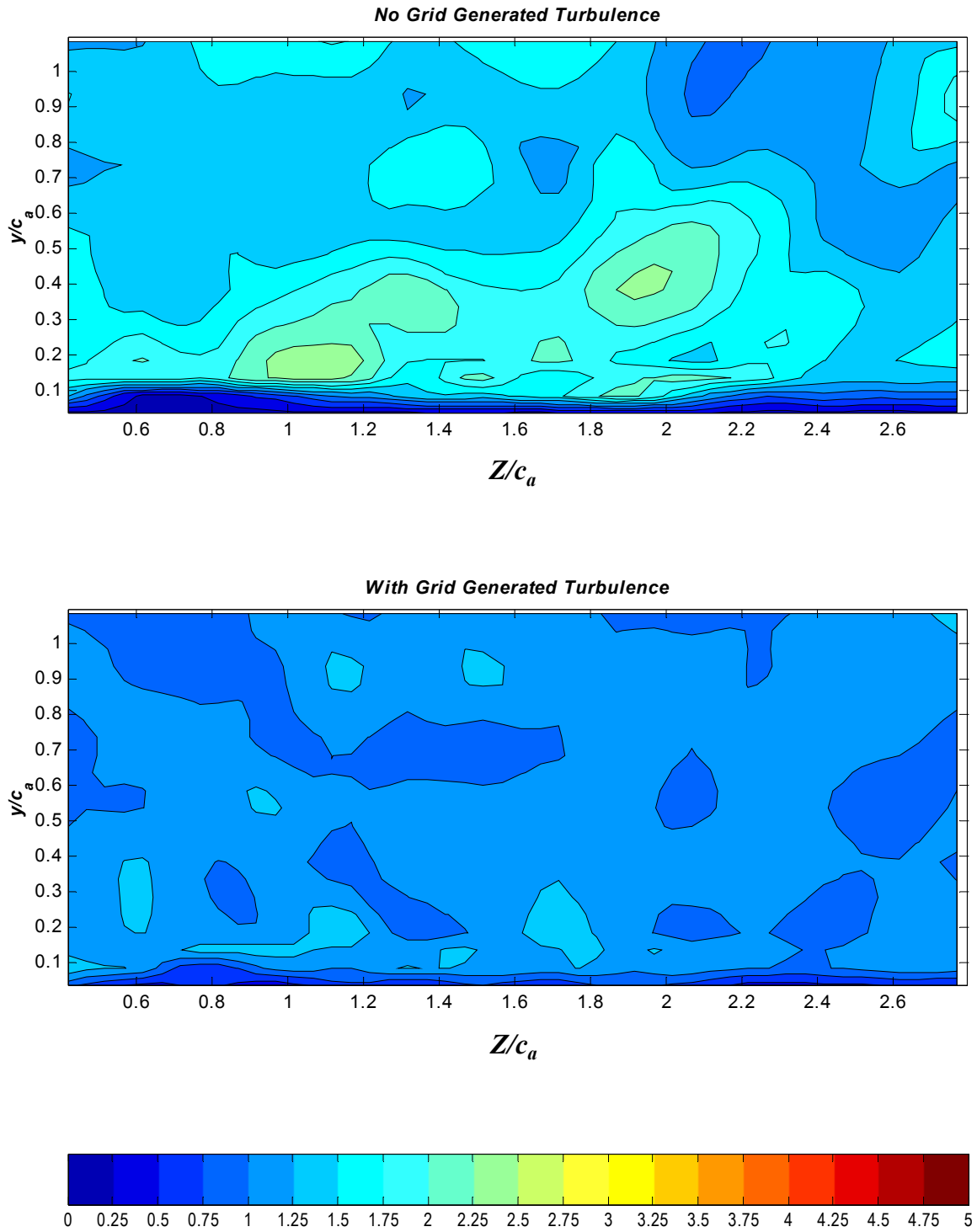


Figure 3.17 : Contours of the lengthscale λ_w (cm) at $X/c_a = -0.80$. Titles on plots indicate inflow turbulence condition

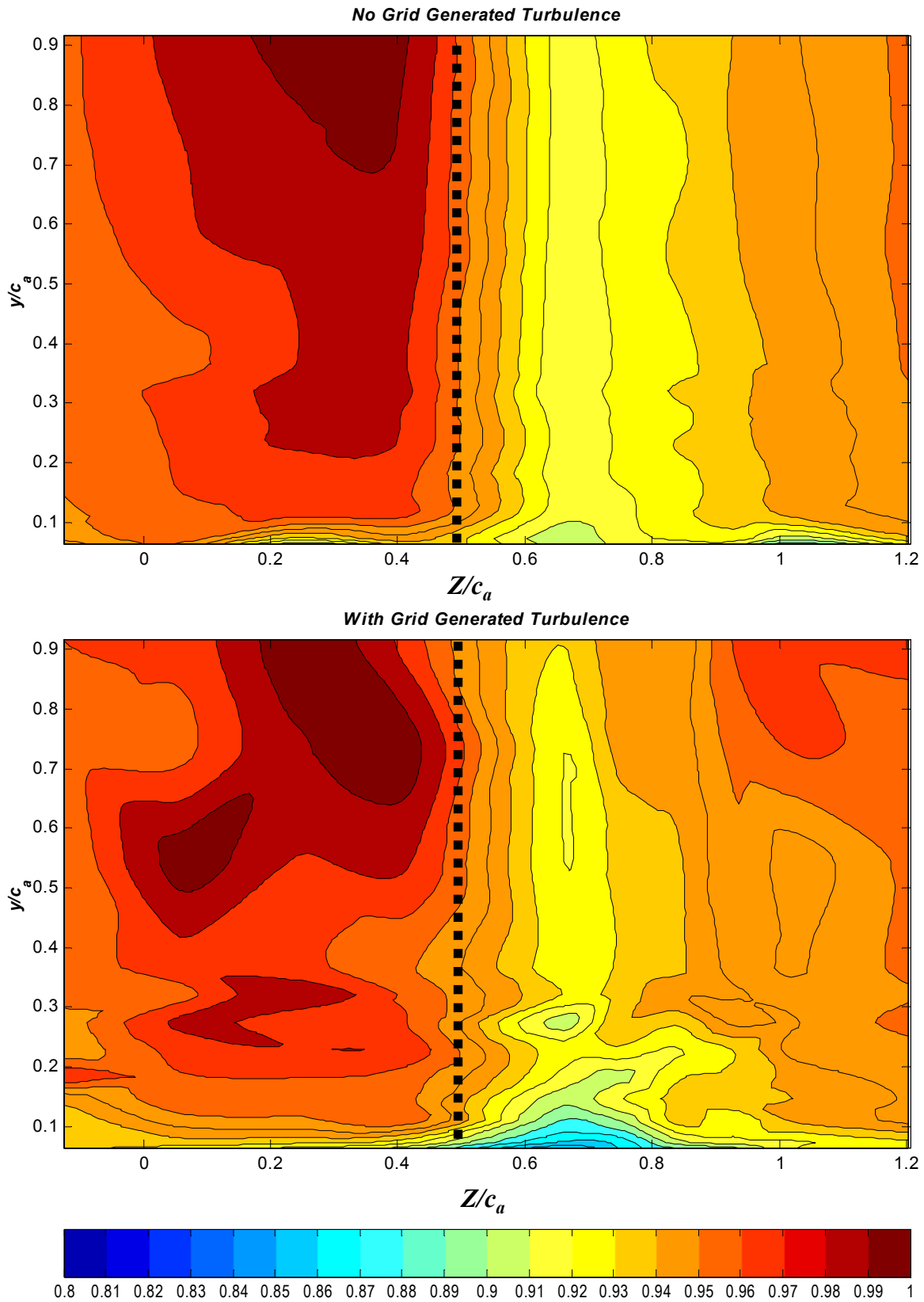


Figure 3.18 : Contours of Normalized Mean Streamwise Velocity, U/U_∞ at $X/c_a = -0.23$. The dashed line on the plots are the upstream projection of the origin of the axial-pitchwise co-ordinate system as defined in Figure 3.1. Titles on plots indicate inflow turbulence condition

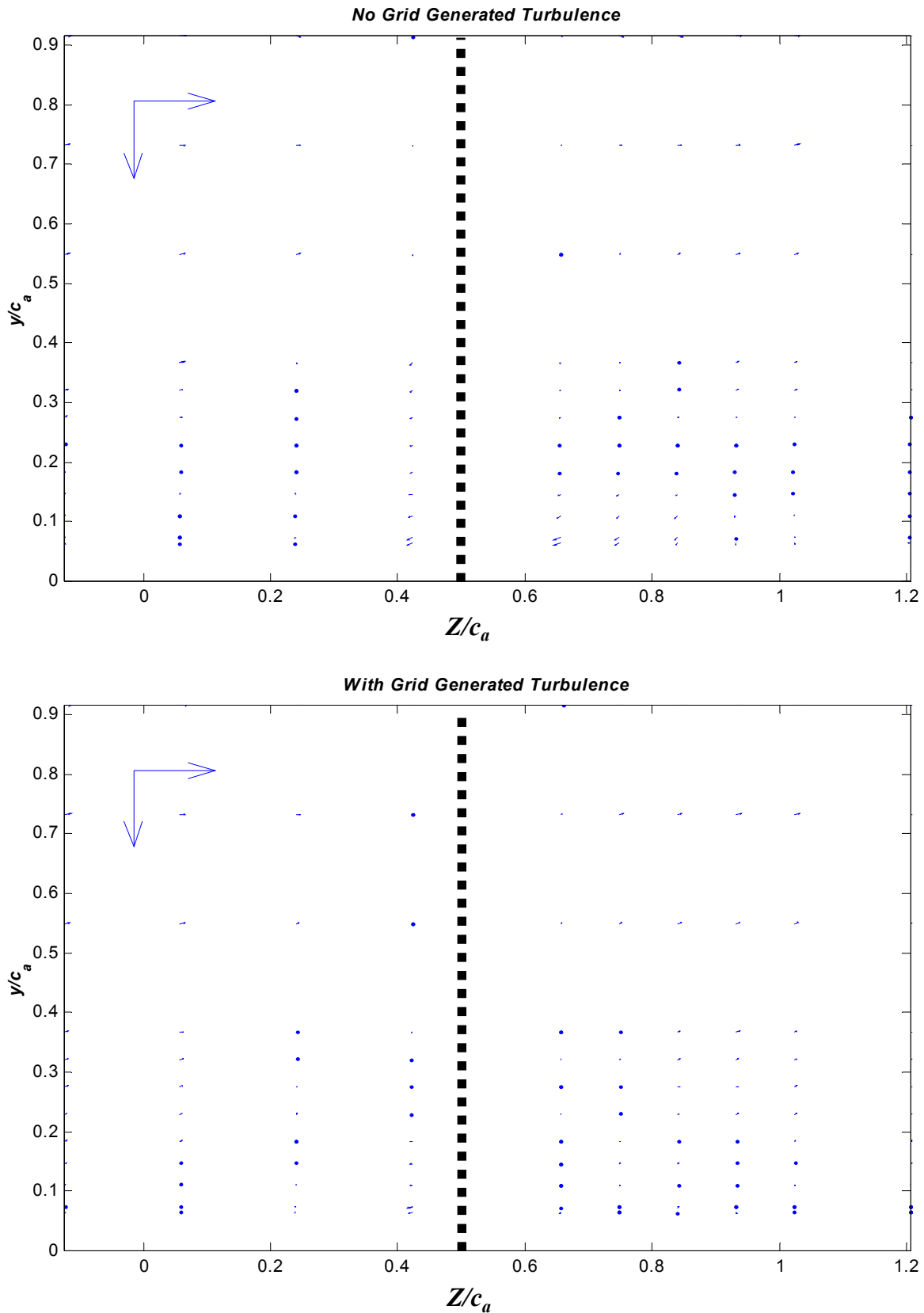


Figure 3.19 : Vectors of the magnitude of the mean normalized crossflow velocity (V , W) at $X/c_a = -0.23$. The dashed line on the plots are the upstream projection of the origin of the axial-pitchwise co-ordinate system as defined in Figure 3.1. Reference vectors of magnitude $0.5U_\infty$ in the y and z direction are given in the top left corner of each plot. Titles on plots indicate inflow turbulence condition

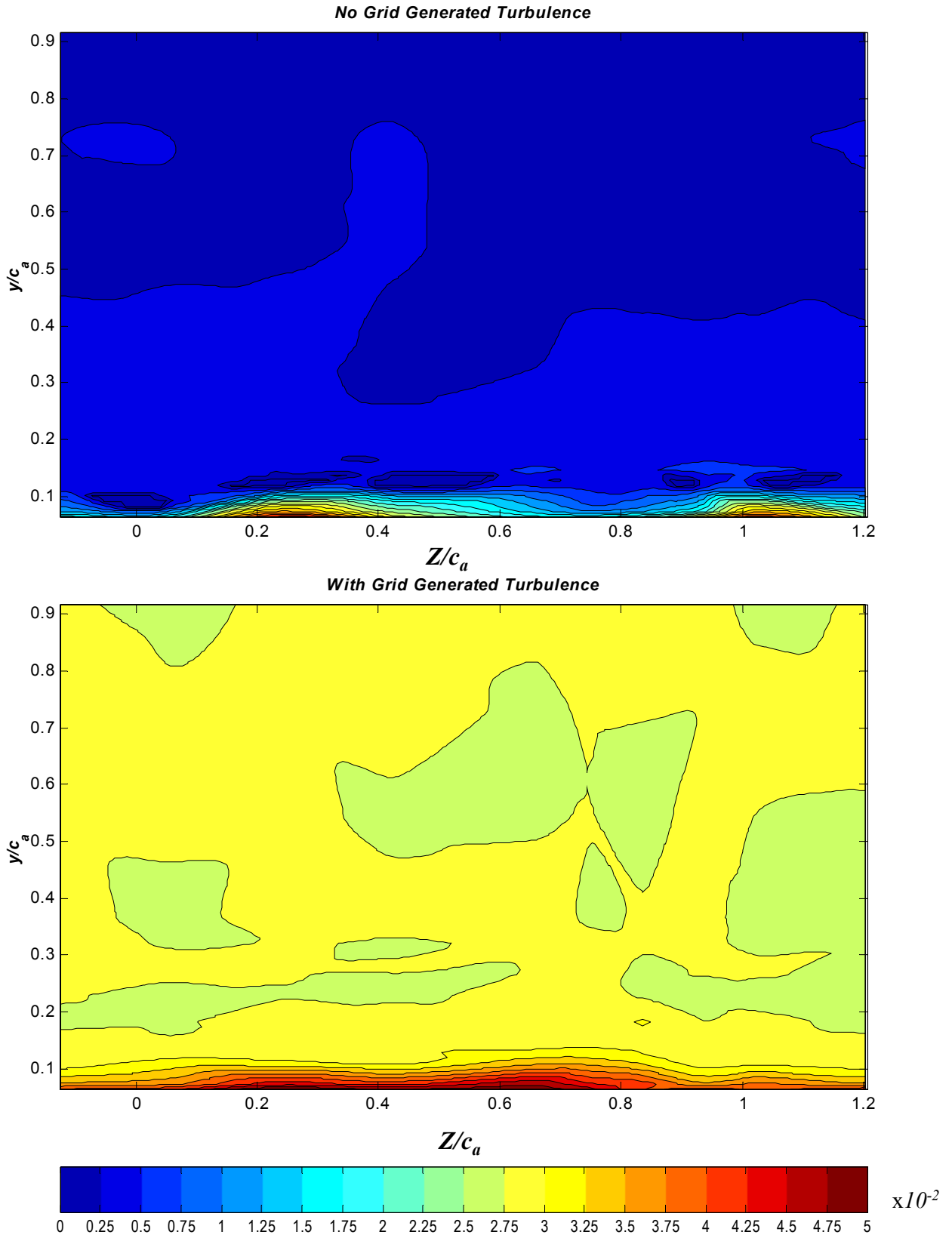


Figure 3.20 : Contours of the square root of the Reynolds Normal Stress $\sqrt{(u^2/U_\infty^2)}$ at $X/c_a = -0.23$. Titles on plots indicate inflow turbulence condition

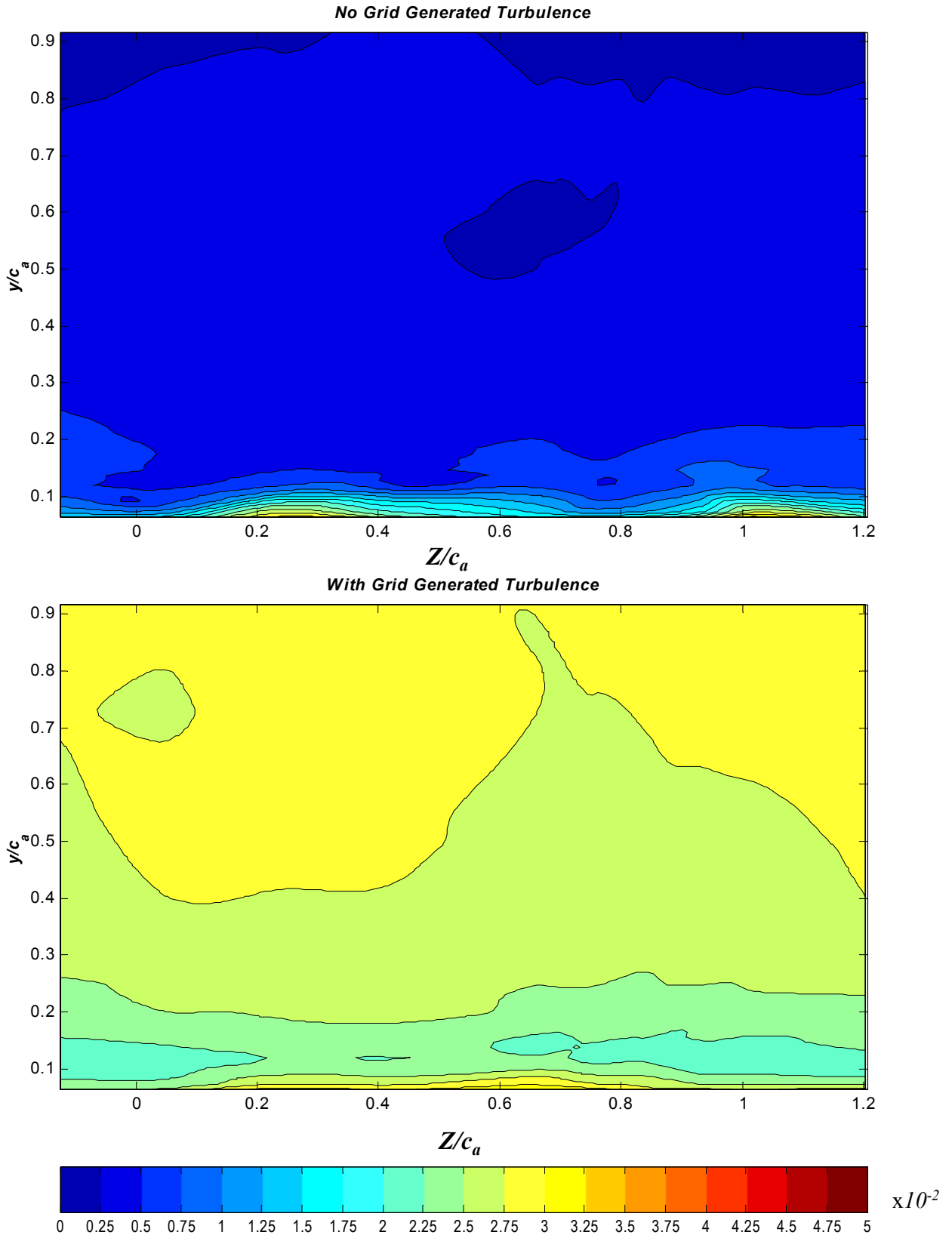


Figure 3.21 : Contours of the square root of the Reynolds Normal Stress $\sqrt{(v^2/U_\infty^2)}$ at $X/c_a = -0.23$. Titles on plots indicate inflow turbulence condition

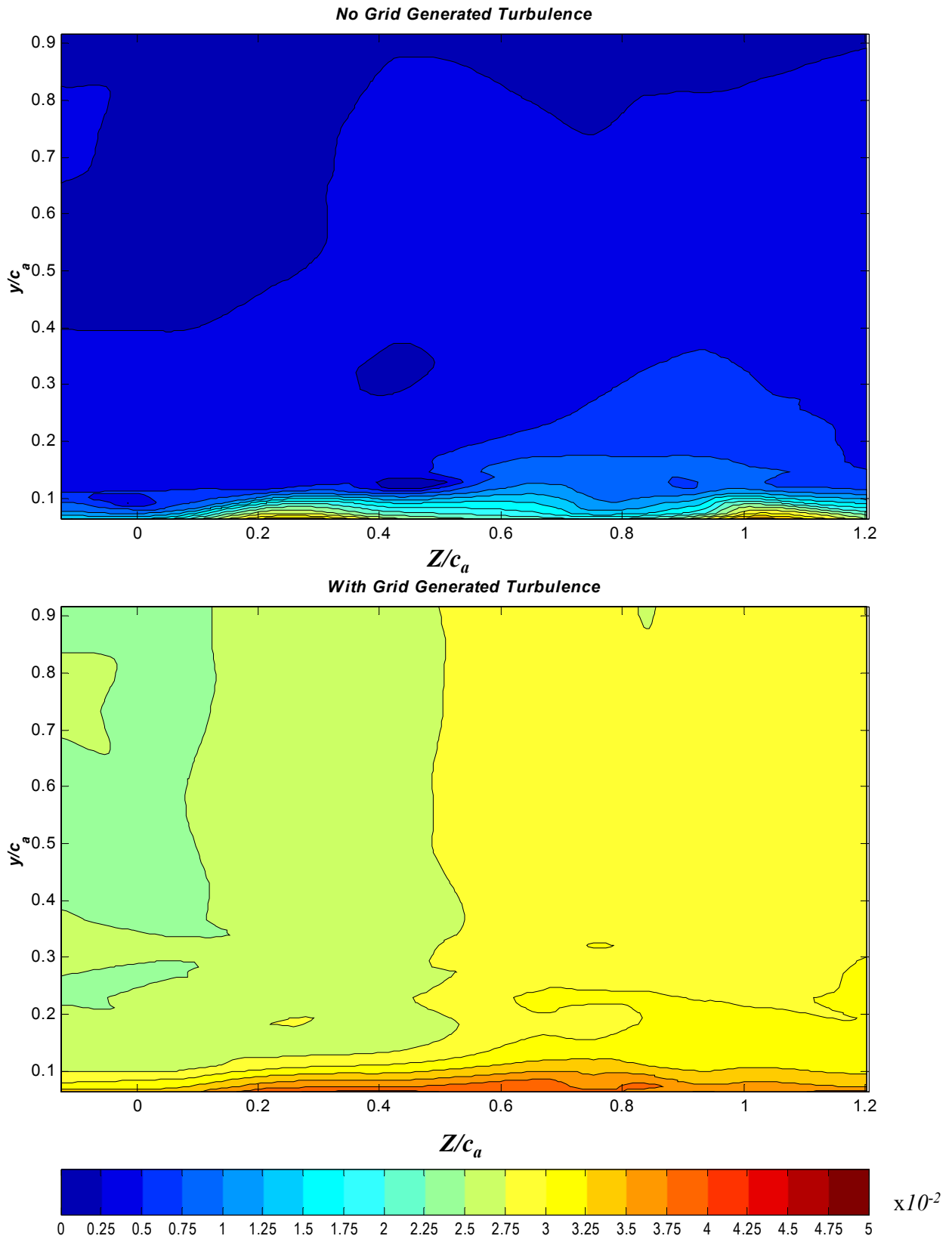


Figure 3.22 : Contours of the square root of the Reynolds Normal Stress $\sqrt{(w^2/U_\infty^2)}$ at $X/c_a = -0.23$. Titles on plots indicate inflow turbulence condition

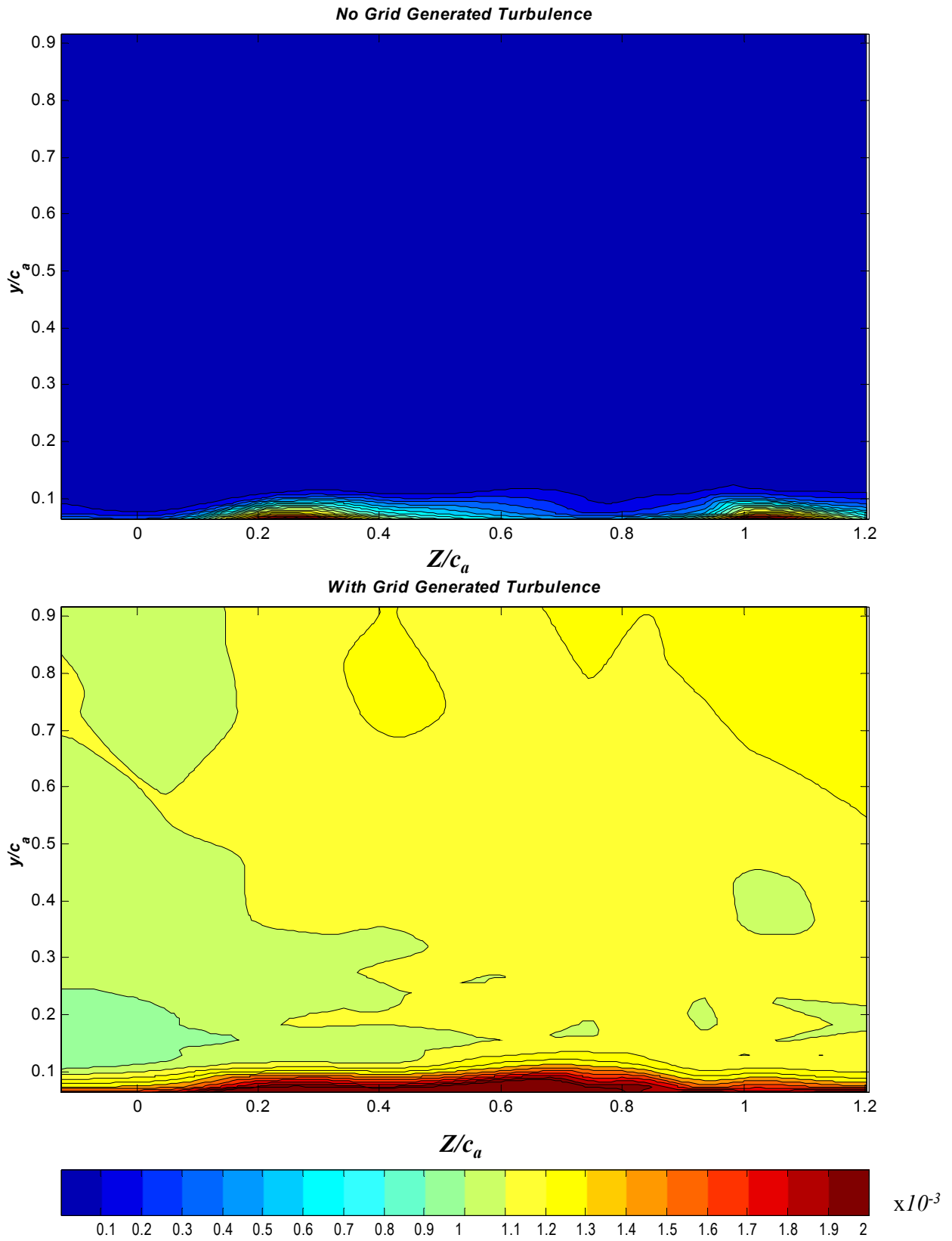


Figure 3.23 : Contours of the normalized turbulence kinetic energy, k/U_∞^2 , at $X/c_a = -0.23$. Titles on plots indicate inflow turbulence condition

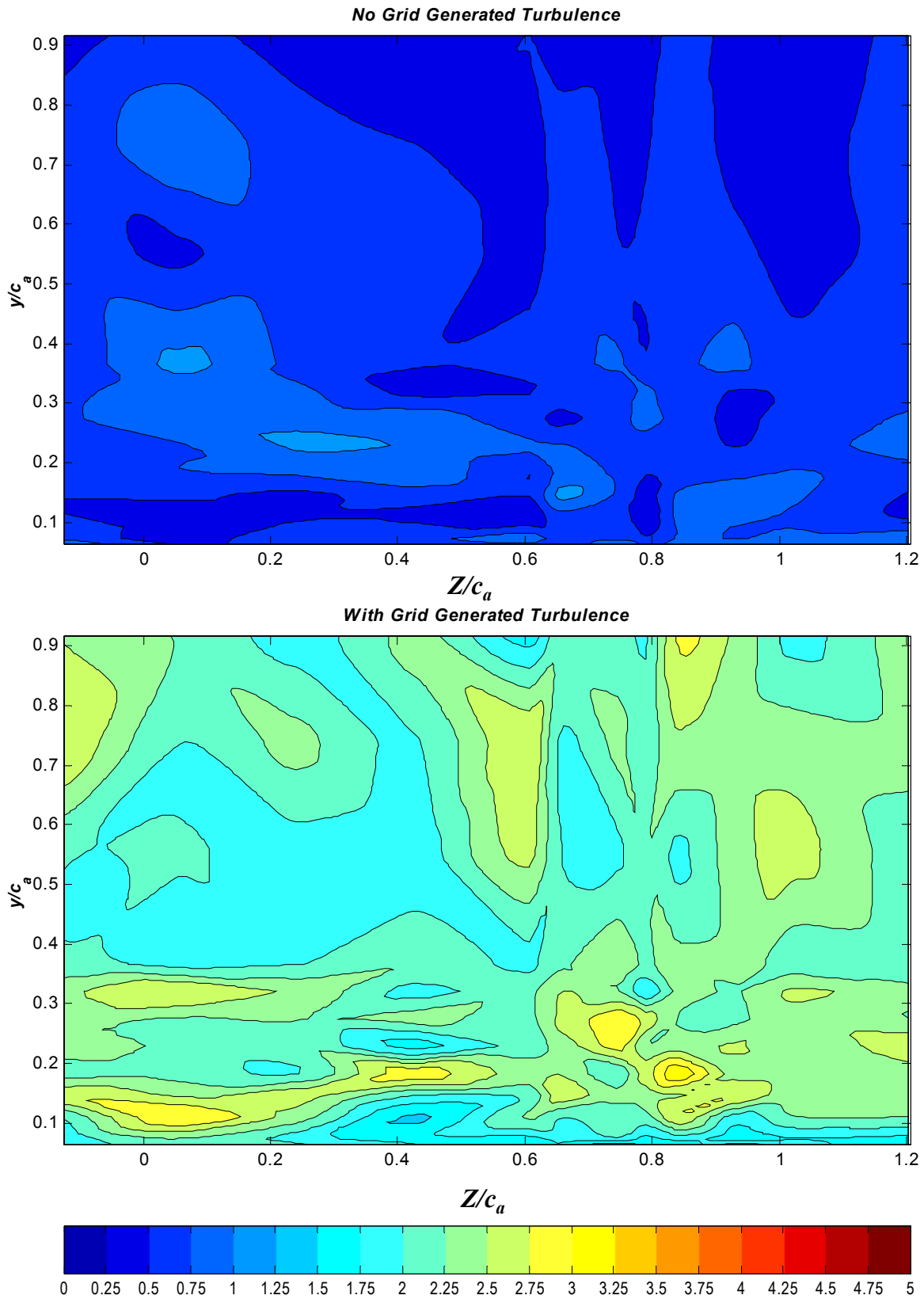


Figure 3.24 : Contours of lengthscale λ_u (cm) at $X/c_a = -0.23$. Titles on plots indicate inflow turbulence condition

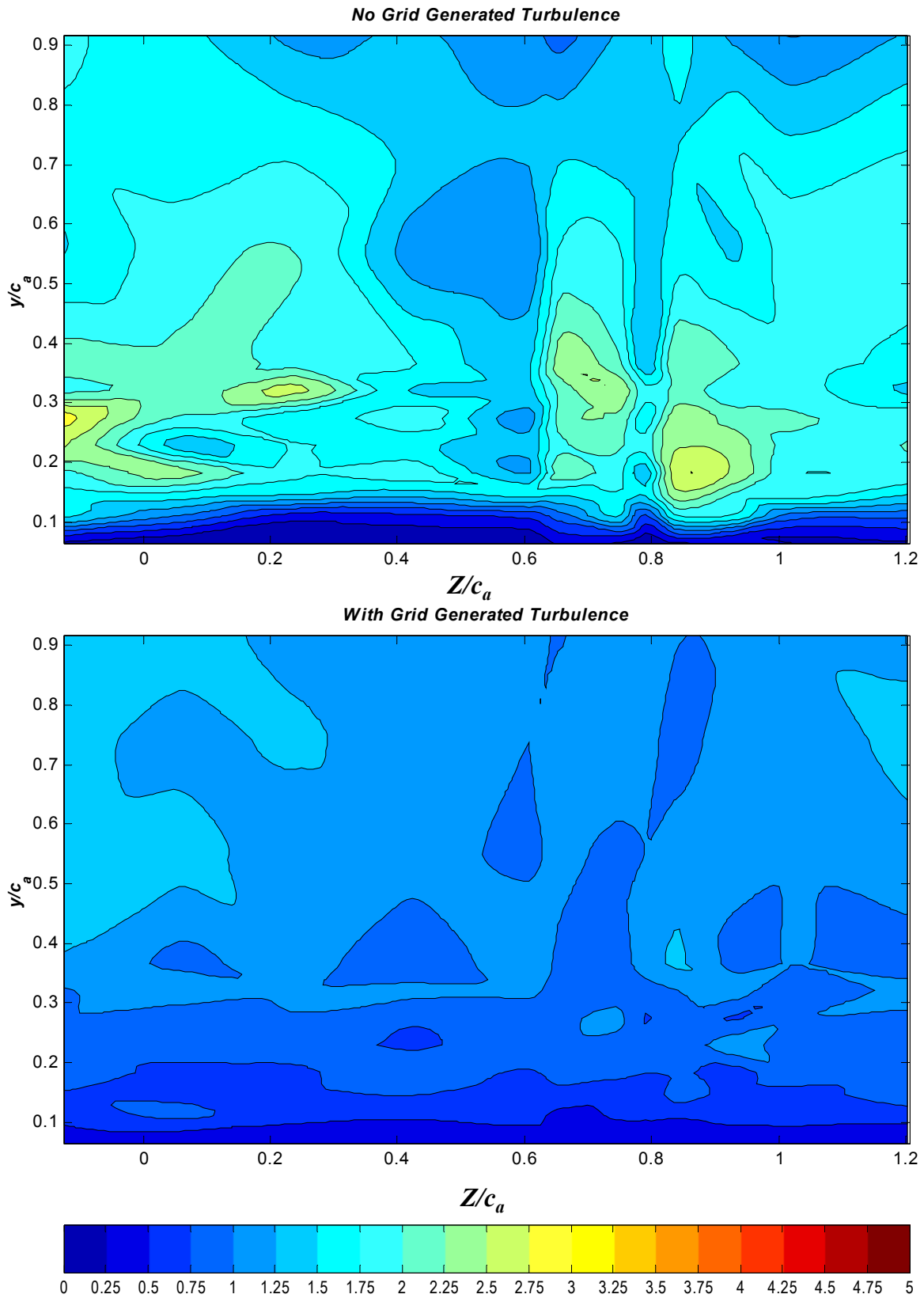


Figure 3.25 : Contours of lengthscale λ_v (cm) at $X/c_a = -0.23$. Titles on plots indicate inflow turbulence condition

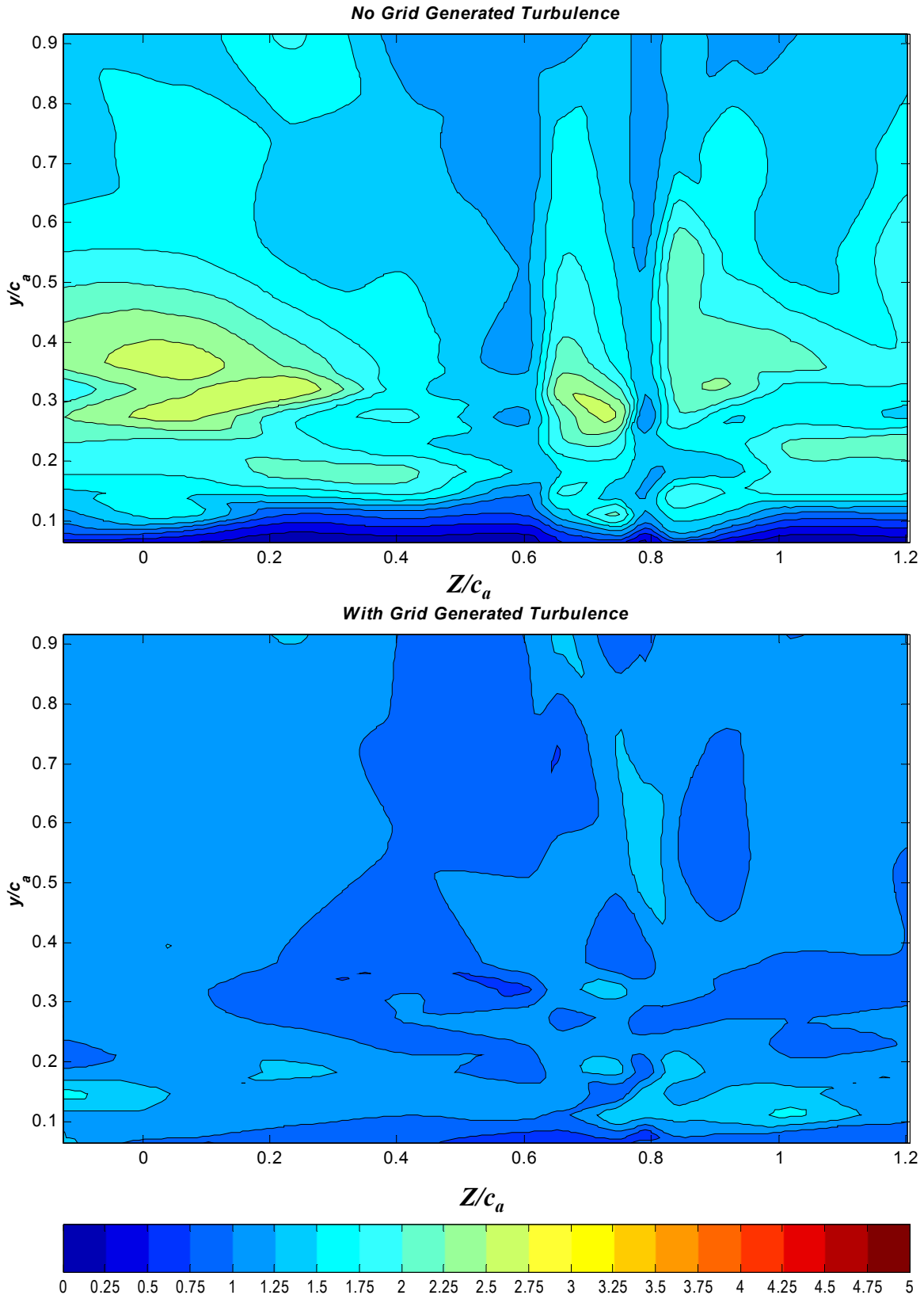


Figure 3.26 : Contours of lengthscale λ_w (cm) at $X/c_a = -0.23$. Titles on plots indicate inflow turbulence condition

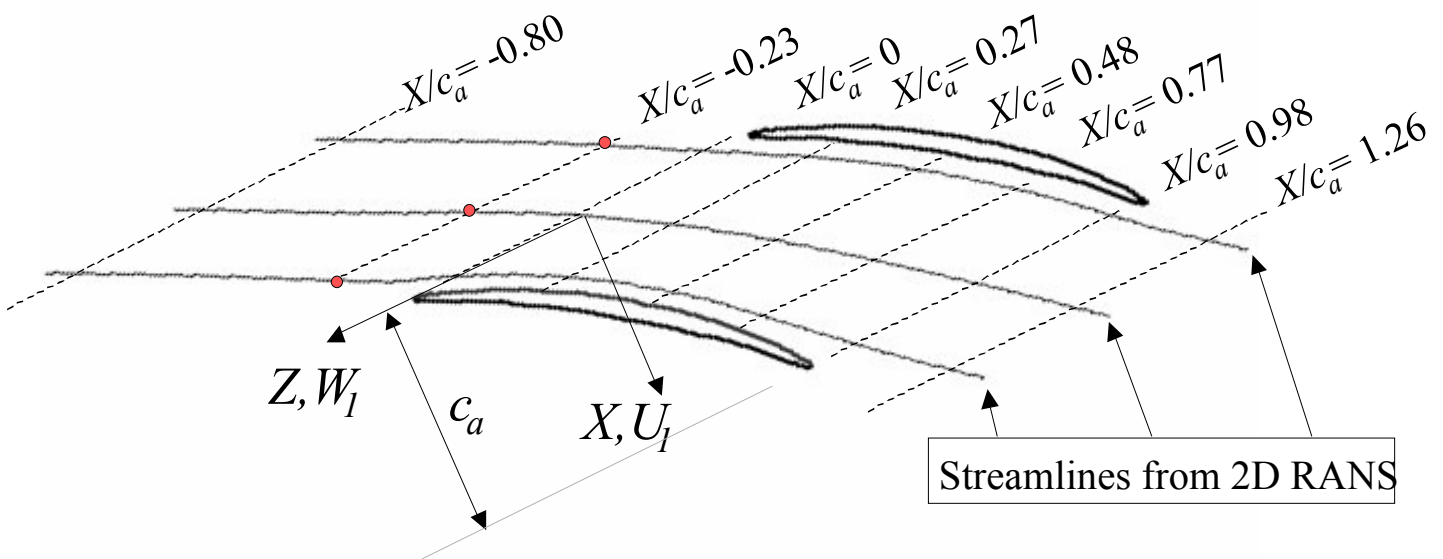


Figure 3.27: Figure showing locations of the boundary layer profiles indicated by the red points at $X/c_a = -0.23$. Z/c_a locations are -0.355 , 0.495 , and 1.345

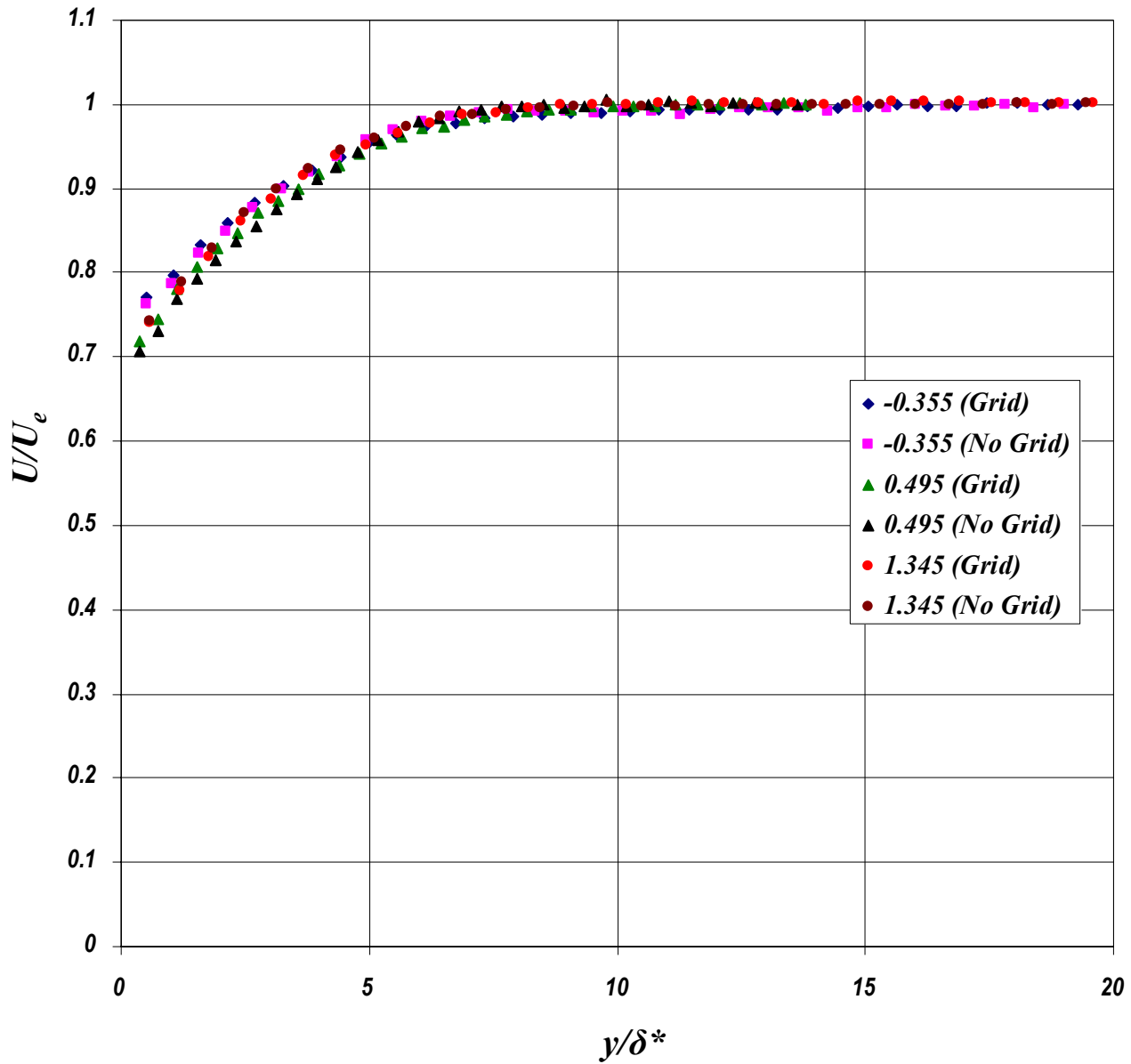


Figure 3.28: Boundary layer profiles of U/U_e vs y/δ^* at $X/c_a = -0.23$. Inflow Turbulence conditions and Z/c_a locations are indicated in the legend on the plot.

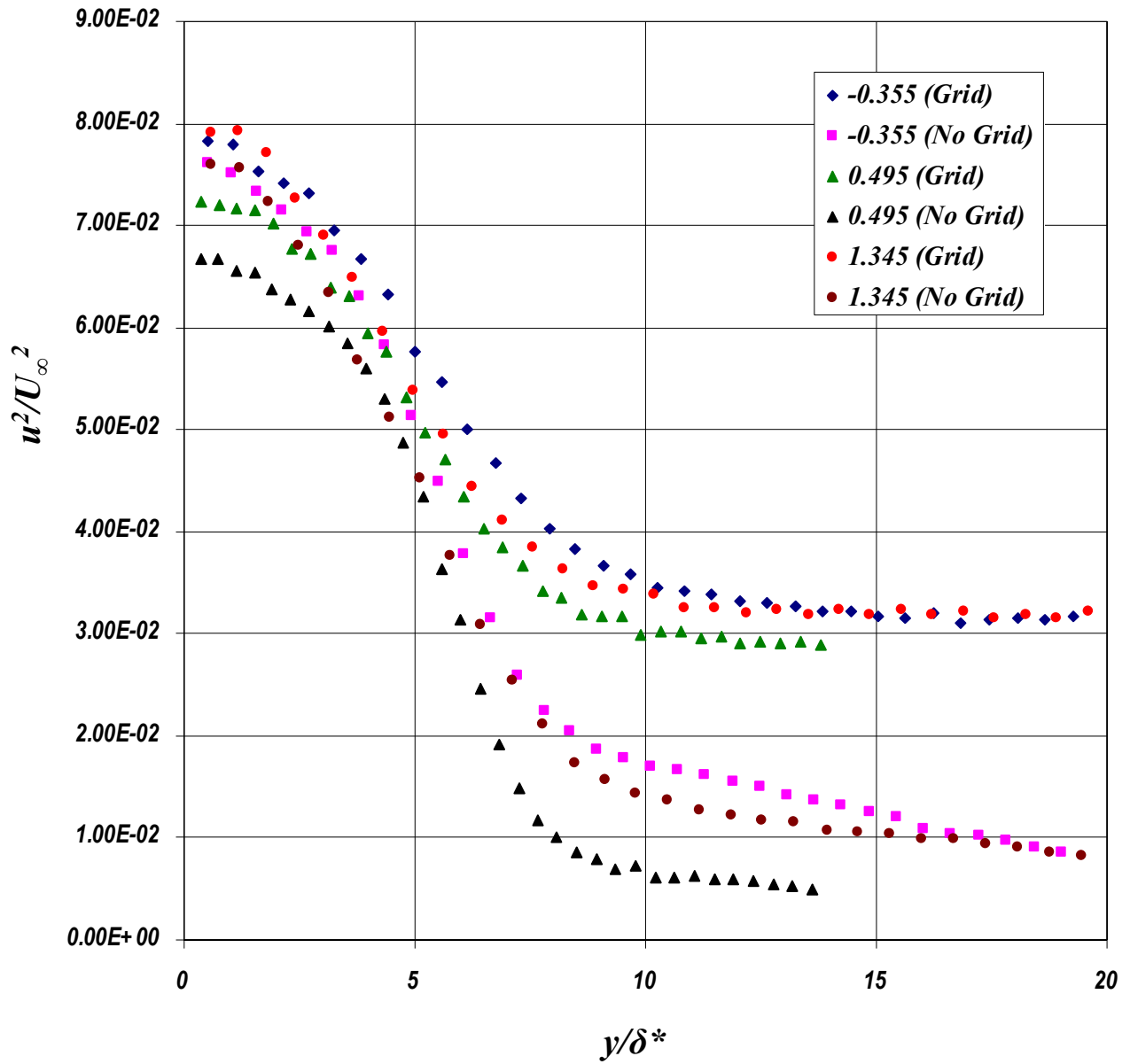


Figure 3.29: Boundary layer profiles of u^2/U_∞^2 vs y/δ^* at $X/c_a = -0.23$. Inflow Turbulence conditions and Z/c_a locations are indicated in the legend on the plot.

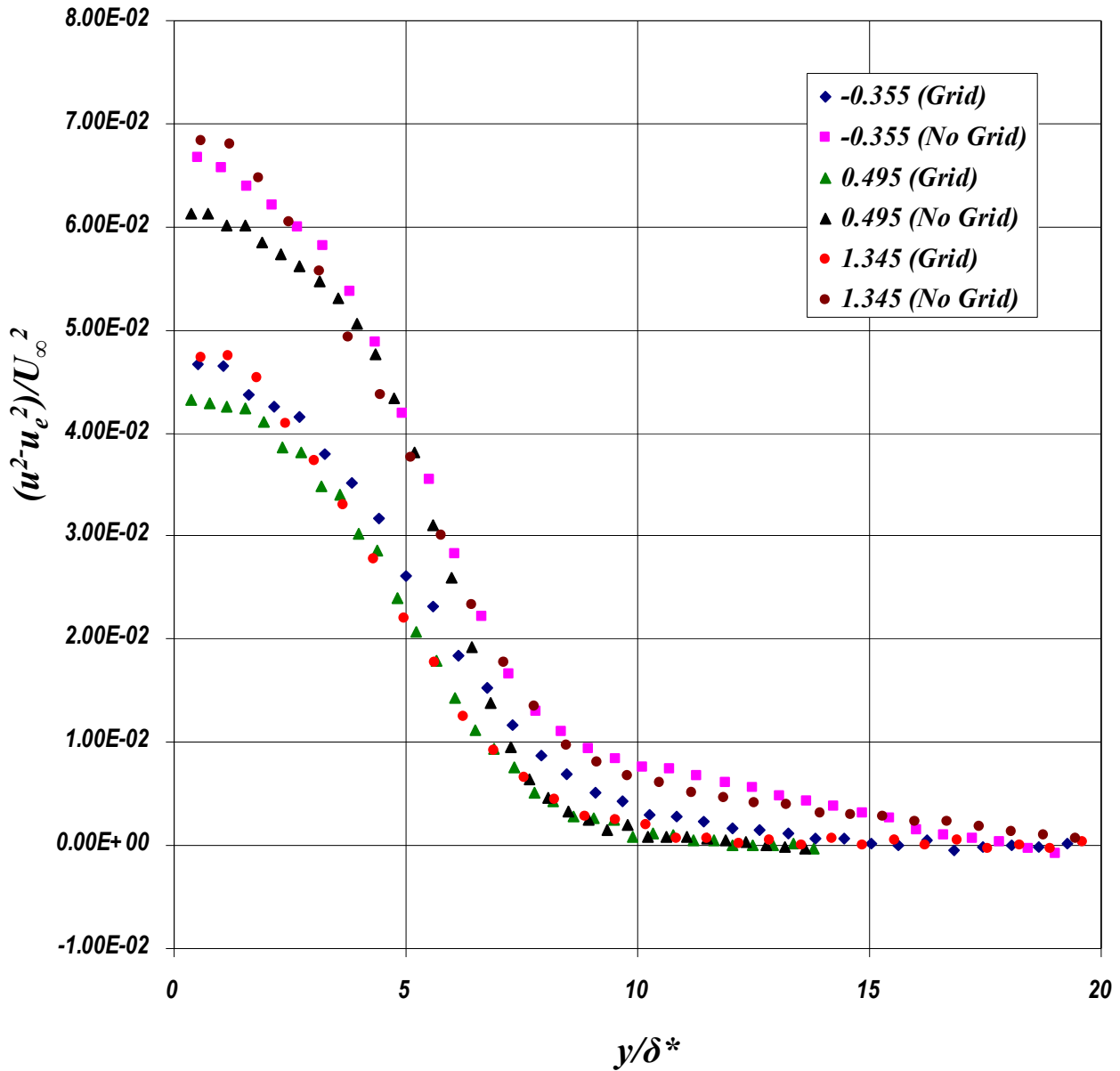


Figure 3.30: Boundary layer profiles of $(u^2 - u_e^2)/U_\infty^2$ vs y/δ^* at $X/c_a = -0.23$. Inflow Turbulence conditions and Z/c_a locations are indicated in the legend on the plot.

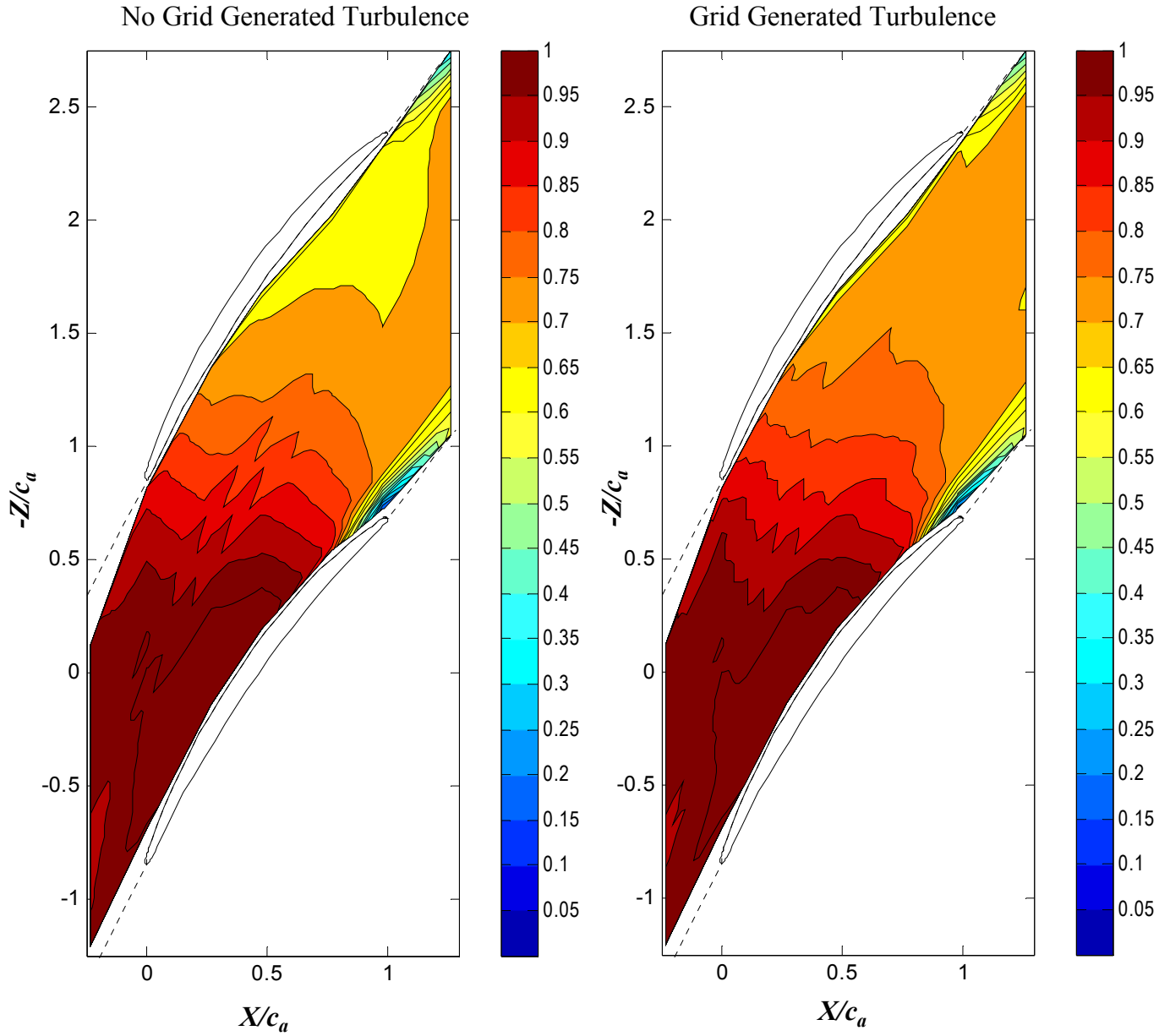


Figure 3.31: Plan view projection of the potential core flow at $y/c_a = 0.73$. Plotted here are the contours of the mean streamwise velocity, U/U_∞ .

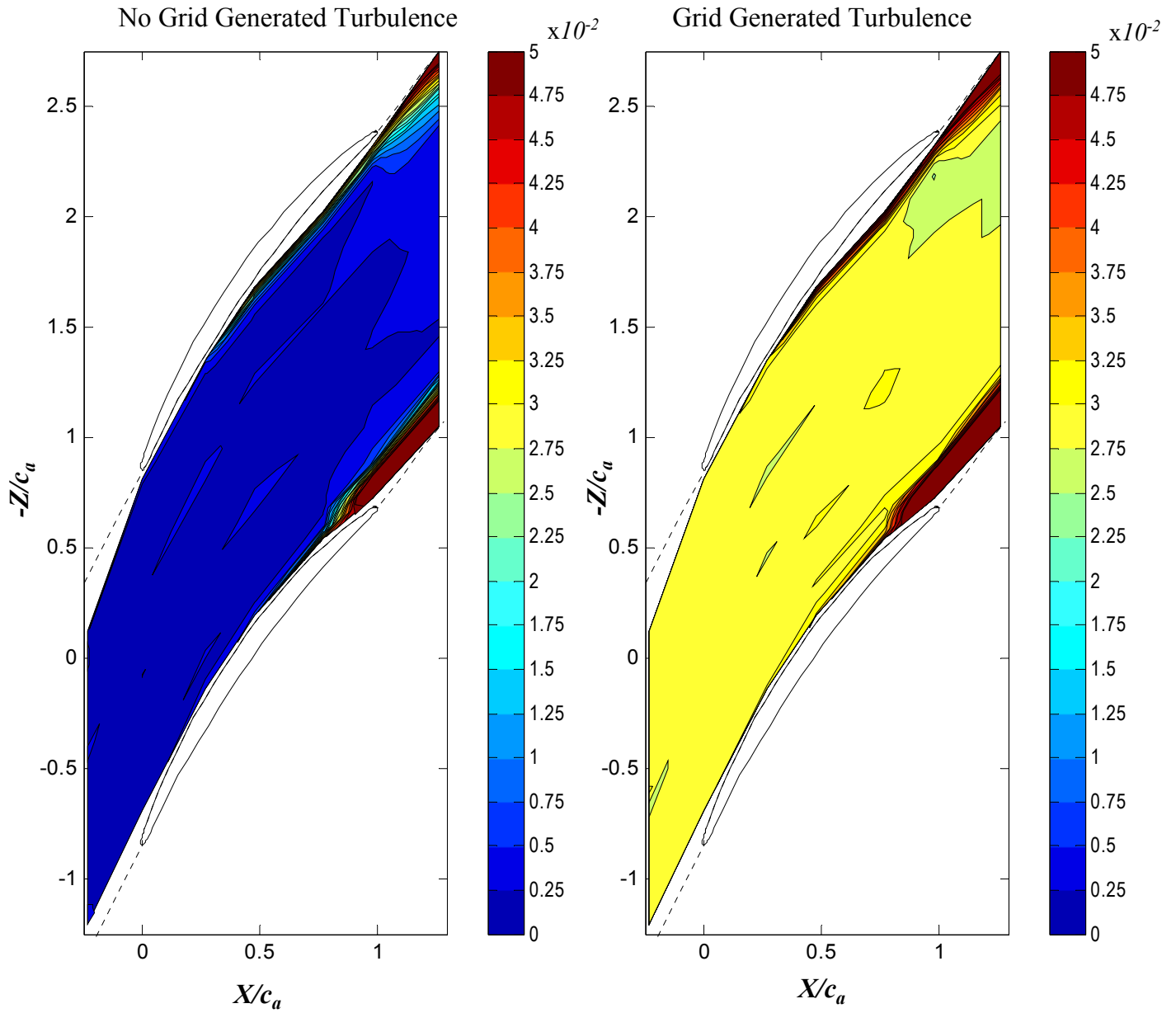


Figure 3.32: Plan view projection of the potential core flow at $y/c_a = 0.73$. Plotted here are the contours of the Reynolds Normal Stress $\sqrt{(u^2/U_\infty^2)}$

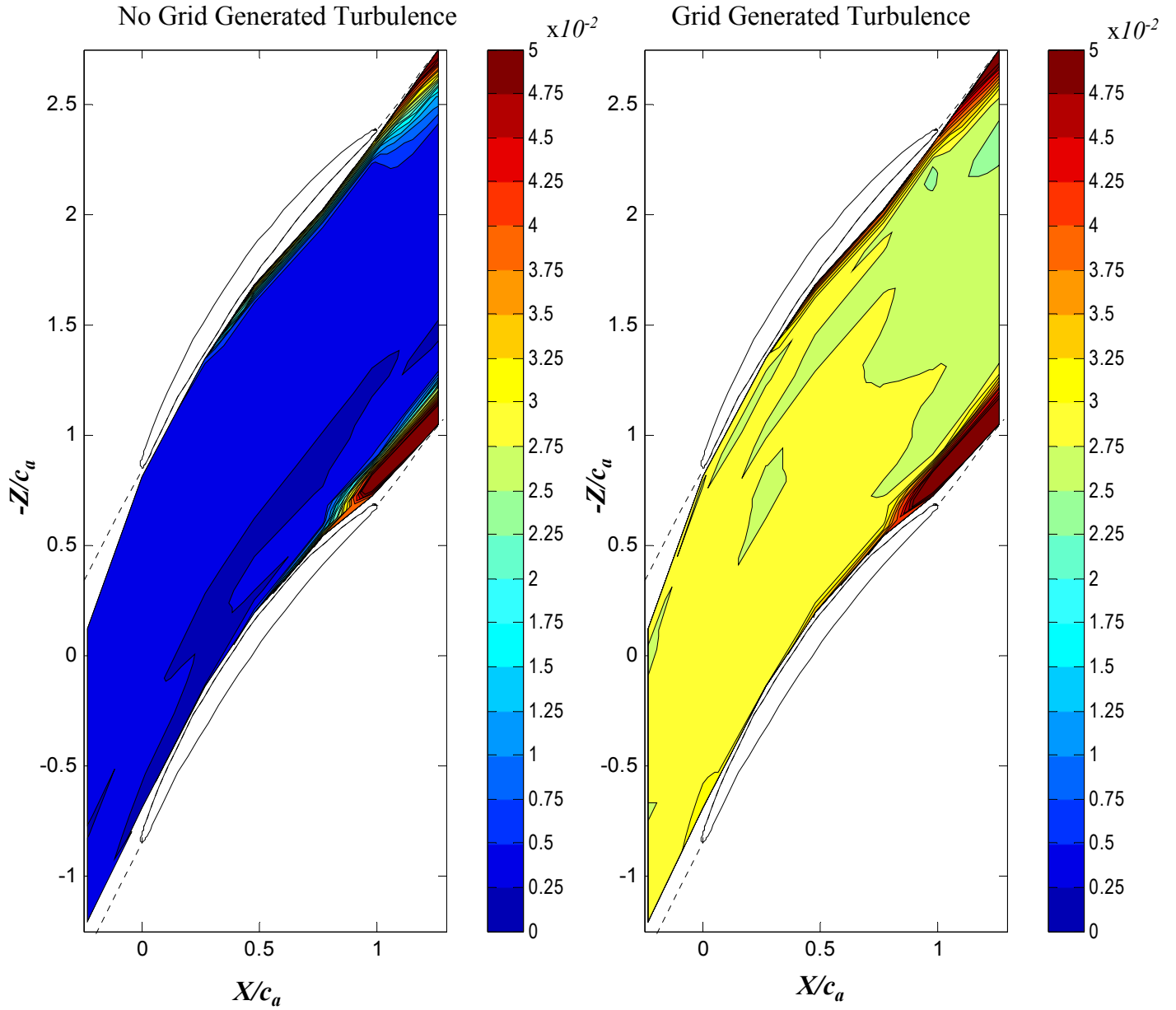


Figure 3.33: Plan view projection of the potential core flow at $y/c_a = 0.73$. Plotted here are the contours of the Reynolds Normal Stress $\sqrt{(v^2/U_\infty^2)}$

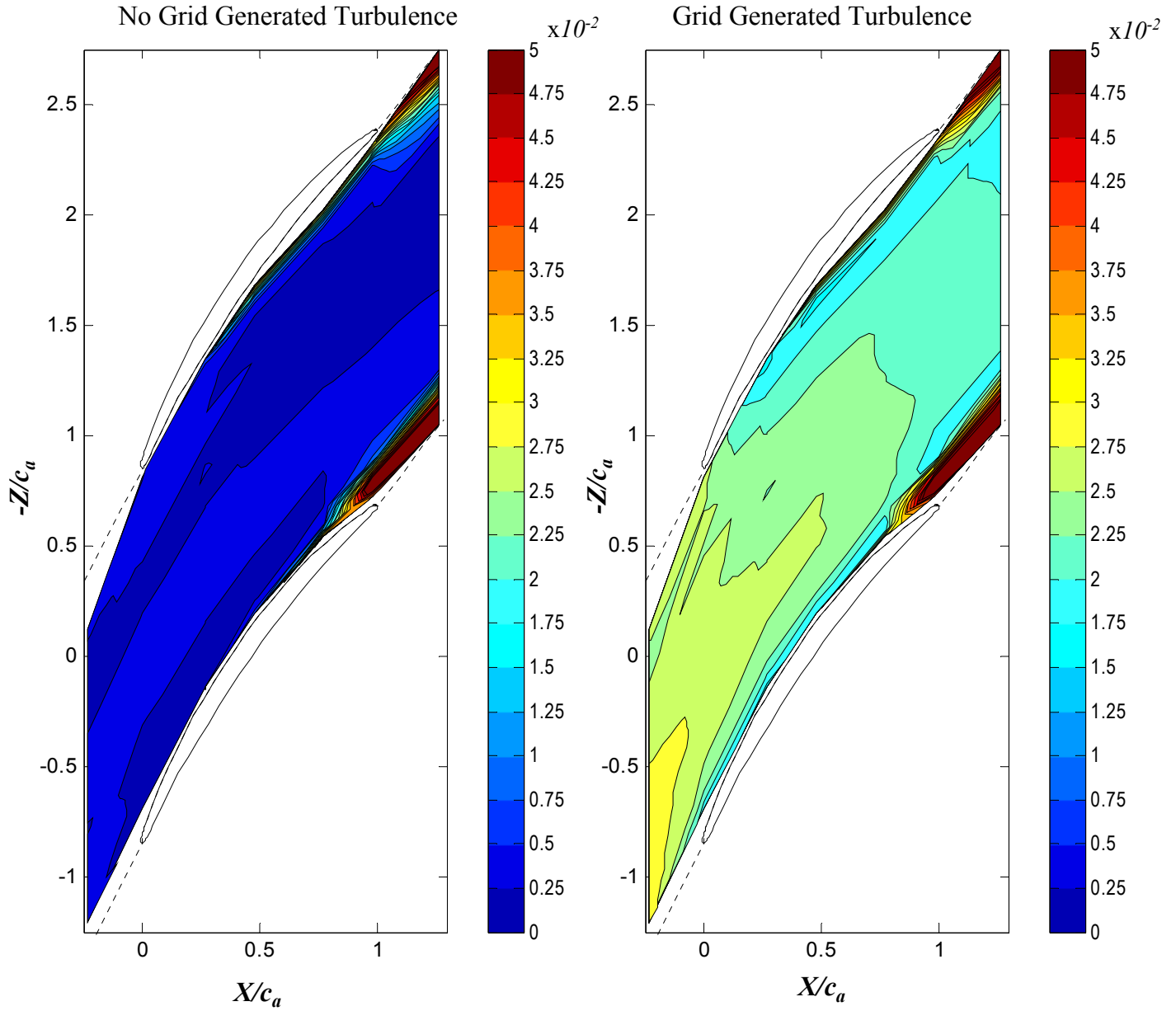


Figure 3.34: Plan view projection of the potential core flow at $y/c_a = 0.73$. Plotted here are the contours of the Reynolds Normal Stress $\sqrt{(w^2/U_\infty^2)}$

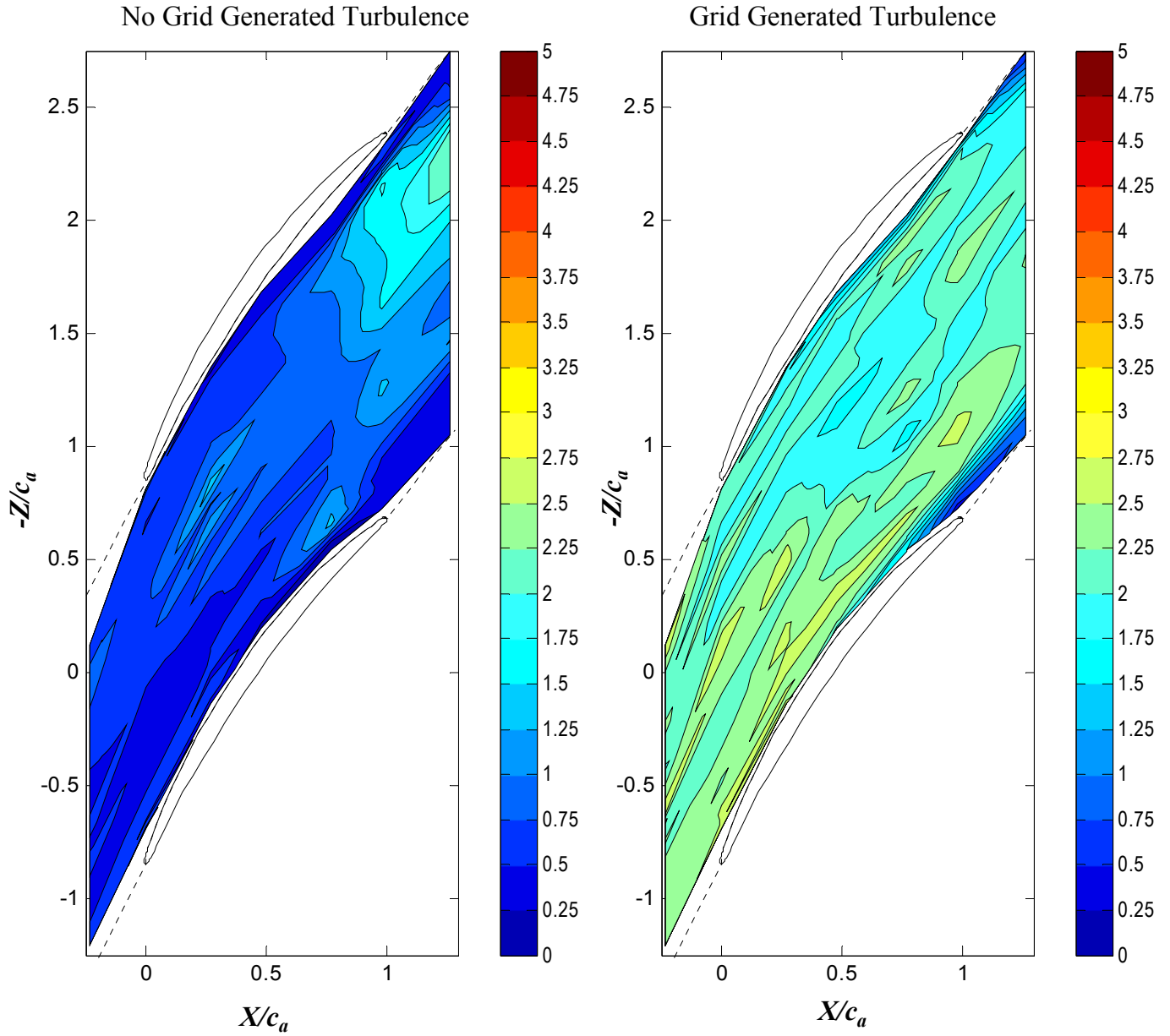


Figure 3.35: Plan view projection of the potential core flow at $y/c_a = 0.73$. Plotted here are the contours of the lengthscale, λ_u (cm)

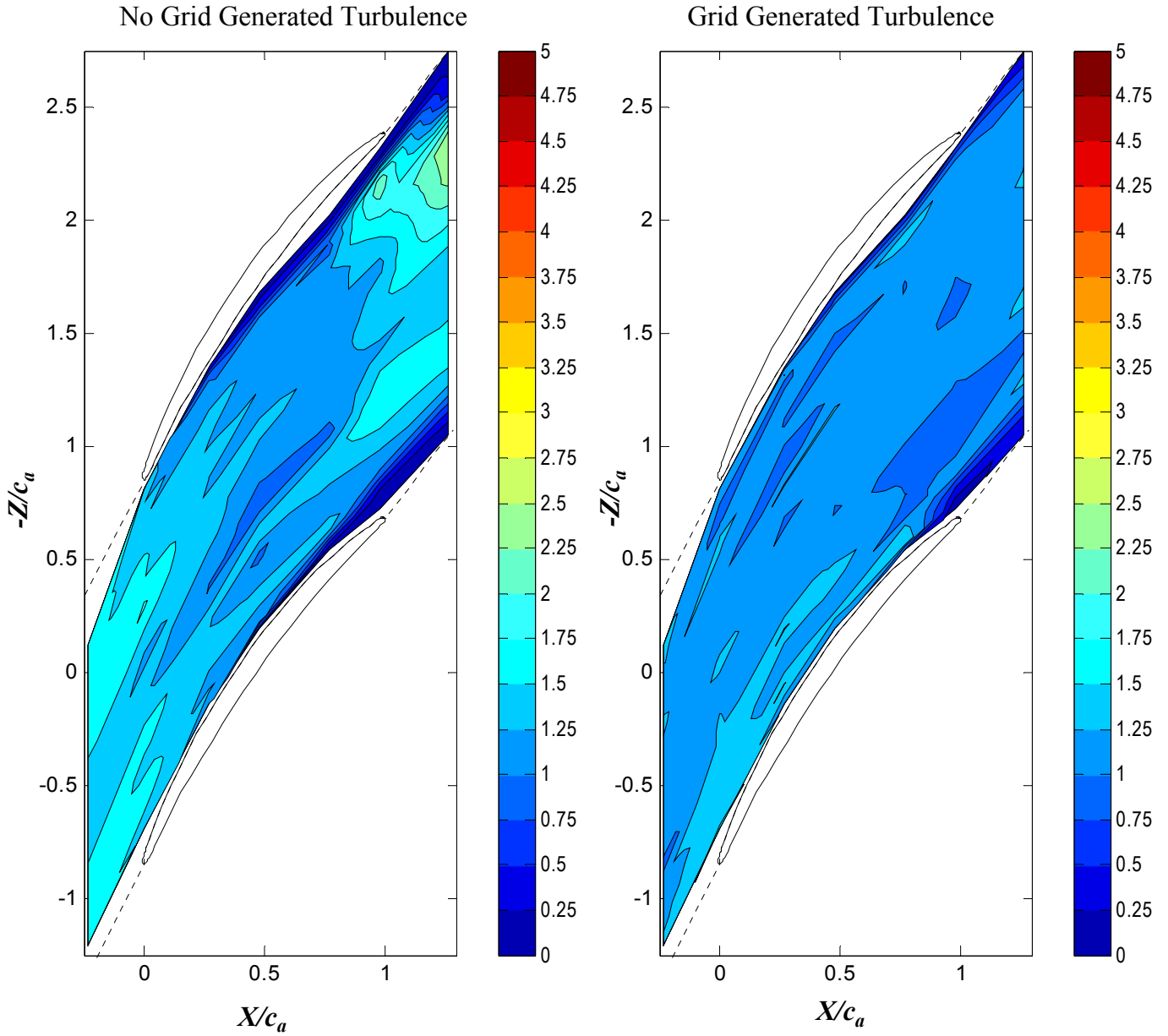


Figure 3.36: Plan view projection of the potential core flow at $y/c_a = 0.73$. Plotted here are the contours of the lengthscale, λ_v (cm)

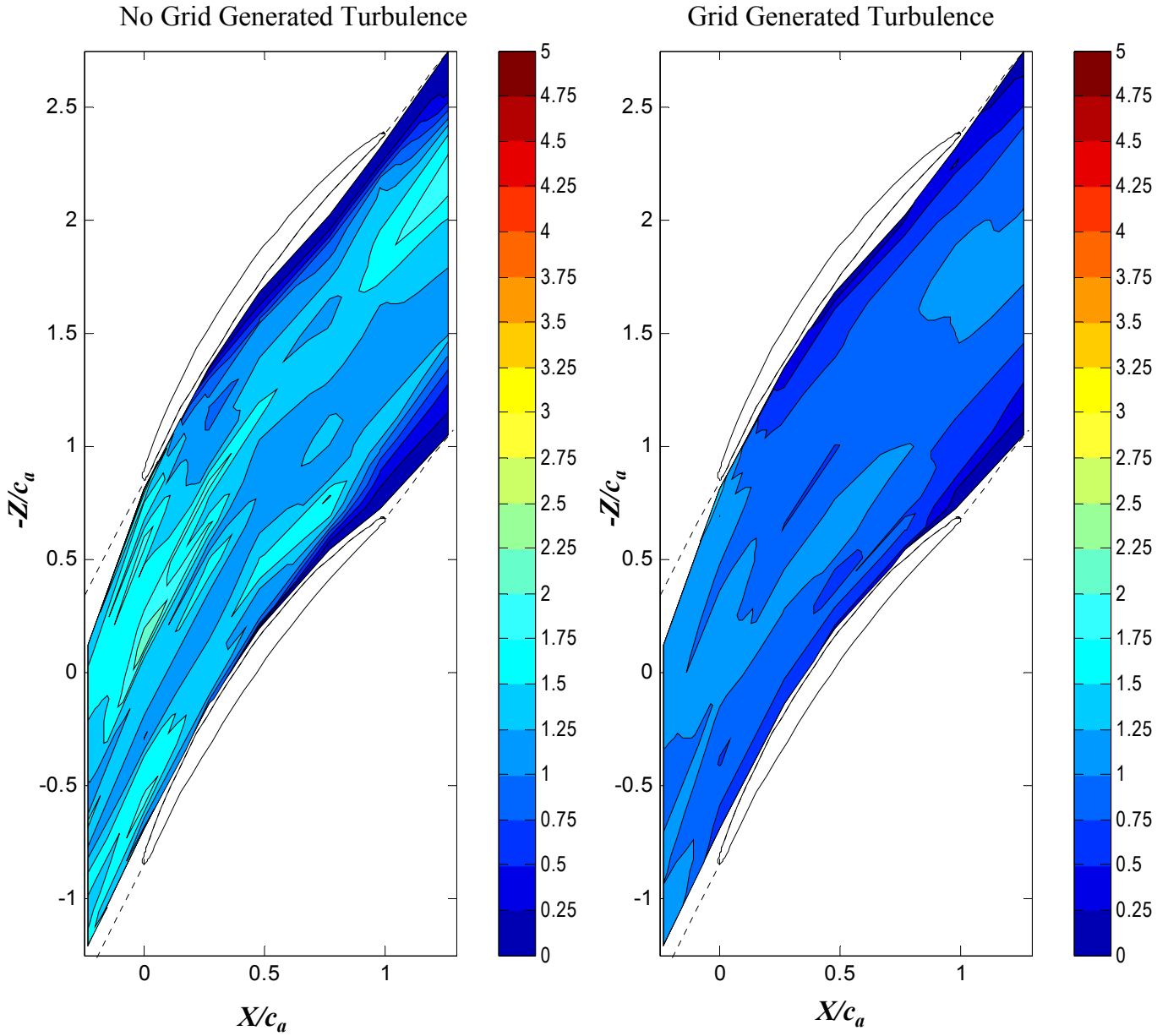


Figure 3.37: Plan view projection of the potential core flow at $y/c_a = 0.73$. Plotted here are the contours of the lengthscale, λ_w (cm)

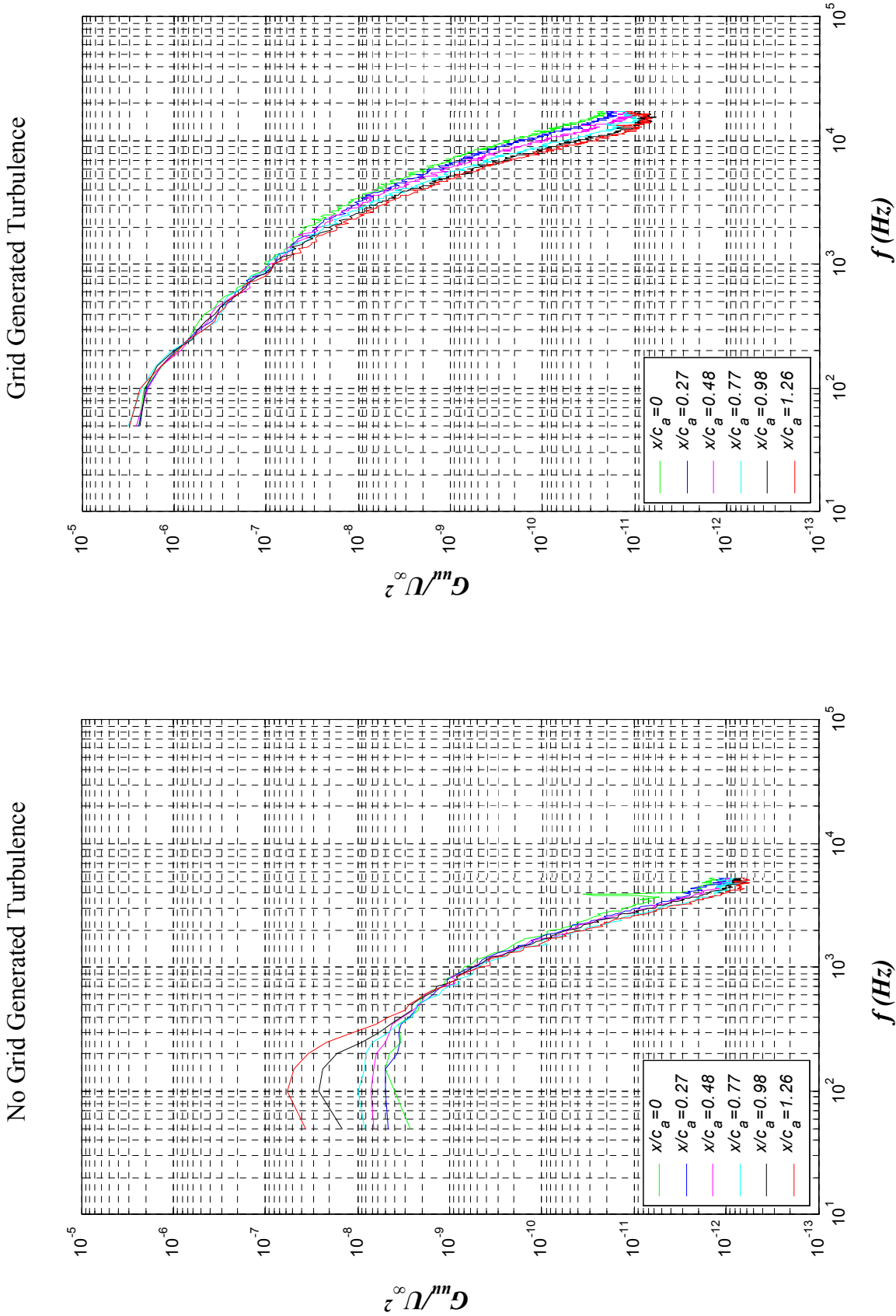


Figure 3.38: Evolution of the normalized autospectra, G_{uu}^m/U_∞^2 in the potential core of the flow. The legend indicates the axial location, and titles indicate the inflow turbulence condition

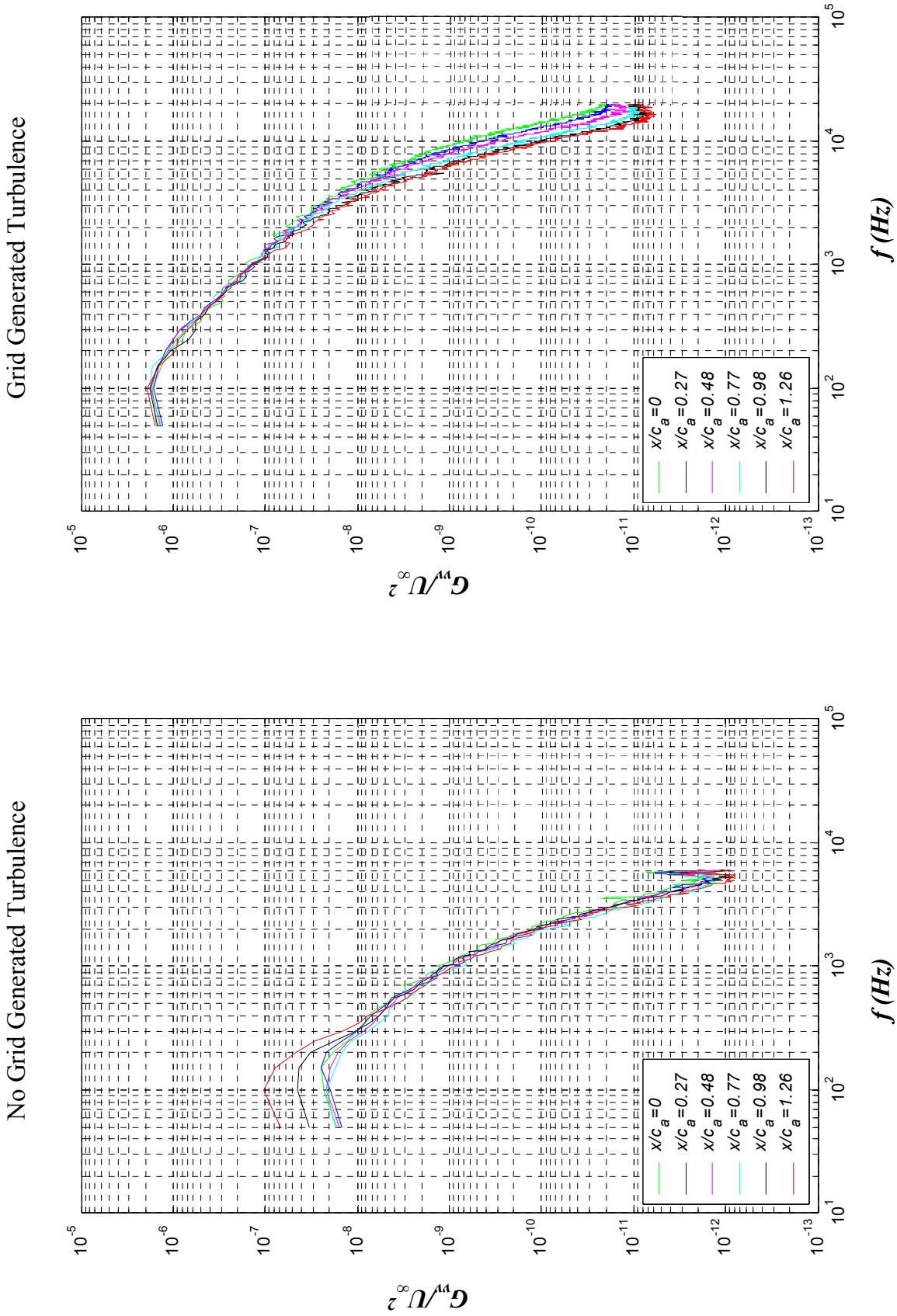


Figure 3.39: Evolution of the normalized autospectra, G_w / U_{∞}^2 in the potential core of the flow. The legend indicates the axial location, and titles indicate the inflow turbulence condition

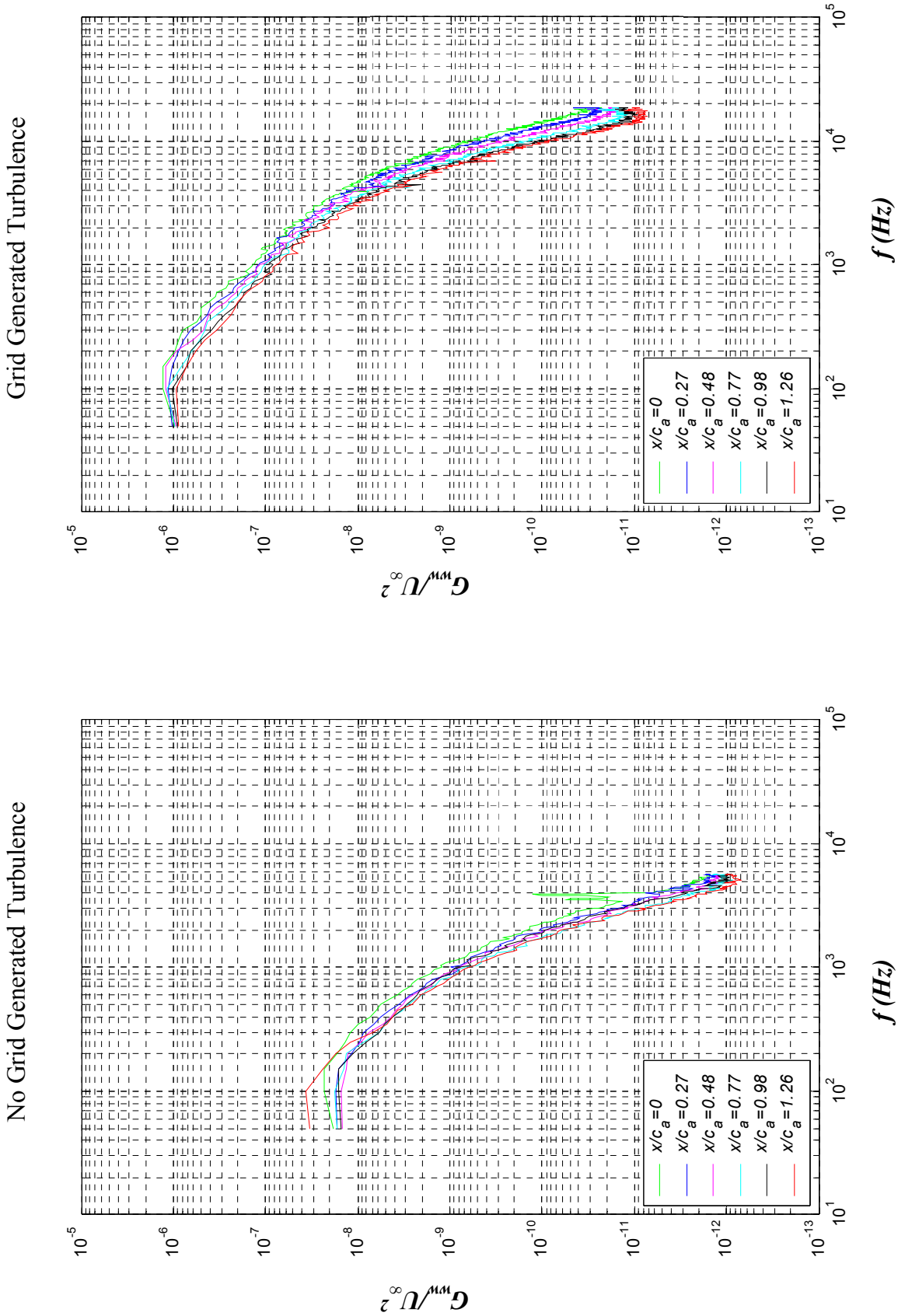


Figure 3.40: Evolution of the normalized autospectra, G_w^w / U_∞^2 in the potential core of the flow. The legend indicates the axial location, and titles indicate the inflow turbulence condition

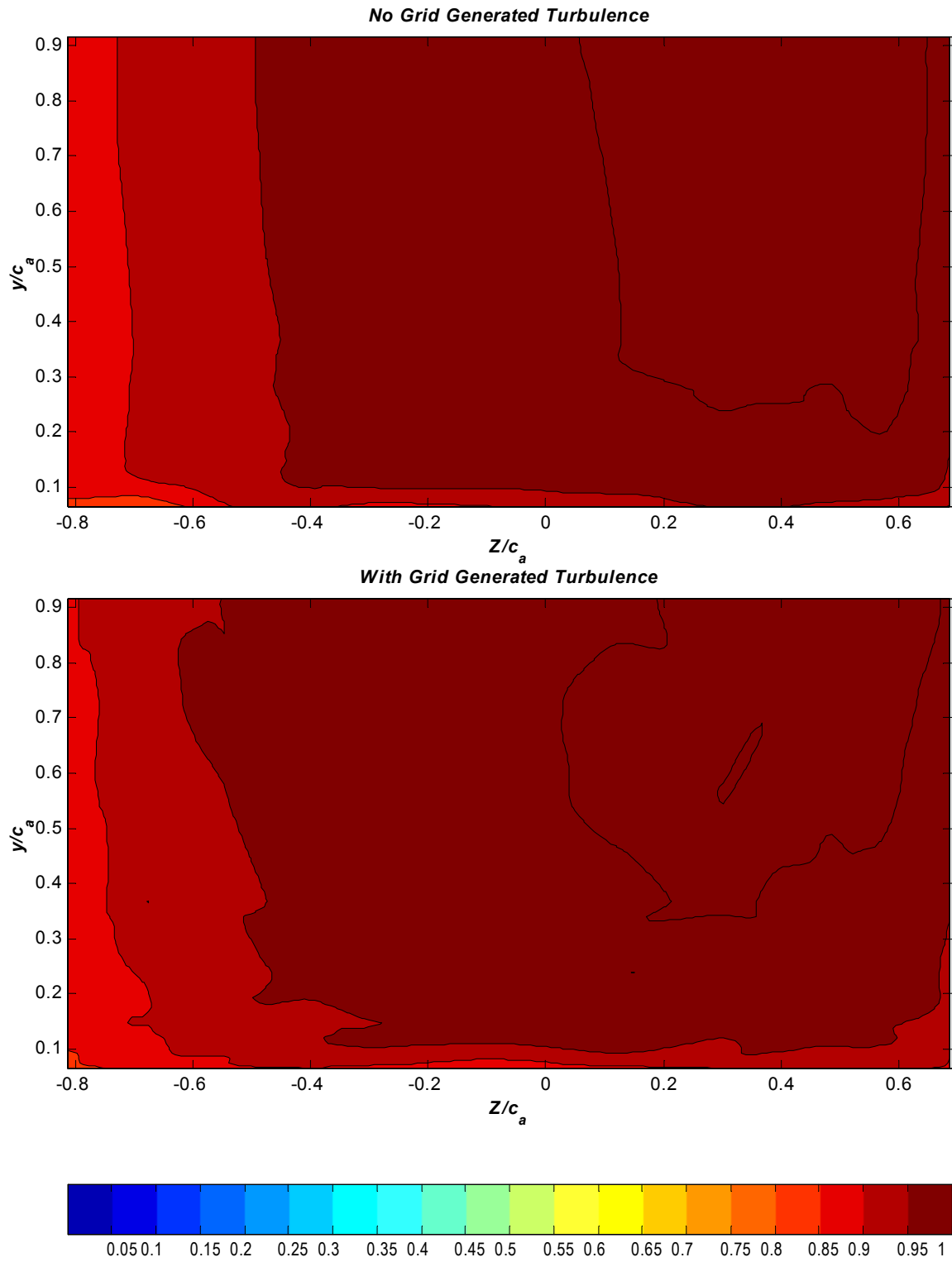


Figure 3.41a : Contours of Normalized Mean Streamwise Velocity, U/U_∞ at $X/c_a=0.0$

Titles on plots indicate inflow turbulence condition

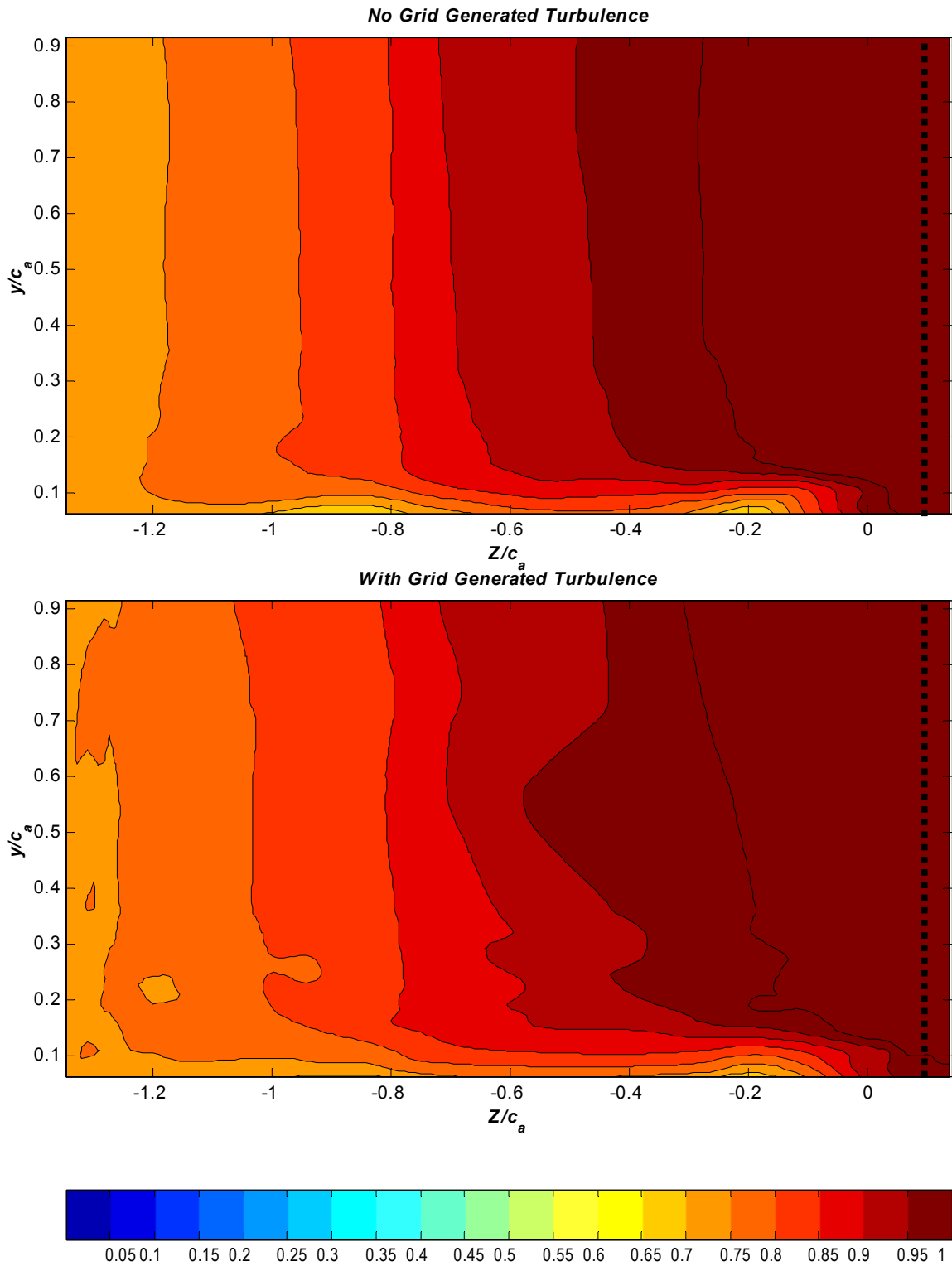


Figure 3.41b : Contours of Normalized Mean Streamwise Velocity, U/U_∞ at $X/c_a = 0.27$. Dashed line in the plots represents the location of the separation line inferred from the oil-flow visualizations. Titles on plots indicate inflow turbulence condition

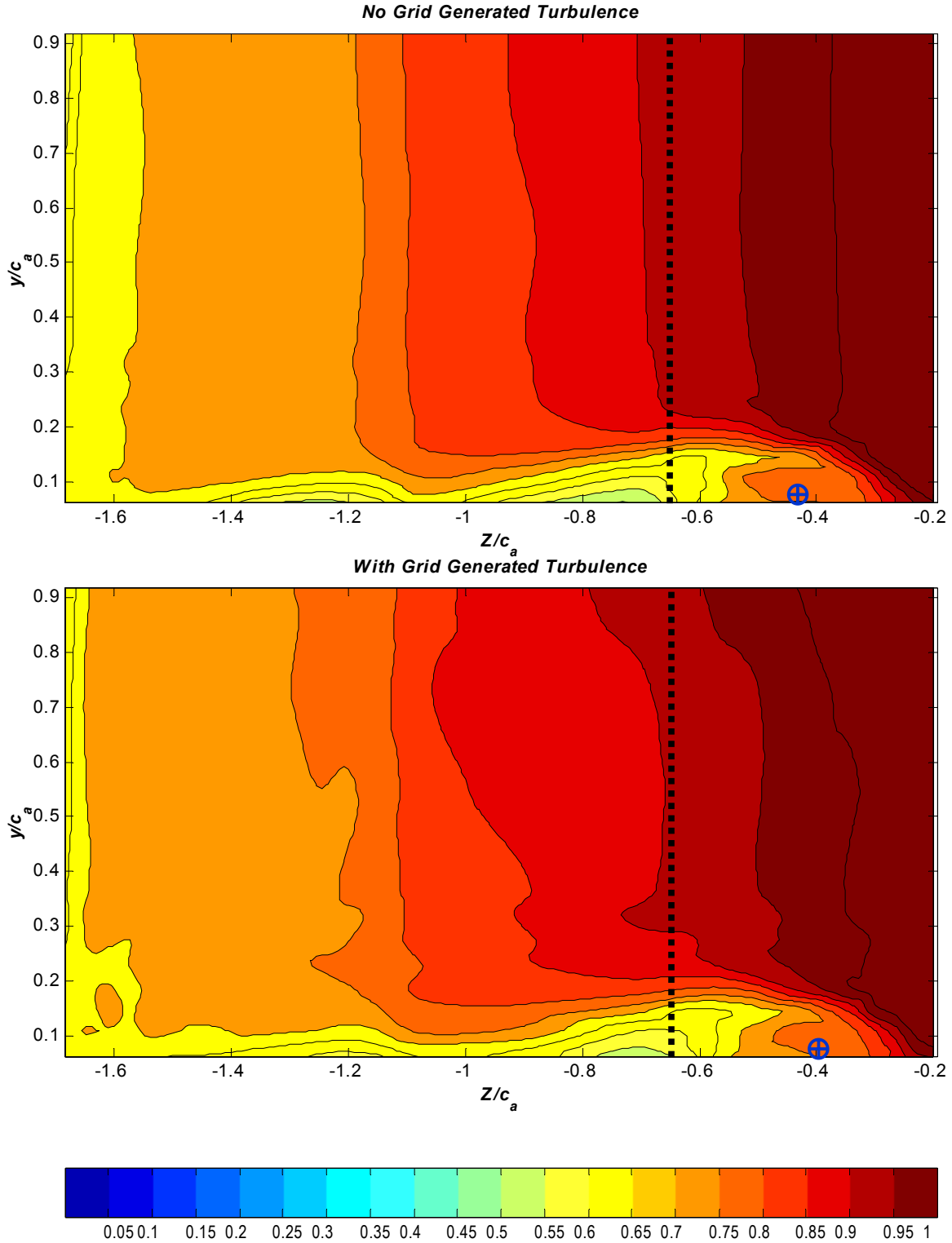


Figure 3.41c : Contours of Normalized Mean Streamwise Velocity, U/U_∞ at $X/c_a=0.48$. Dashed line in the plots represents the location of the separation line inferred from the oil-flow visualizations. Vortex centers defined by peak mean streamwise vorticity are indicated by circular crosses. Titles on plots indicate inflow turbulence condition

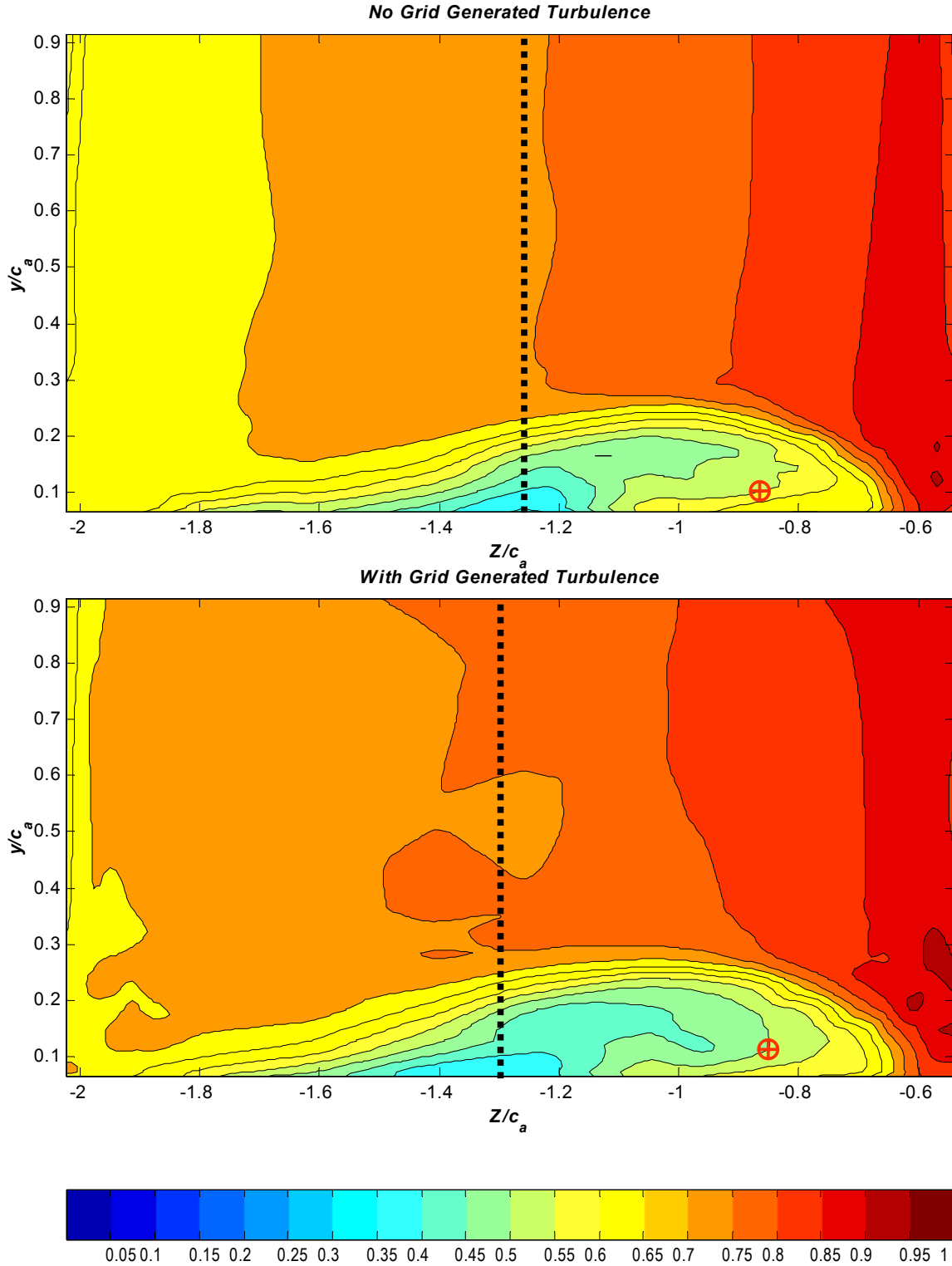


Figure 3.41d : Contours of Normalized Mean Streamwise Velocity, U/U_∞ at $X/c_a = 0.77$. Dashed line in the plots represents the location of the separation line inferred from the oil-flow visualizations. Vortex centers defined by peak mean streamwise vorticity are indicated by circular crosses. Titles on plots indicate inflow turbulence condition

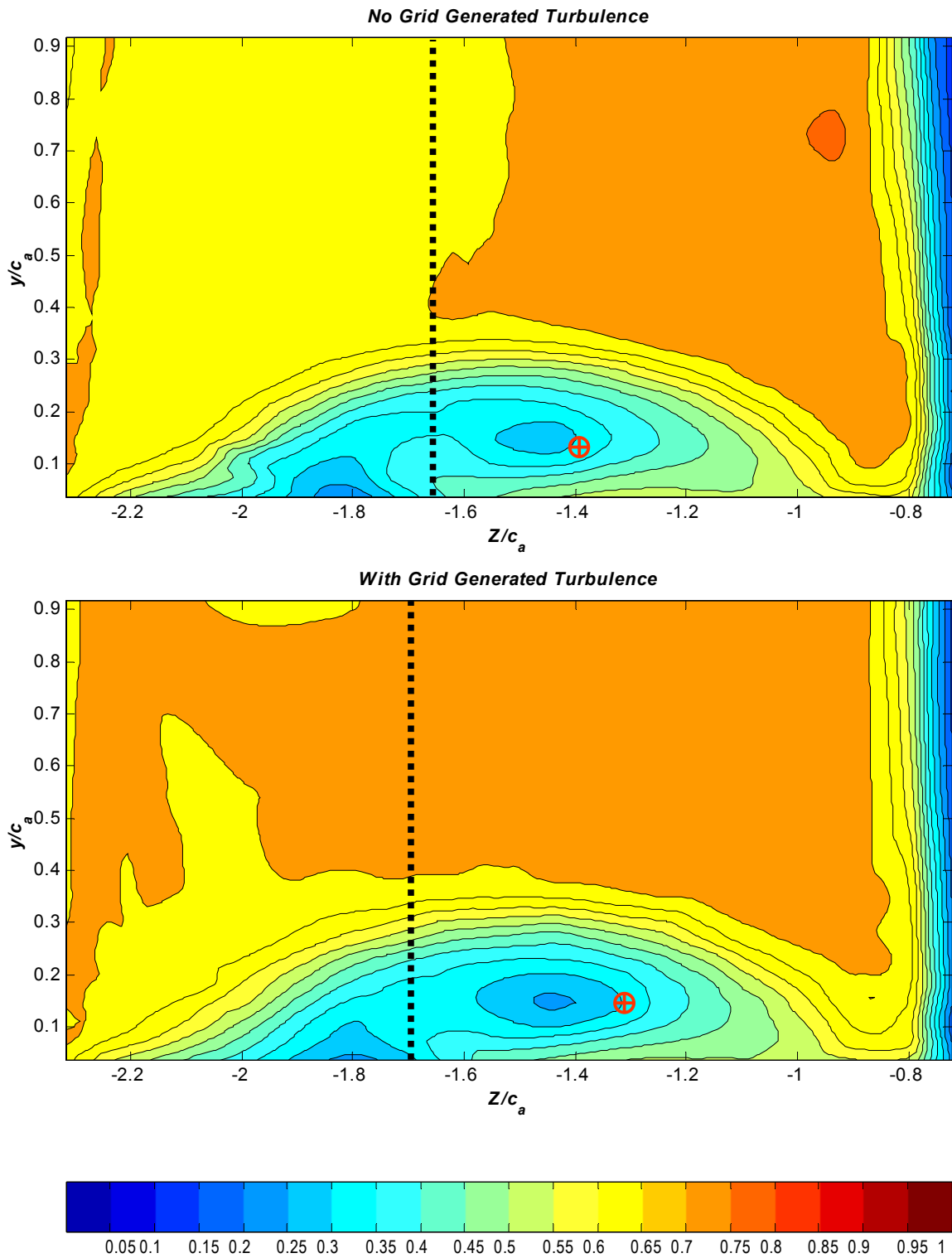


Figure 3.41e : Contours of Normalized Mean Streamwise Velocity, U/U_∞ at $X/c_a=0.98$. Dashed line in the plots represents the location of the separation line inferred from the oil-flow visualizations. Vortex centers defined by peak mean streamwise vorticity are indicated by circular crosses. Titles on plots indicate inflow turbulence condition

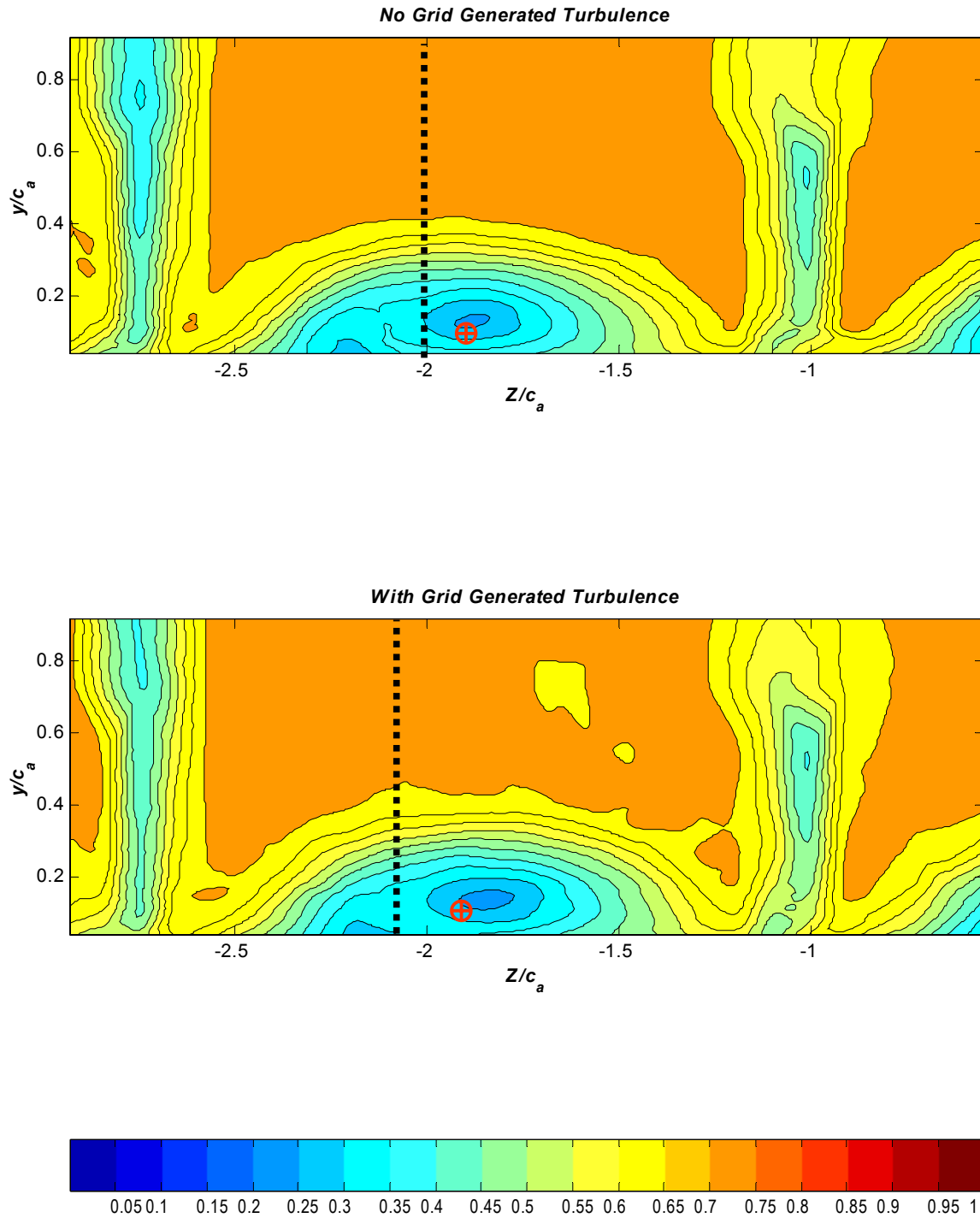


Figure 3.41f : Contours of Normalized Mean Streamwise Velocity, U/U_∞ at $X/c_a=1.26$. Dashed line in the plots represents the location of the separation line inferred from the oil-flow visualizations. Vortex centers defined by peak mean streamwise vorticity are indicated by circular crosses. Titles on plots indicate inflow turbulence condition

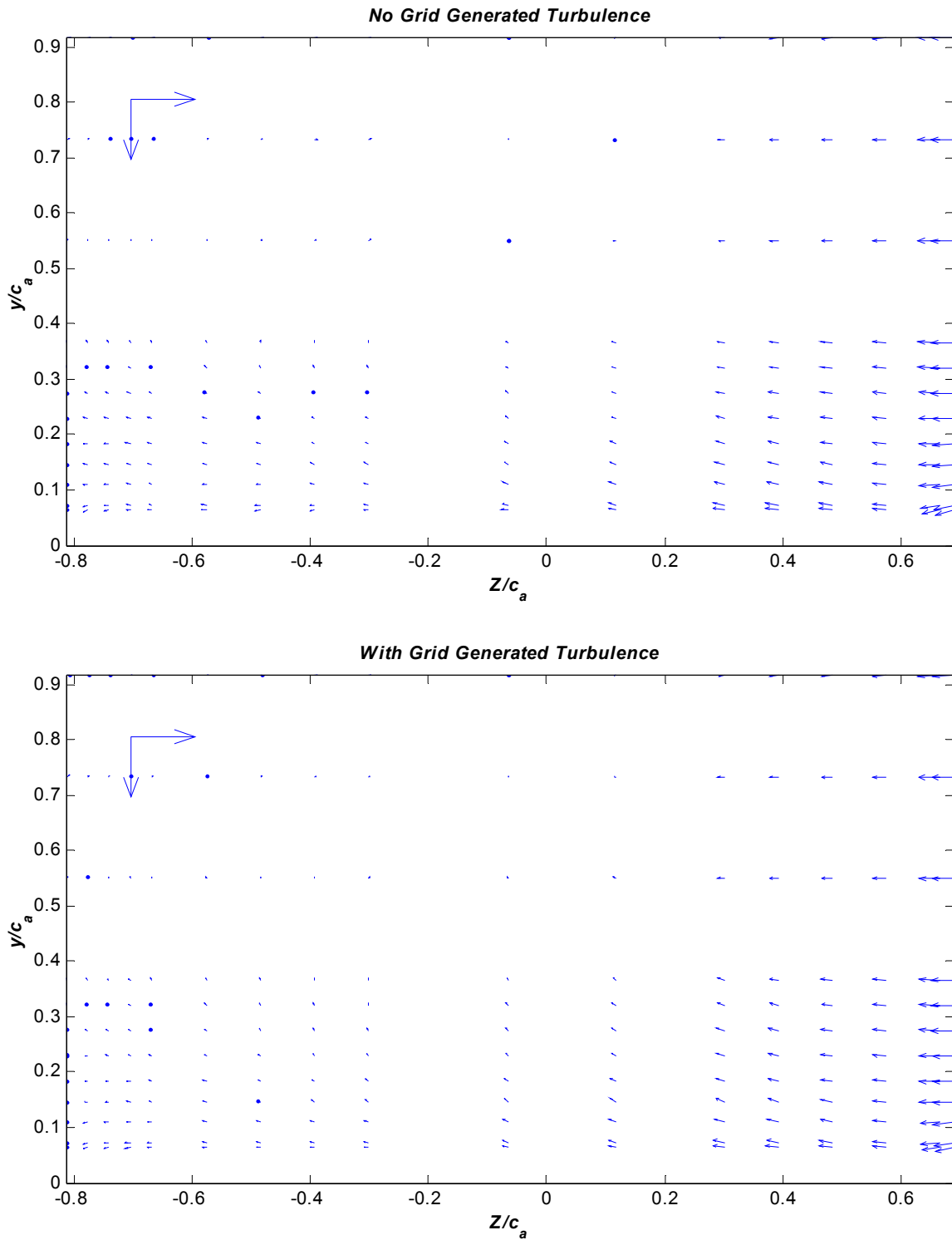


Figure 3.42a : Vectors of the magnitude of the mean normalized crossflow velocity (V , W) at $X/c_a=0.0$. Reference vectors of magnitude $0.5U_\infty$ in the y and z direction are given in the top left corner of each plot. Titles on plots indicate inflow turbulence condition

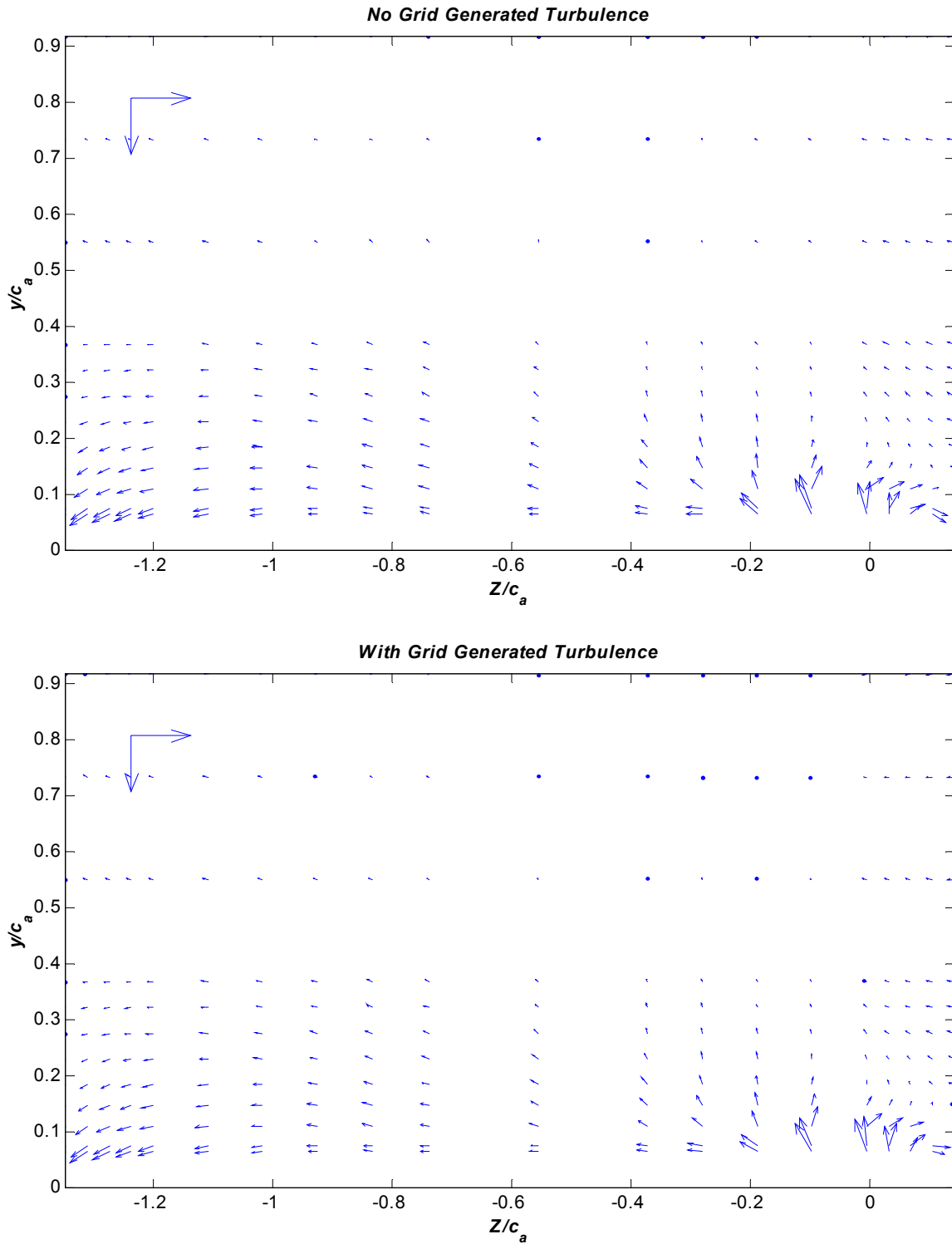


Figure 3.42b : Vectors of the magnitude of the mean normalized crossflow velocity (V , W) at $X/c_a=0.27$. Reference vectors of magnitude $0.5U_\infty$ in the y and z direction are given in the top left corner of each plot. Titles on plots indicate inflow turbulence condition

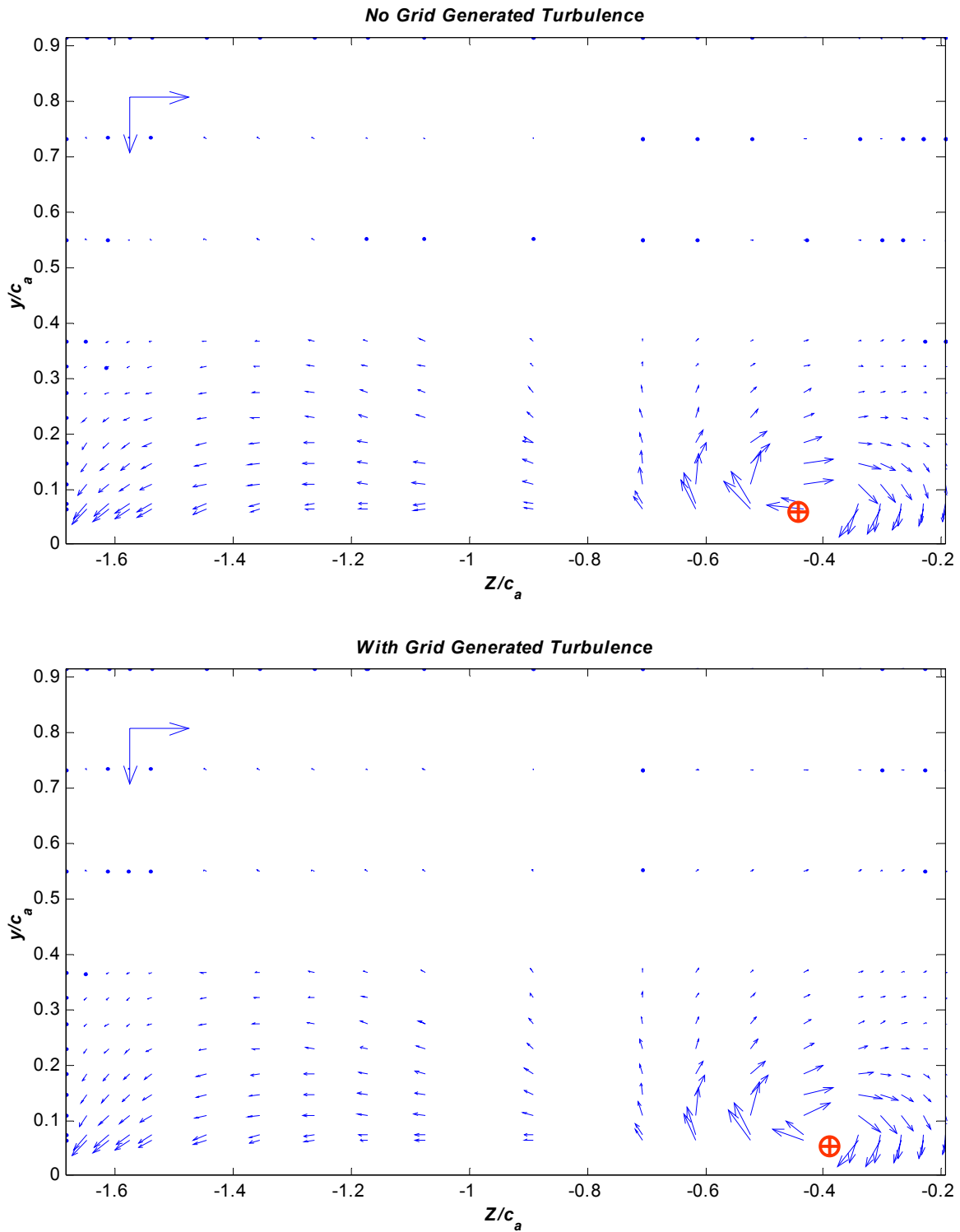


Figure 3.42c : Vectors of the magnitude of the mean normalized crossflow velocity (V , W) at $X/c_a = 0.48$. Vortex centers defined by peak mean streamwise vorticity are indicated by circular crosses. Reference vectors of magnitude $0.5U_\infty$ in the y and z direction are given in the top left corner of each plot. Titles on plots indicate inflow turbulence condition

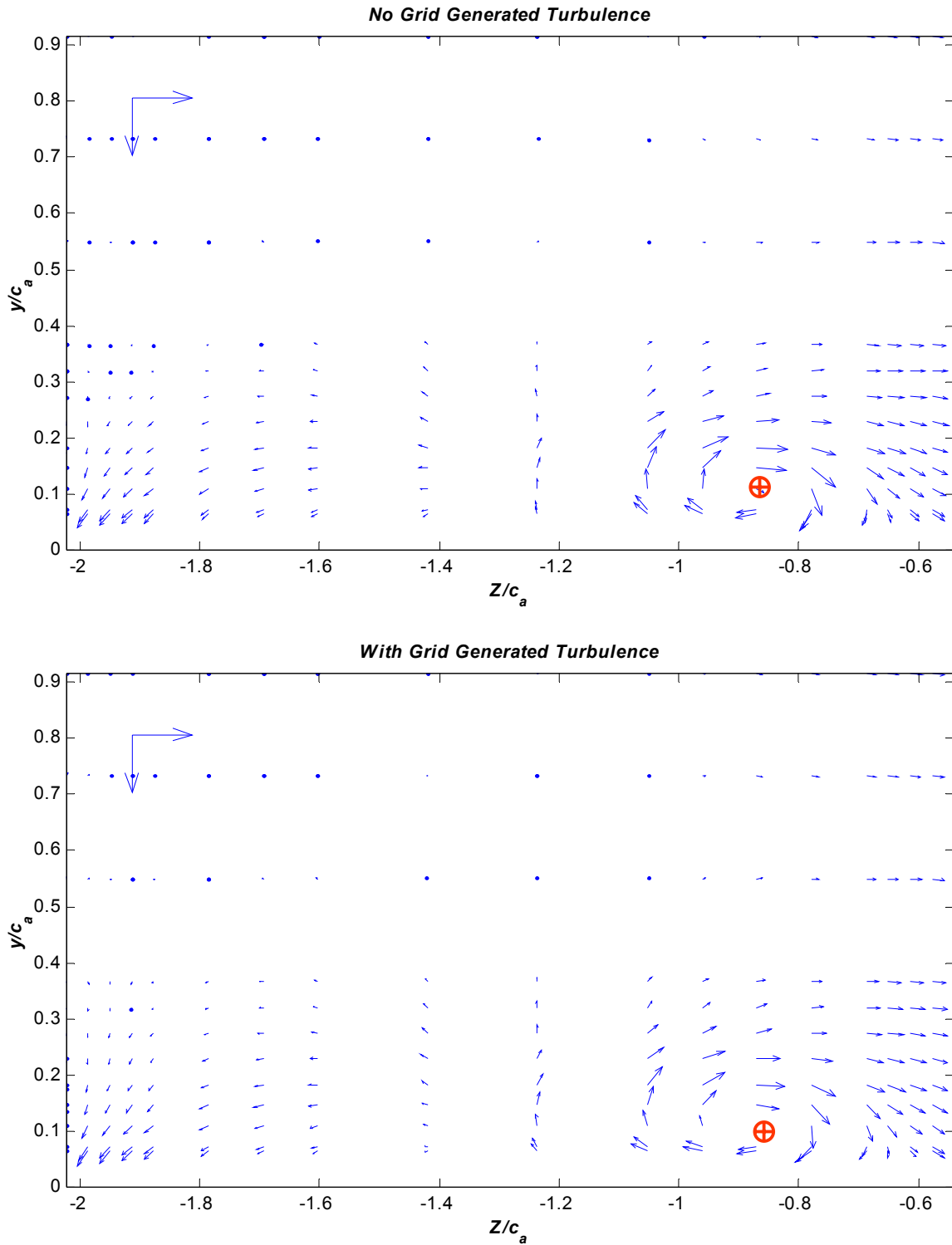


Figure 3.42d : Vectors of the magnitude of the mean normalized crossflow velocity (V , W) at $X/c_a = 0.77$. Vortex centers defined by peak mean streamwise vorticity are indicated by circular crosses. Reference vectors of magnitude $0.5U_\infty$ in the y and z direction are given in the top left corner of each plot. Titles on plots indicate inflow turbulence condition

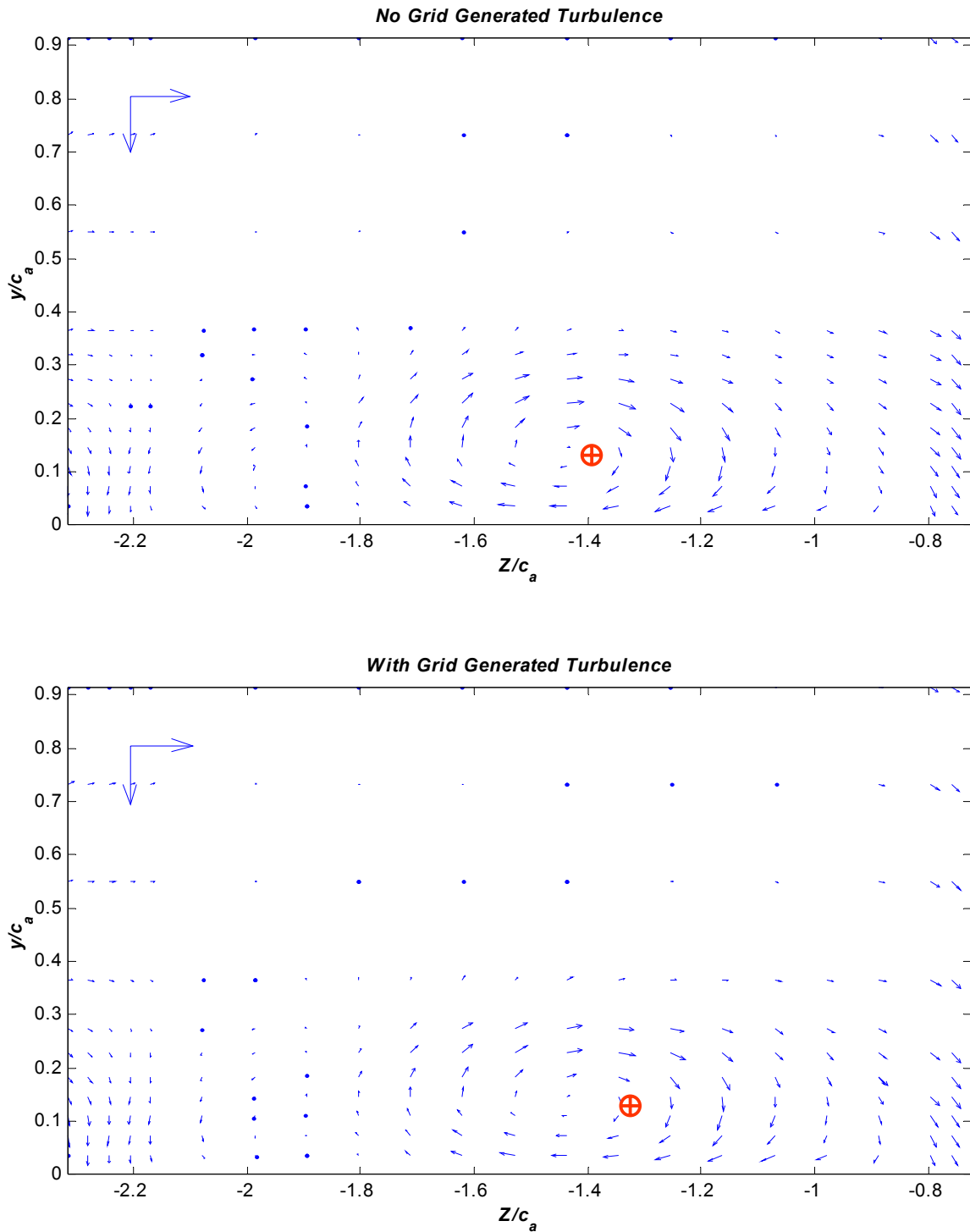


Figure 3.42e : Vectors of the magnitude of the mean normalized crossflow velocity (V , W) at $X/c_a = 0.98$. Vortex centers defined by peak mean streamwise vorticity are indicated by circular crosses. Reference vectors of magnitude $0.5U_\infty$ in the y and z direction are given in the top left corner of each plot. Titles on plots indicate inflow turbulence condition

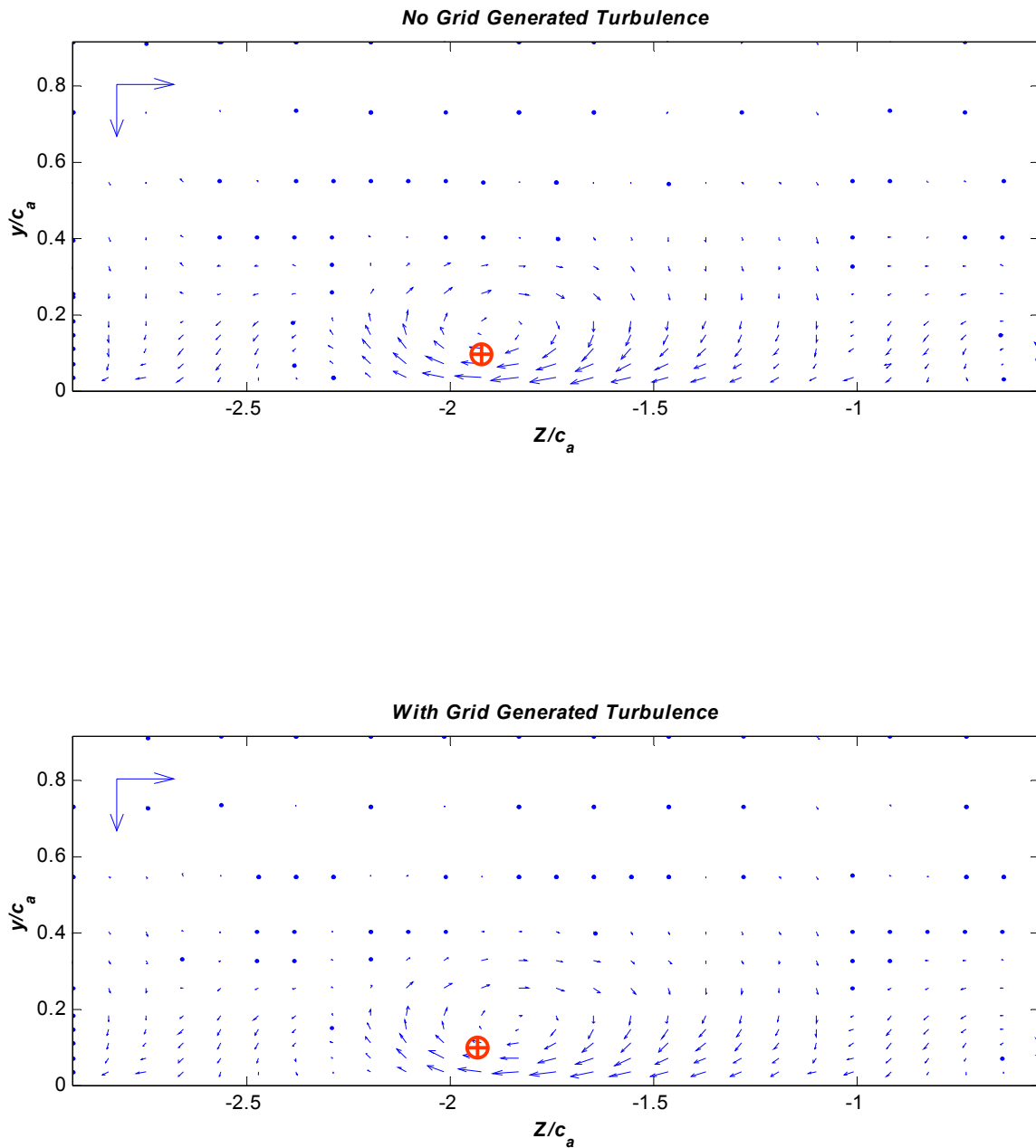


Figure 3.42f : Vectors of the magnitude of the mean normalized crossflow velocity (V , W) at $X/c_a = 0.126$. Vortex centers defined by peak mean streamwise vorticity are indicated by circular crosses. Reference vectors of magnitude $0.5U_\infty$ in the y and z direction are given in the top left corner of each plot. Titles on plots indicate inflow turbulence condition

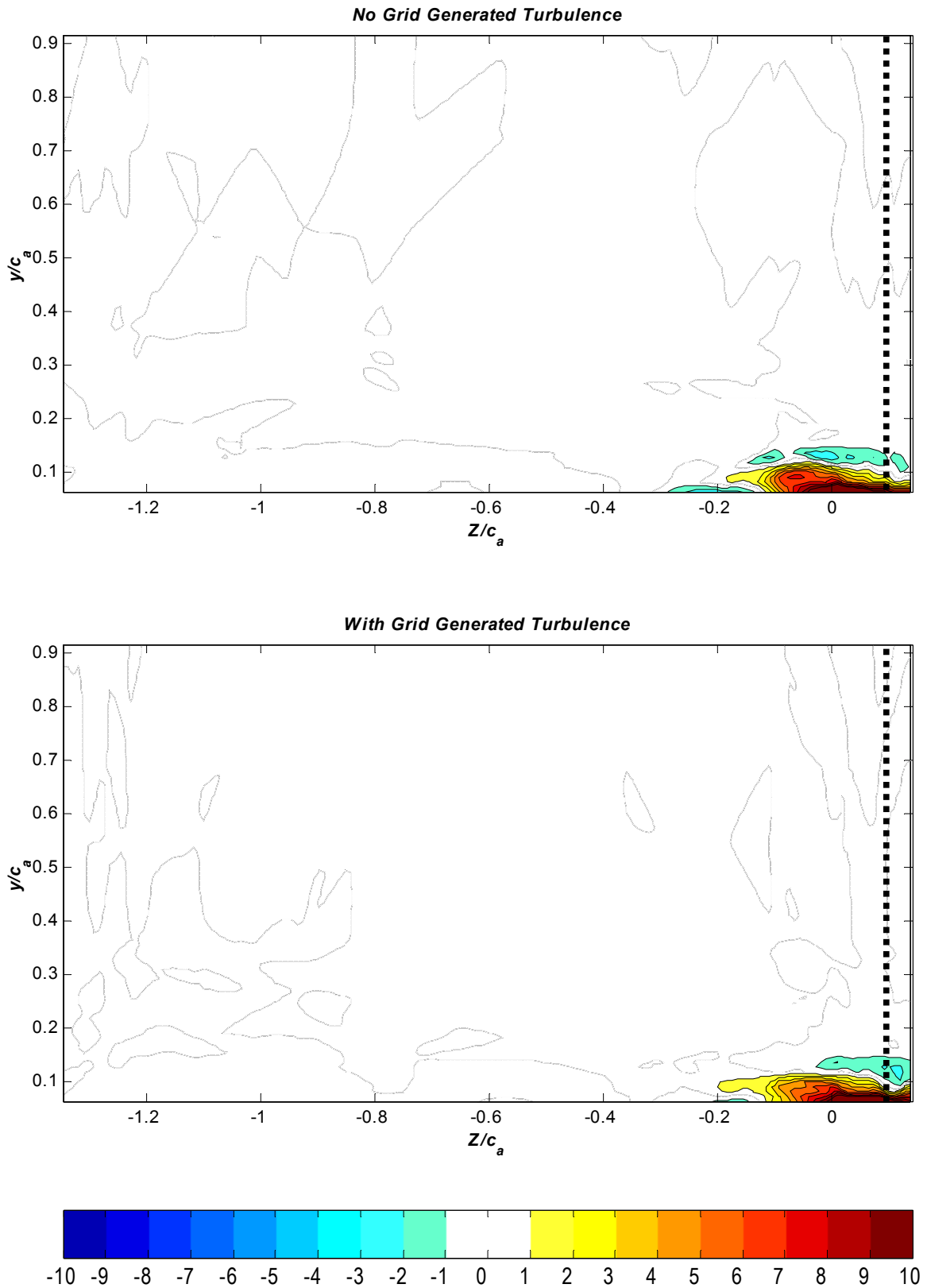


Figure 3.43a: Contours of the normalized streamwise vorticity, $\Omega_x c_a / U_\infty$, at $X/c_a = 0.27$. Dashed line in the plots represents the location of the separation line inferred from the oil-flow visualizations. Titles on plots indicate inflow turbulence condition.

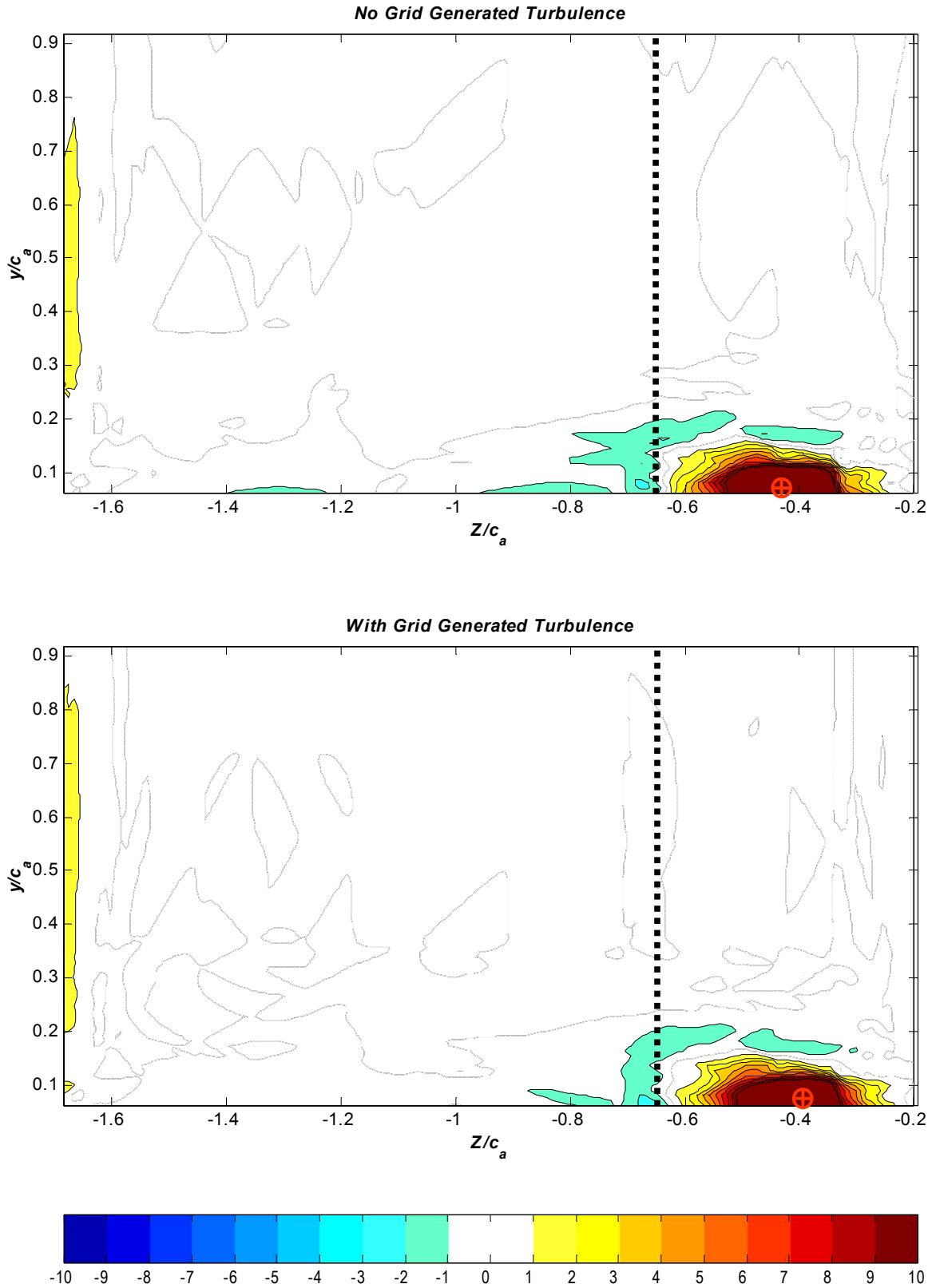


Figure 3.43b: Contours of the normalized streamwise vorticity, $\Omega_x c_a / U_\infty$, at $X/c_a = 0.48$. Dashed line in the plots represents the location of the separation line inferred from the oil-flow visualizations. Vortex centers defined by peak mean streamwise vorticity are indicated by circular crosses. Titles on plots indicate inflow turbulence condition

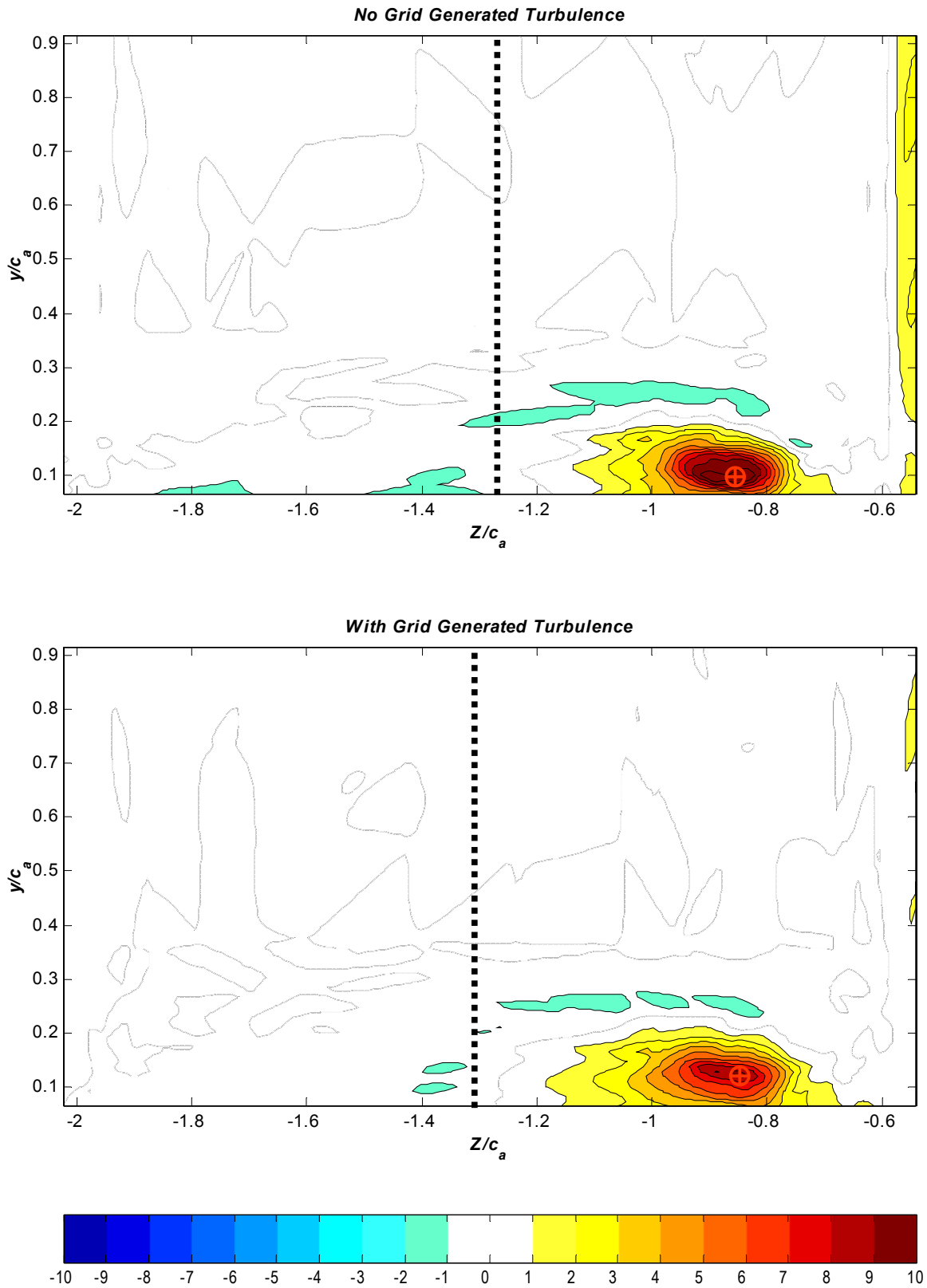


Figure 3.43c: Contours of the normalized streamwise vorticity, $\Omega_x c_a / U_\infty$, at $X/c_a = 0.77$. Dashed line in the plots represents the location of the separation line inferred from the oil-flow visualizations. Vortex centers defined by peak mean streamwise vorticity are indicated by circular crosses. Titles on plots indicate inflow turbulence condition

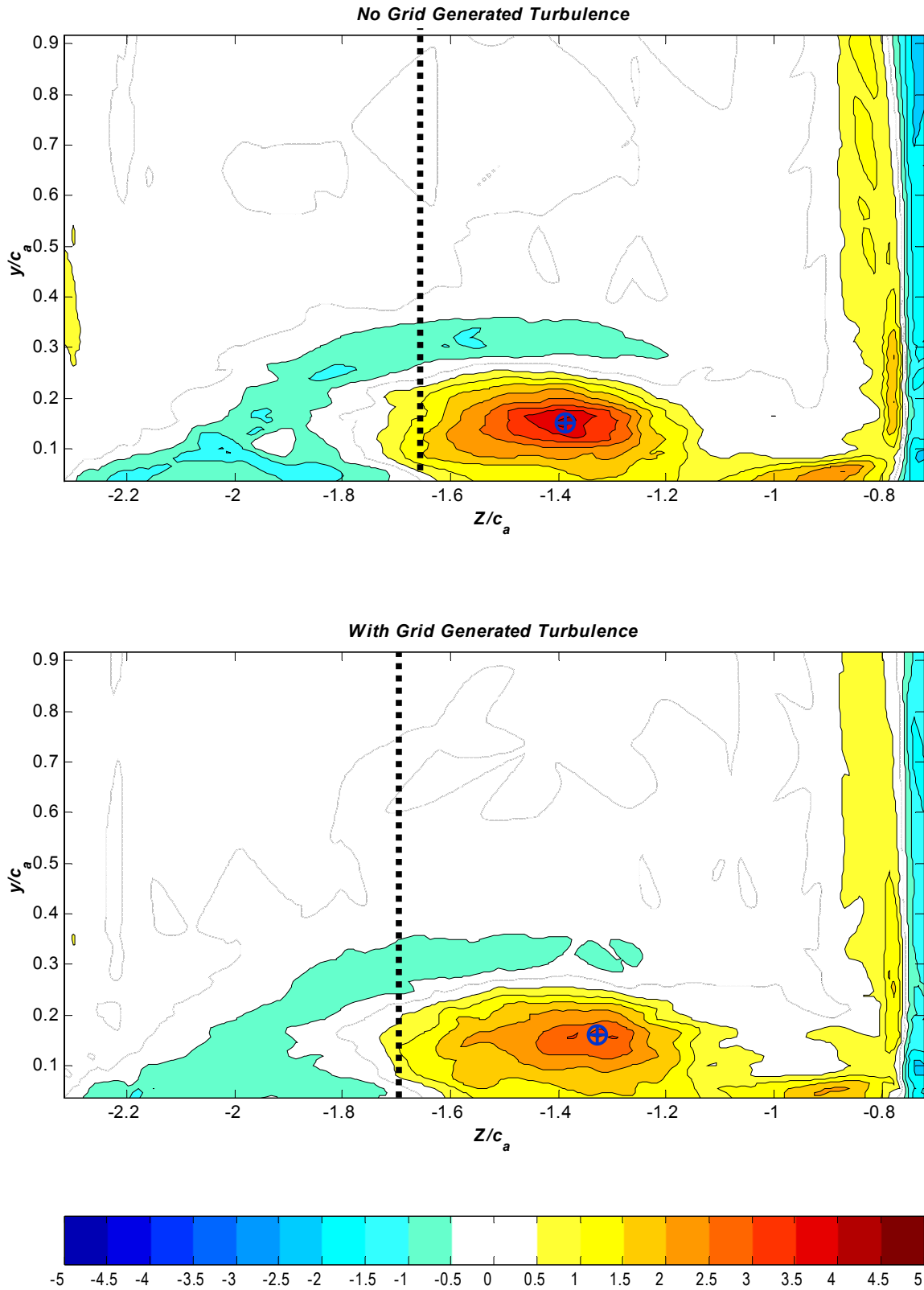


Figure 3.43d: Contours of the normalized streamwise vorticity, $\Omega_x c_a / U_\infty$, at $X/c_a = 0.98$. Dashed line in the plots represents the location of the separation line inferred from the oil-flow visualizations. Vortex centers defined by peak mean streamwise vorticity are indicated by circular crosses. Titles on plots indicate inflow turbulence condition

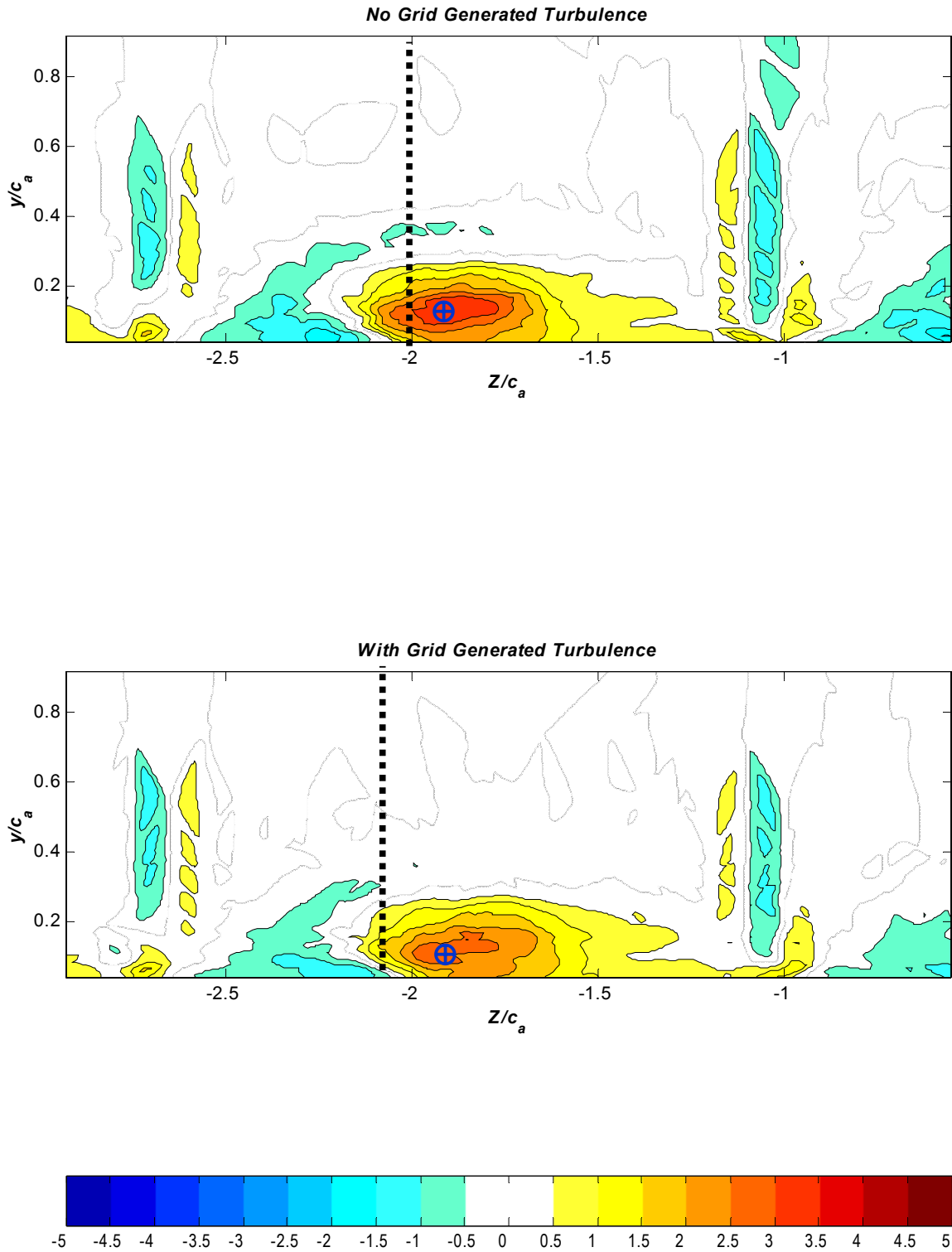


Figure 3.43e: Contours of the normalized streamwise vorticity, $\Omega_x c_a / U_\infty$, at $X/c_a = 1.26$. Dashed line in the plots represents the location of the separation line inferred from the oil-flow visualizations. Vortex centers defined by peak mean streamwise vorticity are indicated by circular crosses. Titles on plots indicate inflow turbulence condition

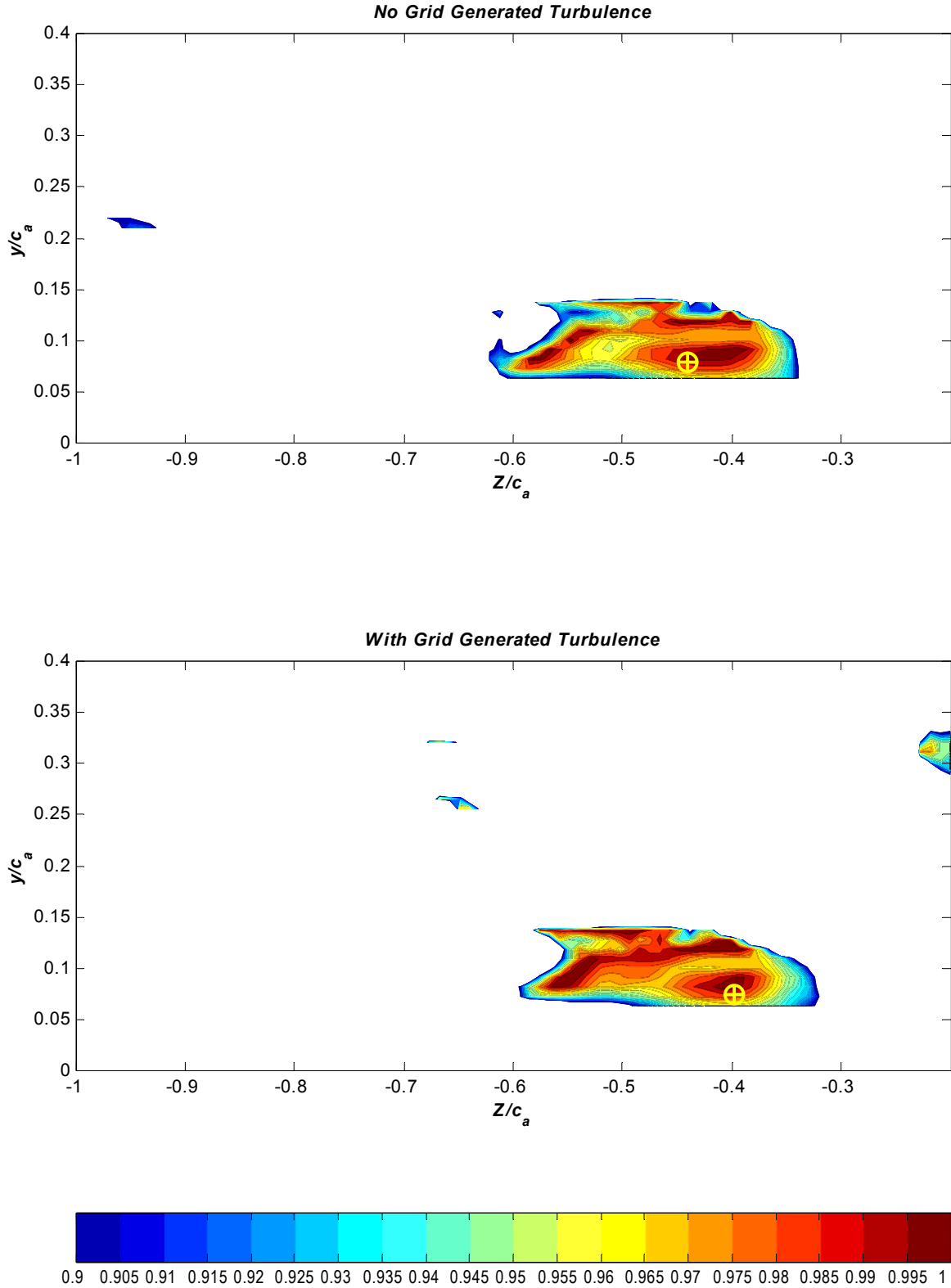


Figure 3.44a: Contours of the normalized Helicity, H , at $X/c_a=0.48$. Vortex centers defined by peak mean streamwise vorticity are indicated by circular crosses. Titles on plots indicate inflow turbulence condition

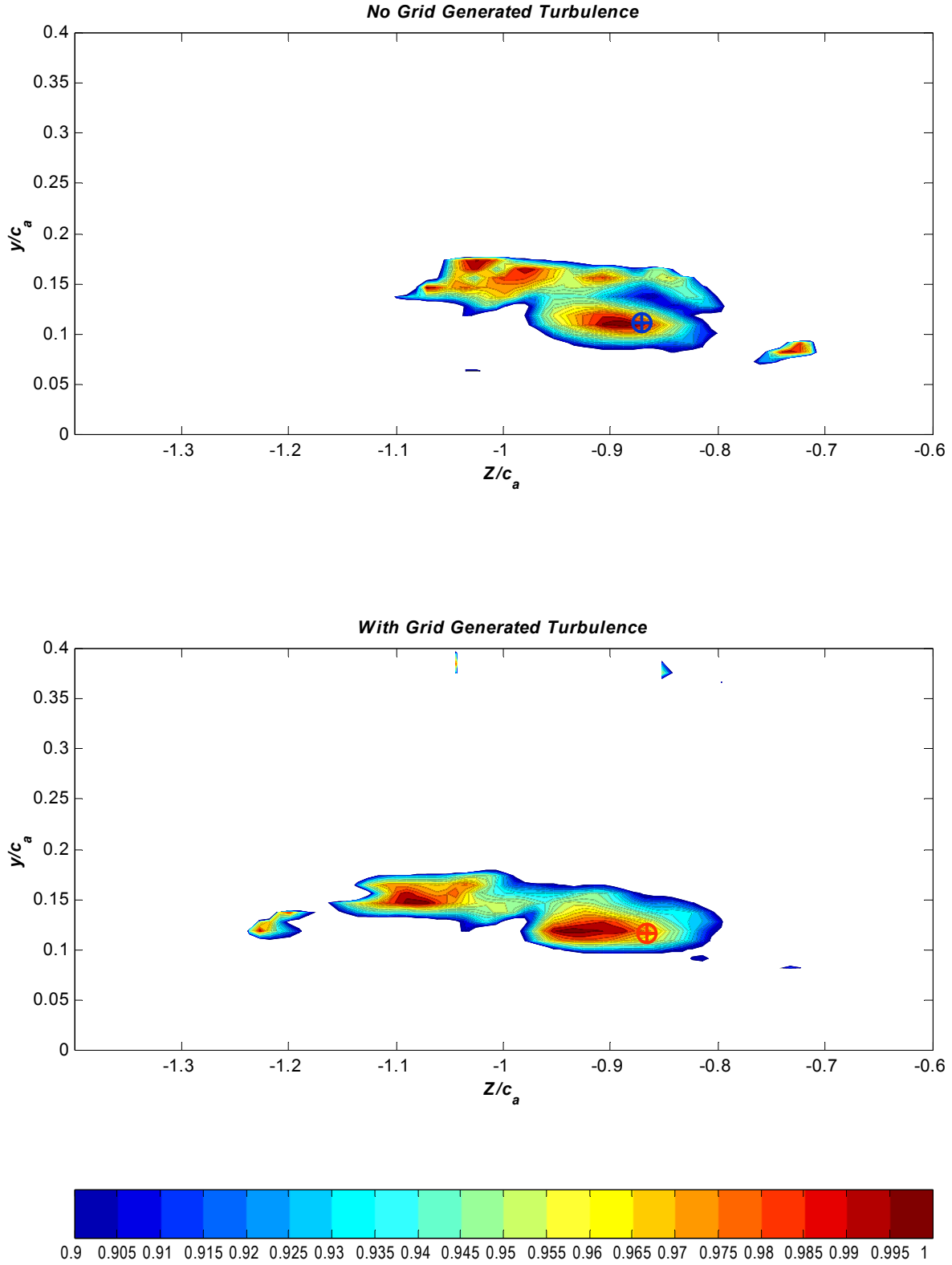


Figure 3.44b: Contours of the normalized Helicity, H , at $X/c_a=0.77$. Vortex centers defined by peak mean streamwise vorticity are indicated by circular crosses. Titles on plots indicate inflow turbulence condition

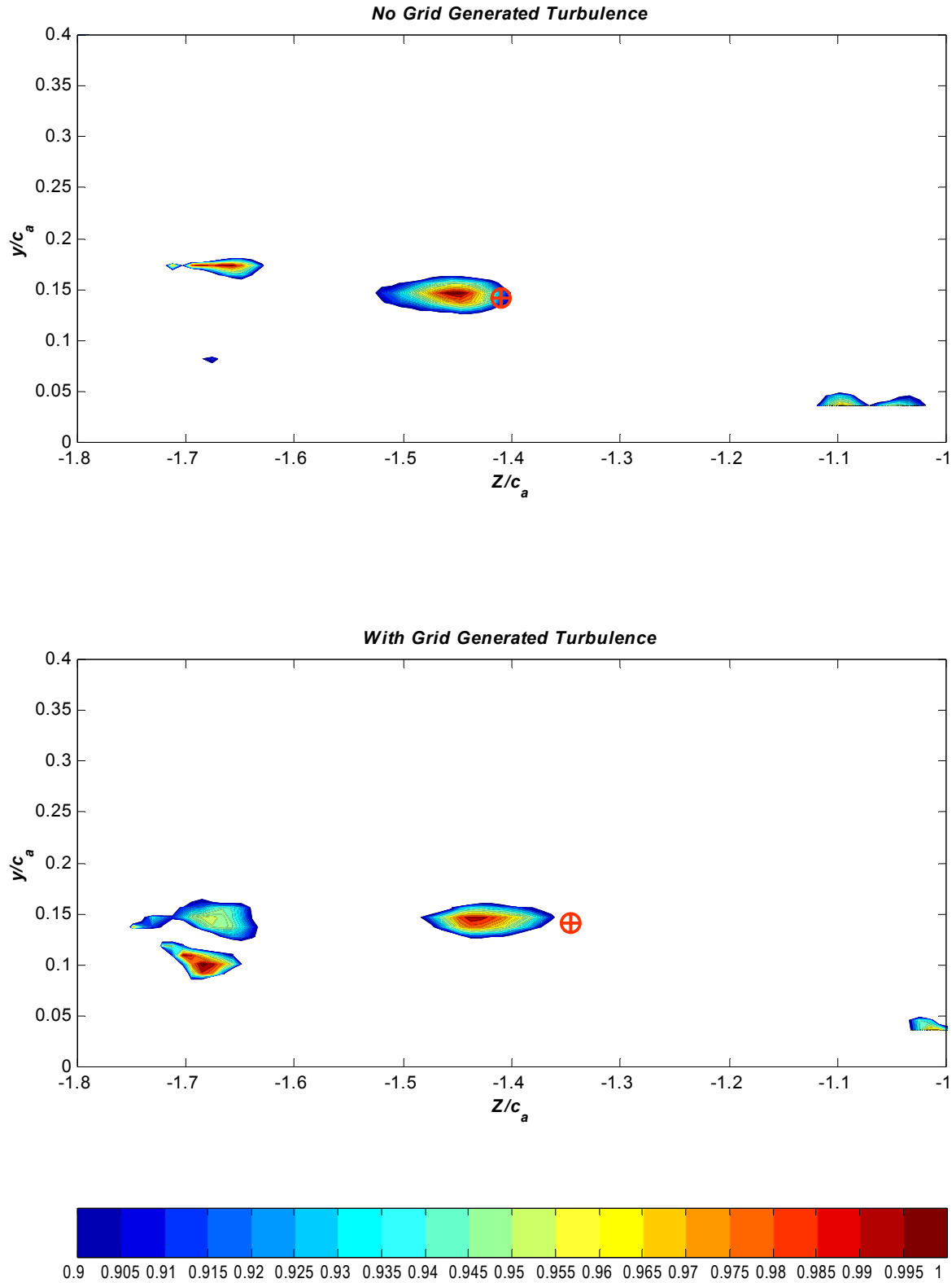


Figure 3.44c: Contours of the normalized Helicity, H , at $X/c_a=0.98$. Vortex centers defined by peak mean streamwise vorticity are indicated by circular crosses. Titles on plots indicate inflow turbulence condition

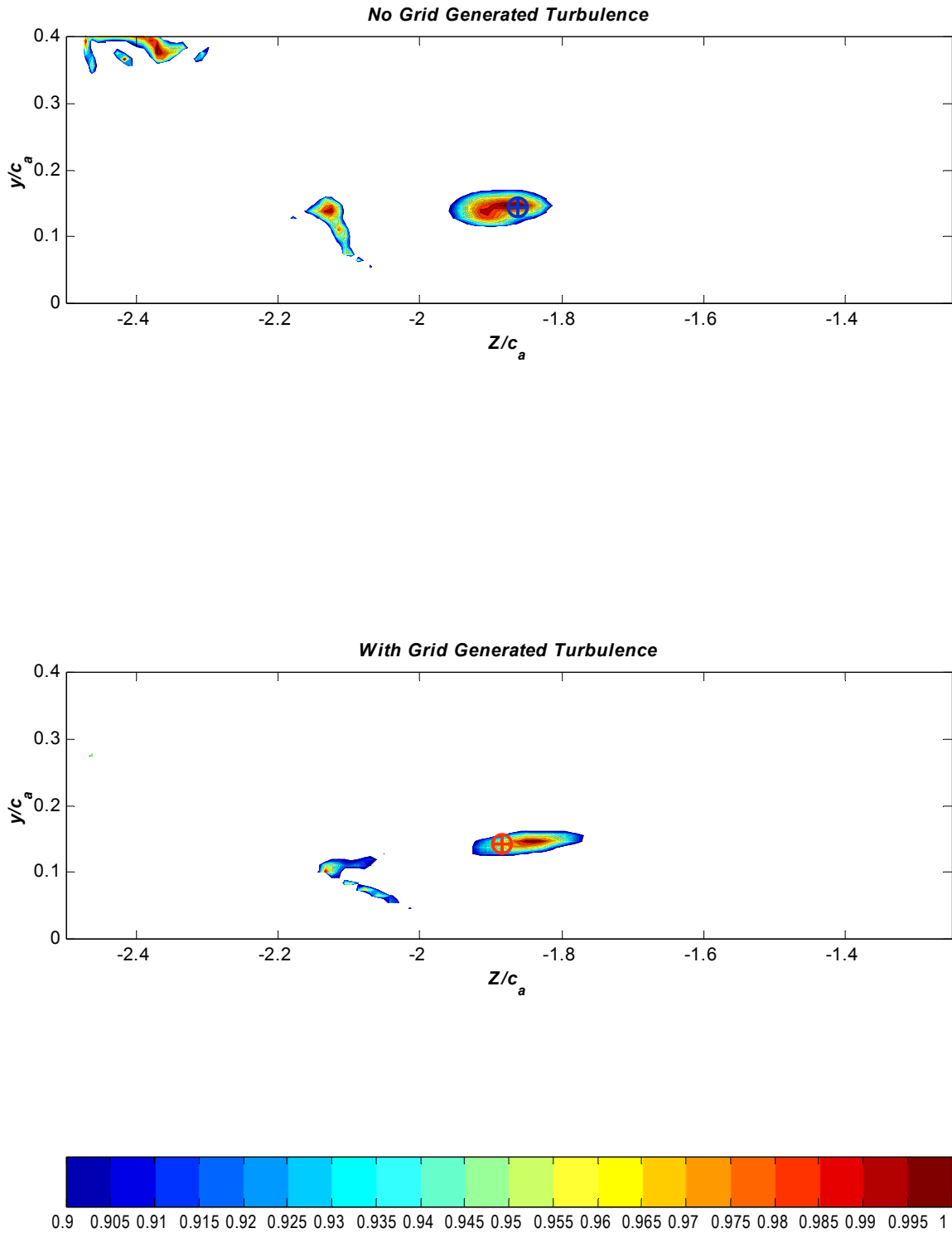


Figure 3.44d: Contours of the normalized Helicity, H , at $X/c_a=1.26$. Vortex centers defined by peak mean streamwise vorticity are indicated by circular crosses. Titles on plots indicate inflow turbulence condition

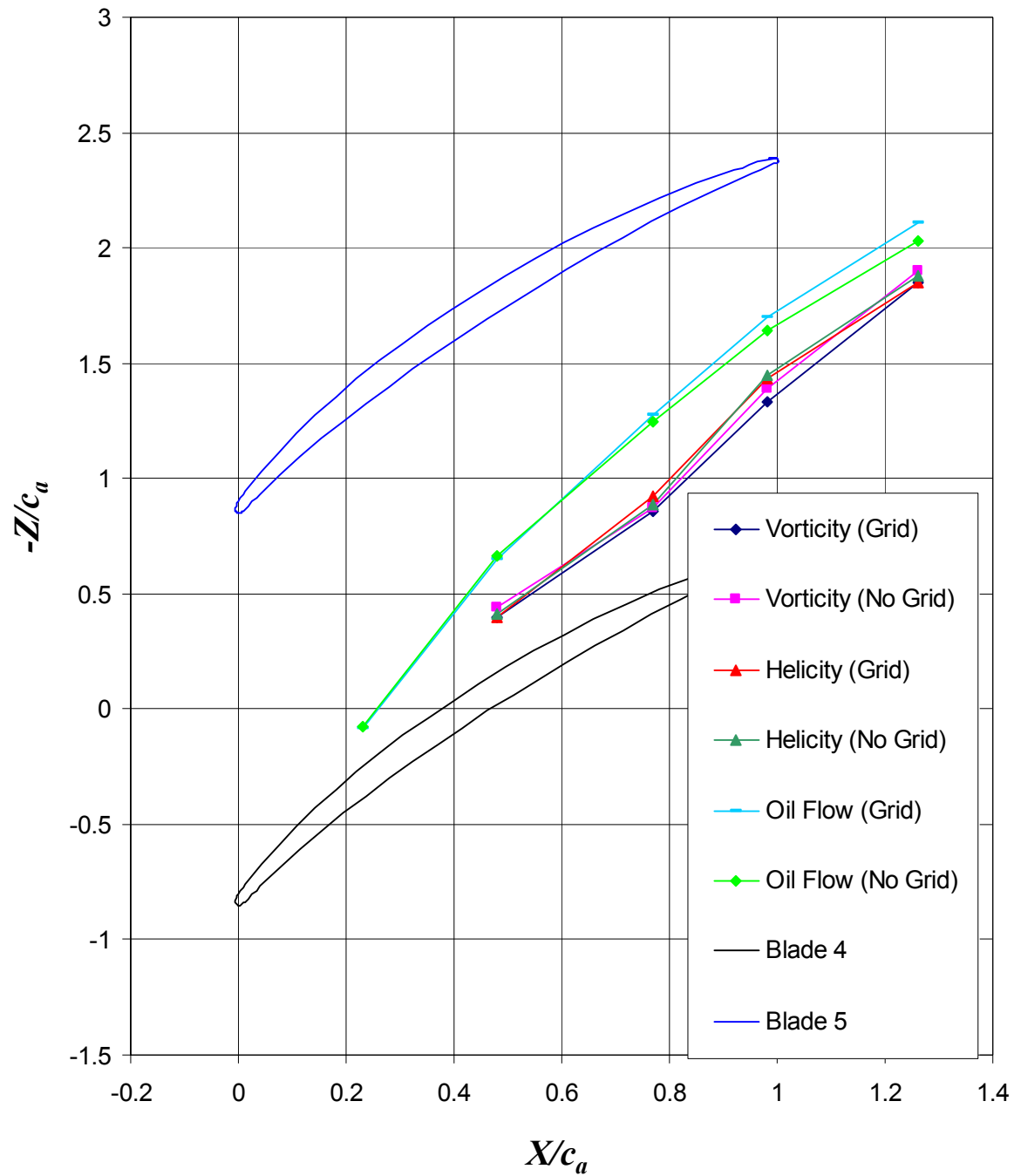


Figure 3.45: Plot showing various markers of the vortex trajectory as given in Tables 3.2, 3.6 and 3.7

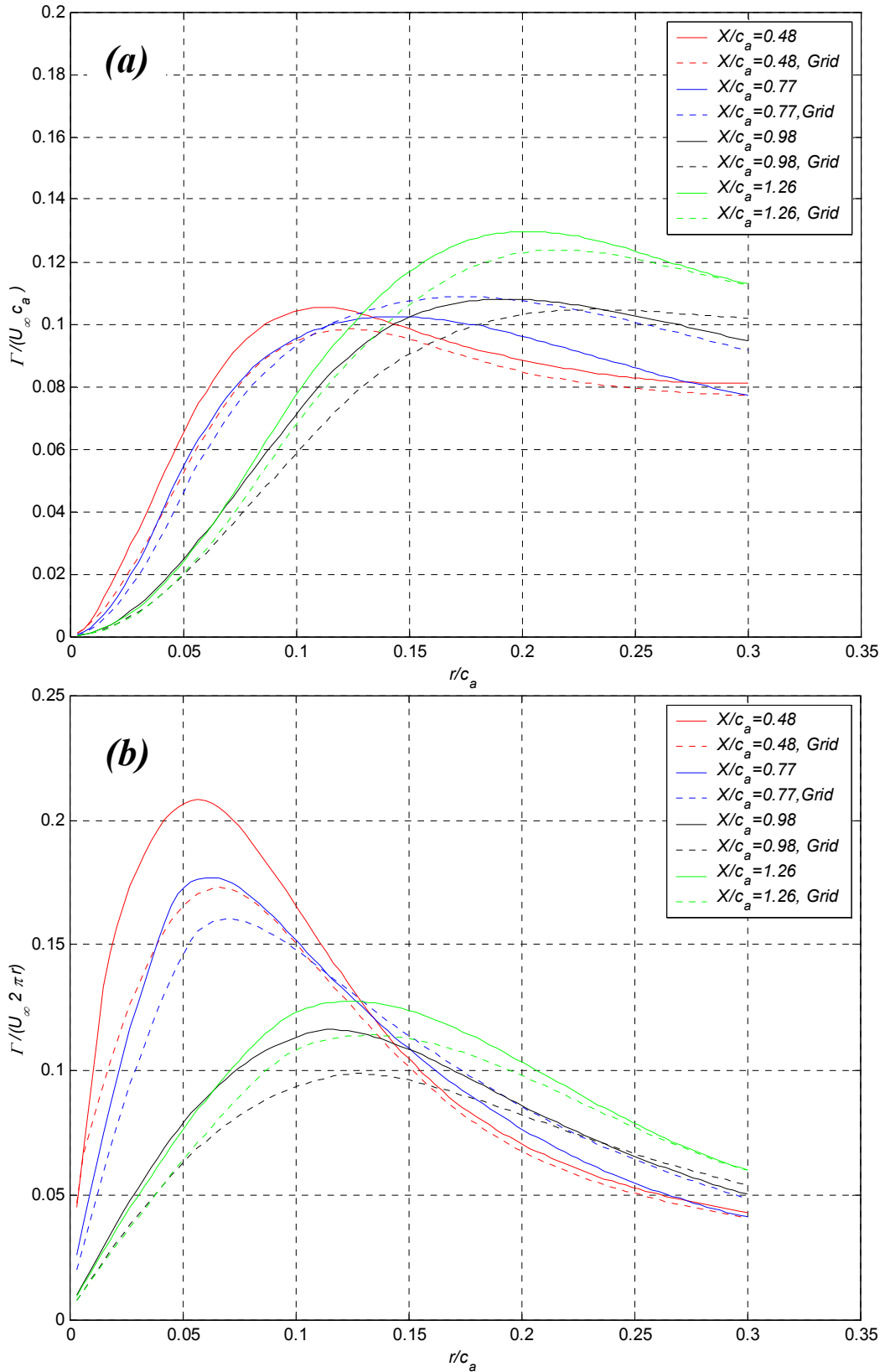


Figure 3.46: Plots of (a) Circulation and (b) Circumferentially averaged tangential velocity in the tip leakage vortex as a function of normalized radius from the vortex center, measured perpendicular to the x direction.

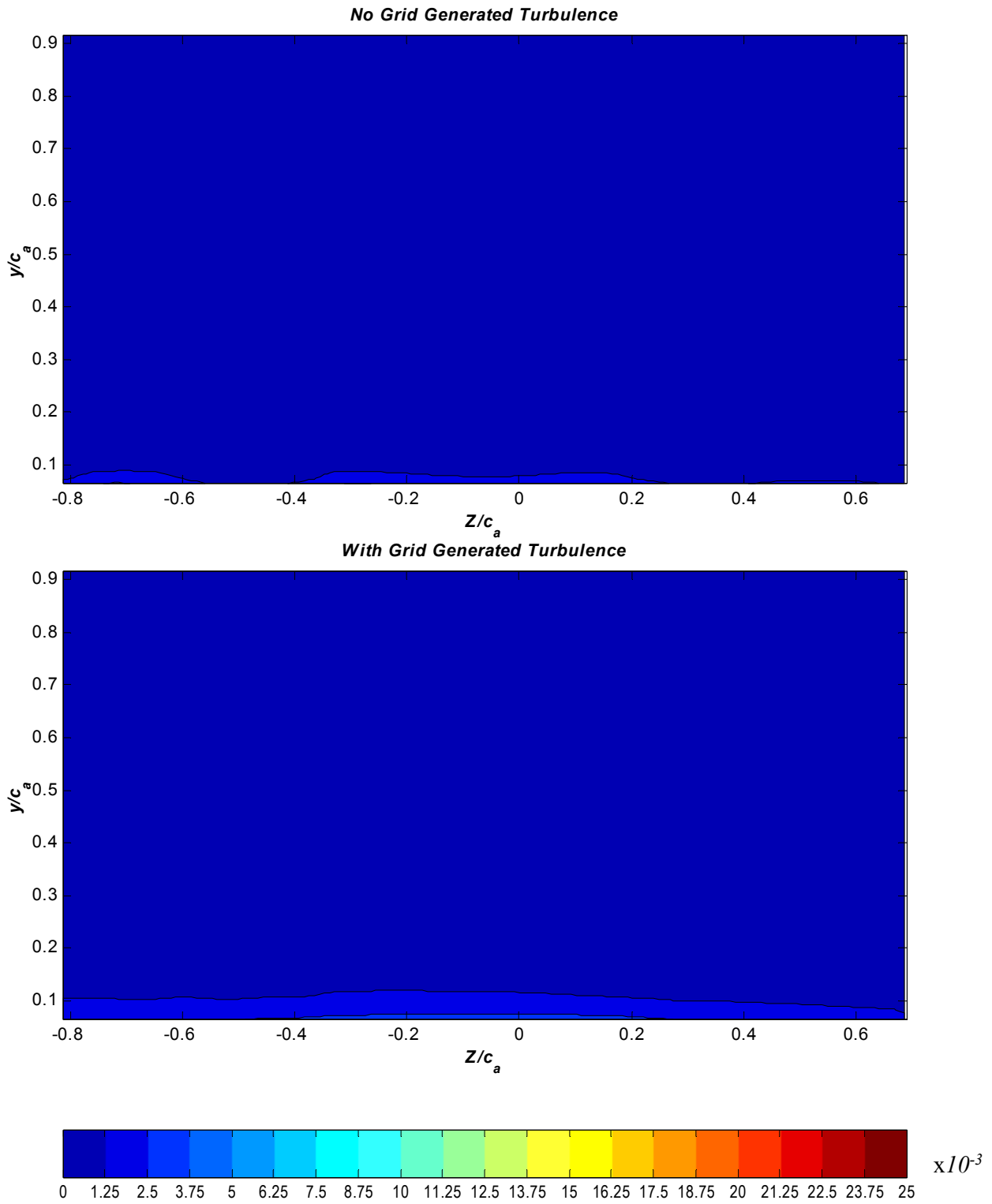


Figure 3.47a: Contours of the normalized turbulence kinetic energy, k/U_∞^2 , at $X/c_a=0.0$
Titles on plots indicate inflow turbulence condition

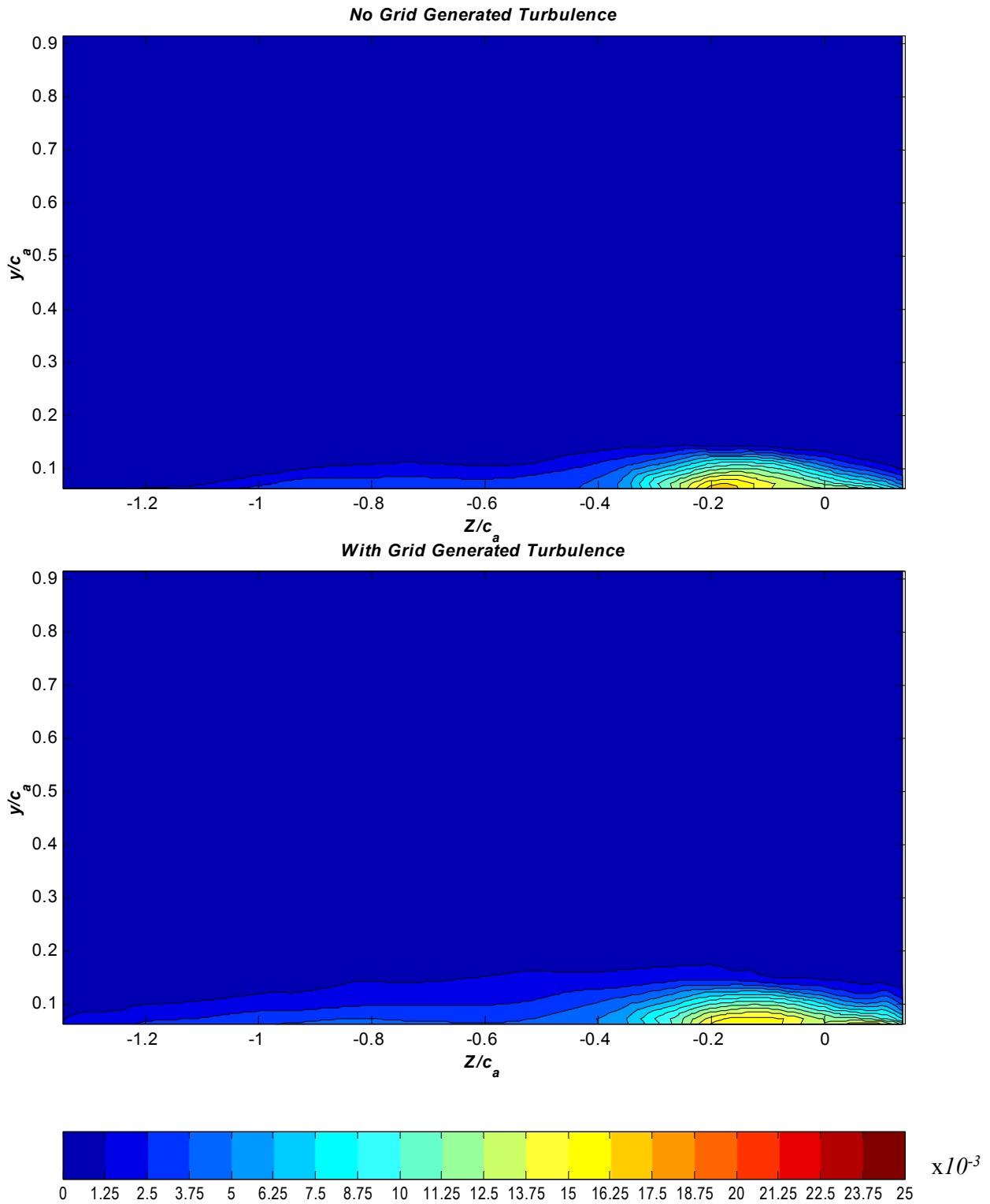


Figure 3.47b: Contours of the normalized turbulence kinetic energy, k/U_∞^2 , at $X/c_a=0.27$. Vortex centers defined by peak mean streamwise vorticity are indicated by circular crosses. Titles on plots indicate inflow turbulence condition

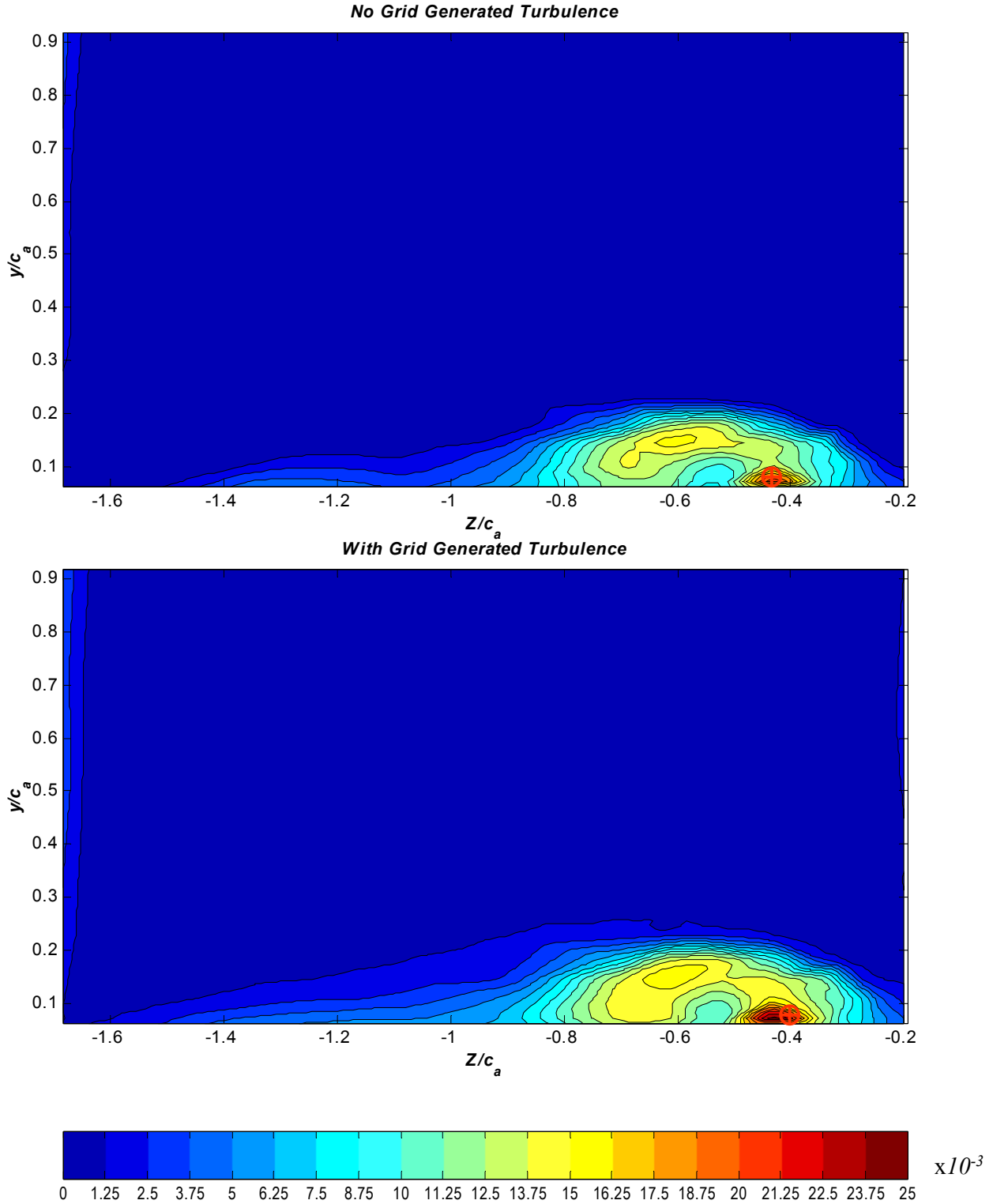


Figure 3.47c: Contours of the normalized turbulence kinetic energy, k/U_∞^2 , at $X/c_a=0.48$. Vortex centers defined by peak mean streamwise vorticity are indicated by circular crosses. Titles on plots indicate inflow turbulence condition

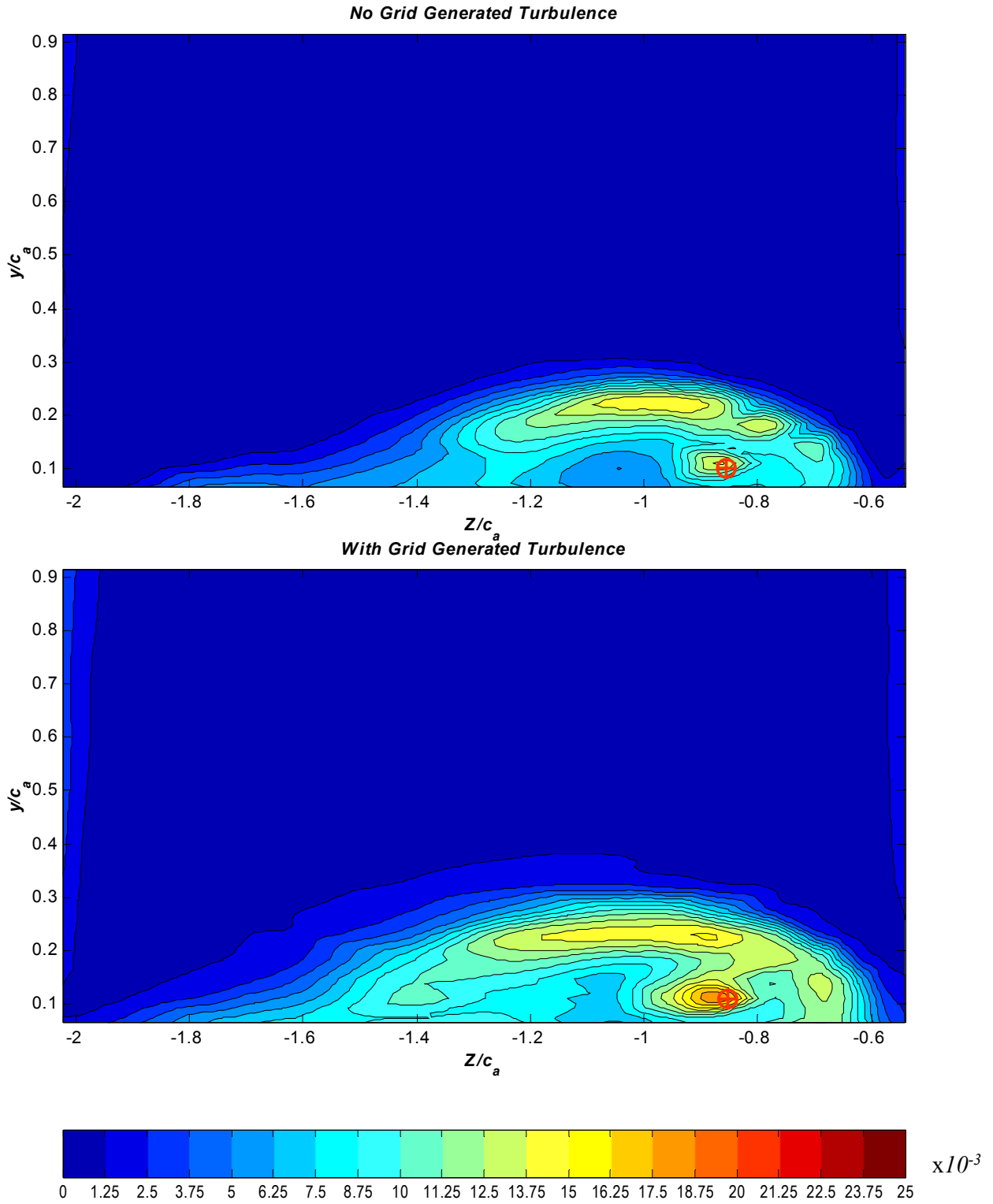


Figure 3.47d: Contours of the normalized turbulence kinetic energy, k/U_∞^2 , at $X/c_a=0.77$. Vortex centers defined by peak mean streamwise vorticity are indicated by circular crosses. Titles on plots indicate inflow turbulence condition

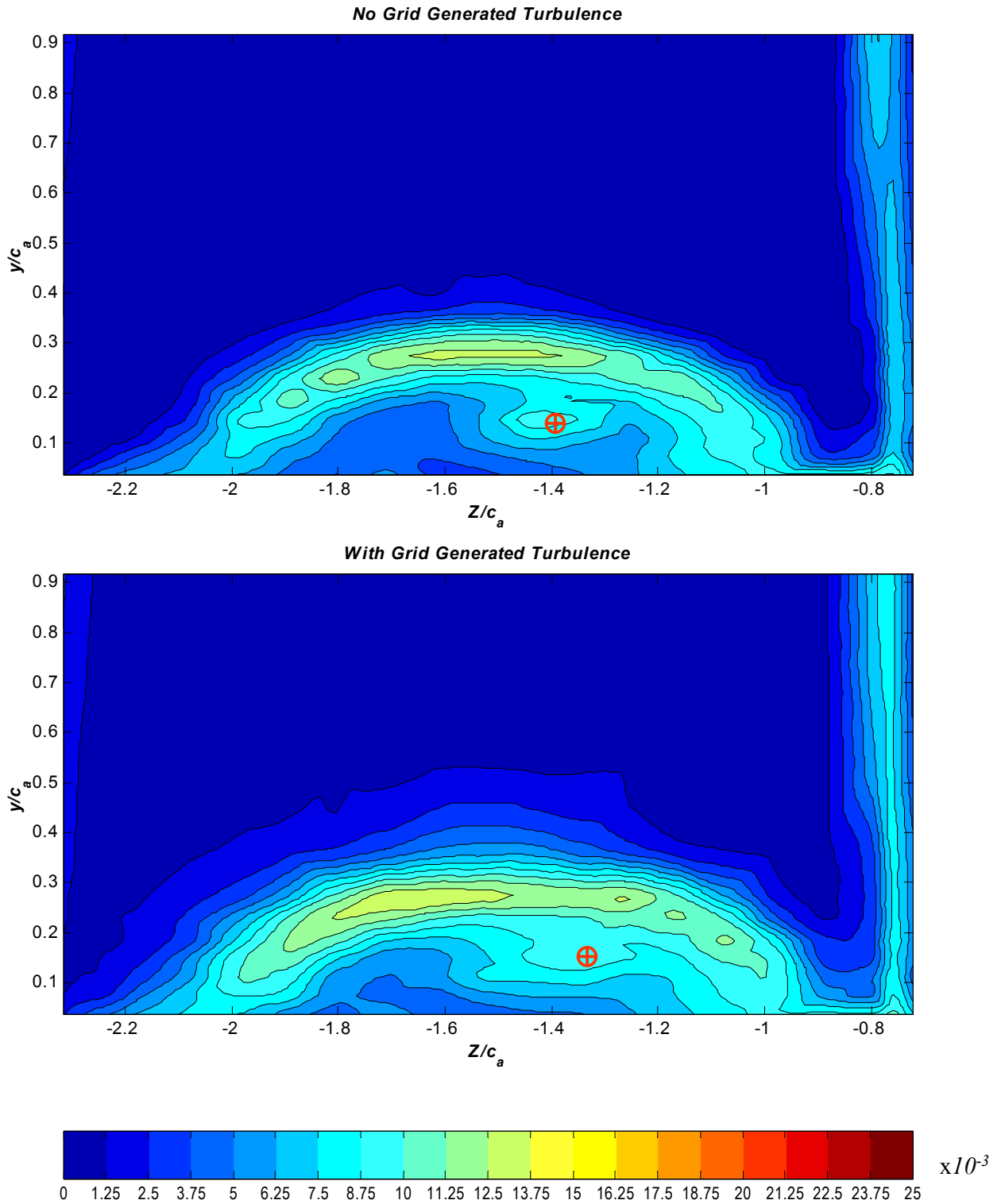


Figure 3.47e: Contours of the normalized turbulence kinetic energy, k/U_∞^2 , at $X/c_a=0.98$. Vortex centers defined by peak mean streamwise vorticity are indicated by circular crosses. Titles on plots indicate inflow turbulence condition

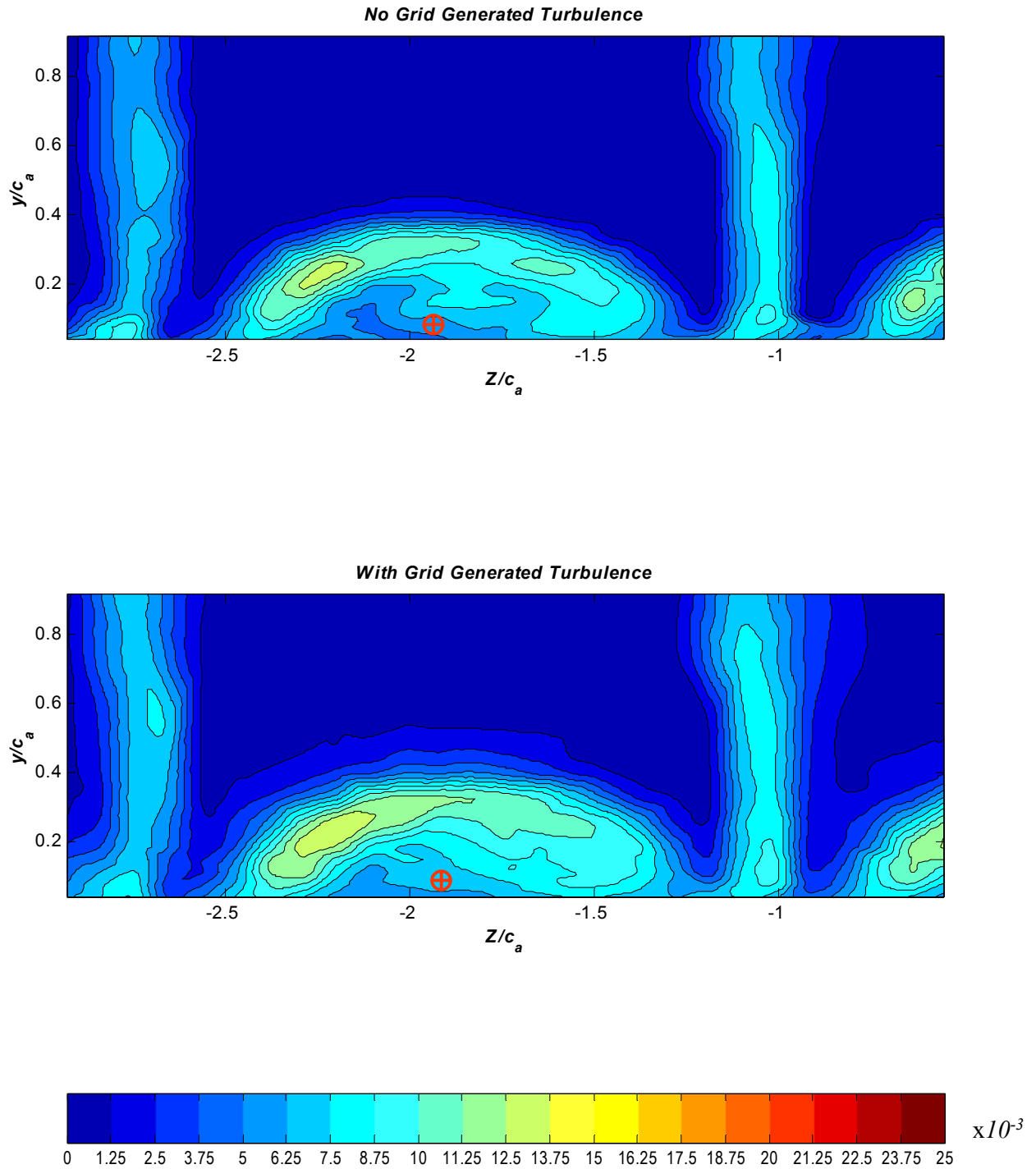


Figure 3.47f: Contours of the normalized turbulence kinetic energy, k/U_∞^2 , at $X/c_a=1.26$. Vortex centers defined by peak mean streamwise vorticity are indicated by circular crosses. Titles on plots indicate inflow turbulence condition

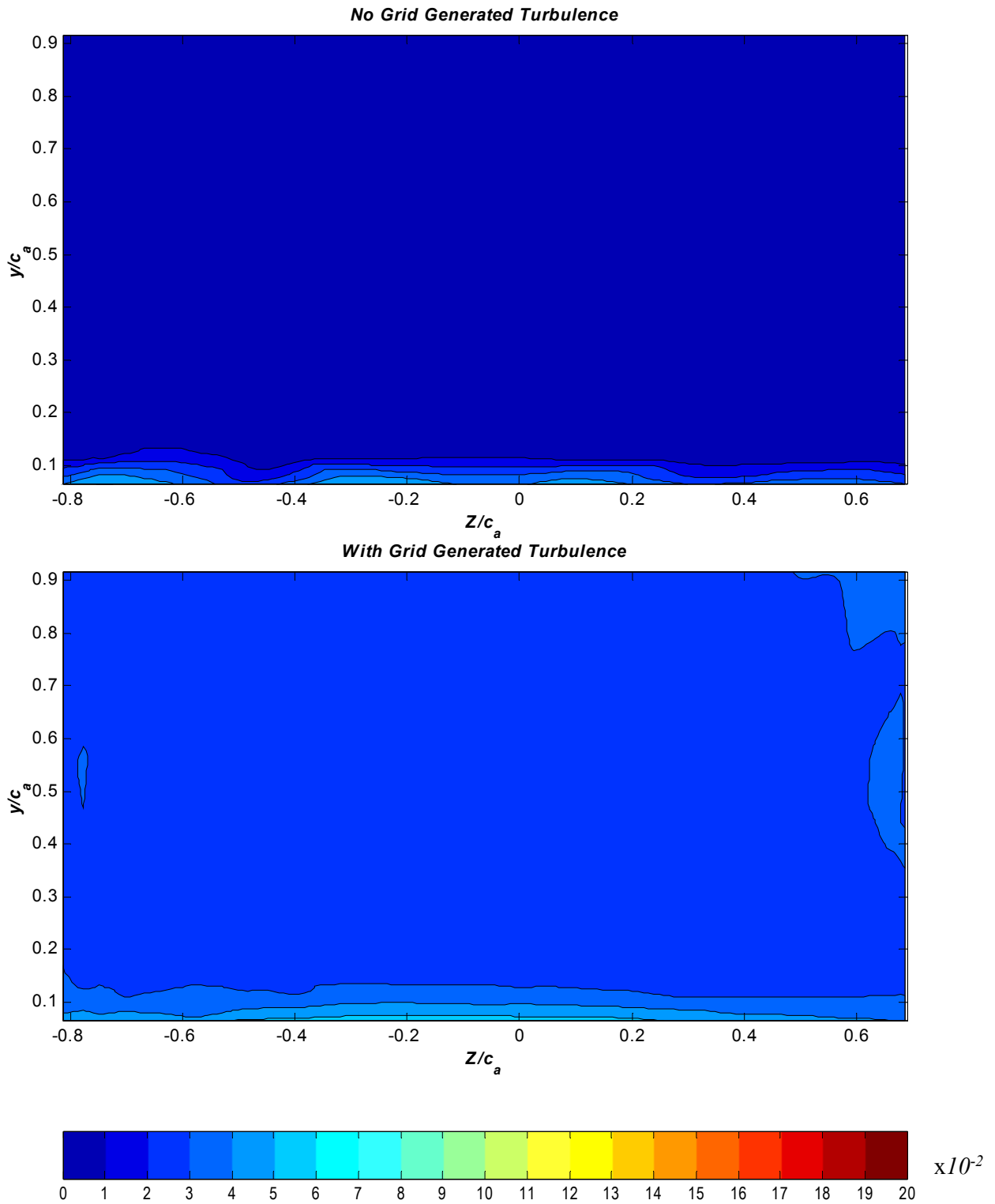


Figure 3.48a: Contours of the square root of the Reynolds Normal Stress, $\sqrt{(u^2/U_\infty^2)}$, at $X/c_a=0.0$. Titles on plots indicate inflow turbulence condition

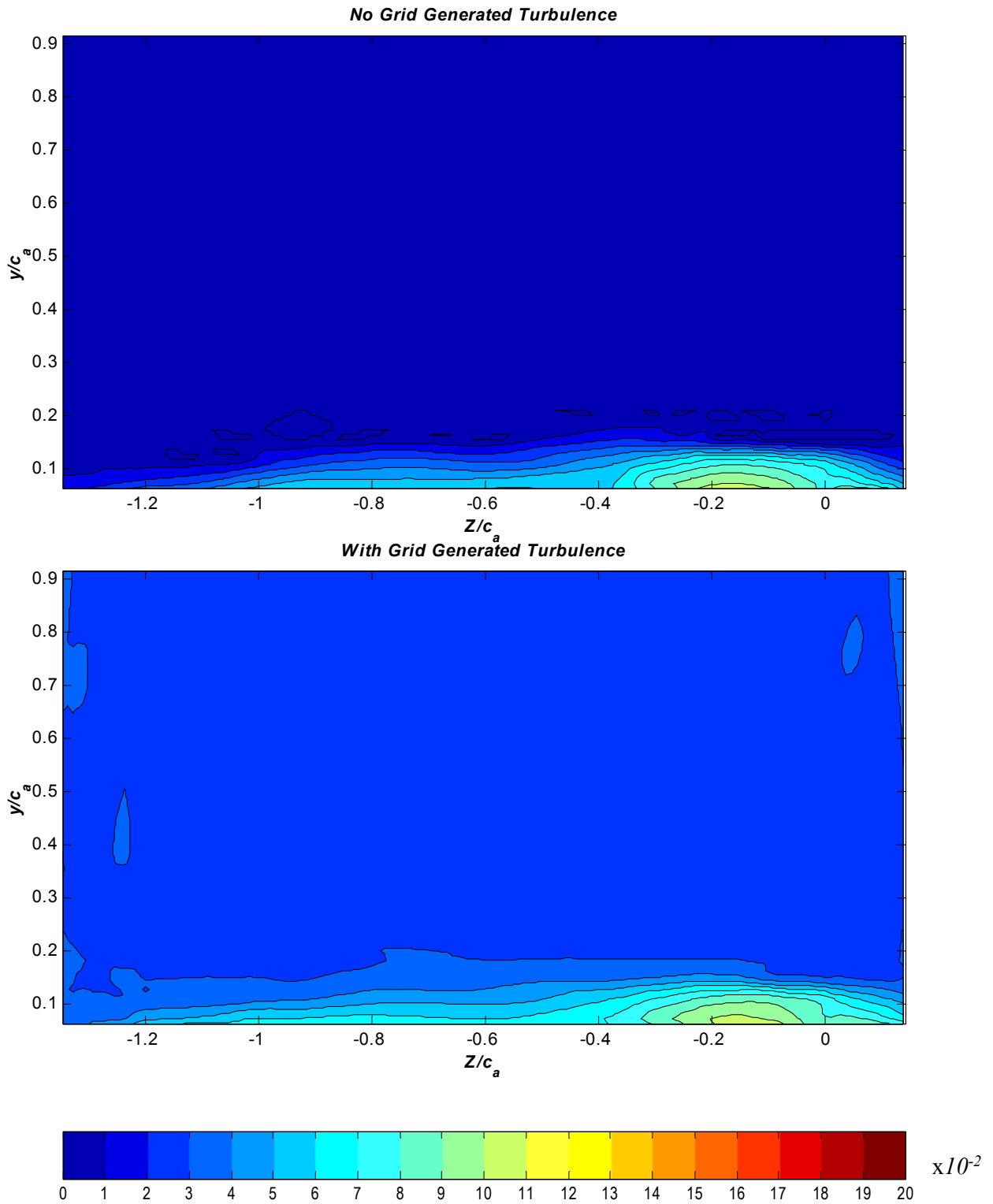


Figure 3.48b: Contours of the square root of the Reynolds Normal Stress, $\sqrt{(u^2/U_\infty^2)}$, at $X/c_a=0.27$. Titles on plots indicate inflow turbulence condition

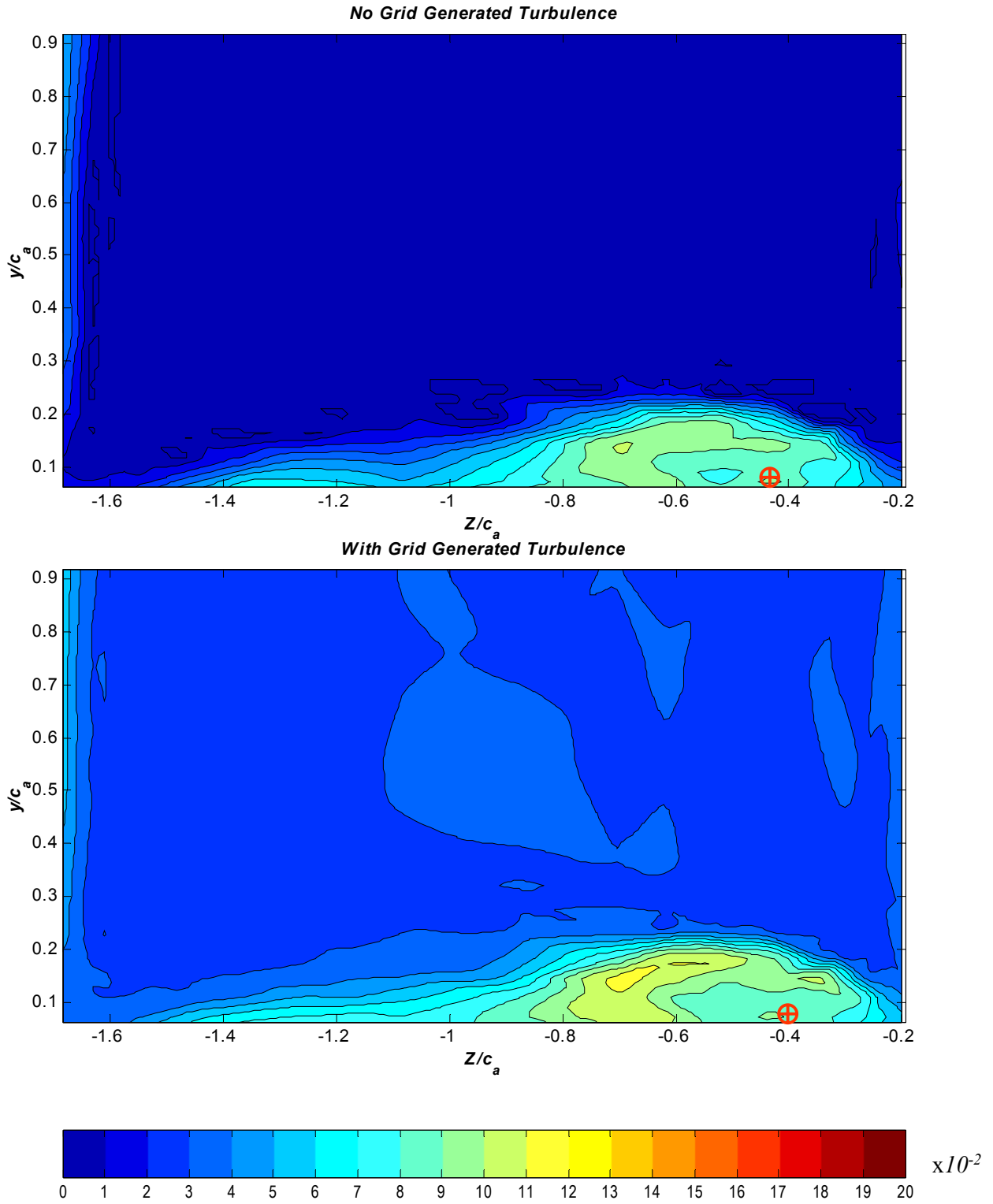


Figure 3.48c: Contours of the square root of the Reynolds Normal Stress, $\sqrt{u^2/U_\infty^2}$, at $X/c_a=0.48$. Vortex centers defined by peak mean streamwise vorticity are indicated by circular crosses. Titles on plots indicate inflow turbulence condition

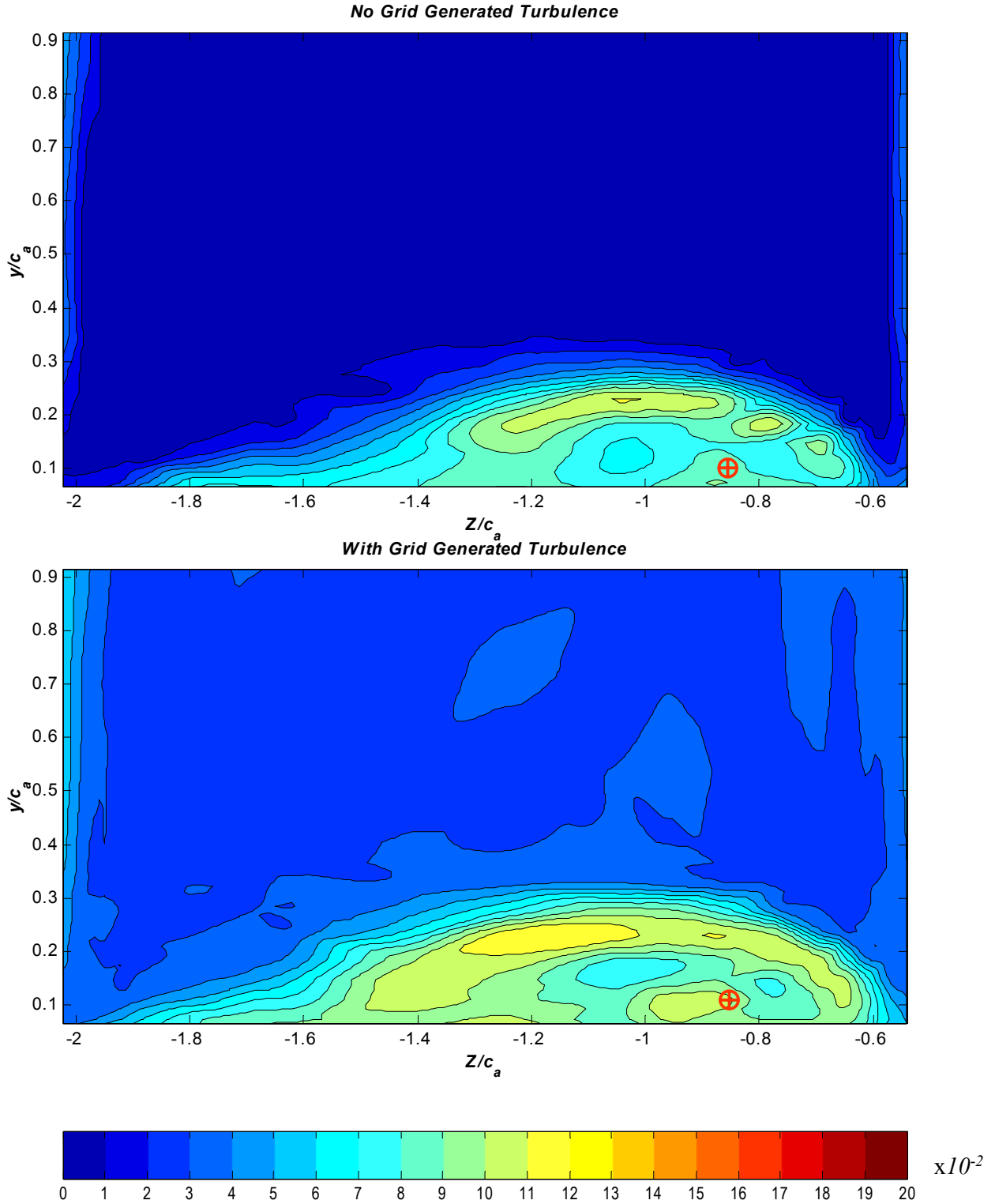


Figure 3.48d: Contours of the square root of the Reynolds Normal Stress, $\sqrt{(u^2/U_\infty^2)}$, at $X/c_a=0.77$. Vortex centers defined by peak mean streamwise vorticity are indicated by circular crosses. Titles on plots indicate inflow turbulence condition

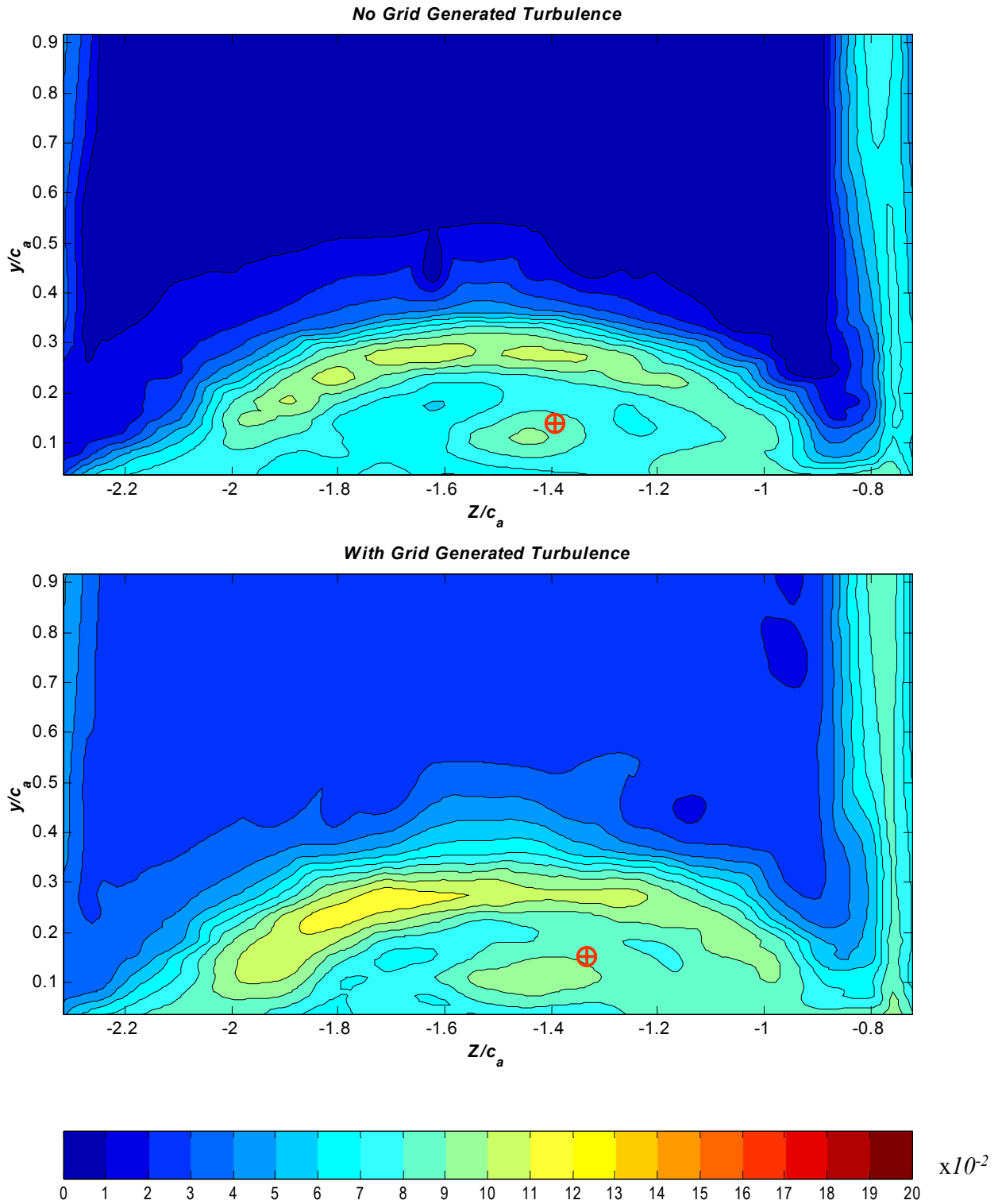


Figure 3.48e: Contours of the square root of the Reynolds Normal Stress, $\sqrt{(u^2/U_\infty^2)}$, at $X/c_a=0.98$. Vortex centers defined by peak mean streamwise vorticity are indicated by circular crosses. Titles on plots indicate inflow turbulence condition

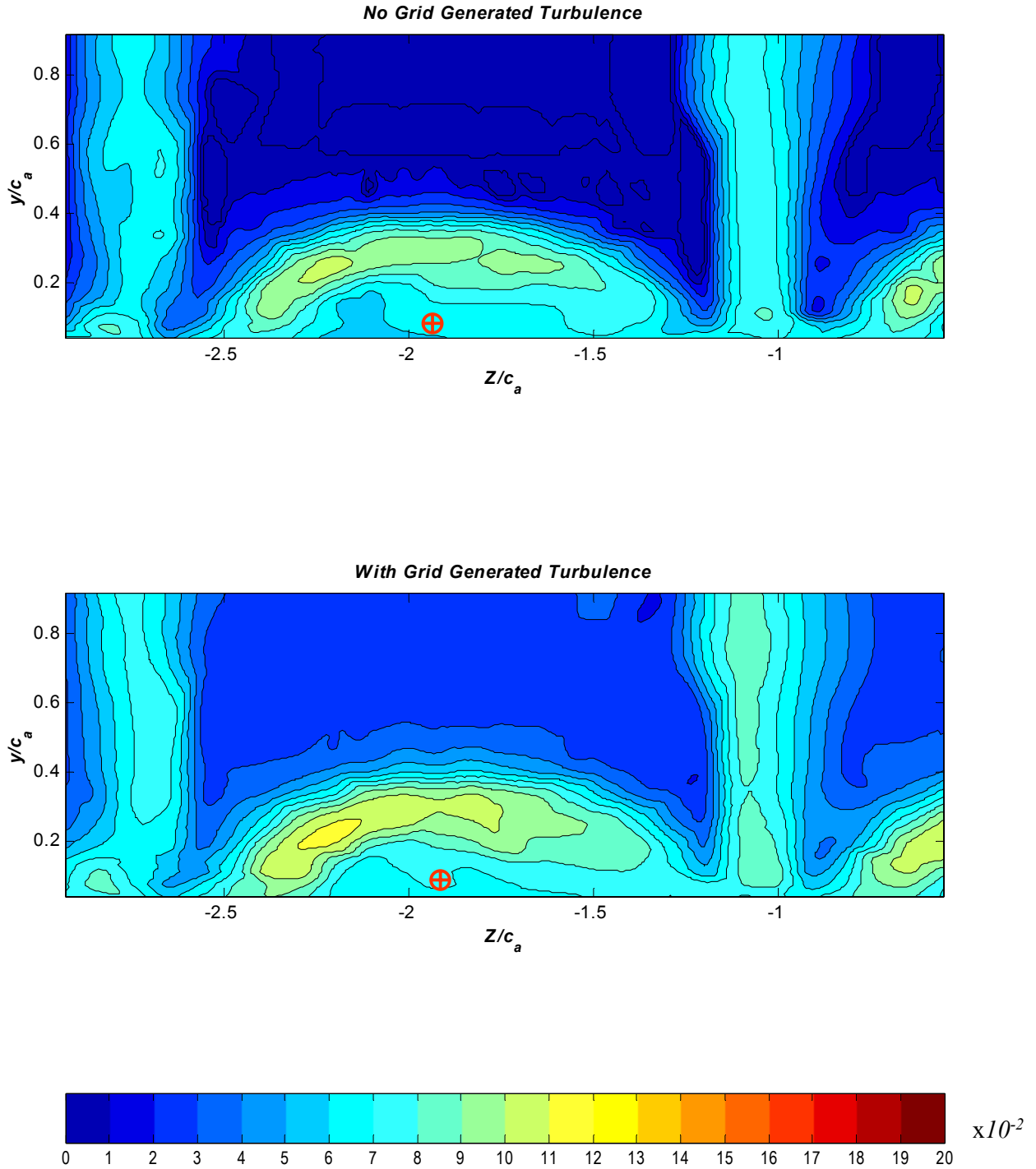


Figure 3.48f: Contours of the square root of the Reynolds Normal Stress, $\sqrt{(u^2/U_\infty^2)}$, at $X/c_a=1.26$. Vortex centers defined by peak mean streamwise vorticity are indicated by circular crosses. Titles on plots indicate inflow turbulence condition

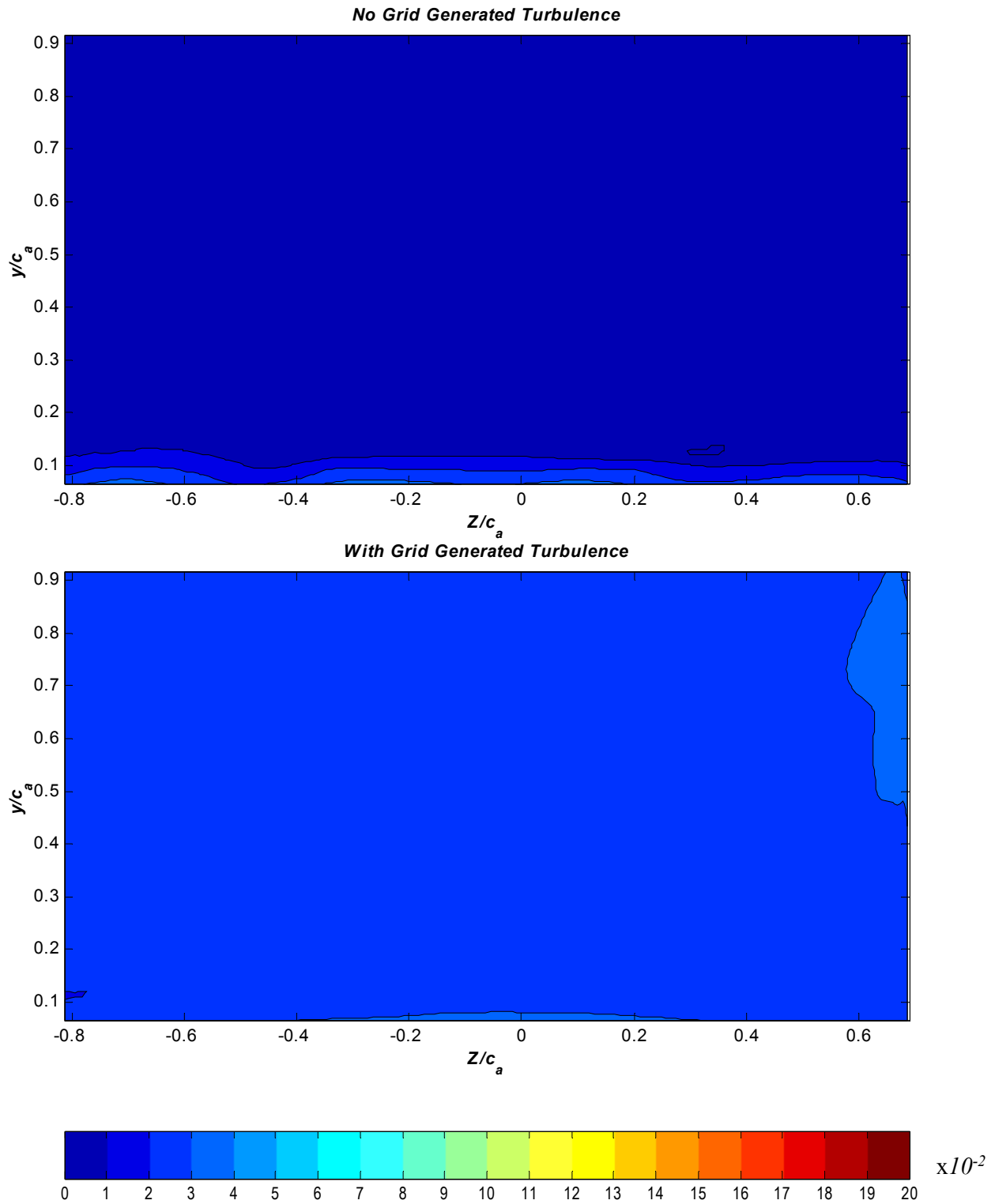


Figure 3.49a: Contours of the square root of the Reynolds Normal Stress, $\sqrt{(v^2/U_\infty^2)}$, at $X/c_a=0.0$. Titles on plots indicate inflow turbulence condition

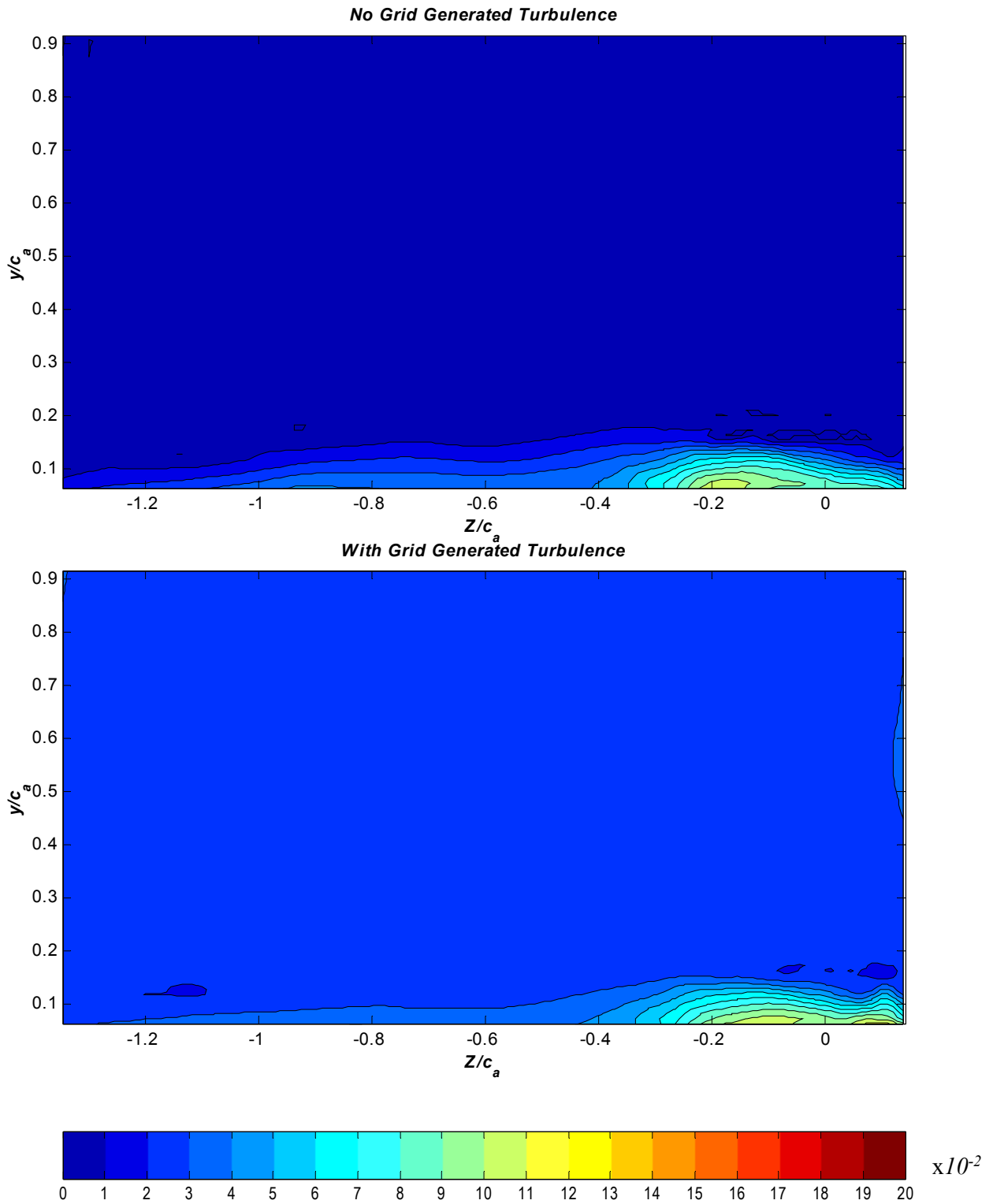


Figure 3.49b: Contours of the square root of the Reynolds Normal Stress, $\sqrt{(v^2/U_\infty^2)}$, at $X/c_a=0.27$. Titles on plots indicate inflow turbulence condition

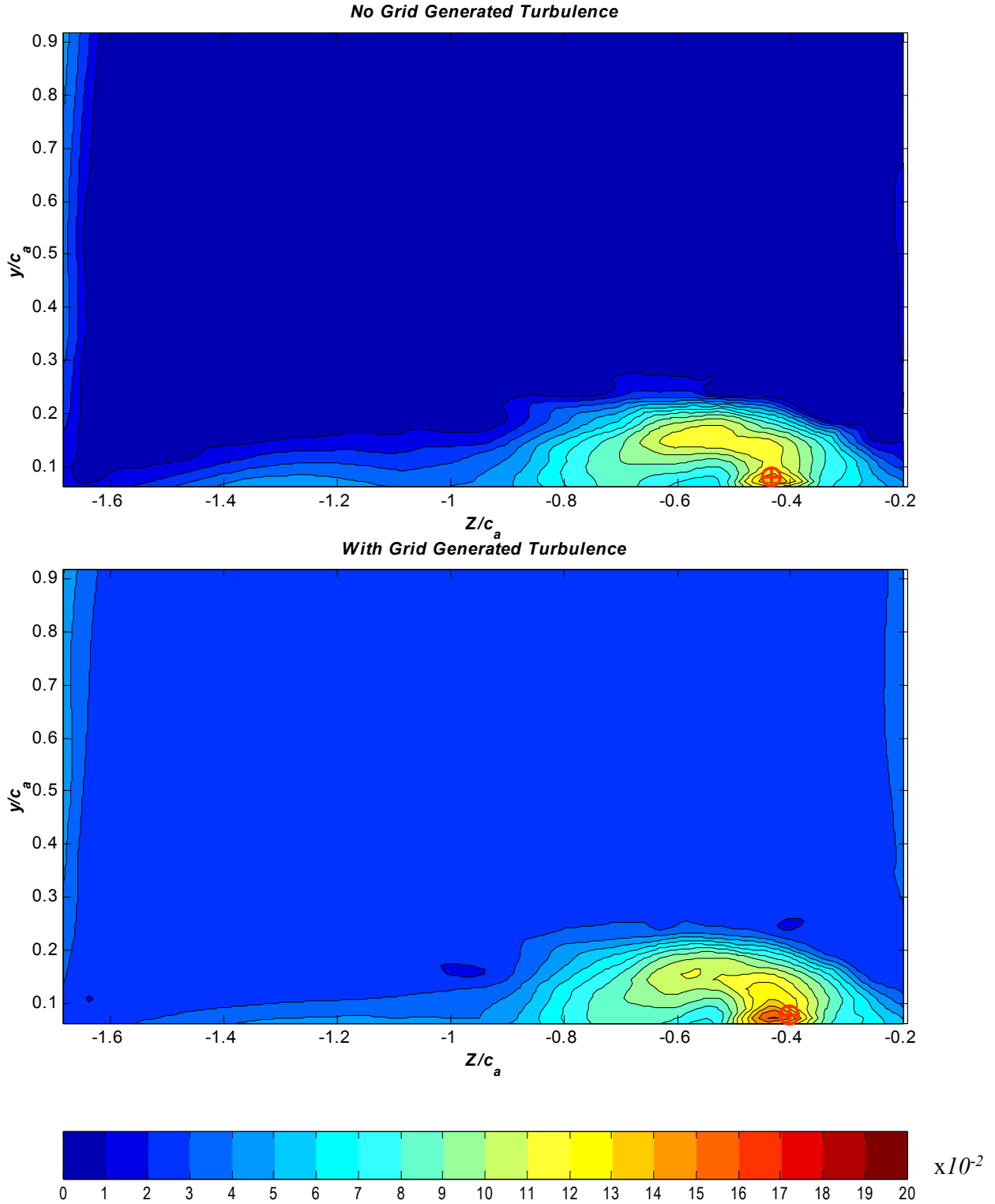


Figure 3.49c: Contours of the square root of the Reynolds Normal Stress, $\sqrt{(v^2/U_\infty^2)}$, at $X/c_a=0.48$. Vortex centers defined by peak mean streamwise vorticity are indicated by circular crosses. Titles on plots indicate inflow turbulence condition

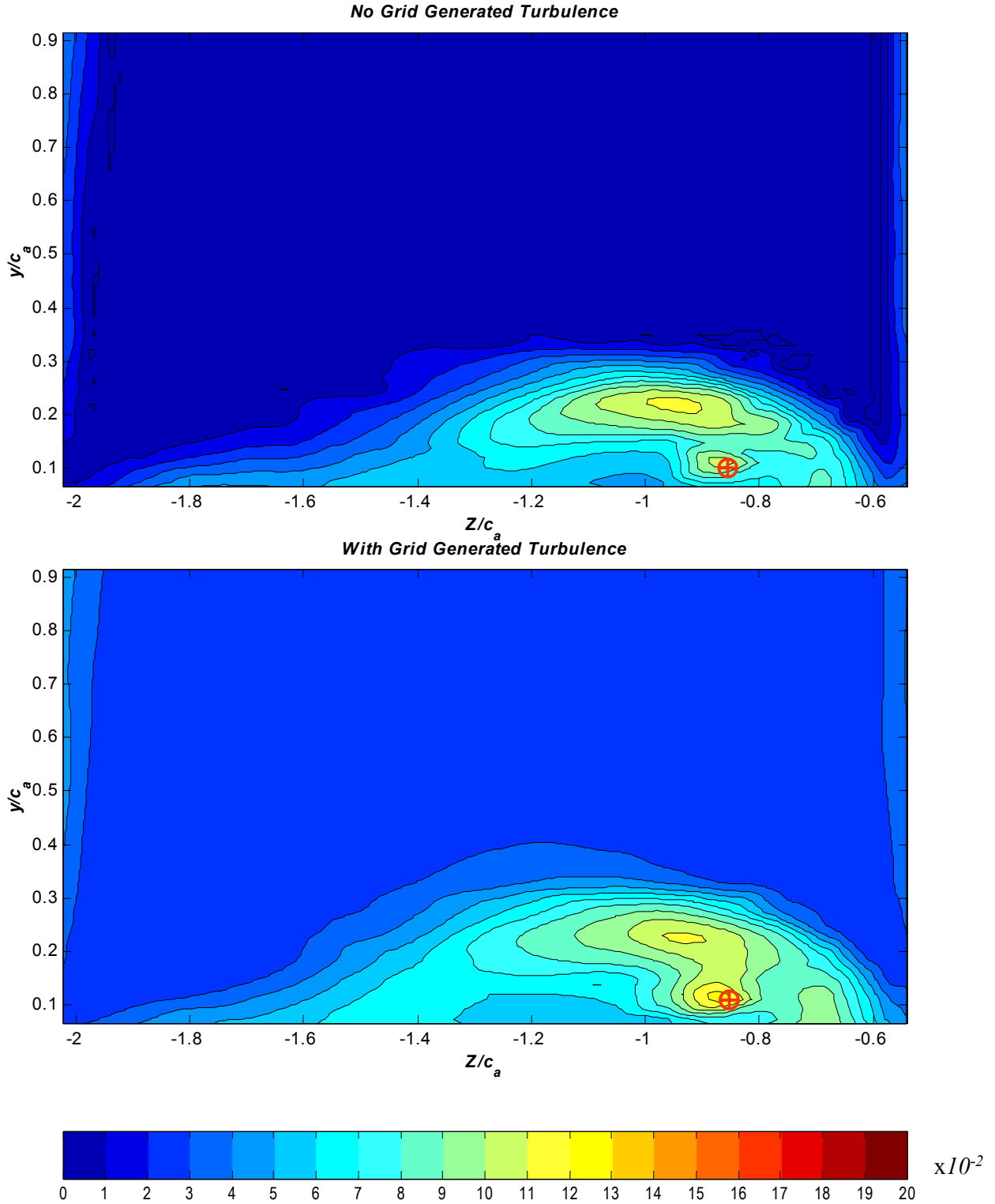


Figure 3.49d: Contours of the square root of the Reynolds Normal Stress, $\sqrt{(v^2/U_\infty^2)}$, at $X/c_a=0.77$. Vortex centers defined by peak mean streamwise vorticity are indicated by circular crosses. Titles on plots indicate inflow turbulence condition

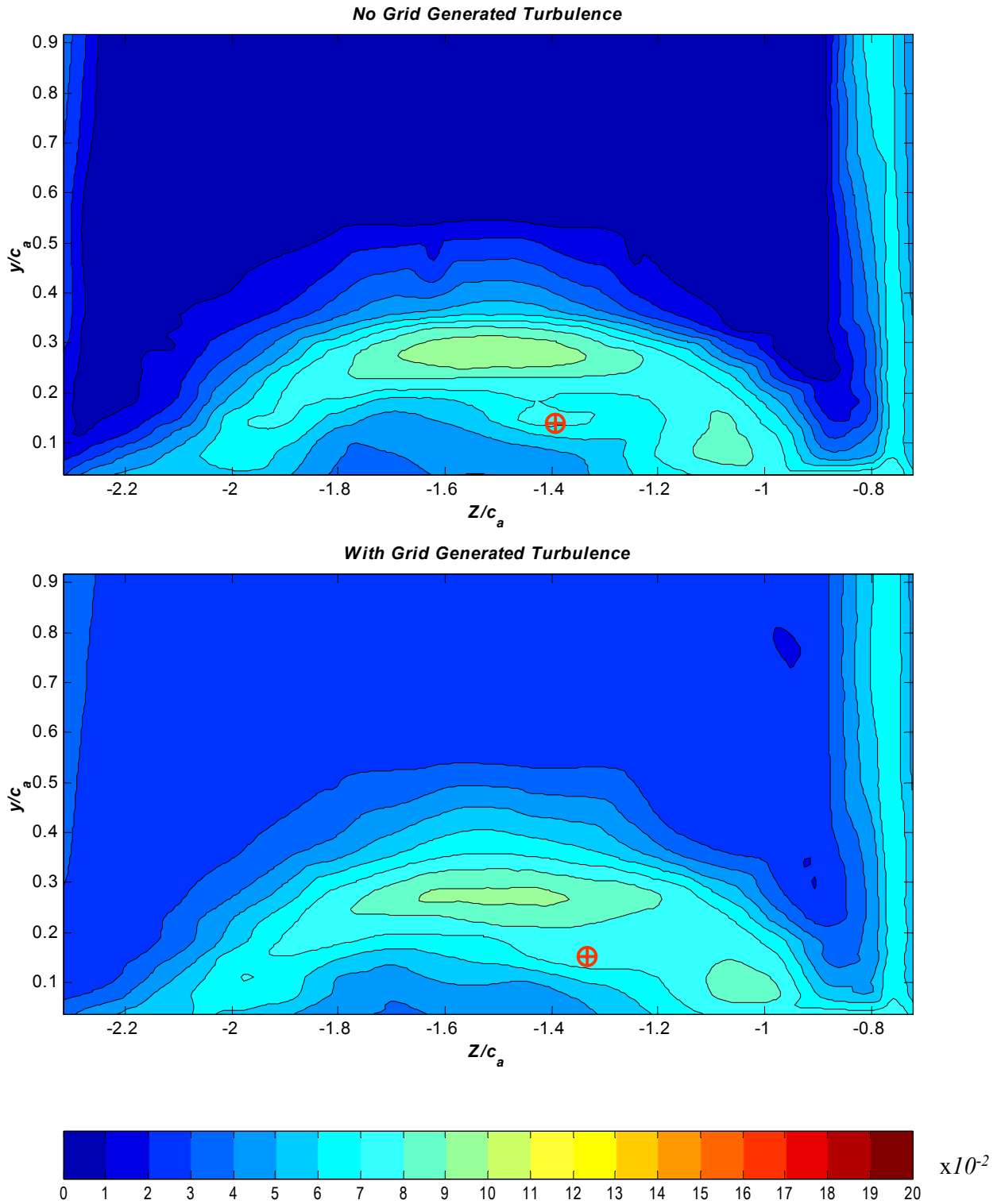


Figure 3.49e: Contours of the square root of the Reynolds Normal Stress, $\sqrt{(v^2/U_\infty^2)}$, at $X/c_a=0.98$. Vortex centers defined by peak mean streamwise vorticity are indicated by circular crosses. Titles on plots indicate inflow turbulence condition

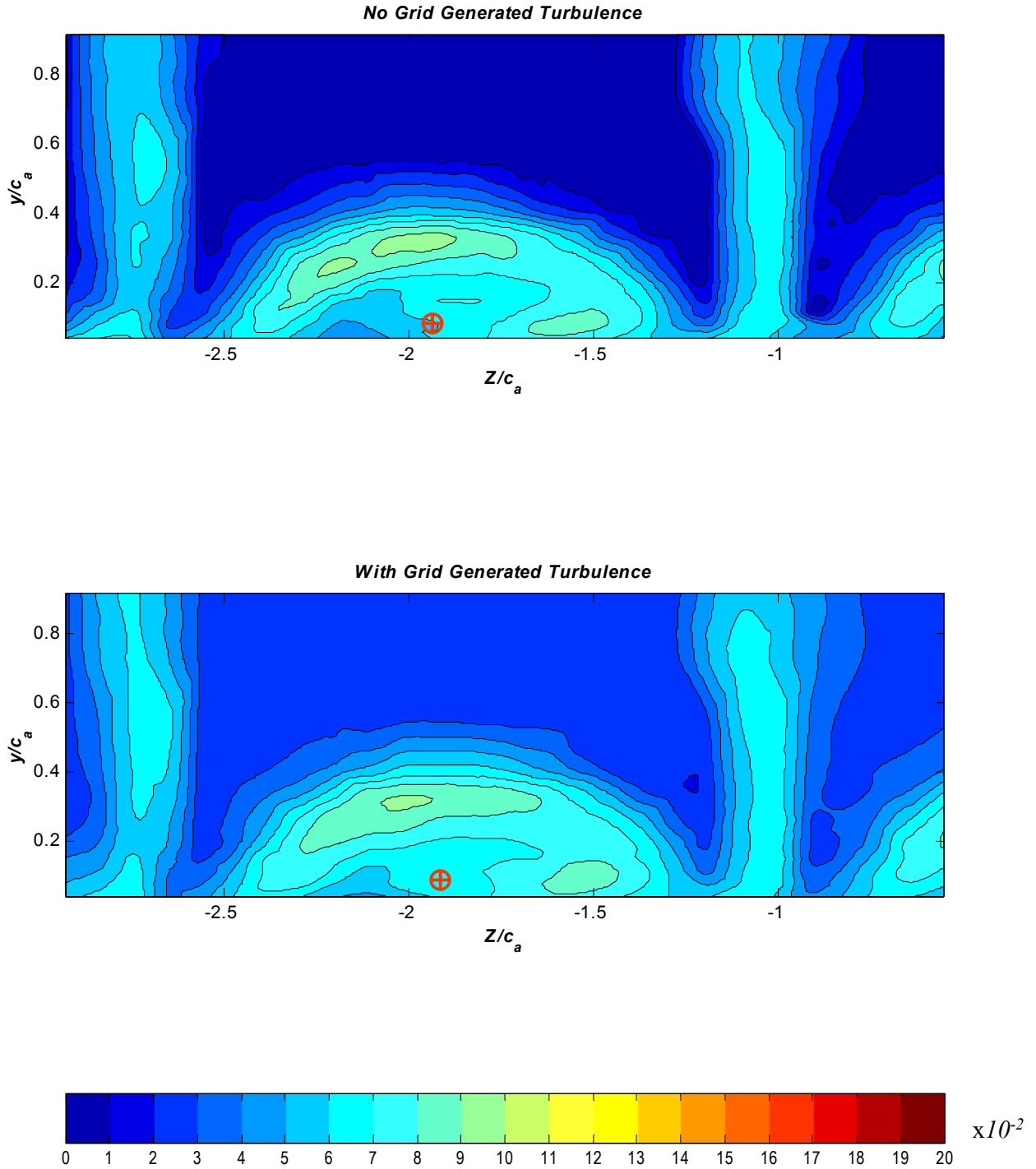


Figure 3.49f: Contours of the square root of the Reynolds Normal Stress, $\sqrt{(v^2/U_\infty^2)}$, at $X/c_a=1.26$. Vortex centers defined by peak mean streamwise vorticity are indicated by circular crosses. Titles on plots indicate inflow turbulence condition

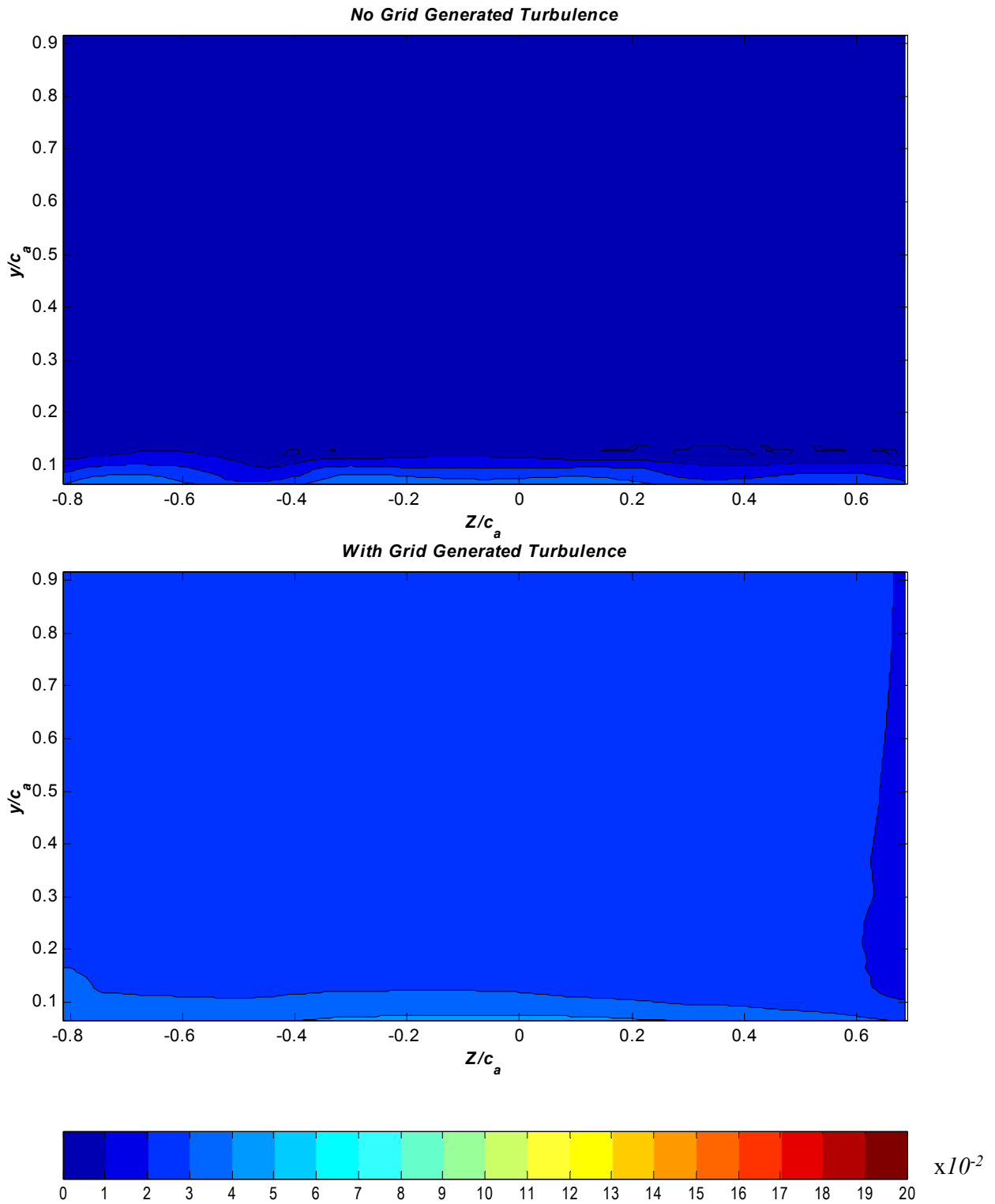


Figure 3.50a: Contours of the square root of the Reynolds Normal Stress, $\sqrt{(w^2/U_\infty^2)}$, at $X/c_a=0.0$. Titles on plots indicate inflow turbulence condition

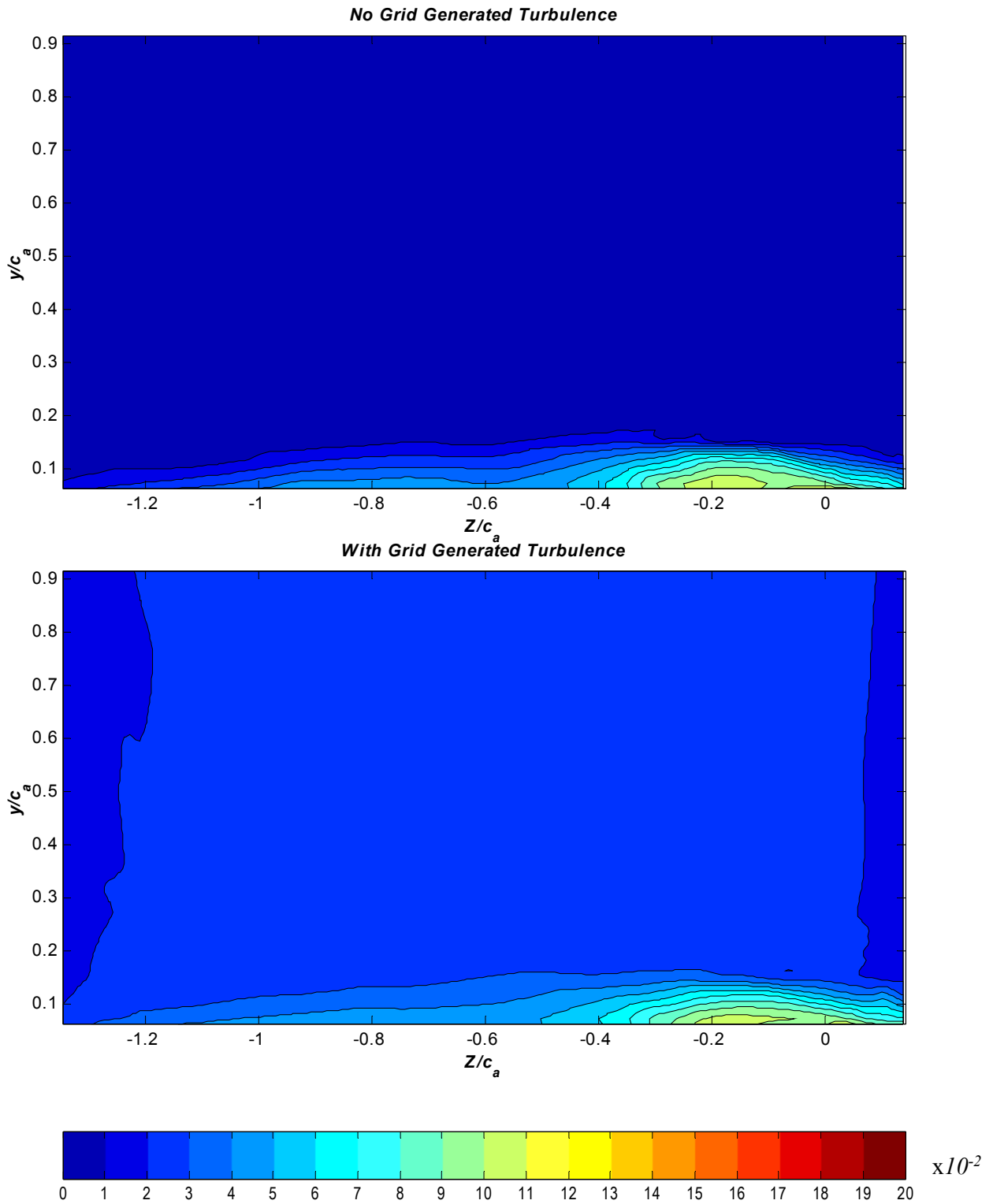


Figure 3.50b: Contours of the square root of the Reynolds Normal Stress, $\sqrt{(w^2/U_\infty^2)}$, at $X/c_a=0.27$. Titles on plots indicate inflow turbulence condition

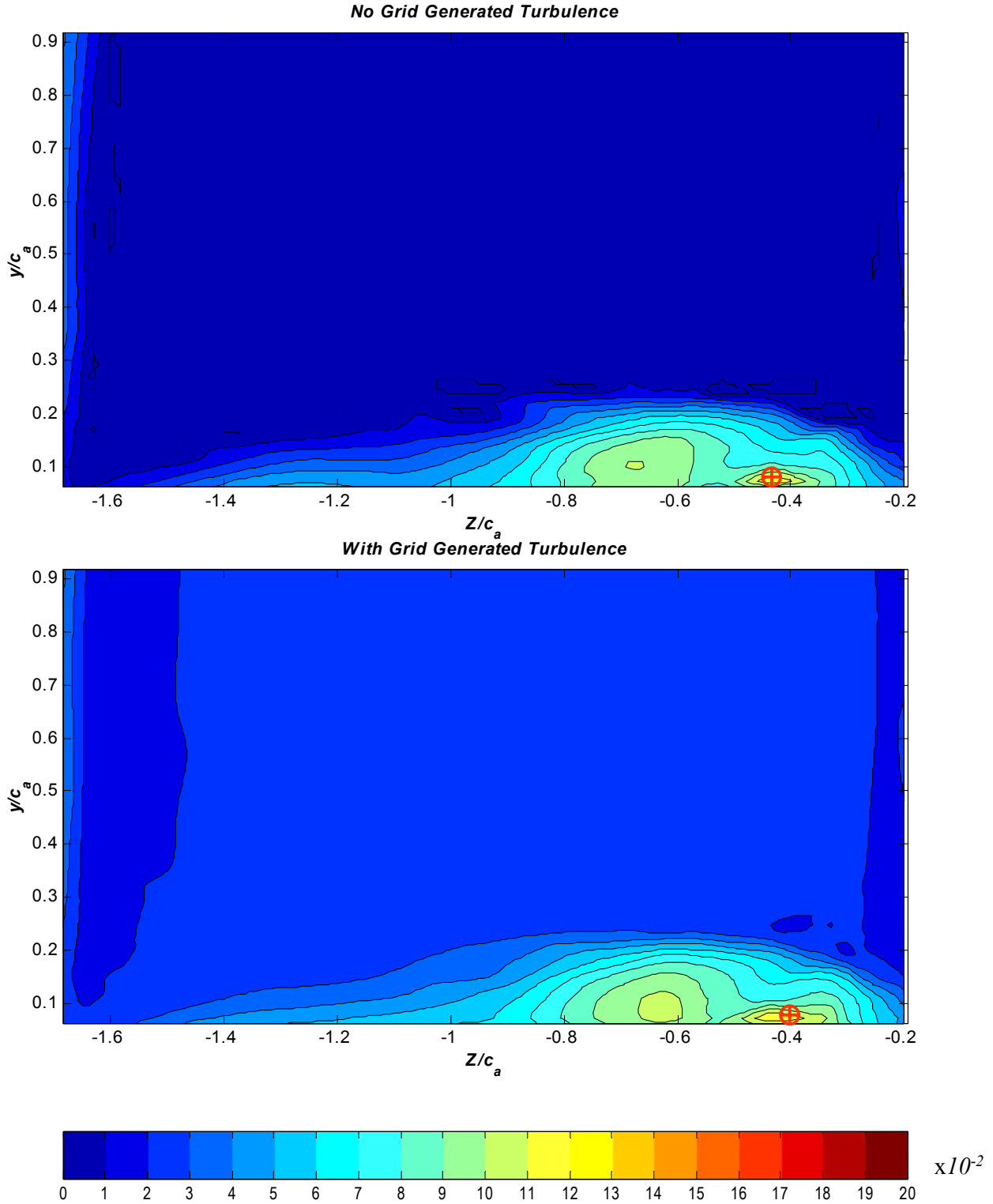


Figure 3.50c: Contours of the square root of the Reynolds Normal Stress, $\sqrt{(w^2/U_\infty^2)}$, at $X/c_a=0.48$. Titles on plots indicate inflow turbulence condition

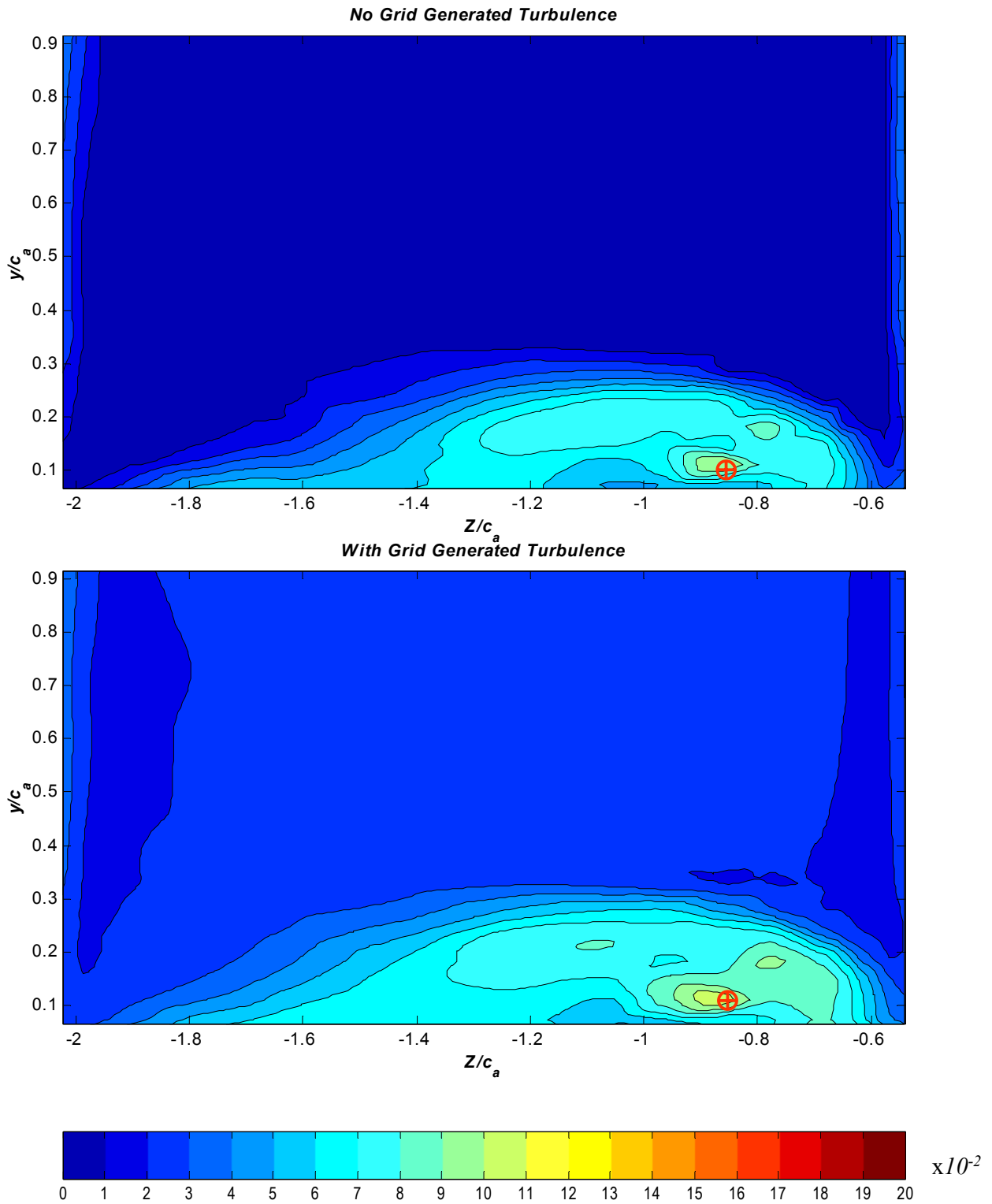


Figure 3.50d: Contours of the square root of the Reynolds Normal Stress, $\sqrt{(w^2/U_\infty^2)}$, at $X/c_a=0.77$. Vortex centers defined by peak mean streamwise vorticity are indicated by circular crosses. Titles on plots indicate inflow turbulence condition

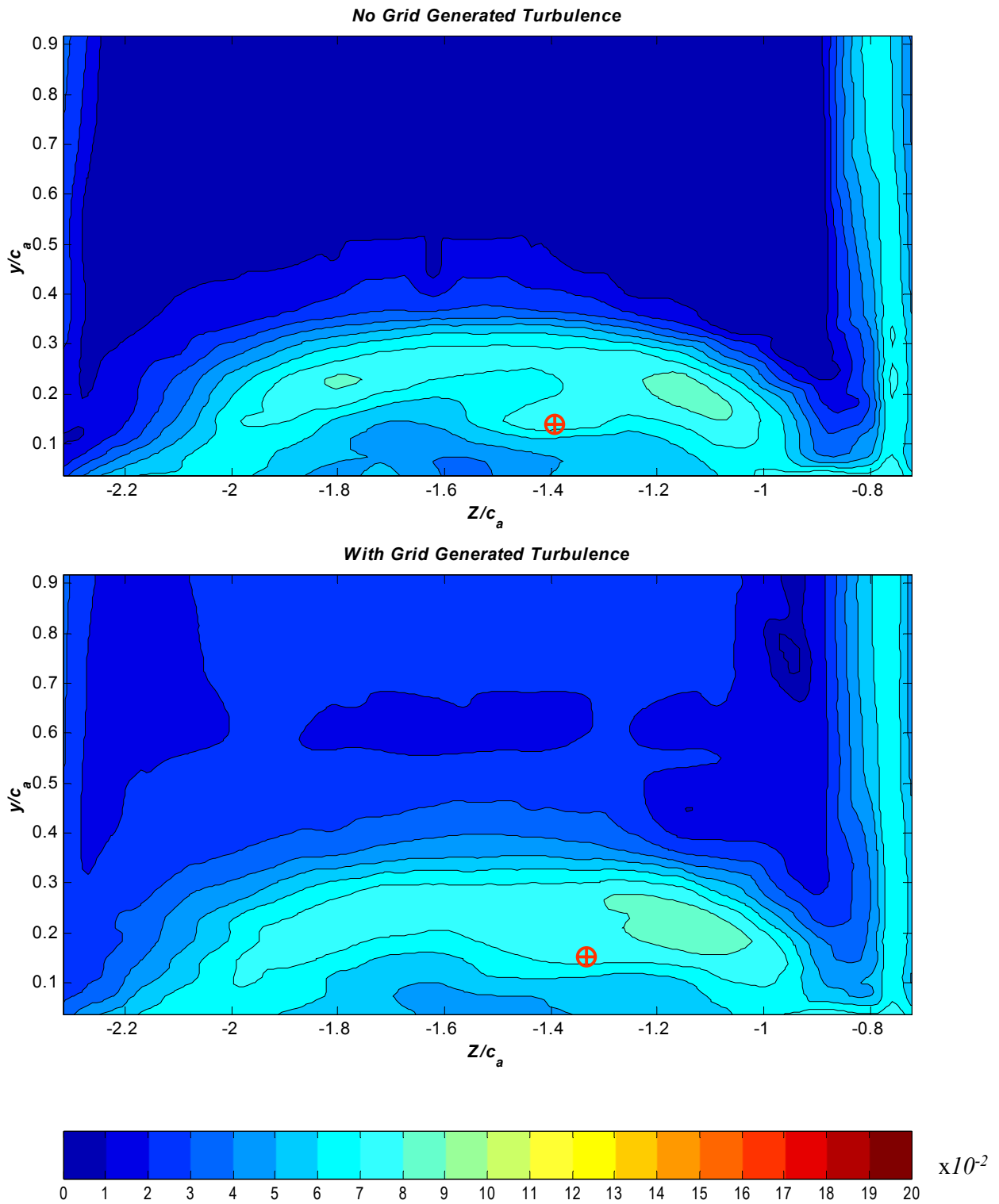


Figure 3.50e: Contours of the square root of the Reynolds Normal Stress, $\sqrt{(w^2/U_\infty^2)}$, at $X/c_a=0.98$. Vortex centers defined by peak mean streamwise vorticity are indicated by circular crosses. Titles on plots indicate inflow turbulence condition

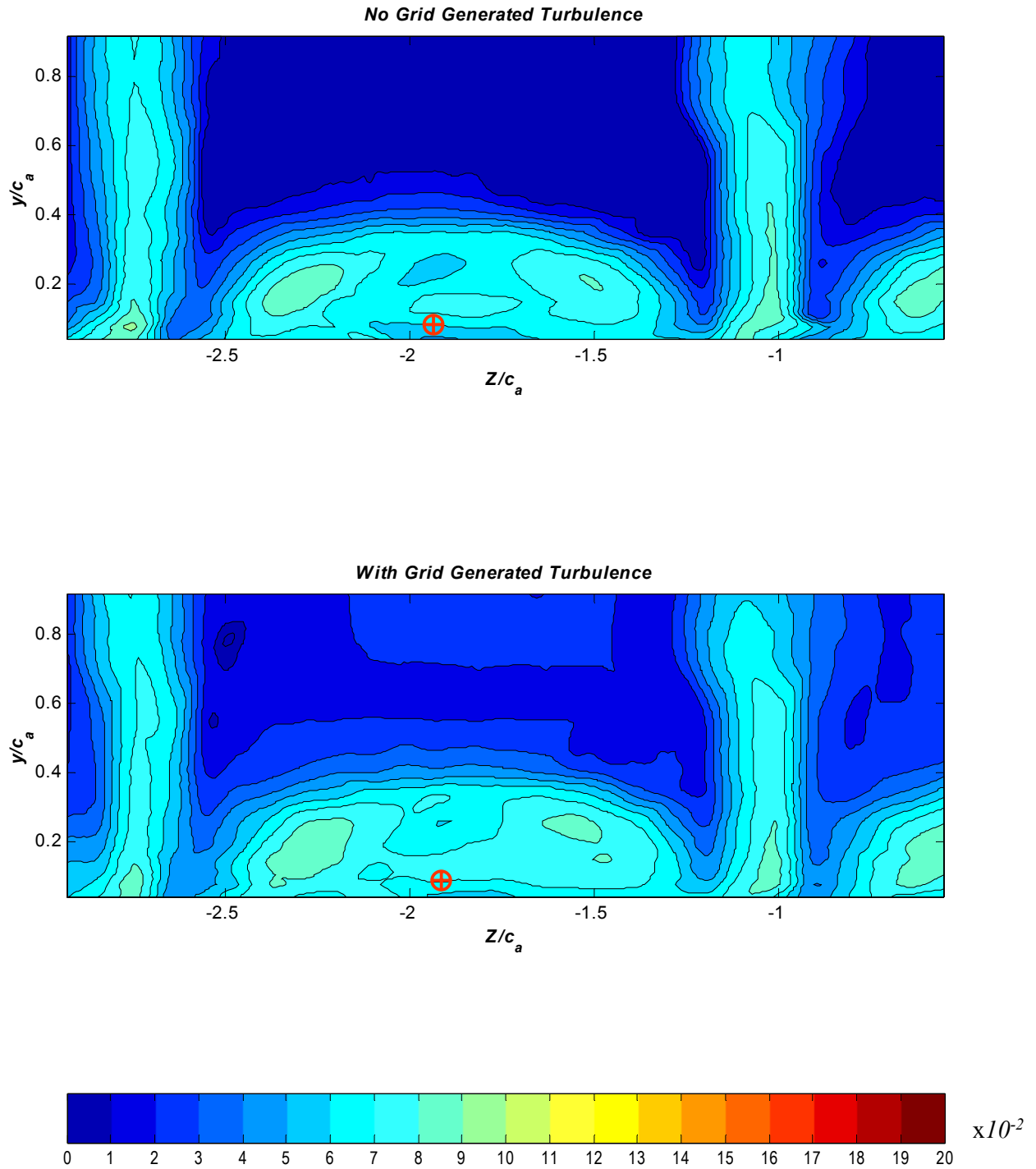


Figure 3.50f: Contours of the square root of the Reynolds Normal Stress, $\sqrt{(w^2/U_\infty^2)}$, at $X/c_a=1.26$. Vortex centers defined by peak mean streamwise vorticity are indicated by circular crosses. Titles on plots indicate inflow turbulence condition

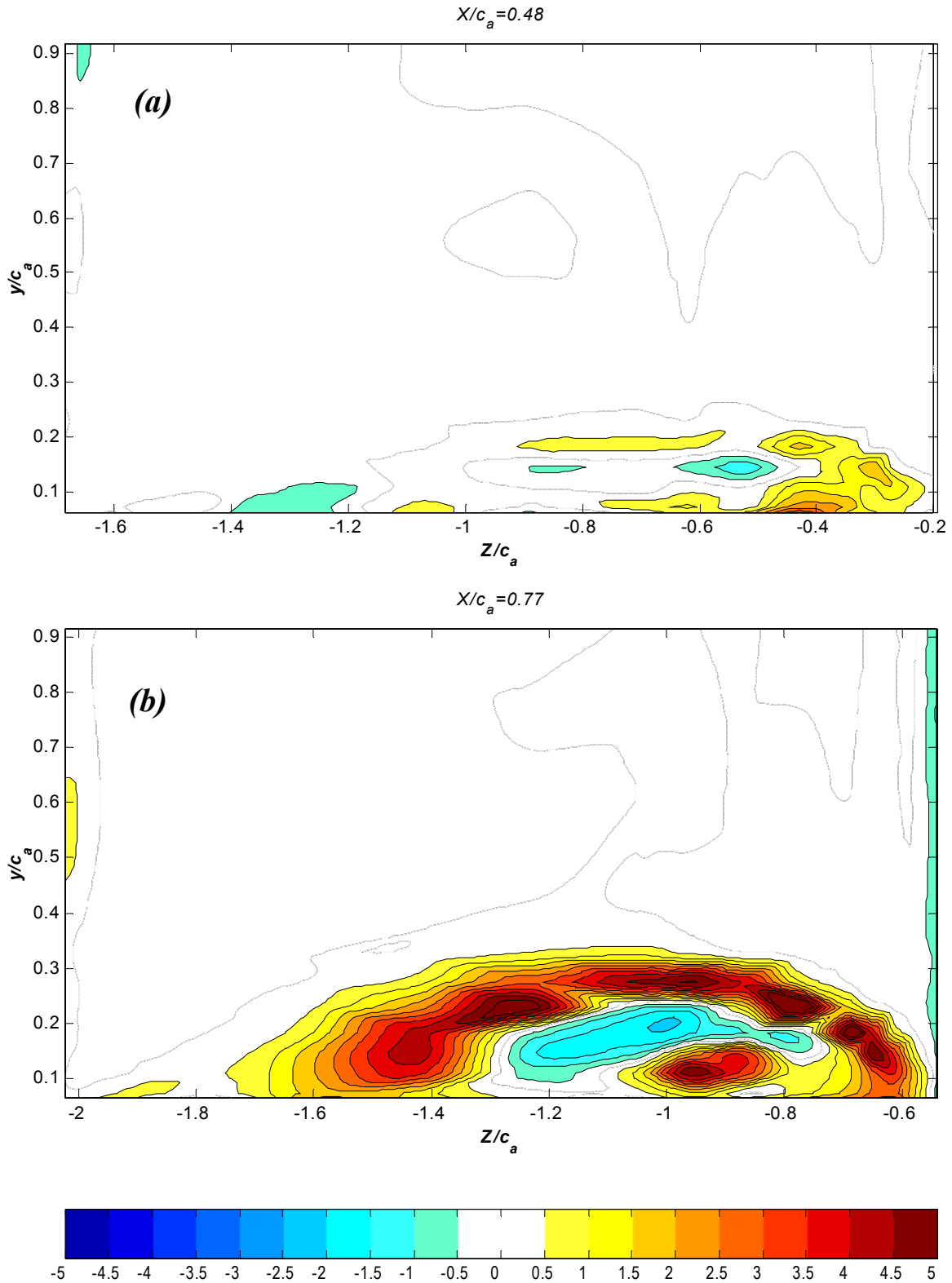


Figure 3.51a,b: Contours of the turbulence kinetic energy difference $\frac{(k_{grid} - k_{nogrid})}{(k_{grid} - k_{nogrid})_{potentialcore}}$

Positive values indicate an increase in the turbulence kinetic energy levels when compared to the difference in the potential core of the flow . Presented are axial locations (a) $X/c_a = 0.48$ (b) $X/c_a = 0.77$

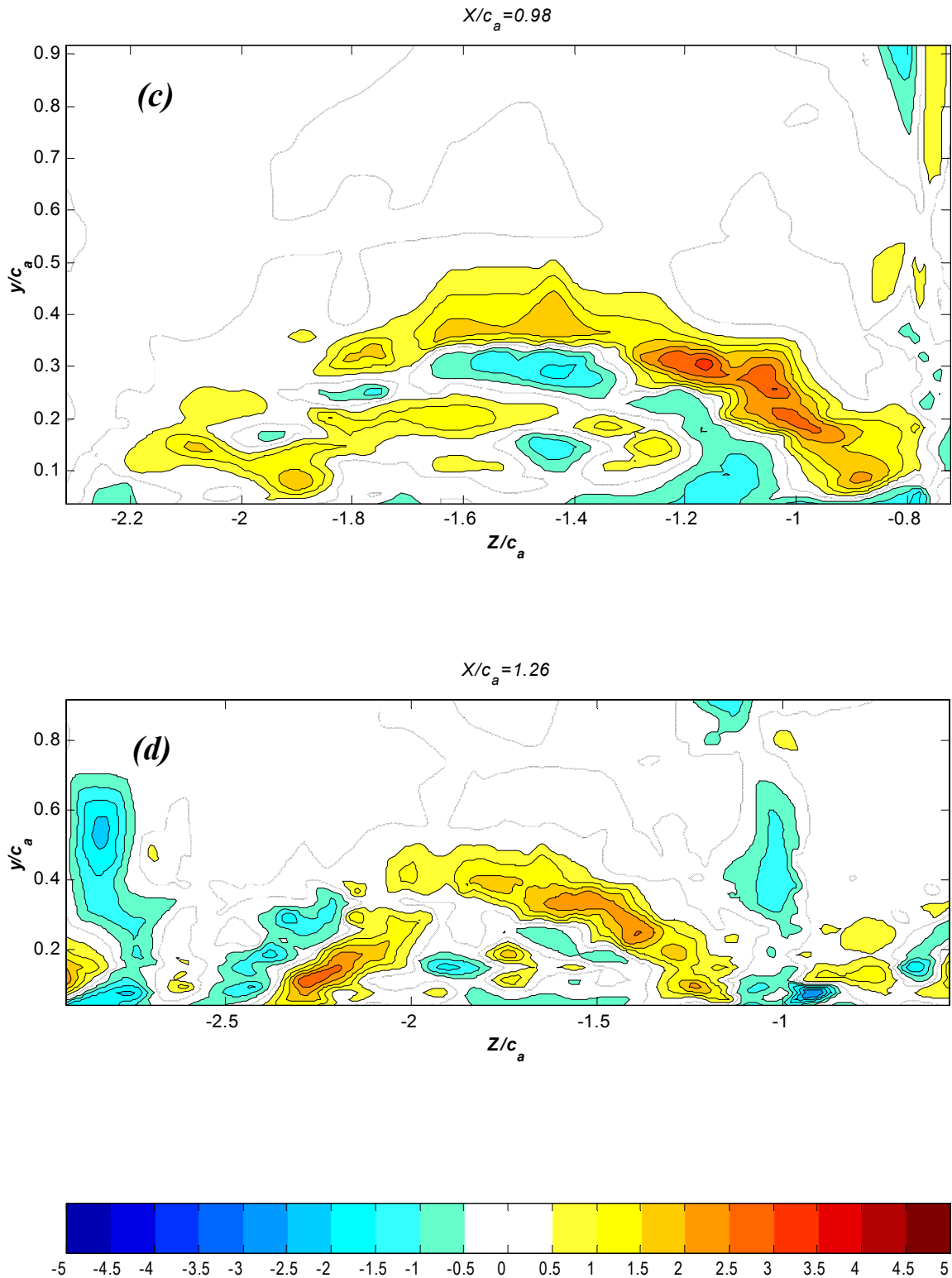


Figure 3.51c,d: Contours of the turbulence kinetic energy difference $\frac{(k_{grid} - k_{nogrid})}{(k_{grid} - k_{nogrid})_{potentialcore}}$

Positive values indicate an increase in the turbulence kinetic energy levels when compared to the difference in the potential core of the flow . Presented are axial locations (c) $X/c_a = 0.98$ (d) $X/c_a=1.26$

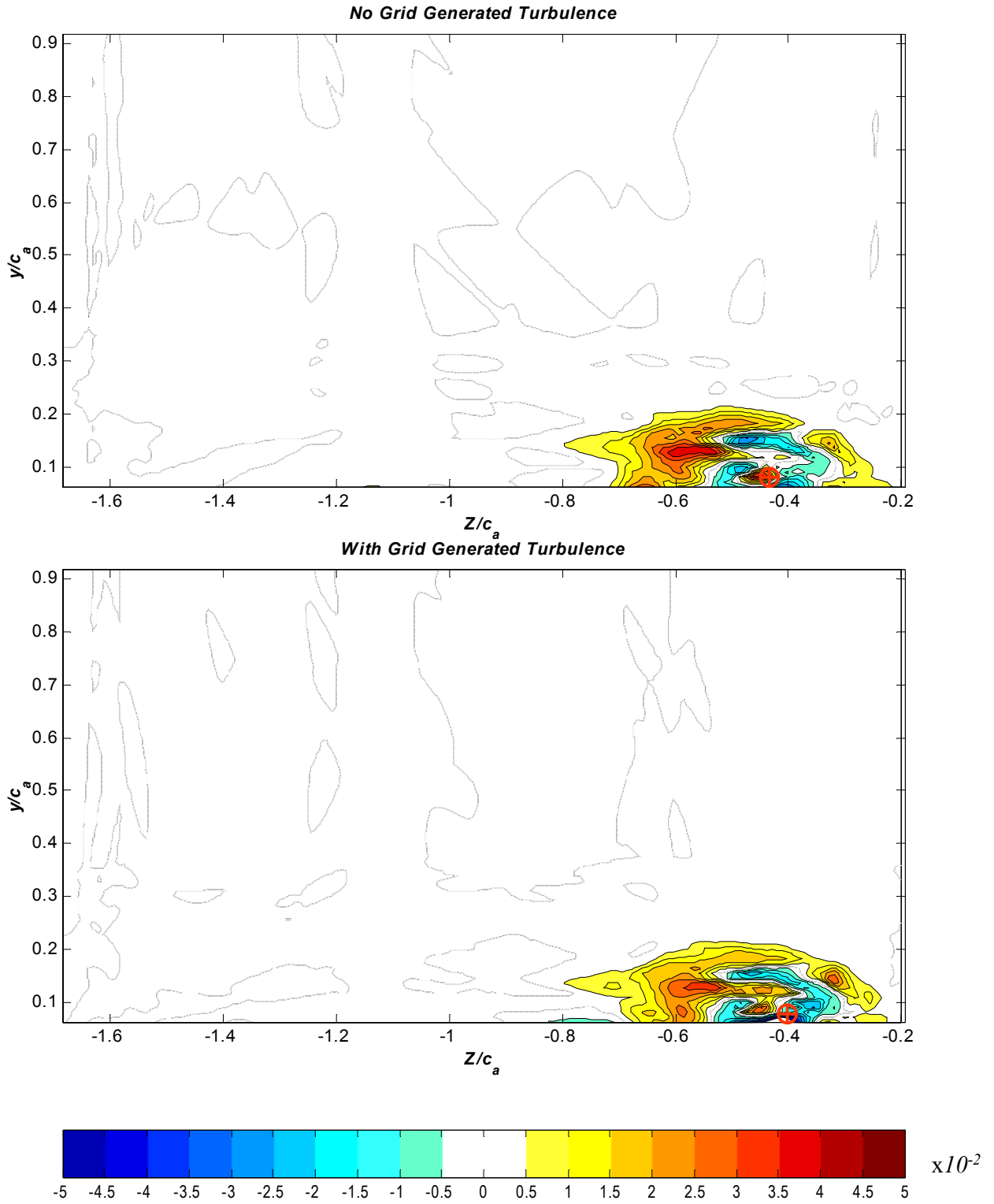


Figure 3.52a: Contours of the turbulence kinetic energy production, at $X/c_a=0.48$. Vortex centers defined by peak mean streamwise vorticity are indicated by circular crosses. Titles on plots indicate inflow turbulence condition

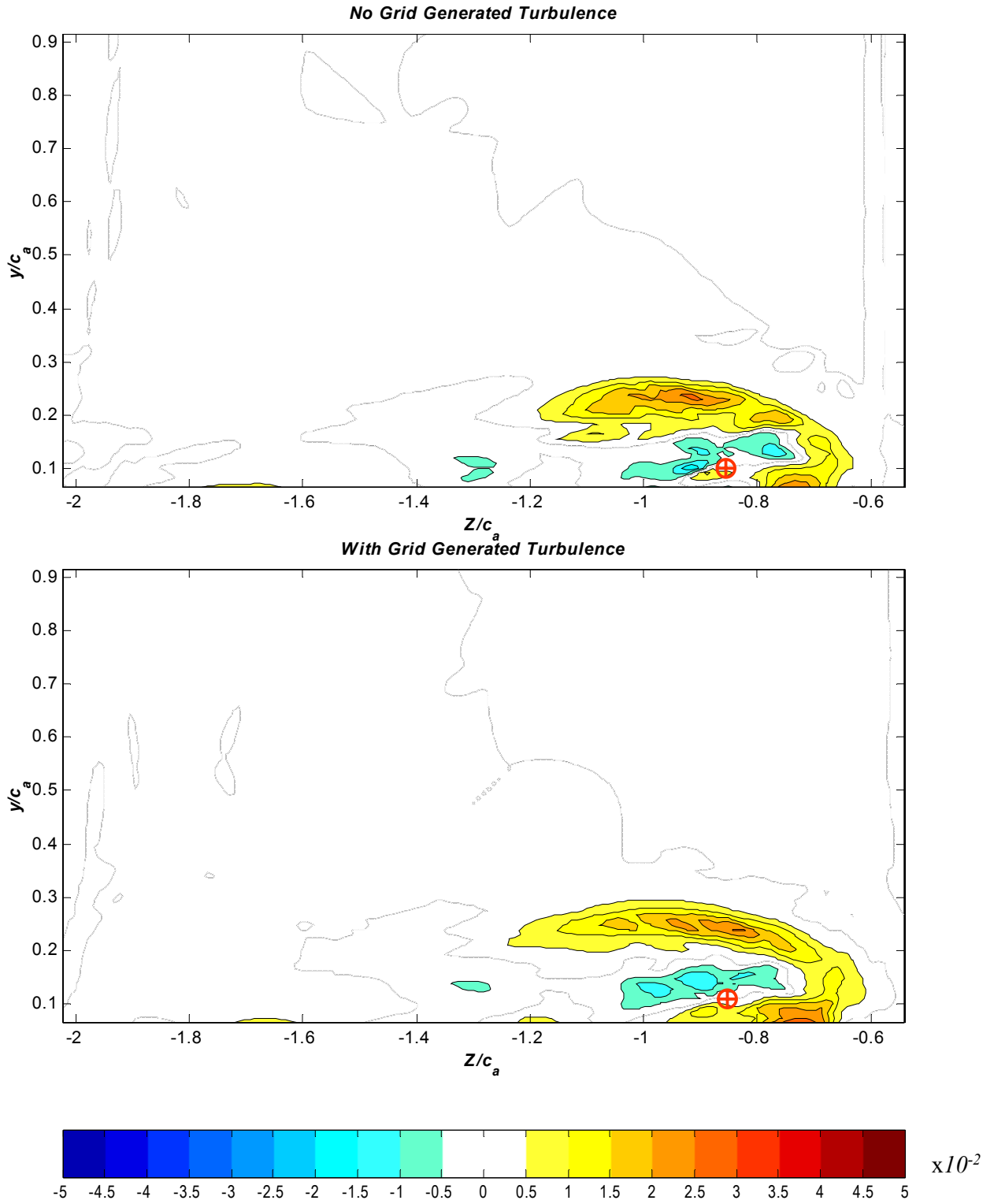


Figure 3.52b: Contours of the turbulence kinetic energy production, at $X/c_a=0.77$. Vortex centers defined by peak mean streamwise vorticity are indicated by circular crosses. Titles on plots indicate inflow turbulence condition

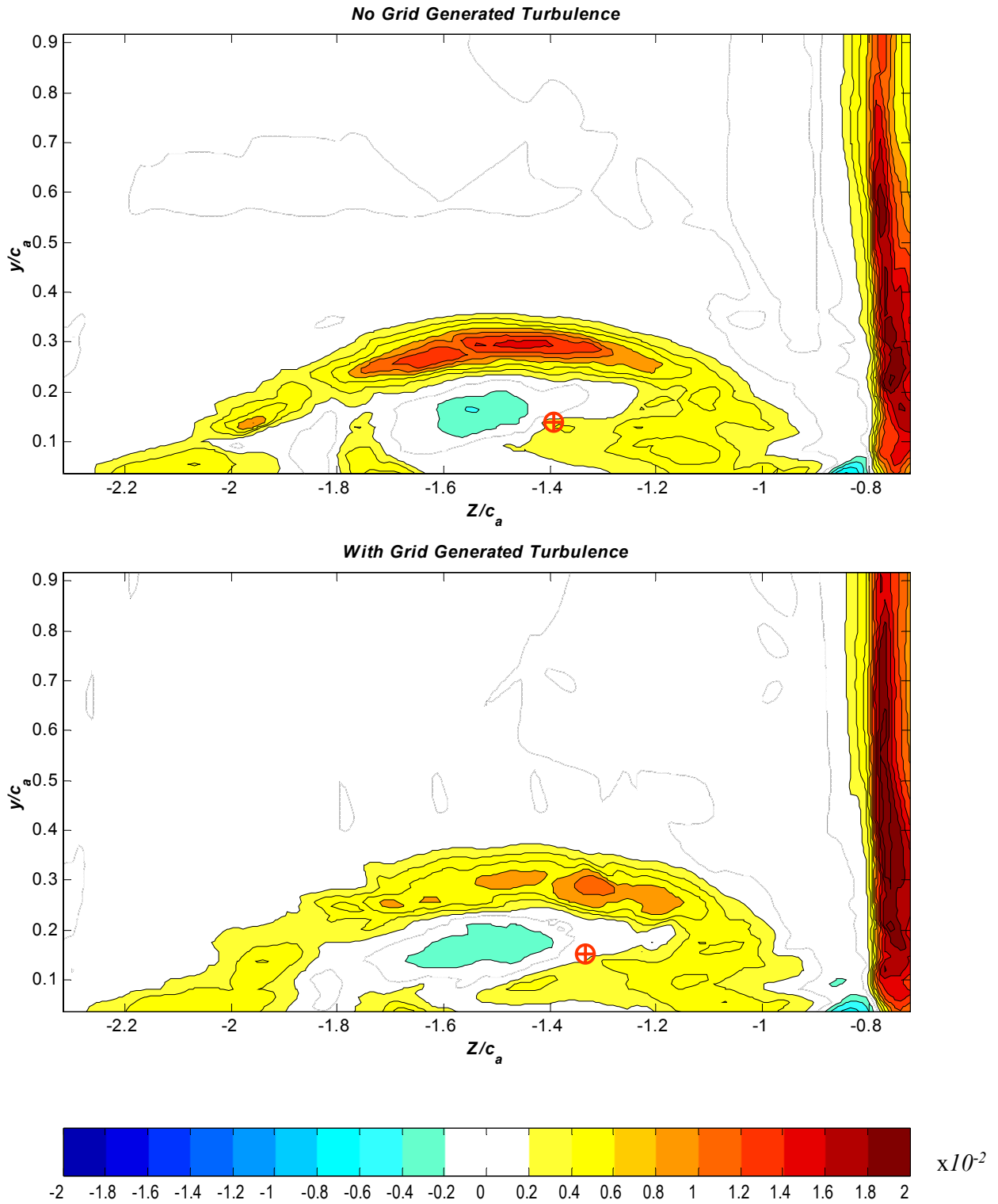


Figure 3.52c: Contours of the turbulence kinetic energy production, at $X/c_a=0.98$. Vortex centers defined by peak mean streamwise vorticity are indicated by circular crosses. Titles on plots indicate inflow turbulence condition

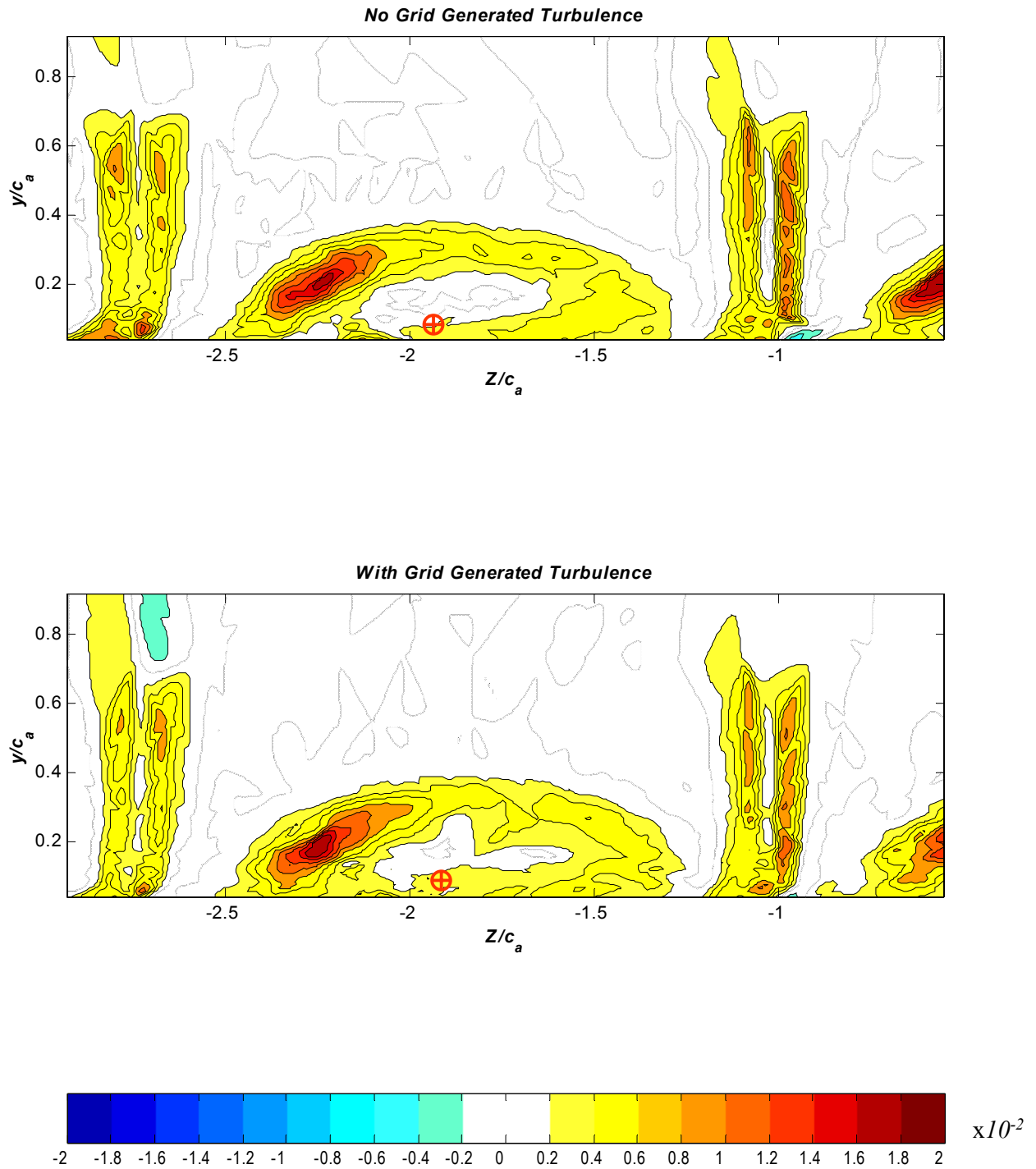


Figure 3.52d: Contours of the turbulence kinetic energy production, at $X/c_a=1.26$. Vortex centers defined by peak mean streamwise vorticity are indicated by circular crosses. Titles on plots indicate inflow turbulence condition

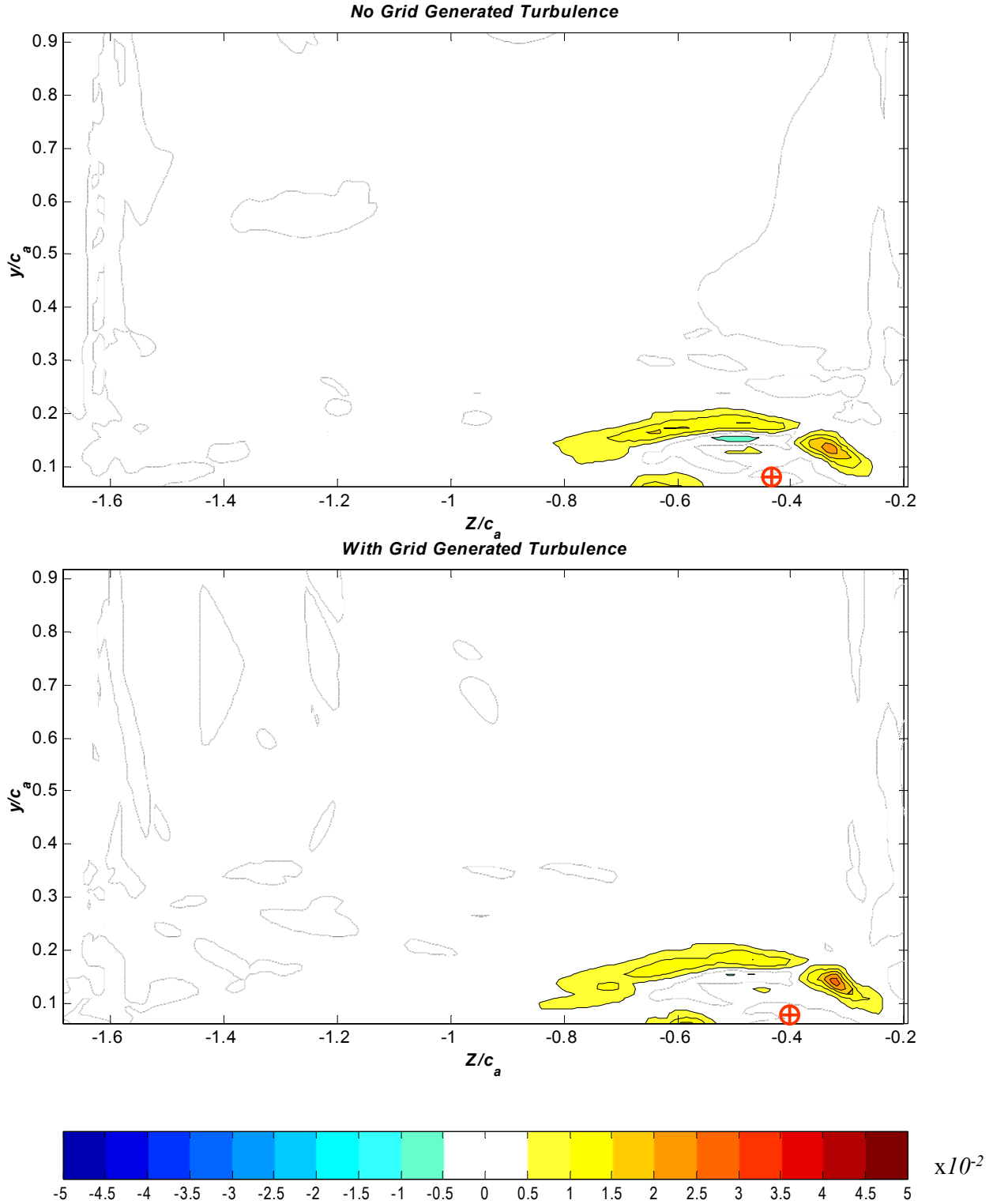


Figure 3.53a: Contours of the turbulence kinetic energy production due to streamwise velocity gradient, at $X/c_a=0.48$. Vortex centers defined by peak mean streamwise vorticity are indicated by circular crosses. Titles on plots indicate inflow turbulence condition

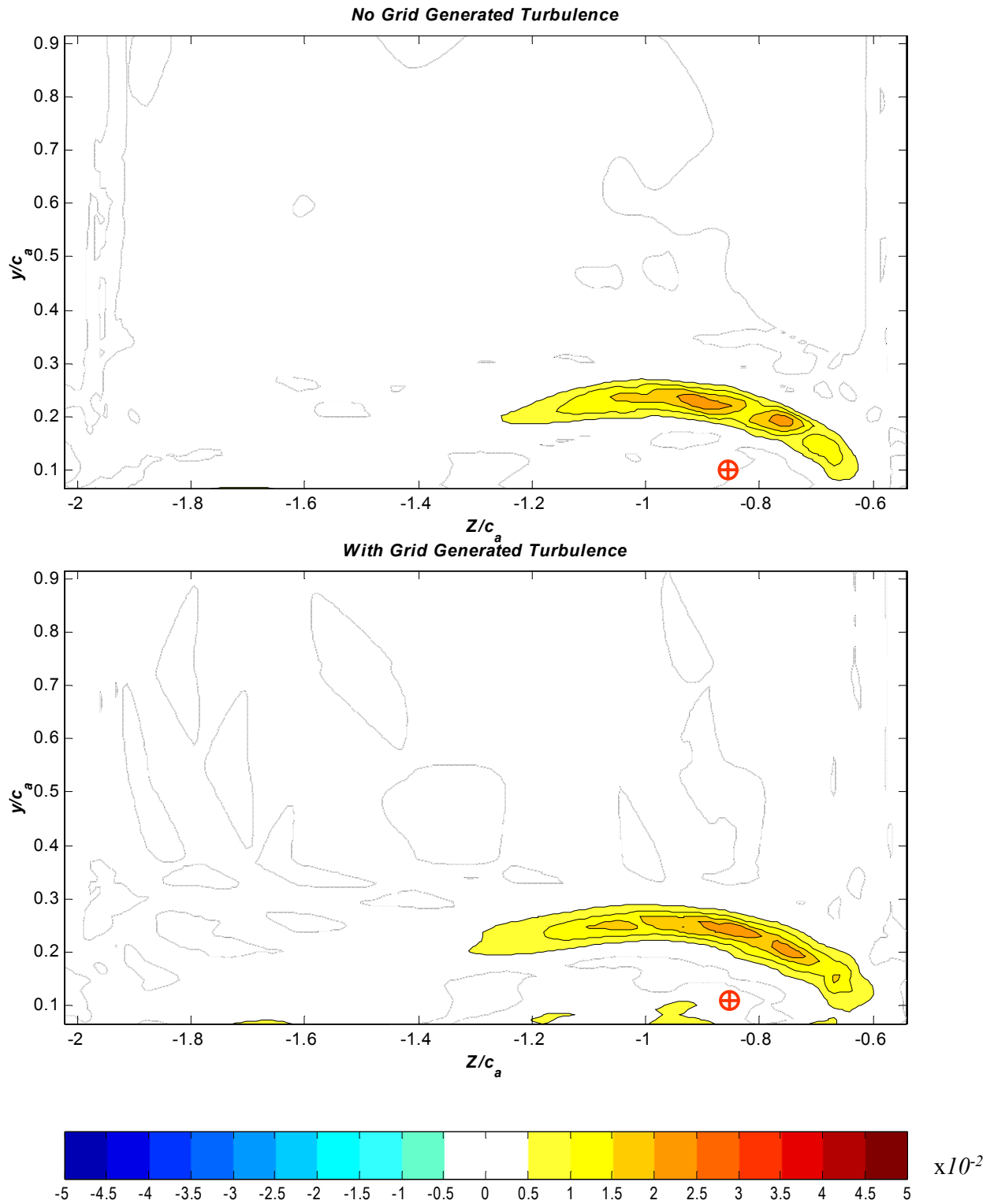


Figure 3.53b: Contours of the turbulence kinetic energy production due to streamwise velocity gradient, at $X/c_a=0.77$. Vortex centers defined by peak mean streamwise vorticity are indicated by circular crosses. Titles on plots indicate inflow turbulence condition

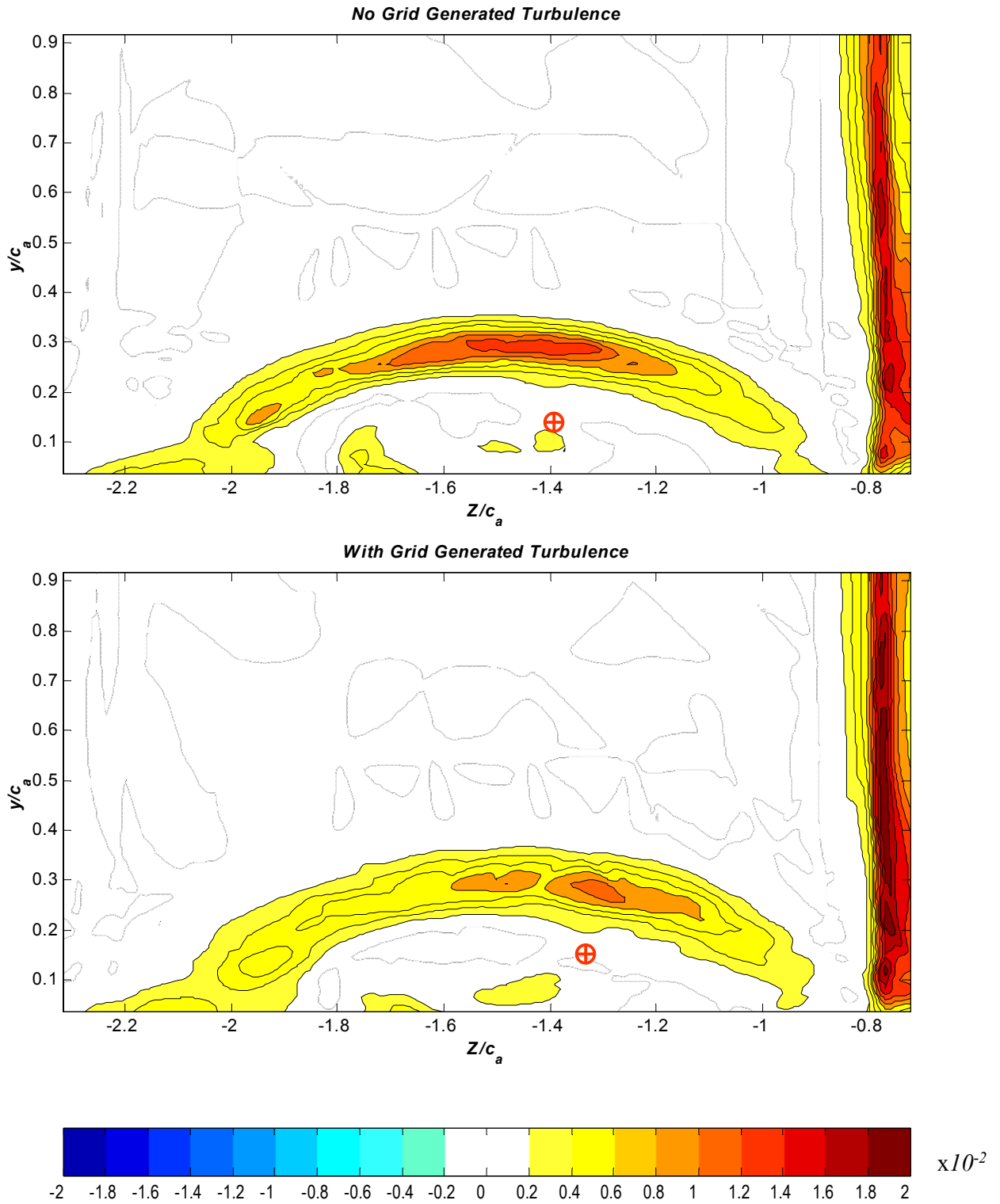


Figure 3.53c: Contours of the turbulence kinetic energy production due to streamwise velocity gradient, at $X/c_a=0.98$. Vortex centers defined by peak mean streamwise vorticity are indicated by circular crosses. Titles on plots indicate inflow turbulence condition

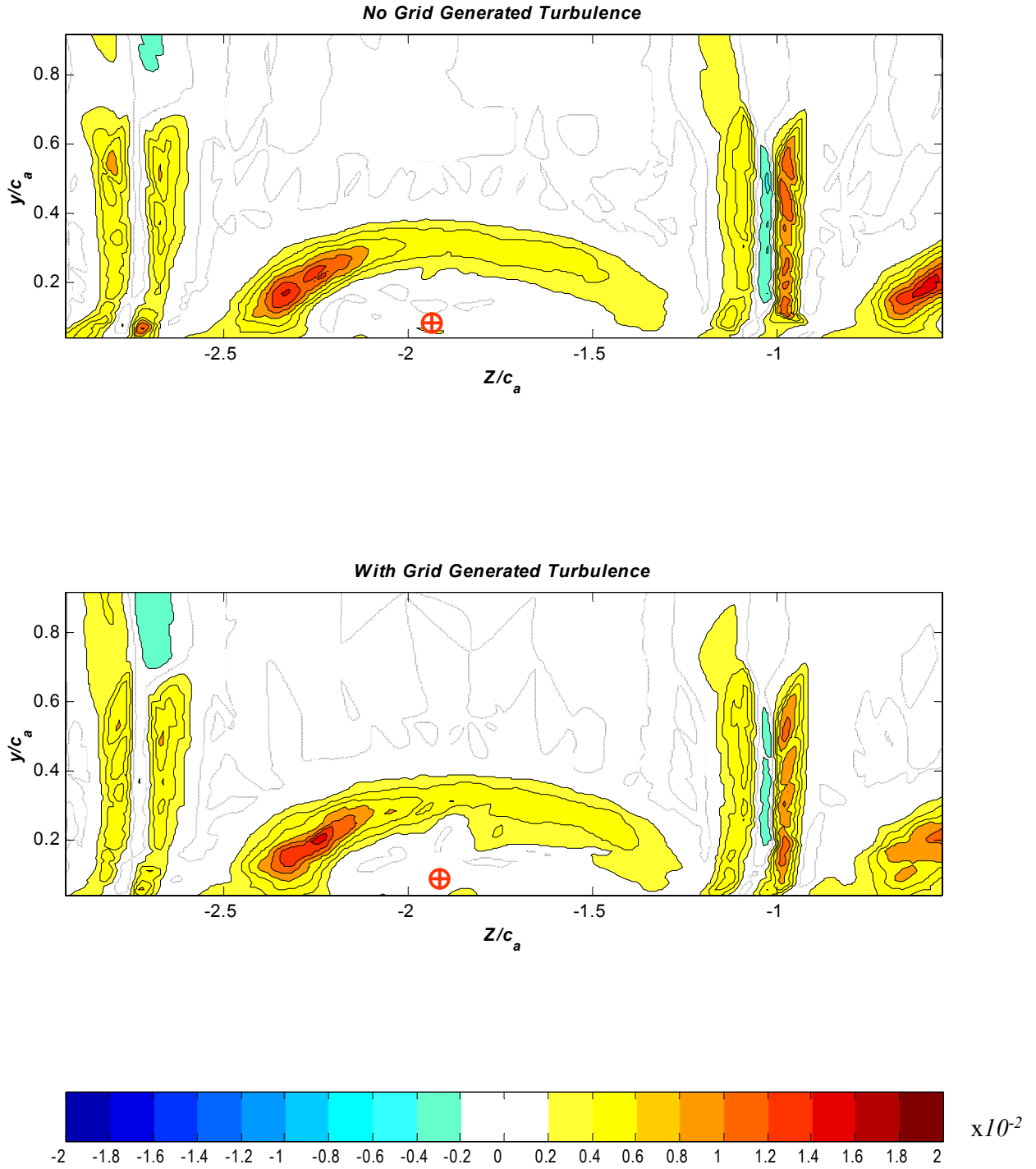


Figure 3.53d: Contours of the turbulence kinetic energy production due to streamwise velocity gradient, at $X/c_a=1.26$. Vortex centers defined by peak mean streamwise vorticity are indicated by circular crosses. Titles on plots indicate inflow turbulence condition

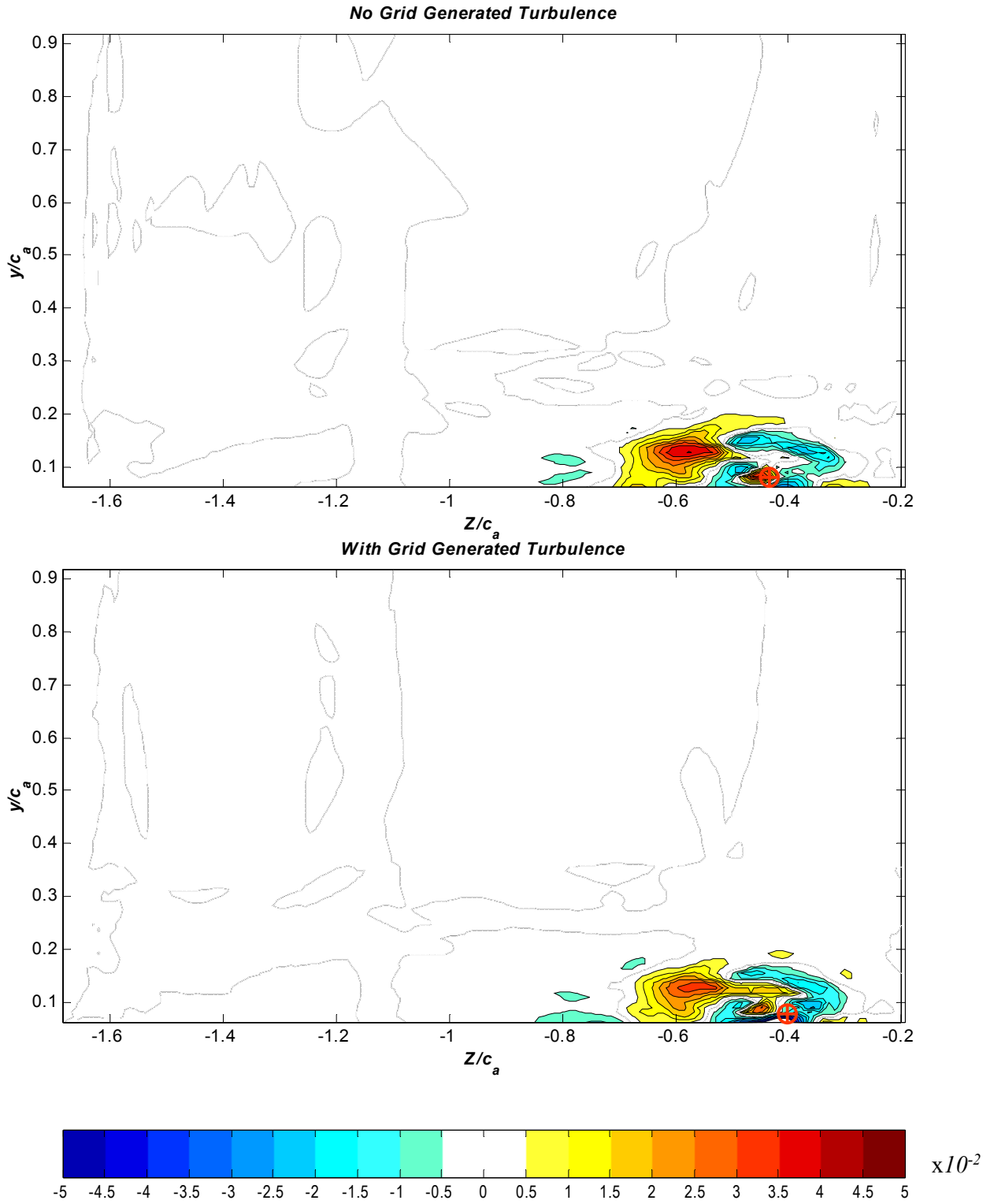


Figure 3.54a: Contours of the turbulence kinetic energy production due to crossflow velocity gradient, at $X/c_a=0.48$. Vortex centers defined by peak mean streamwise vorticity are indicated by circular crosses. Titles on plots indicate inflow turbulence condition

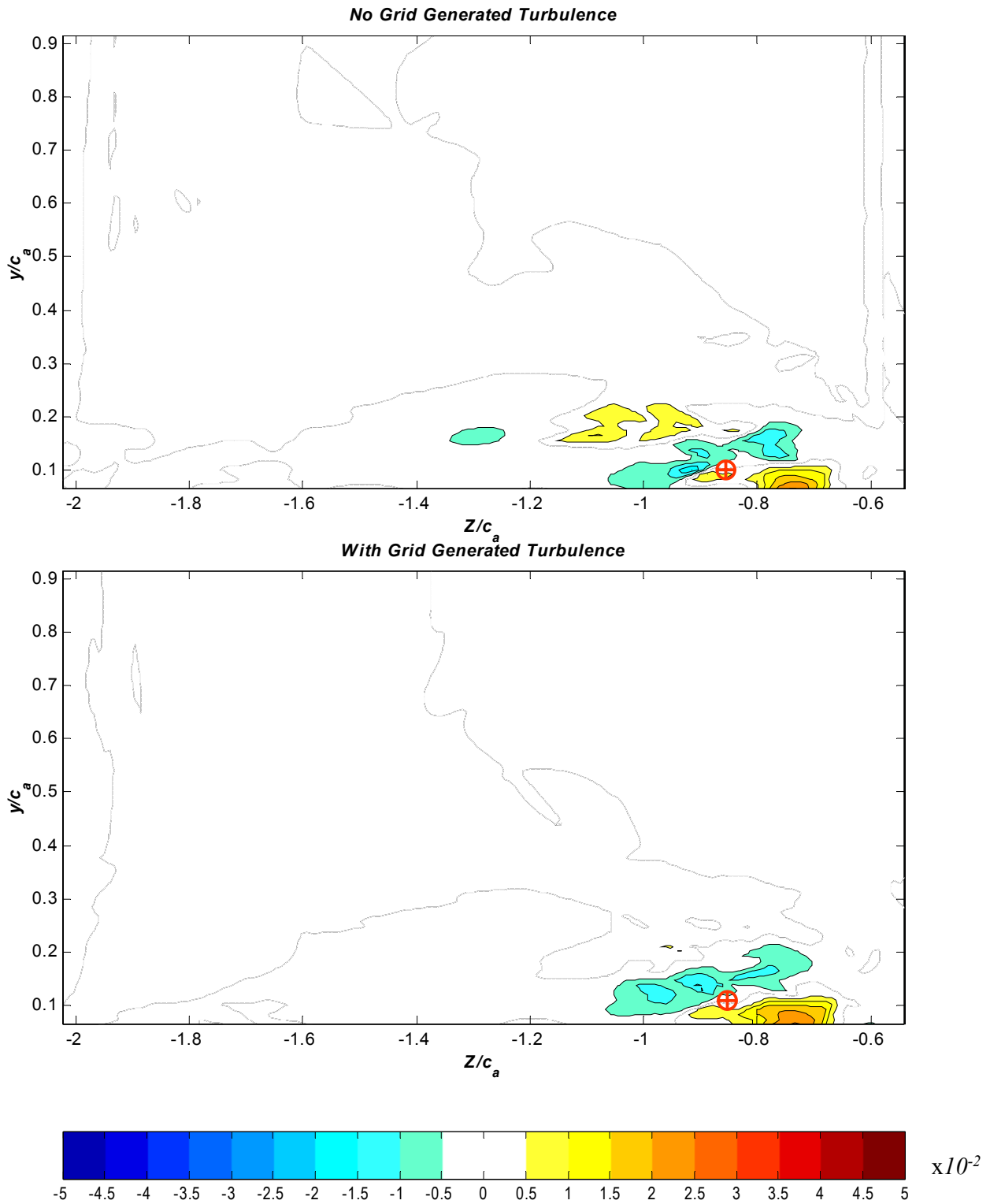


Figure 3.54b: Contours of the turbulence kinetic energy production due to crossflow velocity gradient, at $X/c_a=0.77$. Vortex centers defined by peak mean streamwise vorticity are indicated by circular crosses. Titles on plots indicate inflow turbulence condition

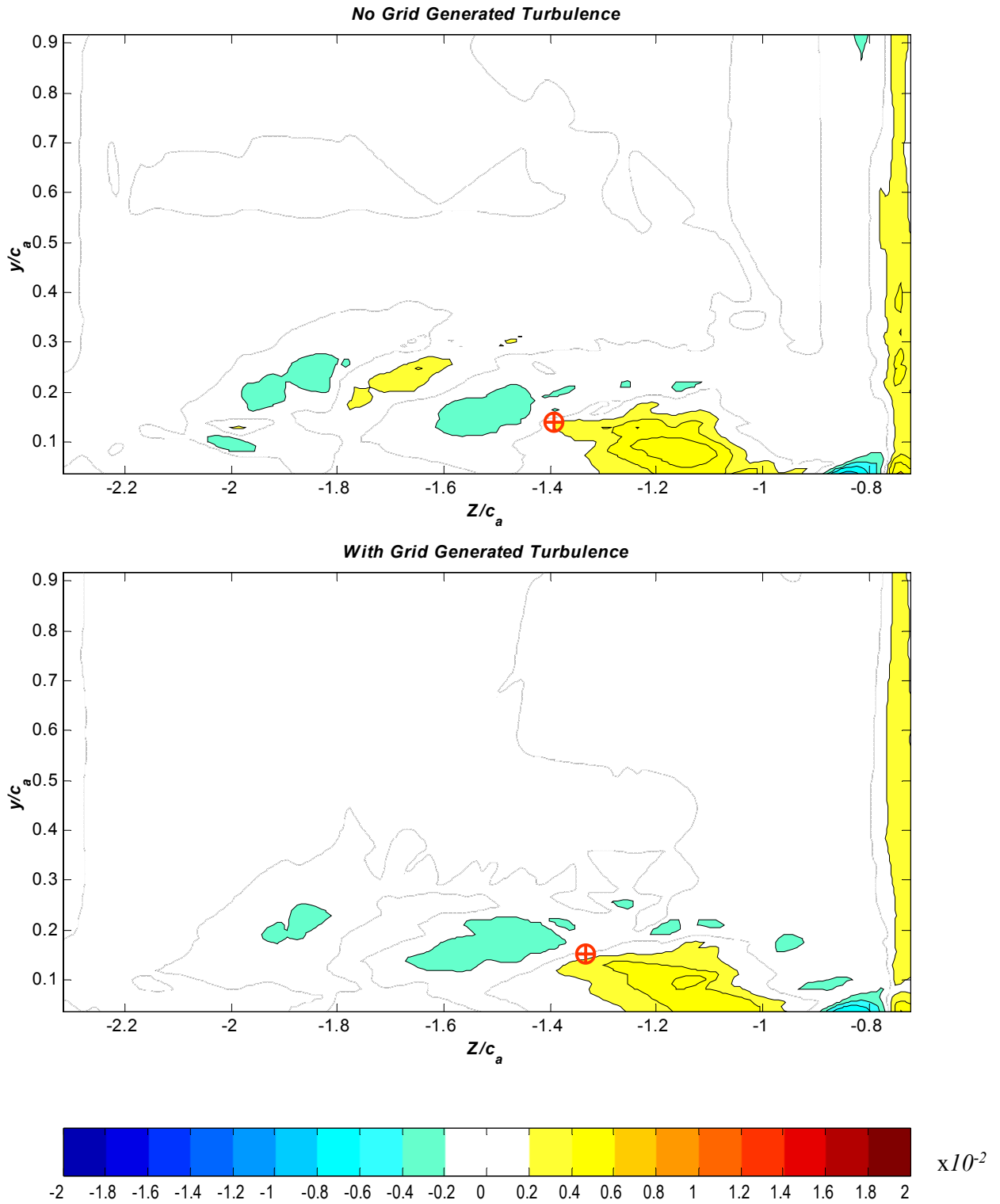


Figure 3.54c: Contours of the turbulence kinetic energy production due to crossflow velocity gradient, at $X/c_a=0.98$. Vortex centers defined by peak mean streamwise vorticity are indicated by circular crosses. Titles on plots indicate inflow turbulence condition

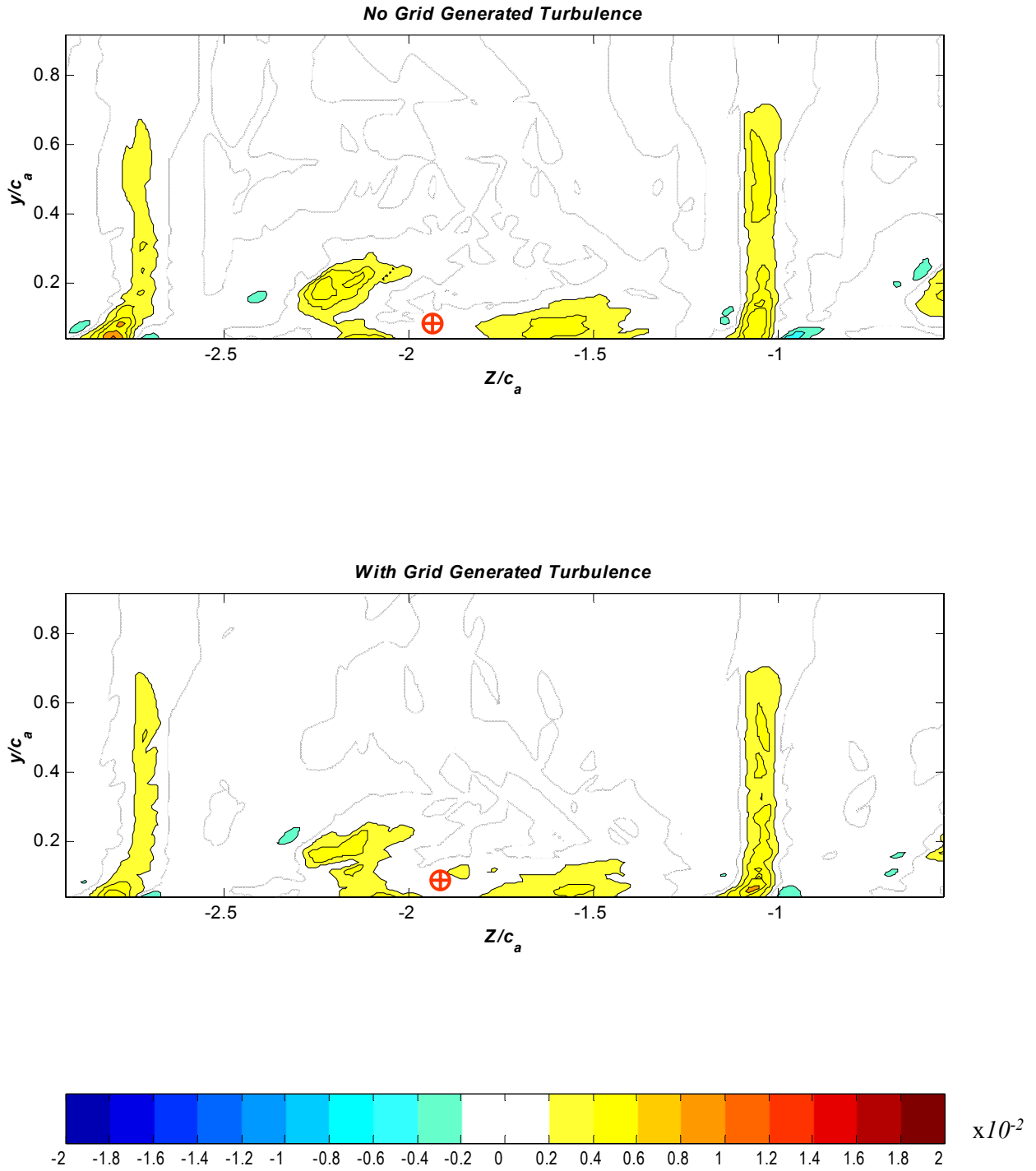


Figure 3.54d: Contours of the turbulence kinetic energy production due to crossflow velocity gradient, at $X/c_a=1.26$. Vortex centers defined by peak mean streamwise vorticity are indicated by circular crosses. Titles on plots indicate inflow turbulence condition

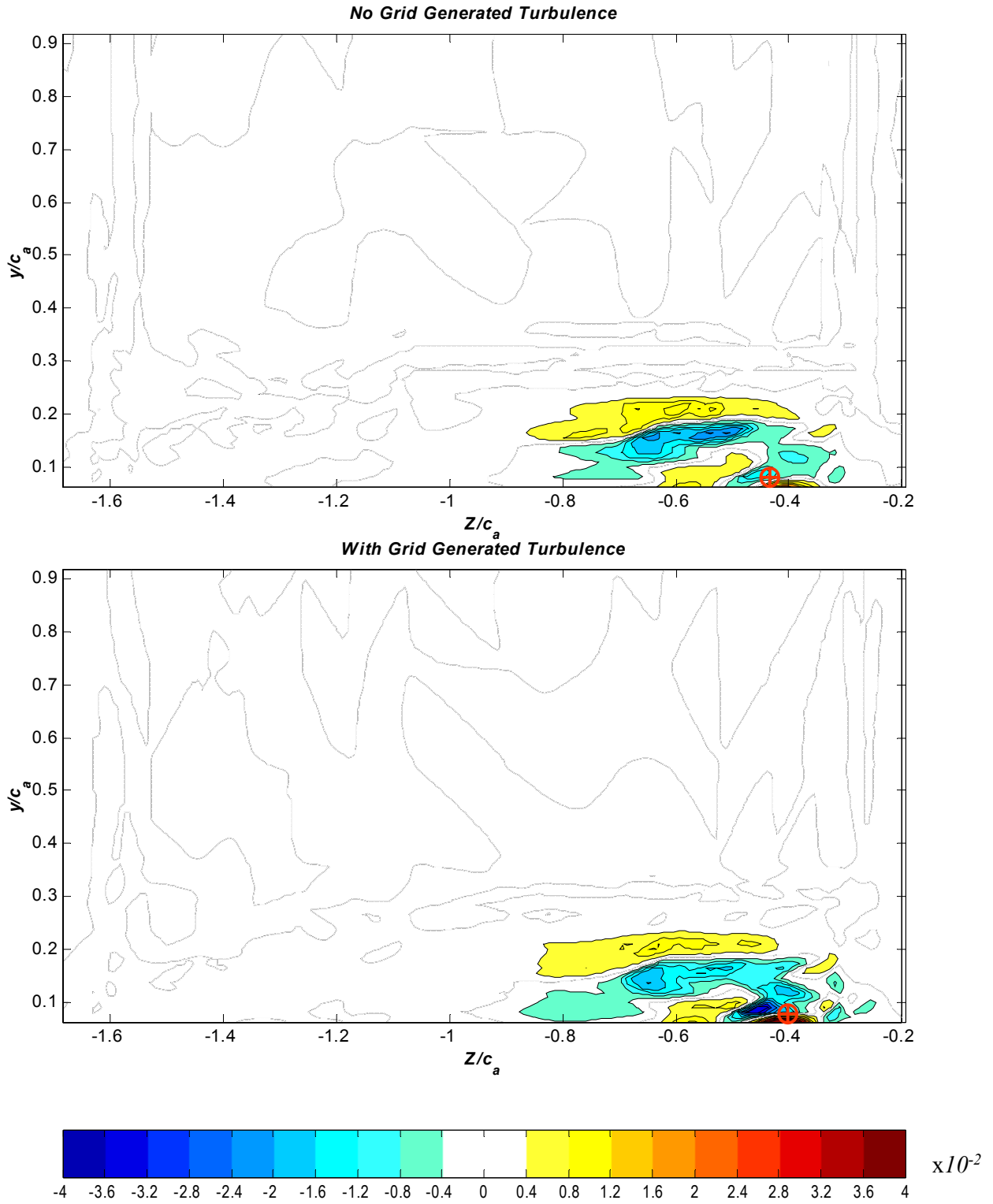


Figure 3.55a: Contours of the turbulence kinetic energy diffusion, at $X/c_a=0.48$. Vortex centers defined by peak mean streamwise vorticity are indicated by circular crosses. Titles on plots indicate inflow turbulence condition

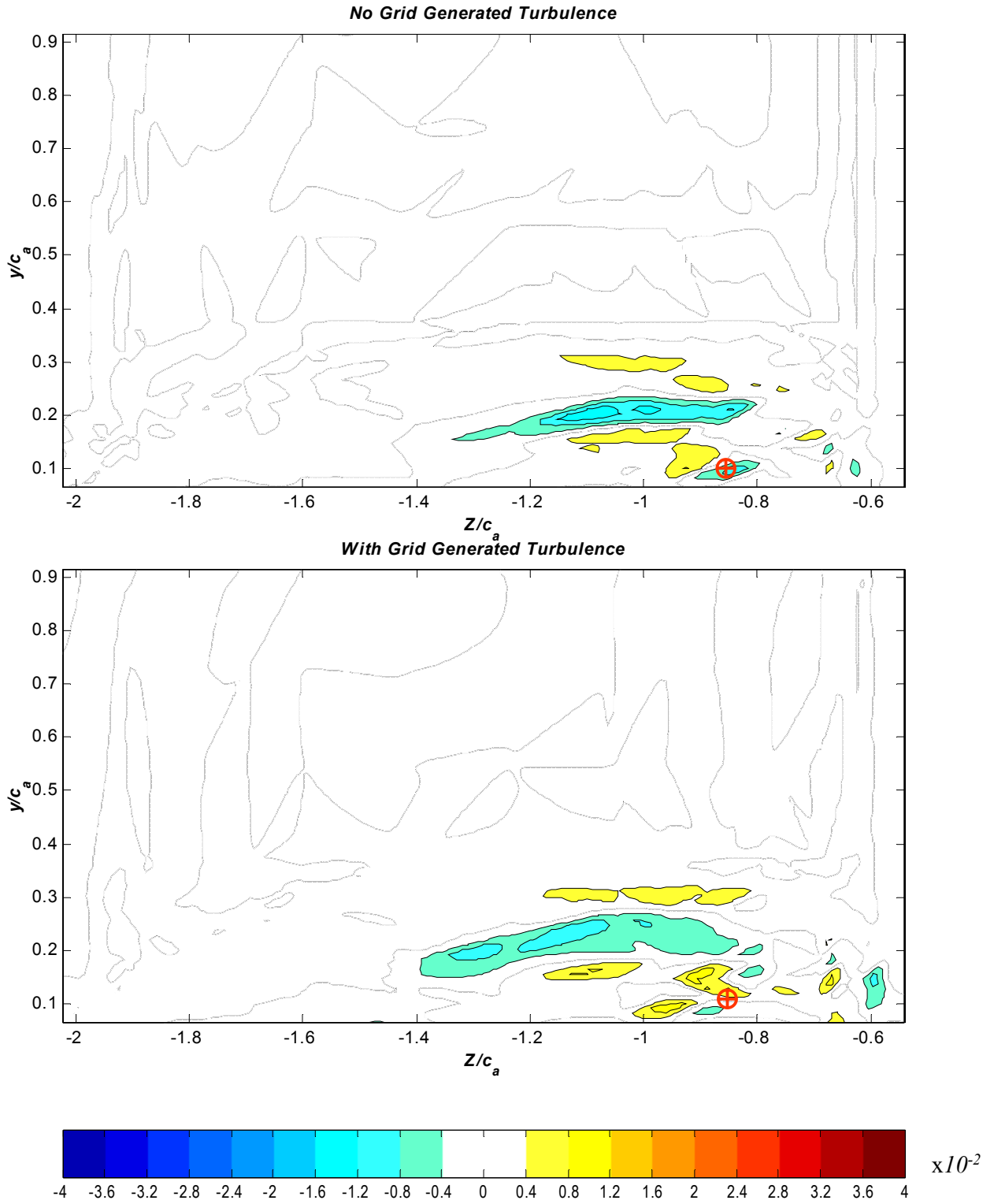


Figure 3.55b: Contours of the turbulence kinetic energy diffusion, at $X/c_a=0.77$. Vortex centers defined by peak mean streamwise vorticity are indicated by circular crosses. Titles on plots indicate inflow turbulence condition

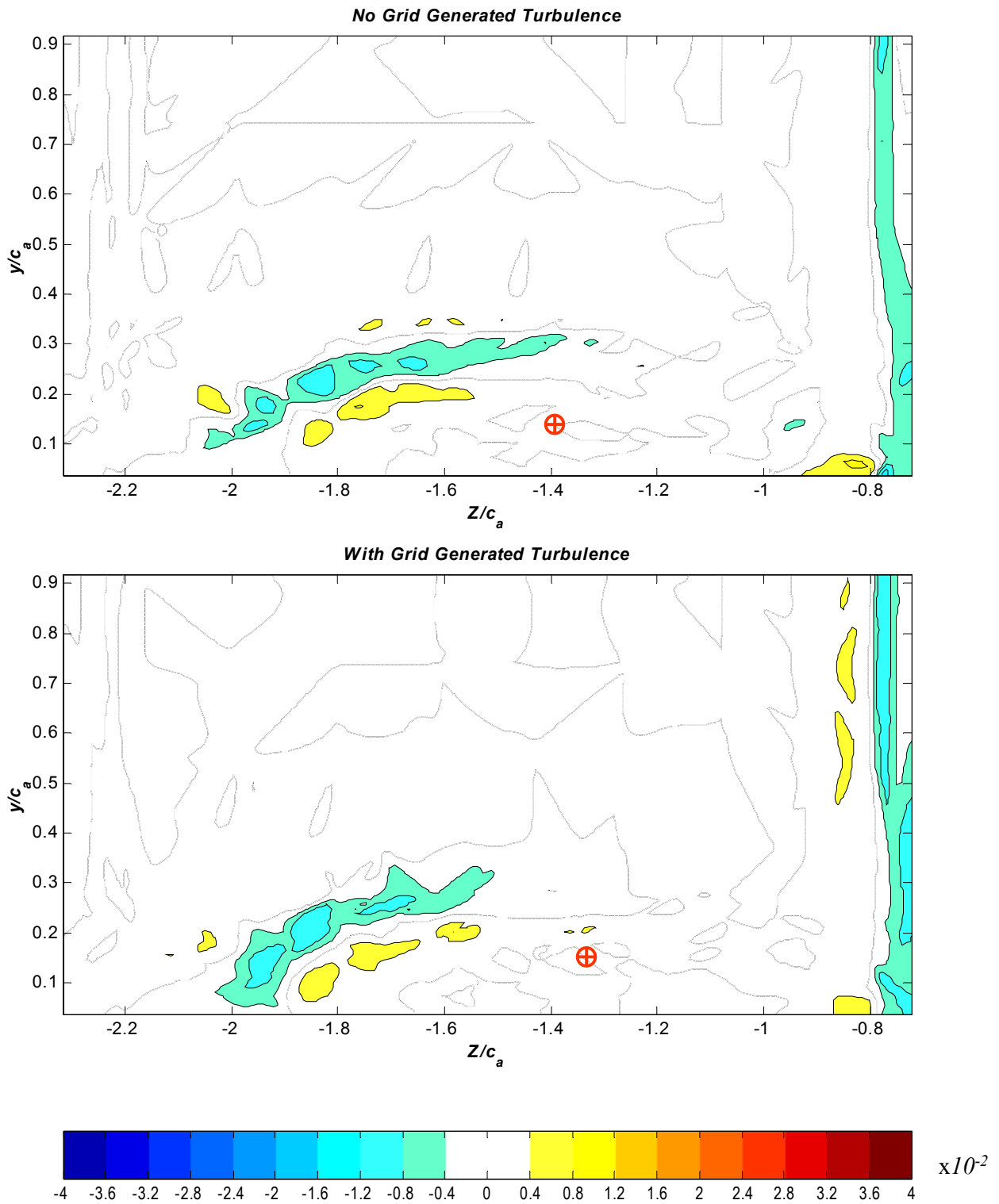


Figure 3.55c: Contours of the turbulence kinetic energy diffusion, at $X/c_a=0.98$. Vortex centers defined by peak mean streamwise vorticity are indicated by circular crosses. Titles on plots indicate inflow turbulence condition

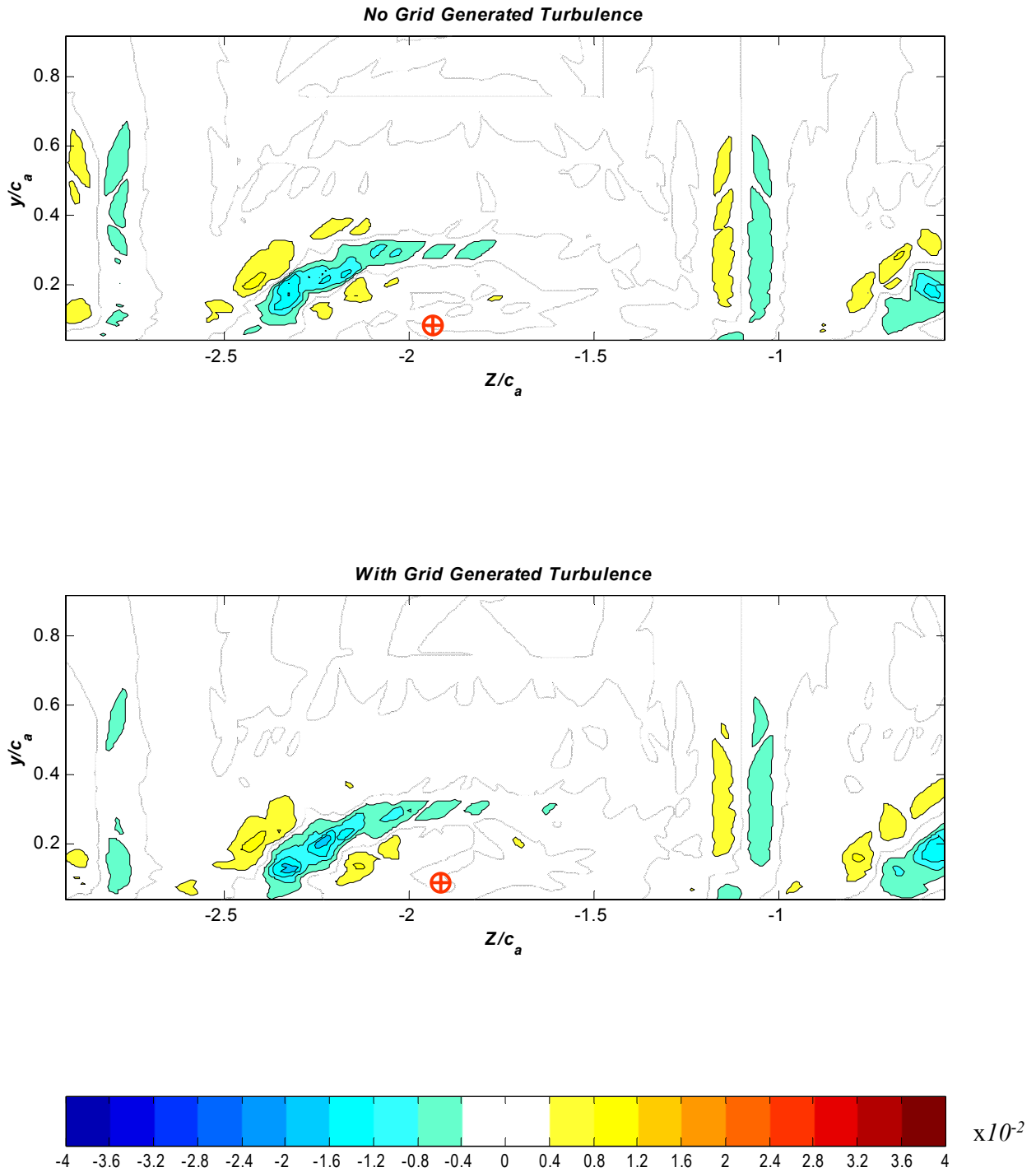


Figure 3.55d: Contours of the turbulence kinetic energy diffusion, at $X/c_a=1.26$. Vortex centers defined by peak mean streamwise vorticity are indicated by circular crosses. Titles on plots indicate inflow turbulence condition

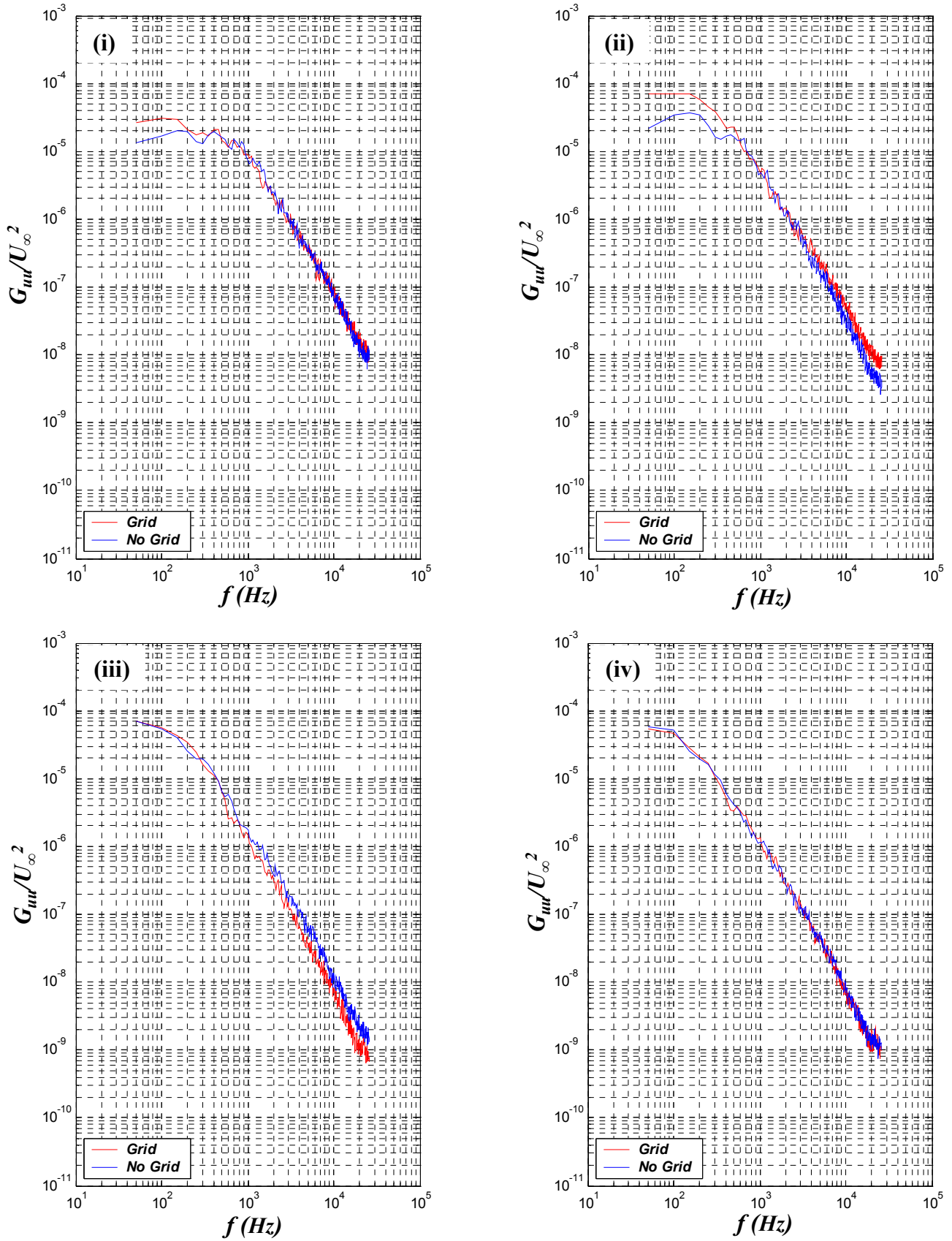


Figure 3.56: Normalized Autospectra, G_{uu}/U_∞^2 , for the two inflow conditions in the vicinity of the vortex center. The locations on the plots correspond to (i) $X/c_a=0.48$, $Z/c_a=-0.43$, $y/c_a=0.07$ (i) $X/c_a=0.77$, $Z/c_a=-0.87$, $y/c_a=0.11$ (i) $X/c_a=0.98$, $Z/c_a=-1.43$, $y/c_a=0.15$ (i) $X/c_a=1.26$, $Z/c_a=-1.92$, $y/c_a=0.15$

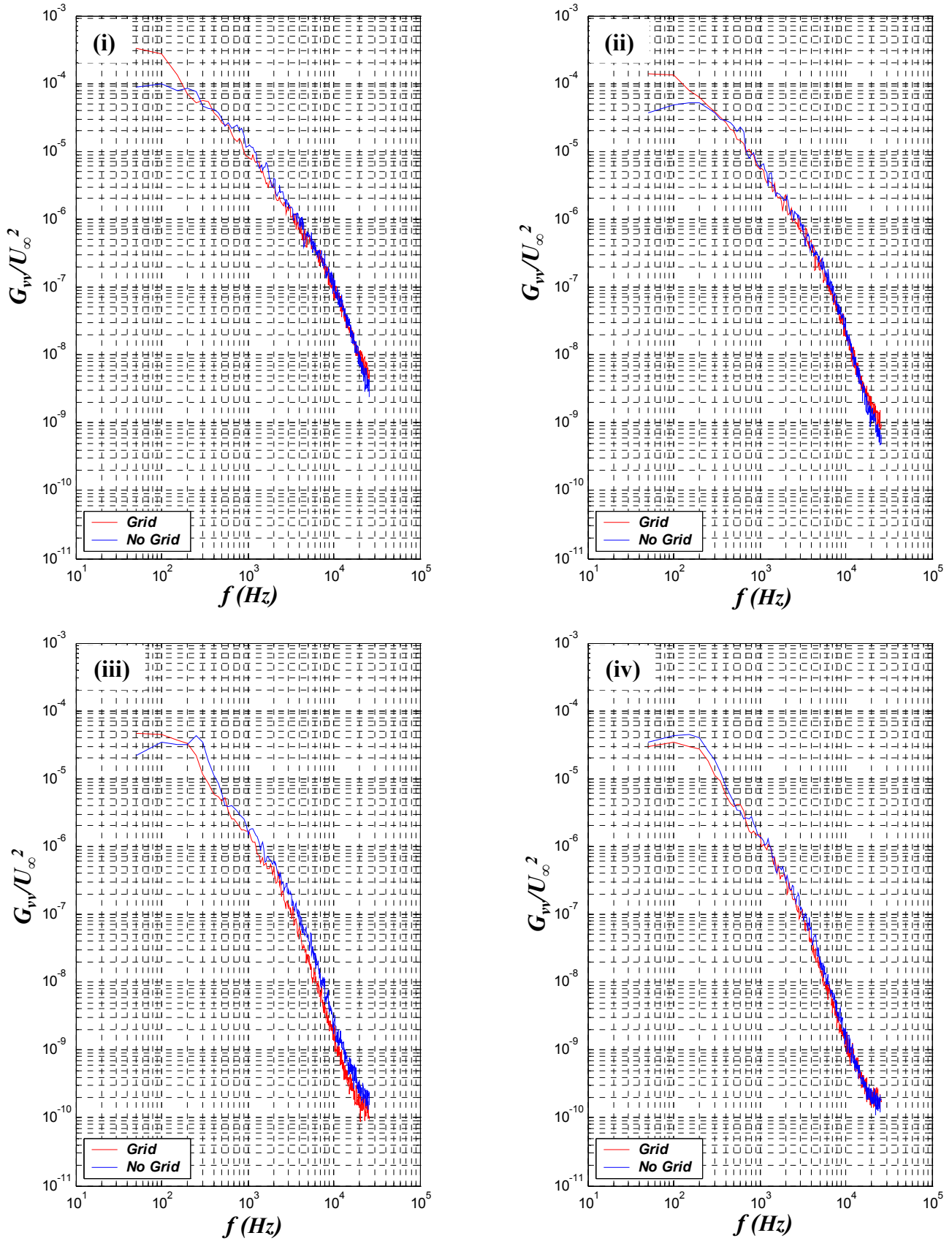


Figure 3.57: Normalized Autospectra, G_{vv}/U_∞^2 , for the two inflow conditions in the vicinity of the vortex center. The locations on the plots correspond to (i) $X/c_a=0.48$, $Z/c_a=-0.43$, $y/c_a=0.07$ (i) $X/c_a=0.77$, $Z/c_a=-0.87$, $y/c_a=0.11$ (i) $X/c_a=0.98$, $Z/c_a=-1.43$, $y/c_a=0.15$ (i) $X/c_a=1.26$, $Z/c_a=-1.92$, $y/c_a=0.15$

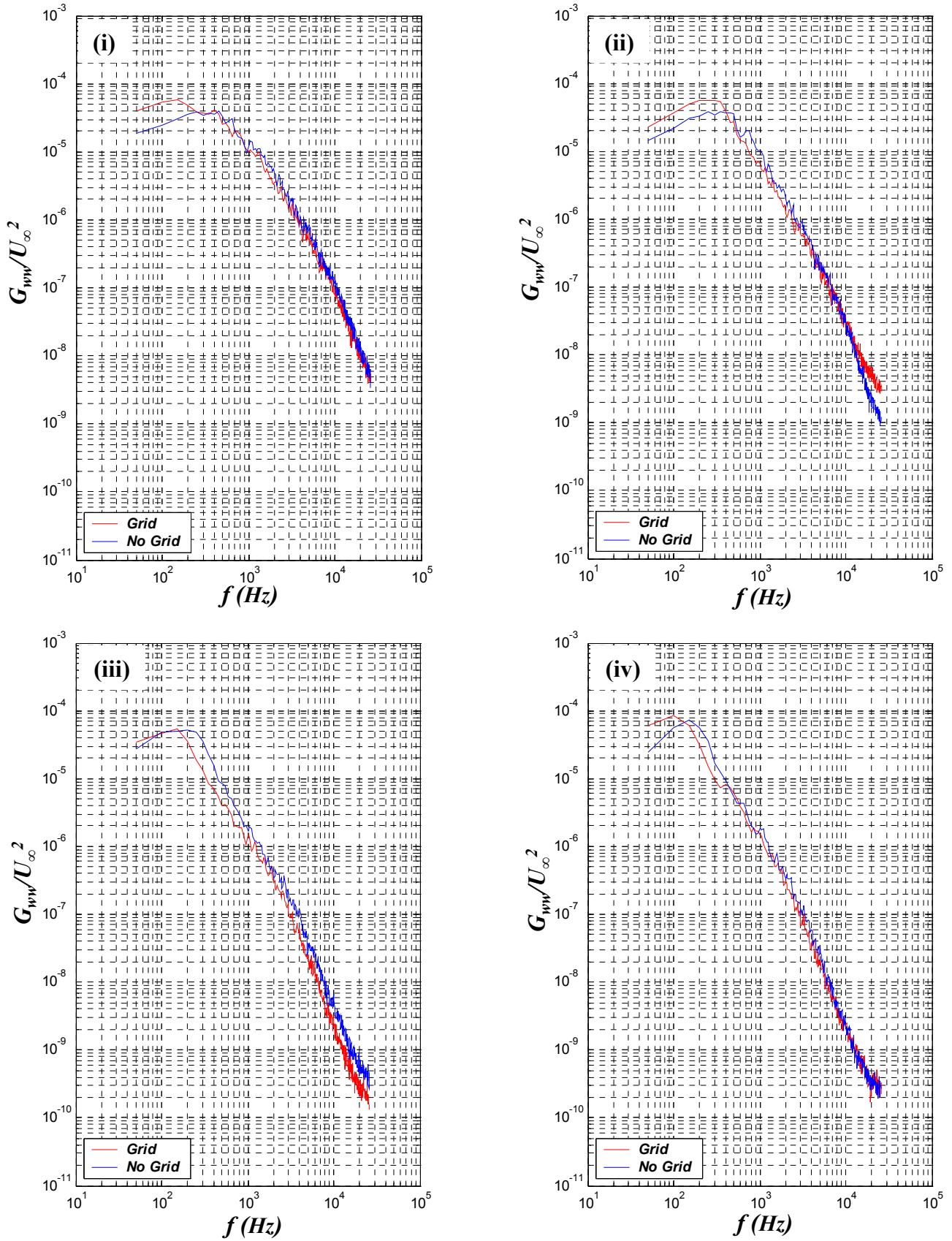


Figure 3.58: Normalized Autospectra, G_{ww}/U_∞^2 , for the two inflow conditions in the vicinity of the vortex center. The locations on the plots correspond to (i) $X/c_a=0.48, Z/c_a=-0.43, y/c_a=0.07$ (ii) $X/c_a=0.77, Z/c_a=-0.87, y/c_a=0.11$ (iii) $X/c_a=0.98, Z/c_a=-1.43, y/c_a=0.15$ (iv) $X/c_a=1.26, Z/c_a=-1.92, y/c_a=0.15$

4. Conclusions

The flow through a compressor cascade with tip leakage has been studied experimentally. The cascade of GE rotor B section blades had an inlet angle of 65.1° , a stagger angle of 56.9° , and a solidity of 1.08. The final turning angle of the cascade was 11.8° . The cascade was operated with a tip gap of 1.65%, and operated at a Reynolds number of 388,000. Measurements were made at 8 axial locations to reveal the structure of the flow as it evolved through the cascade. Measurements were also made to reveal the effects of grid generated turbulence on this flow.

4.1. Conclusions concerning flow structure without grid turbulence

Measurements of the three component velocity and turbulence were made in cross-sections through the cascade without grid turbulence at 8 axial locations upstream, downstream and within the blade passage. Lower endwall oil-flow visualizations and mid-span blade loading measurements were also made. These measurements revealed in detail, the flow approaching the cascade, and the lower endwall flow within the blade passage. In particular, the formation and development of the tip leakage vortex has been documented. The following conclusions from these measurements are drawn:

- The significantly noticeable influence of the blade row on the inflow as seen by a velocity gradient across the measurement grid extends to approximately a quarter chord axially upstream ($X/c_a = -0.23$). This influence has a significant effect in thickening the boundary layer approaching the cascade.
- Oil-flow visualizations on the lower endwall show a strong crossflow in the pitchwise direction in the tip gap region and extends into the passage. This interacts with the lower endwall flow to form the tip-leakage vortex as revealed in mean velocity measurements to produce a distinctive separation line which forms from about the 20% chord location and moves across the passage with downstream distance.

- Measurements in the passage show the tip leakage vortex being apparent at $X/c_a=0.27$. This region then grows to dominate the endwall flow region by the time it approaches $X/c_a=0.77$.
- The tip leakage vortex is characterized by regions of high streamwise mean velocity deficits. At $X/c_a=0.48$ and 0.77 , the high deficits are where the flow is lifted off the lower endwall. Downstream of the trailing edge, the tip leakage vortex changes its structure, and develops a localized region of high deficit near the vicinity of the vortex center.
- The tip leakage vortex produces regions of both positive and negative streamwise vorticity. Regions of positive vorticity are in the vicinity of the vortex center. Regions of negative vorticity are due to the crossflow due to the tip gap underneath the tip leakage vortex.
- Circulation within the tip leakage vortex core decreases with downstream distance until the trailing edge, but then shows an increase downstream of the trailing edge.
- The tip leakage vortex produces high levels of turbulence kinetic energy which are initially highest in the vortex center, and in an arch shaped region above the center at $X/c_a=0.48$ and 0.77 . At $X/c_a=0.98$ and 1.26 , the highest levels are only seen in a region above and around the vortex center.
- Turbulence kinetic energy production in the tip leakage vortex is primarily due to gradients in the streamwise velocity direction, and is dominant in the arch shaped region above the vortex center, and where the flow is lifted off the lower endwall.
- Paths of the vortex centers, defined as the location of maximum streamwise vorticity, show a shift in the vortex direction between $X/c_a=0.77$ and 0.98 , which is coincident to the changes seen in the shape and structure of the vortex, implying that between these two locations in the flow, the tip leakage vortex undergoes significant changes.

4.2. Conclusions concerning the effects of grid generated turbulence on the flow structure.

Elevated free stream turbulence was generated using a bi-planar grid of circular rods positioned $1.6m$ upstream of the center of the cascade entrance. The intensity of the grid generated turbulence at the inflow was approximately 3% at the entrance to the cascade and has lengthscales of approximately $1.75cm$. The turbulence has a decay rate of approximately 18% over a distance of one chord length of the blade. Oil flow visualizations, blade loading measurements, and velocity and turbulence measurements were made with the same level of detail as the flow without grid turbulence. The results revealed a number of subtle effects of turbulence on the flow. Specifically, the following conclusions have been drawn:

- Grid turbulence approaching the cascade is suppressed in the vicinity of the endwall, due to the non-penetration condition there.
- As the turbulence flows through the cascade, the velocity fluctuations normal to the blade surface are suppressed due to the non-penetration condition imposed by the blades.
- The blade loading changes with elevated free stream turbulence levels, showing a 4% reduction in the lift on the blade. The qualitative form of the endwall flow visualization was unaffected by the turbulence. Quantitatively, the path of the separation line shifted by 4% ($0.06c_a$) away from the suction side at the trailing edge of the cascade due to grid turbulence, suggesting that the turning angle of the flow is reduced.
- In the tip leakage vortex, the effects of grid generated turbulence on the mean flow field were apparent, showing only a 2% increase in the peak streamwise velocity deficit in the tip leakage vortex. Mean streamwise vorticity levels were reduced by the introduction of grid generated turbulence by approximately 20%. The overall size of the vortex core increased by 30%, but it was accompanied by a 2.5% decrease in the circulation.
- The path of the vortex center as defined by the peak streamwise vorticity was also influenced by grid generated turbulence, showing a shift in position of the vortex closer to the suction side of the passage by 3% ($0.05c_a$) at the trailing edge, supporting the conclusion the vortex strength is reduced.

- Overall, the turbulence levels in the tip leakage vortex are increased by the grid turbulence. The most dramatic increase in the turbulence kinetic energy levels is at $X/c_a = 0.77$ where there is as much as 5 times the change in the turbulence kinetic energy levels between the two inflow cases when compared to the differences in potential-core turbulence kinetic energy levels.

References

1. Ames F E and Plesniak M W, 1997, "The influence of large-scale high-intensity turbulence on vane aerodynamic losses, wake growth and exit turbulence parameters", *J. Turbo.*, vol. 119, pp. 182-192. April.
2. Ames F E, 1997, "The influence of large-scale high-intensity turbulence on vane heat transfer", *Journal of Turbomachinery*, vol. 119, January, pp. 23-30.
3. Bangert B A, Kohli A, Sauer J H and Thole K A, 1997, "High freestream turbulence simulation in a scaled up turbine vane passage", ASME paper 97-GT-51.
4. Bearman, P W, 1971, "Corrections for the Effect of Ambient Temperature Drift on Hot-Wire Measurements in Incompressible Flow," *DISA Information*, no. 11, pp. 25-30.
5. Bettner, J., L., Elrod C., "The Influence of Tip Clearance, Stage Loading, and Wall Roughness on Compressor Casing Boundary Layer Development", ASME paper 82-GT-153, 1982.
6. Bindon, J.P., "The Measurement and Formation of Tip-Clearance Loss", ASME *Journal of Turbomachinery*, Vol. 111, pp. 257-263, 1989.
7. Blair M F, 1983, "Influence of Free-Stream Turbulence on Turbulent Boundary Layer Heat Transfer and Mean Profile Development, Part 1 – Experimental Data", ASME *Journal of Heat Transfer*, Vol 105, Feb 83, pp 33-40.
8. Chesnakas, C.J., Dancy, C.L., "Three-Component LDA Measurements in an Axial Flow Compressor", *AIAA Journal of Propulsion and Power*, Vol. 6, No. 4, pg. 474-481, 1990.
9. Cumpsty, N. A., 1989, "Compressor Aerodynamics", Harlow, Essex, England : Longman Scientific & Technical ; New York : J. Wiley, 1989.
10. De la Riva D, 2001, "Turbulence Interaction in a Highly Staggered Cascade-Propulsor Configuration", M.S. Thesis, Virginia Tech, Blacksburg VA.
11. Devenport W J, Wittmer K S, Muthanna C, Berekatab S, Moore J, 1997, "Turbulence Structure of a Tip-Leakage Vortex Wake", AIAA paper 97-0440.
12. Devenport W. J, 2002, AOE 3054 Experimental Methods Course Manual, available online at <http://www.aoe.vt.edu/aoe3054>
13. Glegg S A L, 1999, "The Response of a Swept Blade Row to a Three Dimensional Gust", *Journal of Sound and Vibration*, vol 227, pp 29-64.
14. Graham J M R, 1998, "The effect of a two-dimensional cascade of thin streamwise plates on homogeneous turbulence", *Journal of Fluid Mechanics*, vol. 356, pp. 125-147.

15. Gregory-Smith D G and Cleak J G E, 1992, "Secondary flow measurements in a turbine cascade with high inlet turbulence", *Journal of Turbomachinery*, vol. 114, pp. 173-183.
16. Hancock P E, Bradshaw P, 1983, "The Effect of Free Stream Turbulence on Turbulent Boundary Layers", *Journal of Fluids Engineering*, Vol 105, pp.284-289, September 1983.
17. Hancock P E, Bradshaw P, 1989, "Turbulence Structure of a Boundary Layer beneath a Turbulent Free Stream", *Journal of Fluid Mechanics*, vol. 205, pp.45-76.
18. Hinze J O, 1959, "Turbulence, Second Edition", McGraw-Hill, Inc.
19. Hobson G V and Shreve R P, 1993, "Inlet turbulence distortion and viscous flow development in a controlled diffusion cascade at very high incidence", *Journal of Propulsion and Power*, vol. 9, no. 3, pp. 397-404
20. Hoffs A, Drost U, and Bolcs A, 1996, "Heat transfer measurements on a turbine airfoil at various Reynolds numbers and turbulence intensities including effects of surface roughness", ASME paper 96-GT-169.
21. Hoheisel H, Kiock R, Lichtfuss H J and Fottner L, 1987, "Influence of free-stream turbulence and blade pressure gradient on boundary layer and loss behavior of turbine cascades", *Journal of Turbomachinery*, vol. 109, April, pp. 210-219.
22. Holman J P, 1989, *Experimental Methods for Engineers*, 5th Edition, McGraw Hill, New York.
23. Hunt J C R and Graham J M R, 1978, "Free-stream turbulence near plane boundaries", *Journal of Fluid Mechanics*, vol. 84, part 2, pp. 209-235
24. Inoue, M., Kuromaru, M., "Structure of Tip Clearance Flow in an Isolated Axial Compressor Rotor", ASME 88-GT-251, 1988.
25. Inoue, M., Kuromaru, M., Fukuhara, M., "Behaviour of Tip Leakage Flow Behind an Axial Compressor Rotor", ASME paper 85-GT-62, 1985.
26. Kang, S., Hirsch, C., "Experimental Study on the Three-Dimensional Flow within a Compressor Cascade with Tip Clearance: Part I-Velocity and Pressure Fields, and Part II-The Tip Leakage Vortex", ASME *Journal of Turbomachinery*, Vol. 115,pg. 435-443, 1993.
27. Kang, S., Hirsch, C., "Tip Leakage Flow in Linear Compressor Cascade", ASME *Journal of Turbomachinery*, Vol. 116, pp. 657-664, 1994.
28. Krishnamoorthy V and Sukhatme S P, 1989, "The effect of free-stream turbulence on gas turbine blade heat transfer", *Journal of Turbomachinery*, vol. 111, October, pp. 497-501.
29. Kline S J and McClintock F A, 1953, "Describing Uncertainties in Single Sample Experiments", *Mechanical Engineering*, vol. 75, pp. 3.
30. Kuhl D D, 2001, "Near Wall Investigation of Three Dimensional Turbulent Boundary Layers", MS Thesis, AOE Dept, Virginia Tech

31. Kullar I, Graham J M R, 1986, "Acoustic effects due to turbulence passing through cascades of thin aerofoils", *Journal of Sound and Vibration*, vol. 110, No. 1, pp. 143-160.
32. Lakshminarayana, B., Murthy, K.S., "Laser Doppler Velocimeter Measurement of Annulus Wall Boundary Layer Development in a Compressor Rotor", ASME paper 87-GT-251, 1987.
33. Lakshminarayana, B., Pouagare, M., Davino, R., "Three Dimensional Flow Field in the Tip Region of a Compressor Rotor Passage-Part II: Turbulence Properties", ASME paper 82-GT-234, 1982.
34. Lakshminarayana, B., Ravindranath, A., "Interaction of Compressor Rotor Blade Wake with Wall Boundary Layer/Vortex in the End-Wall Region", ASME paper 82-GT/GR-1, 1981.
35. Lakshminarayana, B., Zaccaria, M., Marathe, B., "The Structure of Tip Clearance Flow in Axial Flow Compressors", *ASME Journal of Turbomachinery*, Vol.117, pp. 336-347, 1995.
36. Libby P A, 1996, "Introduction to Turbulence", Taylor & Francis Publishing.
37. Ma R, Saha N, Devenport W J, 2000, "Unsteady Behavior of a Tip Leakage Vortex Produced by Simulated Stator/Rotor Interaction", *Fluids 2000*, June 19-22, Denver Co, AIAA 2000-2217.
38. Mukhraiya J K, Ahmed N A, 1998, "Experimental Investigation of Axial Compressor Cascade Performance under the influence of Low Intensity Turbulence", 21st ICAS Congress, 13-18 September 1998, Melbourne, Australia.
39. Muthanna C, 1998, "Flowfield Downstream of a Compressor Cascade with Tip Leakage", M.S. Thesis, Virginia Tech, Blacksburg VA.
40. Muthanna C, De la Riva D, Devenport W J, Glegg S, 2000, "The Interaction of Free Stream Turbulence with a Compressor Cascade", AIAA Paper 2000-2467.
41. Phillips, W R C, Head M R, 1980, "Flow Visualization in the tip region of a rotating Blade Row", *International Journal of Mechanical Sciences*, vol 22. no 8, 1980, pp 495-521.
42. Poensgen, C.A., Gallus, H.E., "Rotating Stall in a Single-Stage Axial Flow Compressor", *ASME Journal of Turbomachinery*, Vol. 118, pp. 189-196, 1996
43. Pope S B, 2000, "Turbulent Flows", Cambridge University Press.
44. Popovski, P., Lakshminarayana, B., "An Experimental Study of the Compressor Rotor Flow Field at Off-Design Condition using Laser Doppler Velocimeter", ISABE 85-7034, Proceedings from International Symposium on Air Breathing Engines, 7th, September 2-6, (A86-11601-02-07) AIAA, 1985.
45. Radomsky R, Thole K A, 2000, "Highly Turbulent Flowfield Measurements around a Stator Vane", *Journal of Turbomachinery*, vol 122, no.2, pp. 255-262.
46. Radomsky R, Thole K A, 2001, "Detailed Boundary Layer Measurements on a Turbine Stator Vane at Elevated Free Stream Turbulence Levels", 2001-GT-0169.

47. Roach, P E, 1987, "The Generation of nearly Isotropic Turbulence by means of Grids", *International Journal of Heat and Fluid Flow*, Vol 8, pp 82-92.
48. Saha N, Ma R, Devenport W J, 2001, "Characterizing Unsteady Periodic Disturbances in the Tip Leakage Vortex of an Idealized Axial Compressor Rotor Blade" AIAA Paper 2001-0386.
49. Schetz J A, 1993, "Boundary Layer Analysis", Prentice Hall, Inc.
50. Shin S, Ragab S A and Devenport W J, "Numerical Simulation of Highly Staggered Cascade Flow Using an Unstructured Grid", 30th AIAA Fluid Dynamics Conference, Norfolk, VA, June 28-July 1, 1999, AIAA 99-3713.
51. Simpson R, 1999, "Turbulent Shear Flow", AOE 6154 Class Notes/Text, Virginia Tech.
52. Storer, J.A., Cumpsty, N.A., "Tip Leakage Flows in Axial Compressors", ASME paper 90-GT-127,1990
53. Thole K A, Bogard D G, 1996, "High Freestream Turbulence Effects on Turbulent Boundary Layers", *Journal of Fluids Engineering*, Vol 118, pp. 276-284.
54. Volino R J, 1998, "A New Model for Free Stream Turbulence Effects on Boundary Layers", *Transactions of the ASME, Journal of Turbomachinery*, Vol 120, July 1998, pp 613-620
55. Wang Y, 2000, "Tip leakage flow downstream of a compressor cascade with moving end wall", M.S. Thesis, Virginia Tech, Blacksburg VA.
56. Wenger C W, Devenport W J, Wittmer K S and Muthanna C, 1998, "Two-Point Measurements in the Wake of a Compressor Cascade", 29th AIAA Fluid Dynamics Conference, June 15-18, Albuquerque, NM. AIAA-98-2556.
57. Wisler, D. C., "Core Compressor Exit Stage Study, Volume IV-Data and Performance report for the Best Stage Configuration", NASA Report # CR-165357,1981
58. Wittmer K. S., Devenport W. J. and Zsoldos J. S., 1998, "A four-sensor hot-wire probe system for three-component velocity measurement", *Experiments in Fluids*, vol. 24, pp. 416.
59. Wunderwald D and Fottner L, 1996, "Experimental investigation of turbulence structures in the boundary layer of a highly loaded turbine cascade", ASME paper 96-GT-249.
60. Yocum, A.M., O'Brien, W.F., "Separated Flow in a Low-Speed Two Dimensional Cascade: Part I- Flow Visualization and Time-Mean Velocity Measurements", *ASME Journal of Turbomachinery*, Vol. 115, pp. 409-420, 1993
61. Young A D, 1989, "Boundary Layers", AIAA Education Series
62. Zhang L and Han J-C, 1995, "Combined effect of free-stream turbulence and unsteady wake on heat transfer coefficients from a gas turbine blade", *Journal of Heat Transfer*, vol. 117, May.

63. Zierke W C, Straka W A and Taylor P D, 1995, "An experimental investigation of the flow through an axial flow pump" (Data Bank Contribution), *Journal of Fluids Engineering*, vo. 117, September, pp. 485-490.
64. Zierke W C and Straka W A, 1996, "Flow visualization and the three-dimensional flow in an axial flow pump", *Journal of Propulsion and Power*, vol. 12, No. 2, March-April, pp. 250-259

Appendix: Uncertainty Analysis

An uncertainty analysis on the various quantities presented in the study were performed and are presented in this Appendix. In general, the uncertainty analysis involves determining the uncertainty in the primary measurements, and determining the uncertainty in the results derived from these primary measurements. Two methods can be used to determine uncertainties, and these are outlined below.

In the first method as outlined by Kline and McLintock (1953), the uncertainty of the derived value is due to the root sum square of the uncertainties of the primary measurements that define that value. For example, if $V=f(a,b)$, then the uncertainty in V , δV is computed as :

$$\delta V = \sqrt{\left(\delta a \frac{\partial f}{\partial a}\right)^2 + \left(\delta b \frac{\partial f}{\partial b}\right)^2}$$

where δa and δb are the uncertainties in the primary measurements a and b .

In the jitter analysis as described by Hollman (1989), the uncertainties are computed such that the effect of a perturbation on the quantity being considered is calculated and then the overall uncertainty determined. For example, if again we have $V=f(a,b)$, then the uncertainty can be computed as

$$\begin{aligned} \delta V &= \sqrt{(\Delta V(a + \delta a, b))^2 + (\Delta V(a, b + \delta b))^2} \\ \Delta V(a + \delta a, b) &= f(a, b) - f(a + \delta a, b) \\ \Delta V(a, b + \delta b) &= f(a, b) - f(a, b + \delta b) \end{aligned}$$

where again, δa and δb are the uncertainties in a and b .

A.1 Pressure Measurements

The uncertainties in the pitot static measurement are primarily due to the manometer reading connected to the probe ($\delta = 0.05$ in.of water), the thermocouple which measures flow temperature ($\delta = 0.01^\circ\text{F}$), and the barometer reading used to measure atmospheric pressure ($\delta=0.01\text{mbar}$). Using a jitter analysis, the uncertainty in the Pitot-Static Measurements is approximately 1.6% in velocity.

Uncertainties in the blade loading and the circulation on the blades is primarily due to the uncertainties in the pressure coefficient, C_p ($\delta=1.8\%$), and the chordwise position on the blades ($\delta=1\%$) which results in uncertainties in the circulation to be 2%, and in the lift coefficient to be 2.5%.

A.2 Hot Wire Measurements

Uncertainties estimates in the hot wire measurements which pertain to both single and four sensor measurements are dependent on the following conditions:

- Random voltage uncertainty in the A/D converter
- Uncertainty due to velocity calibrations
- Uncertainty due to angle calibrations
- Uncertainty due to sampling schemes
- Uncertainty due to the reference Pitot-static probe

The uncertainties in the final results from the hot wire measurements are dependent on which flow is being measured, with or without grid generated turbulence. Based on the primary uncertainties given above, the tables are the computed uncertainties for the single and four sensor hot-wire probes.

Table A1: Uncertainties for the four sensor hot wire probe

Quantity	Uncertainty (20:1 odds)	
	No Grid Case	Grid Case
U, V, W	$\pm 1\% U_\infty$	$\pm 1\% U_\infty$
u^2	$\pm 4\% u^2$	$\pm 4\% u^2$
v^2, w^2	$\pm 8\% v^2, \pm 8\% w^2$	$\pm 8\% v^2, \pm 8\% w^2$
uv, vw, uw	$\pm 4\% \sqrt{(u^2 v^2)}$	$\pm 3\% \sqrt{(u^2 v^2)}$

Table A2: Uncertainties for the single hot wire probe, for both flow cases.

Quantity	Uncertainty (20:1 odds)
U, V, W	$\pm 1\% U_\infty$
u^2	$\pm 4\% u^2$